

2-P (mx)

NATIONAL AERONAUTICS AND SPACE ADMINISTRATION

Technical Memorandum 33-683

*Mariner Mars 1971 Optical Navigation Demonstration
Final Report*

*G. H. Born, T. C. Duxbury, W. G. Breckenridge,
C. H. Acton, S. Mohan, N. Jerath,
H. Ohtakay*

(NASA-CR-138453) MARINER MARS 1971
OPTICAL NAVIGATION DEMONSTRATION Final
Report (Jet Propulsion Lab.) 333 p HC
CSCL 17G

N74-26144

63/21 Unclas
39742

Reproduced by
NATIONAL TECHNICAL
INFORMATION SERVICE
US Department of Commerce
Springfield, VA. 22151

PRICES SUBJECT TO CHANGE

JET PROPULSION LABORATORY
CALIFORNIA INSTITUTE OF TECHNOLOGY
PASADENA, CALIFORNIA

April 15, 1974

NATIONAL AERONAUTICS AND SPACE ADMINISTRATION

Technical Memorandum 33-683

*Mariner Mars 1971 Optical Navigation Demonstration
Final Report*

*G. H. Born, T. C. Duxbury, W. G. Breckenridge,
C. H. Acton, S. Mohan, N. Jerath,
H. Ohtakay*

JET PROPULSION LABORATORY
CALIFORNIA INSTITUTE OF TECHNOLOGY
PASADENA, CALIFORNIA

April 15, 1974

Prepared Under Contract No. NAS 7-100
National Aeronautics and Space Administration

PREFACE

The work described in this report was performed by the Mission Analysis Division and the Guidance Control Division of the Jet Propulsion Laboratory.

ACKNOWLEDGMENTS

The Mariner Mars 1971 Optical Navigation Demonstration (OND) Team was composed of the following personnel: T. C. Duxbury, G. H. Born, N. Jerath, M. P. Ananda, S. N. Mohan, and G. A. Ransford, from the Mission Analysis Division, and C. H. Acton, Jr., W. G. Breckenridge, M. H. Bantell, and H. Ohtakay from the Guidance and Control Division.

The success of the demonstration was made possible by the contributions of many people throughout JPL and NASA's Office of Aeronautics and Space Technology (OAST). The OND team wishes to acknowledge a few individuals who were particularly helpful to the Demonstration.

Thanks are extended to the members of the Review Board for their guidance of the Demonstration Team's activities. The Board members included T. W. Hamilton, JPL Navigation Board Manager and Chairman of the Review Board; R. V. Powell, of the Office of Research and Development; R. V. Morris, of the Mission Analysis Division; K. M. Dawson, J. W. Moore, and G. Paine, of the Guidance and Control Division; G. M. Smith, of the Space Sciences Division; and T. H. Thornton and N. H. Haynes, of the MM'71 Project Office. Appreciation is also expressed to L. Efron and R. F. Bohling, Division R/AD Representatives of the Mission Analysis and Guidance and Control Divisions, who interfaced between the OND and the Office of Research and Development.

The cooperation of the MM'71 Project was instrumental in the success of the Demonstration. The following MM'71 Project personnel are given special thanks for their efforts on behalf of the Demonstration: R. T. Hayes, J. F. Jordan, P. J. Rygh, D. Schneiderman, T. Vrebalovich, S. Z. Gunter, E. Christensen, G. Holmann, R. Johansen, W. Green, and J. Seidman.

The authors also express their thanks to the American Institute of Aeronautics and Astronautics, the American Astronautical Society, and the Institute of Navigation for permission to reprint various Appendixes that appear in this report, all of which are published here with the approval of the organization that holds the applicable copyright.

CONTENTS

I.	Introduction and Scope of Document	1
II.	MM'71 Optical Navigation Demonstration Overview	1
	A. Introduction	1
	B. Major Conclusions and Recommendations	3
III.	Approach Phase of Demonstration	6
	A. Introduction	6
	B. Mission Operations	6
	C. Image Extraction	7
	D. Instrument Performance	8
	E. Approach Phase Navigation Results	11
IV.	Orbital Phase Navigation Results	16
	A. Introduction	16
	B. Real-Time Orbital Results	16
	C. Orbital Phase Postflight Navigation Results	17
	D. Important Factors for Orbit Determination	19
	E. Concluding Remarks	21
V.	Additional Efforts	22
	A. Orbital Phase Navigation Results Using Landmark Data	22
	B. Results of Mars Limb Tracking	23
	C. Science Fallout from the MM'71 Demonstration	26
	D. Satellite Geodesy	28
	References	31

CONTENTS (contd)

APPENDIXES

- A. Duxbury, T. C., "A Spacecraft-Based Navigation Instrument for Outer Planet Missions," Journal of Spacecraft and Rockets, Vol. 7, No. 8, August 1970.
- B. Duxbury, T. C., and Ohtakay, H., "In-Flight Calibration of an Interplanetary Navigation Instrument," Journal of Spacecraft and Rockets, Vol. 8, No. 10, October 1971.
- C. Duxbury, T. C., Wong, S. K., and Born, G. H., "Encounter Trajectory Accuracy for a 1971 Mars Orbiter Mission," AIAA Paper 71-189, AIAA 9th Aerospace Sciences Meeting, New York, January 1971.
- D. Duxbury, T. C., and Born, G. H., "Tracking Phobos and Deimos Aboard an Orbiting Spacecraft," AAS Paper 71-372, Astrodynamics Specialists Conference, Ft. Lauderdale, Florida, August 1971.
- E. Mohan, S. N., and Ransford, G. A., "Cartography and Orbit Determination From a Mars Orbiting Spacecraft," AAS Paper 71-373, AAS/AIAA Specialists Conference, Ft. Lauderdale, Florida, August 1971.
- F. Breckenridge, W. G., and Acton, C. H., Jr., "A Detailed Analysis of Mariner 9 TV Navigation Data," AIAA Paper 72-866, AIAA Guidance and Control Conference, Stanford University, Stanford, California, August 1972.
- G. Acton, C. H., Jr., "Processing On-Board Optical Data for Planetary Approach Navigation," AIAA Paper 72-53, AIAA 10th Aerospace Sciences Meeting, San Diego, California, January 1972. (Also published in the Journal of Spacecraft and Rockets, Vol. 9, No. 10, October 1972).
- H. Duxbury, T. C., and Acton, C. H., "On-Board Optical Navigation Data From Mariner 71," Journal of the Institute of Navigation, Vol. 19, No. 4, Winter, 1972-1973.
- I. Duxbury, T. C., Born, G. H., and Jerath, N., "Viewing Phobos and Deimos for Navigating Mariner 9," AIAA Paper 72-927, AIAA/AAS Astrodynamics Conference, Palo Alto, California, September 1972.
- J. Miller, J. A., Summary of Results of MM'71 OND TV Data Analysis, "

CONTENTS (contd)

- K. Born, G.H., "Ephemeris Theory for Phobos and Deimos."
- L. Acton, C.H., and Breckenridge, W.G., "MM'71 Orbital Sequence Satellite Picture Summary."
- M. Born, G.H., "Results of Orbital Phase Navigation Study Using Satellite Data."
- N. Born, G.H., "Mars Physical Parameters as Determined from Mariner 9 Observations of the Natural Satellites," AAS Paper, AAS/AIAA Astrodynamics Conference, Vail, Colorado, July 1973.
- O. Mohan, S.N., "Pole Direction, Cartography, and the Shape of Mars."
- P. Mohan, S.N., "Topographical Coordinates From Mariner 9 Observations of the Martian Surface," AAS Paper, AAS/AIAA Astrodynamics Conference, Vail, Colorado, July 1973.
- Q. Mohan, S.N., "Results of Orbit Phase Navigation Study Using Landmark Data."
- R. Ohtakay, H. and Jerath, N., "Mariner Mars '71 Optical Limb Data Measuring Techniques and Navigation Results," AIAA Paper, AIAA 11th Aerospace Sciences Meeting, Washington, D.C., January 1973.
- S. Duxbury, T.C., "Phobos: Control Network Analysis."

7<

ABSTRACT

The primary purpose of the Mariner Mars 1971 (MM'71) Optical Navigation Demonstration was to prove the feasibility of using a combination of spacecraft-based optical data and Earth-based doppler data to perform near-real-time approach navigation for the MM'71 mission. The optical data consisted of Mariner 9 television photographs of Mars' natural satellites Phobos and Deimos against a star background.

The objectives of the demonstration were successfully carried out, and this report documents the important findings, conclusions, and recommendations resulting therefrom. The report is divided into two parts: a formal summary section and a section of appended publications and papers giving additional details on the primary and secondary objectives of the demonstration. The appendixes describe instrument calibration and performance as well as navigation and science results obtained by processing TV data of Mars' natural satellites, Mars' landmarks, and Mars' lit limb taken during both the approach phase and the orbital phase of the MM'71 mission.

I. INTRODUCTION AND SCOPE OF DOCUMENT

This report documents the important findings, conclusions, and recommendations which have resulted from the MM'71 Optical Navigation Demonstration. The report is divided into two parts: (1) a formal summary section which covers the most significant aspects of the demonstration and (2) a section of appended reports and publications which have resulted either directly or indirectly from work on the demonstration (Appendixes A through S). These appendices are referenced in the formal portion of the report and may be consulted for more detail. They cover such areas as instrument performance, navigation and science results, software configuration, and real-time operations.

The formal section of this report is divided into four major subsections. Section II is a general discussion of the demonstration, summarizing major accomplishments, conclusions, and recommendations. This section is recommended to anyone interested in a succinct discussion of the overall demonstration without technical detail. The remainder of the report is an expansion of this section. Section III contains a discussion of the approach phase instrument performance and calibration as well as real-time and postflight navigation results. Orbital Phase real-time and postflight navigation results are included in Section IV. Additional results which were generated either directly or indirectly from performing the assigned functions of the demonstration and the mission are discussed in Section V. These include navigation results from landmark and Mars' limb tracking as well as science fallout such as Mars' gravity field, mass, and spin axis direction. In addition, Phobos and Deimos ephemeris improvement and the results of satellite topography studies are included.

II. MM'71 OPTICAL NAVIGATION DEMONSTRATION OVERVIEW

A. INTRODUCTION

In order to meet stringent navigation accuracy requirements for the outer planet missions, a new concept of using a science TV camera to photograph the natural satellites of a target planet against a star background was proposed (Appendix A). Studies have shown that suitable navigation

system performance is obtainable by combining conventional Earth-based radiometric data with the satellite/star data and that measurement accuracies on the order of a few arc seconds are required (Appendix B). This level of accuracy was shown to be obtainable through the use of a reseau grid to calibrate electromagnetic TV distortion and the use of stars to determine inertial TV pointing directions.

The Mariner Mars 1971 (MM'71) mission offered a unique opportunity to evaluate the satellite/star navigation concept through the use of the Mariner 9 narrow-angle TV camera. This camera had the capability of simultaneously imaging Phobos or Deimos and stars as dim as 9th magnitude. To exploit this opportunity, an Optical Navigation Demonstration (OND) was formed early in 1970. The OND team's function was to prove the feasibility of using satellite/star data together with radiometric data to perform real-time approach navigation for the MM'71 mission.

The OND was a NASA OAST-funded R/AD activity which operated within the MM'71 mission on a noninterference basis. The MM'71 Project agreed to assist the OND to its fullest capabilities. Accordingly, the OND software was accepted into the Mission Software System and the OND team was accepted as part of the Mariner 9 Navigation Team. The OND had no formal commitment to MM'71, except that navigation results were to be supplied on a best-effort basis.

In mid-November 1971, after Mariner 9 was inserted into orbit about Mars, the preflight and real-time activities of the OND came to a successful conclusion. The satellite/star TV data concept, including the in-flight calibration, had been demonstrated successfully. TV pictures of Deimos against a star background were processed in combination with Earth-based radio tracking data to produce the most accurate real-time approach trajectory estimate in the history of interplanetary space flight. This estimate was factored into decision processes for the critical orbit-insertion maneuver.

The success of the OND was due in large part to the great amount of planning, analysis, and training that occurred prior to the real-time operations. The preflight activities were jointly formulated and reviewed by the Jet Propulsion Laboratory Navigation Planning Board (JNP) and the OND

Team. The review board included JPL management from three technical divisions, from the JPL Research and Advanced Development office, and from the MM'71 Project Office. Based on the success of the OND, both Viking and Mariner Jupiter/Saturn Projects are committed to the use of the satellite/star technique, and the OND software is the baseline system for Viking. This concept is also being employed in navigation studies for the proposed Mariner Jupiter/Uranus and Jupiter Orbiter Satellite Tour missions.

B. MAJOR CONCLUSIONS AND RECOMMENDATIONS

The following subsections give an overview of the major conclusions and recommendations of the demonstration of importance to future missions which may consider satellite/star imaging as a potential source of navigation data. More detailed discussions are given in Sections III, IV, and VI.

1. Satellite/Star Data Concept

The concept of using satellite/star data in combination with Earth-based radiometric data for navigation was proved to be technically sound (Appendix I). The satellite/star data allows determination of the spacecraft's trajectory relative to a satellite directly and relative to the planetary bary-center indirectly through the dynamics of the system. In addition the motion of the satellite about the planet gives added parallax over planet observations. The satellite-relative aspects of this data type makes it particularly attractive to missions considering close satellite flybys. The satellite/star data also yielded significant science information on the dynamics of the planet/satellite system (Appendix N).

In the case of MM'71, satellite/star data was shown to be superior to planet limb data for navigation purposes (Appendix R). This was due primarily to small center-finding errors (3 arc seconds, 1σ) for the satellites, combined with pointing data accurate to 3 arc seconds, 1σ obtained from stars. Center-finding errors for Mars limb data are an order of magnitude greater than those for the satellites. Also, the star images allowed a determination of TV pointing which was independent of, and a factor of 25 more accurate than, the telemetered engineering data.

2. Science TV Camera as a Navigation Sensor

The narrow-angle (500-mm focal length) TV camera proved to be an ideal instrument for producing the satellite/star data for the MM'71 mission. The TV camera demonstrated a capability of detecting 9th magnitude stars, a dynamic range of 10^6 in brightness and a measurement accuracy of 3 arc seconds (1σ). This measurement accuracy, which is on the order of the angular resolution of the camera, was achieved through both ground and in-flight calibration of the TV system.

In general, a navigation sensor should have arc second level accuracy and have the sensitivity to detect 9th magnitude stars of type B through K. Its sensitivity should be sufficient to allow the detection of these dim stars with short exposures to minimize image smear during exposure. Image blooming of the target body should be less than 1% of the body diameter when imaged simultaneously with stars. The sensor field of view should be sufficiently large to image at least one 9th magnitude star with the target body. Also, it is desirable for image distortions to be stable for the navigation observations.

3. Team Staffing

The OND team comprised analysts from the Mission Analysis Division and the Guidance and Control Division of JPL. This staff provided the necessary expertise to carry out the objectives of the demonstration. For future missions in which optical navigation is a prime requirement, it is recommended that the staff be expanded to also include personnel from the Space Sciences and Data Systems Divisions. The expanded staff will provide a broadened expertise in the areas of imaging instrument performance and imaging data processing and display.

4. Software System Performance

All data were processed and internal interface functions were performed without significant error and within specified timelines (Appendix H). The OND lacked the software to produce or the authority to request hard-copy photographic products of the digital imaging data in real time, other than those normally produced by the Mission Test Computer (MTC). These

hard-copy displays, consisting of stretched and filtered digital imaging data, were found to be superior to either printouts or plots of the digital data for dim image detection, and comparable to digital data for determining center-of-image location. Future missions should consider having special imaging display products, optimally stretched and filtered for navigation purposes, supplied by the MTC or the Image Processing Laboratory (IPL) or their equivalent.

Preflight prediction of star detection capability was limited by predicted software image detection capabilities and predicted instrument performance. Consequently, preflight picture planning was somewhat hampered. Because the OND was self-contained, its software overlapped that of the MM'71 mission to some extent. Future missions may find it desirable to eliminate some of this overlap.

5. Mission Interfaces

With one exception, all mission interface functions were performed properly and within planned times. The only problem encountered was a 4- to 6-hour delay in obtaining the digital imaging data on tape and an additional 1-hour delay in copying the data from tape into the navigation computer. Access time to processed and displayed imaging data can be minimized by using real-time mission data-processing computers such as the MTC, IPL, or their equivalent to perform the optical navigation image-processing functions.

6. Satellite Ephemerides

The satellite ephemeris theory used for Phobos and Deimos, which contained only the effects of J_2 , had a precision of 3 km relative to a numerical integration containing solar and Mars gravitational perturbations during the Mariner 9 approach phase, thus meeting the preflight objective of 5 km (Ref. 1). The real-time data processing reduced the position uncertainties of Phobos to 50 km (1σ) and Deimos to 10 km (1σ), which met the preflight objectives of 50 km and 20 km respectively. However, the ephemeris model lacked solar and tesseral gravity perturbations, which limited its accuracy for long-term prediction. A new theory was developed

for postflight data reduction which included the zonal and tesseral harmonics of Mars' gravity field as well as solar gravity perturbations. The internal consistency of this theory relative to numerical integration is 0.5 km (Appendix K). Postflight evaluation revealed that Wilkins' theory (Ref. 2) has an internal precision of 10 km for prediction periods of a few years and would be well suited for Mars missions requiring this level of accuracy.

7. Engineering Data

A secondary effort of the demonstration was to evaluate additional sources of TV pointing data for navigation. Star data was found to be a factor of 25 more accurate than telemetered scan platform and attitude sensor data for determining TV pointing (Appendixes F and H). Also, the errors associated with the engineering data were found to have a systematic as well as a random component. Consequently, engineering data was not found to be an acceptable alternative to star data for determining TV pointing when kilometer-level approach navigation accuracies are required. However, the data is useful in the image identification process.

III. APPROACH PHASE OF DEMONSTRATION

A. INTRODUCTION

This section describes the activities of the OND that were related to the approach phase of the MM'71 mission. The topics discussed are a summary of real-time operations procedures, instrument calibration and performance, and methods of image extraction. Finally, both real-time and postflight navigation results are presented.

B. MISSION OPERATIONS

The approach navigation pictures were part of three Pre-Orbital Science (POS) sequences which began approximately 3 days before Mars orbit insertion. POS I and II were to contain 6 and 7 Deimos/star pictures respectively and were scheduled for playback prior to orbit insertion. Consequently, they formed the data base for the real-time phases of the demonstration. A third science sequence, POS III, which was scheduled to contain

5 Deimos and 3 Phobos pictures, was to be played back after Mars orbit insertion. Hence, this data could be used only for postflight evaluation.

Prior to playback of a science sequence, a priori TV pointing estimates were obtained by processing telemetered spacecraft engineering data. The telemetered data was received in real-time and was immediately accessible to the OND from teletype printout. After playback, TV digital data was processed and displayed on computer printouts. Satellite and star image locations were manually identified and measured from the printout. Then, using the telemetered pointing data as a priori values, the satellite/star data was validated and TV pointing based on star data was determined. Next the optical data was processed by the OND orbit-determination software to determine improved estimates for such factors as spacecraft state, satellite ephemerides, and TV biases and pointing. Using these new estimates, an optical data file containing partial derivatives and image line and pixel residuals was generated. This file, combined with a comparable file for radiometric data generated by the Mariner 9 Navigation Team, was processed with the JPL Orbit Determination Program to produce combined radio/optical solutions. After each Pre-Orbital Science sequence, the improved estimates of satellite and TV parameters were used to update the TV pointing commands for future pictures.

C. IMAGE EXTRACTION

Video data was made available to the demonstration in the form of digital data on magnetic tapes and hardcopy photographs constructed from stretched and filtered digital imaging data. The digital tapes were processed by the Image Processing Program (IMP), which was part of the demonstration's software (Appendix H). The hard-copy display was scanned directly by analysts to detect and identify images and to approximate image location.

IMP was designed to work in both automatic search and directed display modes. In the automatic search mode, an entire picture or selected portion was scanned for image signals. Suitable filters were used to reject random noise and bit errors. The digital data surrounding each detected signal was displayed on a line printer for evaluation by an analyst who

ultimately identified the signal and determined the observation coordinates. This procedure proved effective in detecting all Phobos and Deimos images and most stars brighter than magnitude 8.

The directed display mode was used to detect dim star image locations. In this mode, expected star image locations were scanned by predicting their locations relative to known bright star images in the same picture. This process was used to eventually identify images of stars between magnitudes 8 and 9.

Examination of hard-copy photographs also proved effective in detecting most star images. In fact, the hard-copy photographs supplied in near-real-time by the MTC were most effective in detecting dim star images. Simulated picture overlays generated by demonstration software were necessary to effectively use the hardcopy display.

Delays in receiving the video products for processing were, by far, the most time-consuming portion of the optical orbit-determination process. Future missions should consider the use of high-speed interactive video processing/display devices. These devices could interface with the MTC or the IPL or their equivalent to provide real-time video data.

D. INSTRUMENT PERFORMANCE

The optical navigation measurements used for determining the spacecraft trajectory were formed using data from sensors on board the spacecraft. The pictures from the TV camera provide measurements of the directions to objects within the field of view relative to the TV camera line of sight (LOS). When there are stars (having accurately known directions) in the picture, both the direction of the LOS and of other objects (e.g., a satellite) in the picture can be accurately determined. The attitude control sun and star sensors provided information on spacecraft orientation, while scan platform actuator data indicated the direction of the TV camera LOS with respect to the spacecraft. Together these data can provide a measure of the inertial direction of the TV camera LOS when there are no stars in a picture, but with less accuracy.

The accuracy of the optical navigation measurements depends upon the accuracy with which the measured angles can be reconstructed from the TV or other sensor data. TV and sensor output models contain parameters for mechanical alignment, null offset, scale factor, nonlinearity, etc. The accuracy of the reconstructed angles depends on the accuracy of calibration of these models plus the inherent data noise due to quantization of sensor outputs for digital telemetry.

The distortion in the TV camera was calibrated, using both reseaux and stars in the pictures, with calibration residuals over the whole frame of about 0.6 pixel (3.5 arc seconds) 1σ , including both residual distortion and image location errors. The residual error was smaller for the central part of the frame, where distortion is less. More details regarding the results of the calibration are found in Appendix F. The calibration of the attitude control and scan platform measurements was done using a series of TV pictures of stars and resulted in a posteriori model parameter errors contributing about 0.005 deg 1σ bias to the total error in determining the inertial pointing direction of the TV LOS. The error in determining TV pointing was observed to be as predicted except that the platform cone gimbal angle had a clock-angle-dependent hysteresis which was not included in the model and degraded cone angle knowledge from 0.018 deg to 0.026 deg 1σ .

The value of in-flight calibration over preflight ground calibration is indicated by the size of parameter value changes. Corrections of up to 0.5 deg were made in attitude control sensor and scan platform models. Pointing control errors of this size would seriously affect the capability to obtain a picture of specified objects. Once a picture containing stars is taken, the camera pointing can be determined accurately if the stars can be identified, but the identification process is made more difficult if the expected picture content (based on pointing knowledge) is inaccurate. The ground calibration of TV distortion (nonlinear terms) was unchanged by in-flight calibration, but there was a small linear shift and rotation of the scan lines, equivalent to a camera alignment error but not affecting relative locations of star/satellite images.

Another TV performance parameter important to optical navigation is the star detection threshold, i. e., the dimmest star that has a detectable

signal in the video data. Preflight estimates of this threshold were as low as 6.5 visual magnitude; however, inflight, it was found that 8.5 magnitude stars were easily detected and stars as dim as 9.5 were occasionally seen. Stray light effects did not hinder detection of dim star images even when the lit limb of Mars was only 0.2 deg outside the TV field of view. The analysis of some of the factors affecting star detectability is discussed in Appendix J and Ref. 5.

The star/satellite pictures for the OND were taken with an exposure time of about 6 seconds, the maximum allowable, to maximize the possible signal magnitude. The selection of the best shutter time is an area where a tradeoff can be made. The exposure time for a single pixel of the picture is limited by the attitude control rate (i. e., how long it takes the image to traverse the pixel). For brighter stars, a longer exposure does not increase the signal amplitude, and hence makes the star no easier to detect, but will smear the image, making its location less accurate. For dim stars, some smearing enhances detectability by enlarging the very small image. Very bright images (e. g., planets or satellites) can introduce local distortion if the image charge deflects the scanning beam; thus shorter exposures would produce less charge and less distortion. The optimum exposure time for a picture is thus a balance of detectability and location accuracy of the images, depending on attitude control rate, detection threshold, and the number and brightness of the expected images in the picture.

The sensor performance observed during calibration was confirmed by the performance for the satellite/star pictures taken for optical navigation during the approach to Mars. The knowledge of TV pointing from attitude control and scan platform data was 0.012 deg (43 arc seconds) 1σ in clock angle and 0.025 deg (90 arc seconds) in cone, while the accuracy obtained from star images was considerably more accurate, 0.4 pixel (2.5 arc seconds), as indicated by the residuals in relative star image locations in pictures with more than one star. An average of 2.5 stars per picture (range: 1 to 4) was detected during real-time operations. More detail regarding the evaluation of those optical navigation pictures is found in Appendix H and of the resulting navigation performance in Appendix I.

The performance of the on-board measurements used for optical navigation generally met or exceeded the preflight expectations but can be improved. For the primary data type, star/satellite TV pictures, the accuracy was determined mainly by three things: the geometric resolution (arc second/pixel), image location error, and unmodeled local distortion. Further hardware and software developments can improve all three; e. g., the use of longer focal length optics or larger image format, improved software algorithms for image location, and lower distortion cameras or more detailed distortion models.

The performance of the attitude control sensor measurements was limited by the telemetry resolution. The scan platform gimbal measurements were affected by telemetry resolution, residual calibration errors in the fine potentiometers, and unmodeled hysteresis. These factors can be improved by telemetry system design/scaling, better ground calibration of the fine potentiometers, and development of software, including hysteresis models.

E. APPROACH PHASE NAVIGATION RESULTS

1. Introduction

This section presents real-time and postflight navigation results of the approach phase of the MM'71 Optical Navigation Demonstration, included are discussions of data distribution and accuracy, encounter parameter solutions, and associated sensitivities to error sources and estimation strategy. More details on the topics of this section are given in Appendix H and I.

2. Data Distribution

The real-time navigation results of the MM'71 OND were generated on the basis of 12 Deimos/star photographs. These were taken by the narrow-angle TV camera during POS I and II. POS I and II encompassed the time period from Encounter - 66 (E-66) hours to E - 22 hours. POS I, which contained 6 Deimos/star photographs, occurred between E - 66 and E - 53 hours. This sequence of photographs was played back to Earth at E - 45 hours; however, the first Deimos picture was lost in transmission to JPL.

The 7 photographs taken between E - 44 and E - 23 hours (Pos II) was played back at E - 17 hours.

The postflight navigation results were based on Pos I and II data as well as 5 Deimos and 2 Phobos photographs recorded during POS III. These pictures were taken between E - 16 and E - 8 hours but were not played back until after Mars orbit insertion. (See Appendix H for more details on the data and pointing information).

3. Navigation Results - Optical Plus Radio Data

Solutions for encounter conditions based on a combination of doppler and optical data are of particular value because of the complementary nature of these data types (Appendix I). Solutions derived from Earth-based radio-metric data are susceptible to planetary ephemeris errors, station location errors, and non-gravitational accelerations, while optical data is insensitive to these errors since it directly relates planet and spacecraft positions. On the other hand, optical data suffers from an inability to accurately determine spacecraft velocity, which in the case of Mariner 9 is well determined by radio data. Consequently, optical and radio data can be combined to give good estimates of encounter conditions much earlier than either data type taken separately.

For the MM'71 demonstration a short arc (4 days) of doppler was combined as independent data with the 12 Deimos/star pictures of POS I and POS II to form the real-time navigation solutions of the demonstration. The object was to use enough radio data to determine spacecraft velocity but not enough to dominate the optical data. This strategy was dictated by preflight covariance analysis.

The star data in the pictures was preprocessed by the demonstration's software to remove TV pointing, distortion, and biases errors. Next the Deimos data, together with the radio data, were processed with the JPL Satellite Orbit Determination Program (SATODP). This program was run in the batch processor mode and was capable of estimating spacecraft state, satellite ephemeris, Mars mass, spin axis direction, and zonal harmonics. The optical images were weighted at ± 6 arc seconds (1σ) while the doppler data was assumed accurate to 1 mm/second. The solution was loosely constrained with an a priori covariance matrix; however, this was not necessary.

An analytical satellite theory which contained the secular and periodic effects of Mars oblateness (J_2) was used to propagate the position of Deimos throughout the encounter period. For this brief period of time, the theory was accurate to ± 3 km relative to numerical integration, including the effects not only of J_2 but also Mars' second-order tesseral harmonics and solar gravity.

The optical demonstration's estimate of encounter parameters was available 10 hours before encounter and was a significant influence in confirming that the encounter conditions of Mariner 9 would be within acceptable limits. This solution was within 70 km of the best solution based on radiometric data alone at that time. Postflight analysis showed this real-time estimate based on a combination of Deimos/star and doppler data to be within 10 km of the current best estimate (CBE) of encounter conditions. Consequently, it is the most accurate solution generated during any real time approach operations.

4. Real-Time Results - Optical Only

In addition to the combined data solutions, two solutions using a nominal spacecraft trajectory based on radio data but generating encounter solutions based solely on Deimos/star data from POS I and II were generated. These solutions were within 40 to 60 km of the CBE; hence, as preflight covariance analysis indicated, (Appendix C) they were not as accurate as the combined data type solutions. They were, however, well within their 1σ formal uncertainties.

The optical-only solutions were generated with demonstration software using a sequential filter which had the added capability of solving for constant and time-correlated TV pointing parameters. Hence, preprocessing of the data to solve for TV pointing errors was not necessary as in the case of the SATODP batch filter. Because of this added flexibility, the sequential processor is recommended for future missions.

5. Postflight Results

The POS III playback, which occurred after Mars orbit insertion, contained 5 Deimos and 2 Phobos pictures taken between E - 16 and E - 8 hours.

These were used in the postflight analysis, together with the 12 Deimos pictures processed in real time. The addition of the POS III data shifted the solution for the encounter conditions to within 5 km of the current best estimate. Consequently, postflight evaluation has confirmed the real-time trajectory estimates. Post-fit residuals have shown 3-arc second accuracy of the optical data. All navigation results generated by the demonstration were well within expected accuracies based on preflight covariance analysis.

6. Solution Sensitivities

The sensitivity of the solutions for B-plane encounter parameters to such things as the number and type of parameters in the solution list, the number of stars per picture, TV distortion, and Mars stray light are reported in Appendix I. The salient points are summarized below:

- (1) Two elements, inclination and mean anomaly, were adequate to define Deimos' orbit since the remaining elements were accurately known before the flight. Estimates of encounter parameters were insensitive to the solution list parameters as long as these two elements of Deimos orbit, together with the spacecraft state, were included in the solution list. Solution sensitivity to Mars mass, spin axis direction, and oblateness were negligible since the data was relatively insensitive to these parameters because of large Mars-spacecraft distance.
- (2) At least one star, combined with a priori pointing data, is required to ensure accurate TV pointing information. Solutions were insensitive to more than one star per picture; however, from a reliability standpoint, several stars per picture are desirable to provide independent checks on TV pointing and TV distortion.

7. Important Factors for Orbit Determination

The important factors for approach-phase orbit determination can be summarized as follows:

- (1) The picture sequence should contain satellite pictures from at least one complete orbit spaced so that the satellite ephemeris

can be accurately determined if it is not well known a priori. Whenever possible, the satellite theory should be validated preflight, preferably by fitting real data, such as Earth-based observations.

- (2) Sufficient doppler data must be available to determine spacecraft velocity. Items (1) and (2) are best analyzed through covariance analysis.
- (3) The first-order satellite theory containing periodic effects of J_2 was adequate (± 3 km) during the brief encounter phase. Moreover, an even simpler theory such as that of Wilkins, which is a secularly precessing ellipse relative to the Laplacian plane and accurate to ± 5 km for this time period, would also have been adequate. However, neither of these theories models the effects of tesseral harmonics on Phobos (± 2 km) or the long-period perturbations of the sun on the longitude of Deimos (± 120 km with a period of 54 years).
- (4) Deimos' size, shape, albedo, and rotational properties had a negligible effect on approach results, primarily because of its small size. However, for larger satellites, these effects could be significant.
- (5) TV distortion was not a limiting error source to navigation, since it was stable and could be modeled to subpixel accuracy.
- (6) Two factors contributed significantly to the success of the MM'71 OND. The first was accurate pointing information (3 arc seconds 1σ) obtained by imaging the satellite with stars. The second was the resolution of the narrow-angle camera, which allowed the center of figure of the Deimos images to be determined to ± 3 arc second (1σ).

8. Concluding Remarks

The MM'71 Optical Navigation Demonstration proved satellite/star data to be a valuable complement to Earth-based radio data for planetary approach navigation. All navigation results generated by the demonstration

were well within expected bounds, based on preflight covariance analysis. As a result of the MM'71 demonstration the Viking and Mariner Jupiter/Saturn (MSJ) Projects have been committed to the use of satellite/star data for navigation. In addition, the combination of optical and radio data is now routinely considered in advanced mission navigation studies at JPL.

IV. ORBITAL PHASE NAVIGATION RESULTS

A. INTRODUCTION

This section of the report presents real-time and postflight navigation results of the orbital phase of the MM'71 Optical Navigation Demonstration. More details on the topics of this section are given in Appendixes M and N.

B. REAL-TIME ORBITAL RESULTS

The real-time phase of the demonstration consisted of updating the Phobos and Deimos ephemerides to assure acquisition of these satellites for future orbital pictures. In addition, members of the demonstration team worked closely with members of the TV imaging team in science picture planning by generating the necessary timing and pointing data for all satellite pictures. The picture planning effort was funded by the MM'71 Project from the third quarter of FY72 through the extended mission. With the exception of a few early orbit phase satellite pictures which were lost because of a software error coupled with Phobos ephemeris errors, the real-time responsibilities of the orbital demonstration were successfully met.

Since the satellite pictures taken during the orbital phase of MM'71 were for science purposes, the exposure times were too short to image stars. Consequently, the camera pointing was determined from spacecraft telemetry data which in the orbital phase was about a factor of 35 less accurate than if stars were visible in the picture. This fact, coupled with the sparsity of satellite pictures, made a real-time navigation demonstration impractical. However, the feasibility of overexposing satellite images in order to detect star images was successfully demonstrated. The final picture received from the Mariner 9 spacecraft during its operative lifetime was an overexposed picture of Phobos in which 10 stars were visible. This

picture was taken at the request of the Mariner Jupiter/Saturn Project. Since image blooming was shown to be small, overexposure of Galilean satellites in order to detect star images is now part of the MJS mission plan.

The orbital phase pointing data was less accurate than the approach data because pictures were taken throughout the scan platform angular range, whereas during the approach phase the scan platform was practically fixed. In addition, there were no periodic calibrations to redetermine TV bias parameters.

C. ORBITAL PHASE POSTFLIGHT NAVIGATION RESULTS

The optical data processed for the postflight phase of the demonstration consisted of a set of 62 hardcopy photographs of Phobos and Deimos taken between revolutions 25 through 221 of Mariner 9, as follows:

- 21 Phobos A (wide-angle) frames
- 27 Phobos B (narrow-angle) frames
- 3 Deimos A (wide-angle) frames
- 11 Deimos B (narrow-angle) frames

Data from these pictures consisted of camera pointing angles and the line and pixel locations of the center of figure of the Phobos and Deimos image. Computer-generated overlays supplied by the TV team and produced from a triaxial model of the figure of the satellites were used to determine the center of figure of the images. These overlays were generated to scale for each picture and contained the terminator as well as the center of figure location for the satellite. A summary of the orbital phase data is given in Appendix L.

Preflight covariance analysis has shown that a combination of optical and radio data can be very effective in determining the state of an orbiting vehicle. The procedure is to use a short arc of radio data (one revolution or less) together with 10-12 satellite/star pictures (see Appendix D). As in the case of planet encounter, the radio and optical data complement one another. Radiometric data determines all elements of the spacecraft state with the exception of the node of the orbit relative to the plane of the sky

(referred to as Ω_{pos}). The plane of the sky is perpendicular to the Earth-Mars line. Satellite/star data then determines Ω_{pos} and the state is completely known.

In the case of MM'71, the scarcity of optical data precluded a demonstration of short arc orbit determination capabilities of combined data. However, a long arc analysis of combined optical and radiometric data is possible with the data.

The long arc analysis was accomplished by processing the data in a two-stage filter. In the first stage a batch filter was used to process the doppler data in short arcs to determine a series of apoapsis state vectors (Ref. 6). This was done for each orbit from revolutions 5 through 200. These 195 state vectors, referred to as radio normal points, together with the center of image coordinates of the satellites become the data for the second stage of the filter.

The second stage of the filter was a sequential processor which had the capability to solve for TV camera bias and offset parameters, spacecraft and satellite state vectors, and the spherical harmonic coefficients of Mars' gravity field, as well as its mass and spin axis direction.

The optical data were weighted at 0.02 deg (72 arc second). The radio normal points were weighted in a manner to be consistent with the accuracy of the analytical theory used to propagate the spacecraft state and the Ω_{pos} uncertainty of the radio normal points (see Appendix N). An a priori covariance matrix was chosen with an uncertainty on Ω_{pos} of 0.05 deg while values of other spacecraft state parameters were held at the values obtained from radiometric data. In other words, the optical data was allowed to determine the Ω_{pos} history while the radiometric data determined the remaining state elements.

A first-order analytical theory which includes the effects of zonal and tesseral harmonics of Mars' gravity field as well as solar gravity and radiation pressure was used to propagate the motion of Mariner 9, Phobos, and Deimos. For a discussion of the Phobos/Deimos satellite theory, see Appendix K. Since Mariner 9 is in shallow resonance with Mars' even-order tesseral harmonics, large down-track perturbations are induced in the

orbital motion. As a result, a first-order analytical theory is inadequate to model the spacecraft's motion. Consequently, the theory was extended to include the dominant second-order effects of resonance (Appendix N). Use of analytical theories allows rapid and inexpensive long arc processing of the data. An additional benefit of using analytical theories is that quantities such as the mass of Mars, its spin axis direction, and its gravity field can be estimated from the long-term evolution of the spacecraft's and satellite's orbits (see Section V).

The Ω_{pos} history from the combined optical and radiometric data is in very good agreement with that obtained independently from processing Mars landmark data. In fact, the radio plus Phobos/Deimos results agree to 0.007 deg with those obtained from landmark data before the trim maneuver and within 0.005 deg after the trim. This is well within the formal uncertainties of the two solutions.

The Ω_{pos} histories determined from this analysis are discussed more fully in Appendix M. In addition, Ω_{pos} histories determined from Mars landmark tracking during the orbital phase are discussed in Appendix Q.

From a study of the post-fit residuals, it appears that B-camera pointing data was accurate to 75 arc second (1σ); however, the A camera data was good to only 140 arc seconds (1σ). Taken as a whole, the A and B camera pointing data was accurate to 100 arc seconds. Recall that the orbital phase pointing was generated almost exclusively from spacecraft telemetry data, since only two orbital-phase pictures contained stars and a satellite.

D. IMPORTANT FACTORS FOR ORBIT DETERMINATION

The important factors for orbital phase orbit determination can be summarized as follows:

- (1) A priori knowledge of the satellite and spacecraft ephemeris is more important in the orbital phase than in the encounter phase because of smaller spacecraft-satellite range.
- (2) The satellite theory used during the orbital phase modeled the periodic and secular effects of zonal and tesseral harmonics of

Mars' gravity field as well as solar gravity. This theory has an accuracy of ± 0.5 km for the time period considered here.

- (3) The irregular shape of Phobos and Deimos necessitated using at least a triaxial model for their figure to minimize center-finding errors. Knowledge of their rotational properties was also important so that computer-generated overlays could be properly oriented for determining the center of figure of the image. Using this technique, center-finding errors were on the order of 12 to 18 arc second (2-3 pixels) primarily because of the irregular shape of the satellites.
- (4) Camera pointing was the largest error source in the orbital phase data. Overall accuracy for the A and B cameras was about ± 100 arc seconds (1σ). If a twin-camera system (imaging stars in one camera and a satellite in the other) or overexposed pictures were used, pointing errors could be reduced by an order of magnitude, thus making center-finding the dominant error source.
- (5) Camera resolution was more than adequate for the orbital phase of the mission, since errors induced by pointing and center-finding were an order of magnitude larger than those induced by camera resolution.
- (6) Long arc analysis showed that estimates of Ω_{pos} for the spacecraft's orbit using optical and radiometric data was determined to the order of 0.007 deg, almost an order of magnitude better than from radiometric data alone. The estimates of other elements of the spacecraft state were not improved over values based on radiometric data.

The major problem with the orbital phase of the demonstration was the acquisition of Phobos during the early part of the mission. The ephemeris of Phobos was not well determined from the approach data, since only two pictures were obtained, and only one had stars. Furthermore, Mars' gravity field was poorly determined at this time, so that the predicted spacecraft ephemeris used for picture planning contained errors equivalent

to pointing errors of 0.25 to 1.0 deg. Picture planning was done about one week in advance. The spacecraft ephemeris errors were overcome by updating the camera pointing 1 to 2 hours before shutter time. However, this was an inefficient procedure because the opportunity for human error was amplified.

After the first 38 revolutions of Mariner 9, the spacecraft's ground-track had covered 360 deg of longitude and the global gravity field was better defined. Thereafter, the satellite ephemerides and spacecraft prediction capabilities improved to the extent that ground command of pictures was no longer necessary and the demonstration encountered no further problems with data acquisition.

E. CONCLUDING REMARKS

The feasibility of using satellite optical data in conjunction with radiometric data to improve spacecraft trajectory estimates has been successfully demonstrated by postflight analysis. Unfortunately, because of science constraints, no sequence containing satellite/star pictures optimized for navigation purposes was taken during the mission and, therefore, the value of processing this data for real-time precision orbit determination could not be demonstrated.

The feasibility of overexposing satellite images in order to enhance star images was demonstrated. However, the success of this procedure depends on such factors as camera type, center-finding accuracy, length of exposure time, motion of the satellite relative to the camera line of sight, and spacecraft limit-cycle motion during exposure. These factors become more significant as spacecraft-satellite range decreases. For these reasons, this technique may be unsuitable for obtaining navigation data for some missions. In this case, a twin-camera system wherein one camera images stars while the other photographs the satellite would be preferable.

29<

V. ADDITIONAL EFFORTS

In addition to the prime efforts of the OND described in the previous sections, several supplementary studies were made with the optical data taken by Mariner 9. The first section summarizes a navigation study using orbital phase pictures which contained selected Mars landmarks. Presented next is an approach navigation study based on Mars limb data. The final section is a discussion of science fallout from the demonstration.

A. ORBITAL PHASE NAVIGATION RESULTS USING LANDMARK DATA

1. Introduction

This section of the report presents postflight navigation results in the orbital phase using landmark data of the MM'71 Optical Navigation Demonstration. A description of data used, the procedures of data reduction, and the potential of such imaging data in improving radiometric accuracies is given in Appendix Q.

2. Data Distribution

The postflight navigation results of the MM'71 OND were generated on the basis of 28 narrow-angle picture frames and 134 wide-angle picture frames. Each of these TV frames contained images of one or more of a set of 12 selected surface features (listed in Appendix Q). The total time span of this data was contained within the first 232 orbits of Mariner 9. Consequently, the navigation results presented here pertain to the first 232 orbits of Mariner 9, divided into 21 segments, each of which was the result of processing doppler tracking data.

3. Postflight Navigation Results

The residual navigational error after processing Earth-based doppler tracking data is dominant along the direction of the node of the spacecraft orbit relative to the Earth's plane-of-sky. A detailed discussion is contained in Ref. 3 and its relevance to the problem at hand is given in

Appendix Q. Solutions for the node in the plane-of-sky based on (1) combined radio and landmark optical data and (2) landmark optical data alone show a pre-trim II difference of 0.007 deg and a post-trim II difference of 0.001 deg. Comparisons with similar solutions resulting from satellite data (Appendix M) reveal a mutual agreement within 0 to 0.007 deg. Considering the a priori uncertainty of 0.05 deg, the effect of adding optical data appears to significantly reduce this knowledge uncertainty.

B. RESULTS OF MARS LIMB TRACKING

1. Introduction

A postflight investigation of navigation accuracy was performed using the photographs taken during the Mars approach. This section presents the results of this investigation. Included are discussions of optical data sources, limb data reduction, and results of simulated real-time processing and the detailed postflight analyses. More details on the topics of this section are given in Appendix R.

2. Data Distribution

During the two Mars calibration sequences which took place 5 and 4 days before Mars encounter, 22 narrow-angle TV pictures which contained Mars lit limb images were taken. Wide-angle TV pictures of Mars during the Mars calibration sequences were not processed because of poor angular resolution. During the POS I, II, and III sequences, 36 narrow-angle TV pictures and 4 wide-angle TV pictures were selected for lit limb data processing. Towards the end of POS II and throughout POS III sequences, the Mars images exceeded the field of view of the narrow-angle TV camera to the extent that only a small portion of the lit limb was visible; hence such frames were not processed.

3. Limb Data Processing

The limb-finding algorithm searched the digital video data TV scan line by scan line. That is, the limb search started from a point off the planet image and continued onto the limb. The first of three adjacent pixels,

all having video intensity levels exceeding a predetermined threshold level, was selected as the location of the lit limb on that line. The requirement for three adjacent pixels eliminated the detection of false limb point caused by one- or two-pixel bit-error noise. Typical lit limb structure imaged by the narrow-angle camera indicates a relatively sharp increase in brightness near the equator and a gradual increase at the pole regions.

To model the lit limb, Mars was assumed to be an ellipsoid with small eccentricity (0.145). Since the Mariner spacecraft approached Mars only about 20 deg below the equatorial plane, the image of Mars can be reasonably well modeled by an ellipse, with the center of the ellipse being coincident with the center of the ellipsoidal planet body.

The apparent lit limb data was processed for TV distortion rectification based upon the in-flight calibration of the TV instruments. Then a minimum-variance estimation algorithm was used to identify the true image shape, size, and orientation as well as the image center location.

The results indicate that the lit limb of the imaged planet does not represent the Martian surface but light scattered from the Martian atmosphere. In fact the radius estimates obtained from the lit limb data are approximately 100 km greater than the mean equatorial radius of Mars. Similarly, the identified shape parameter of the planet is smaller than the accepted value ($e = 0.145$) by about 3 percent.

4. Simulated Real-Time Orbit Determination Results

The TV data available in real time for computing the Mars orbit insertion maneuver, namely the data through POS II, was processed using as a priori estimates the best trajectory available at that time. This trajectory was based on radio tracking data processed through E - 13 hours.

The parameters estimated were the spacecraft cartesian state at epoch, TV pointing biases and errors, and image center-finding errors. The a priori value for the optical data arc was the a posteriori estimate from a short radio data arc (5 days) through E - 13 hours. The error ellipse for the final estimate at the end of POS-II data had a semimajor axis of 70 km. However, the estimate was within 25 km of the current best estimate (CBE).

32<

The center-finding errors, modeled here as being proportional to the image size, appeared to be very small and independent of phase angle. The pointing errors in the raw data included systematic as well as random components.

5. Sensitivity to Radio Tracking

The addition of Mars limb data to radio data reduces sensitivity to planetary ephemeris errors, nongravitational spacecraft acceleration errors, and Earth-based tracking station location errors. To study the reliance of optical limb data solutions on a priori values obtained from radio data arcs, two different analyses were carried out. In the first, a few hours of radio tracking was assumed beyond the first midcourse maneuver at launch (L) + 5 days, and no more radio data thereafter. The spacecraft state estimate and covariance at that time were input as a priori estimates to the optical data arc. The mapped B-plane uncertainties were very large at this point, owing to large maneuver execution uncertainties being mapped several months forward.

The a priori estimate was more than 2500 km from the CBE in the B-plane. The estimate at the end of POS II was 450 km from the CBE. The addition of 4 POS III wide-angle TV data moved the estimate to within 30 km. This accuracy is within mission requirements for inserting Mariner 9 into orbit.

The second analysis was performed with no radio data at all. The injection conditions, for purposes of planetary quarantine (PQ) had a 25,000-km aim-point bias and 22 hours lag in time of flight at Mars. The analysis made here for this optical-only solution was not cognizant of the midcourse maneuver performed at L + 5 days, which removed the PQ bias. The B-plane trajectory solution stabilized at about 7000 km from the CBE, with negligible improvement in time of flight.

The large final error involved here indicates that for optimum results, limb data must be combined with radio tracking data. Even small radio data arcs, when used to give a priori estimates and covariances, improve the effectiveness of optical limb-data enormously.

6. Concluding Remarks

Orbit determination results using limb data taken by Mariner 9 were a factor of 4 better than those from the MM'69 mission. This can be attributed primarily to better TV pointing estimation owing to the in-flight calibration performed. Despite this, the major source of error was still found to be the TV pointing. For future missions, significant improvement in navigation using limb data would result from two TV cameras, wherein one of them would be used for imaging stars to determine TV camera pointing.

C. SCIENCE FALLOUT FROM THE MM'71 DEMONSTRATION

1. Introduction

As either a direct or indirect result of performing the assigned tasks of the demonstration, a considerable amount of science relative to Mars and its natural satellites evolved. These added benefits of the demonstration are discussed in this section.

2. Mars' Spin Axis Direction

Mars' spin axis direction was estimated from satellite observations during both the approach and orbit phase of the mission. During approach, the star background was used to fix the Mars-Deimos position in inertial space. Then the spin axis direction was determined by fixing the inclination of Deimos relative to Mars' equator at the preflight value. This was done because the inclination relative to Mars' equator was well determined from earth based observations (Ref. 4).

This procedure yielded a value for the spin axis direction which differed from the preflight value in the American Ephemeris and Nautical Almanac by approximately 0.5 deg. Later, this result was confirmed by solutions based on Mariner 9 orbital phase radio tracking and Mars landmark pictures from both orbital and approach phases. The orbital phase satellite pictures also confirmed this value; however, in this case it was not necessary to constrain the satellite's inclination since a sufficient data base was available to estimate it (see Appendix N). The Mariner 9 values also

agreed with results published by A. T. Sinclair (Ref. 4) obtained from Earth-based observation of the position of Phobos and Deimos during the period 1877-1969.

3. Mass of Mars

The mass of Mars was also estimated from the orbital-phase Phobos/Deimos pictures. The optical data yields direct information on the semimajor axis of the satellite's orbits. Since the orbital periods of the satellites are well known, the mass of Mars can be determined. Appendix N presents these results, which are in excellent agreement with previously published results.

4. Mars' Gravity Field

The spherical harmonic coefficients of Mars' gravity field, determined from combined radiometric and satellite data taken by Mariner 9, are presented in Appendix N. This field contains zonal coefficients through degree 6 and tesseral coefficients through degree and order 6. It agrees quite well with results published by the MM'71 Celestial Mechanics Team. However, it is unique in that it is the only field to include the satellite data. Furthermore, it is based on long term (110 days) evolution of the spacecraft's and satellite's orbits.

5. Orbits of Phobos and Deimos

The satellite theory of Appendix K was used to model the motion of the satellite relative to Mars' equator and equinox of date. This theory is in error by less than 0.5 km since it includes all first-order effects of zonal harmonics through J_6 as well as second-degree and order tesseral harmonics and solar gravity. In addition, second-order secular effects of oblateness are included.

As a result of processing the Mariner 9 data, small corrections to preflight values were made to all orbital elements; however, significant corrections were made to the satellite's longitudes. An important aspect of the Mariner 9 results is that they tend to corroborate results by Sinclair showing the possible existence of a secular acceleration in the longitude of Phobos (Ref. 4).

35<

The longitude for Phobos, determined from the Mariner 9 data, is 0.2 deg less than the longitude predicted for this epoch by Sinclair from a solution which included a secular acceleration term for longitude. The longitude predicted for Phobos by Sinclair from a solution which does not contain a secular acceleration term is 2 deg less than that obtained from the Mariner 9 data¹. This tends to confirm the existence of a secular acceleration of 7.2×10^{-9} deg/day² as published by Sinclair. Additional work is being done in this area to combine the MM'69 Phobos pictures with the MM'71 pictures to yield a data baseline sufficiently long to estimate the secular acceleration.

6. Conclusions

The feasibility of using satellite data for dynamical science was successfully demonstrated by the MM'71 OND. Consequently, satellite and satellite/star data should be considered as a science data type of major importance. The value of the orbital-phase satellite pictures for dynamical science would have been enhanced if they had contained star images, thereby decreasing pointing errors by an order of magnitude.

D. SATELLITE GEODESY

1. Introduction

Highlights of the geodesy results for Phobos and Deimos are presented. This effort was funded by the Mariner 9 Imaging Team and was not part of the OND. However, outputs of this effort were used by the OND. These outputs consisted of computer-drawn satellite picture overlays which reflected an accurate knowledge of the size, shape, and orientation properties of the satellites. The overlays were used by the OND to measure the locations of the large, irregularly shaped satellite images obtained during the orbital phase (see Section IV).

¹A. T. Sinclair, personal communication, November 1973.

2. Data Selection

Computer-generated overlays were drawn for each of the high-resolution satellite pictures. The ellipsoid axes a, b, and c were varied until a reasonable match was obtained between the ellipsoid and the lit limb of Phobos. Because of the highly irregular surface, which was only partially illuminated in the pictures, the ellipsoid for Phobos represent more of an upper bound of the surface, as indicated by the surface generally being inside the overlays. These overlays, with a latitude and longitude grid network, were sufficient to initially verify that Phobos was in a synchronous rotation about Mars with a libration amplitude of less than 10 deg. Overlays were then used in identifying surface features from picture to picture to establish a control network of 50 landmarks. A priori body-fixed coordinates were obtained by interpolating the positions of the surface features relative to the latitude/longitude grids and assuming the landmarks were on the mean surface (see Appendix S).

3. Data Reduction

For the data reduction, special hard-copy products of the TV imaging data were used. High-pass filtering, stretching, and magnification of the Phobos imaging data were performed by the JPL Image Processing Laboratory to accentuate the surface features from the limb to the terminator. Image locations in raw (distorted) picture coordinates were measured manually from hard-copy photographs and used as observables in the data reduction. Computed observables were based on a priori control-point locations determined from overlays, spacecraft trajectory data determined from Earth-based radiometric data, celestial TV camera pointing data determined from telemetered spacecraft data, TV distortion parameters based on reseau data, and Phobos ephemerides obtained by using Mariner 9 imaging data to update parameter values in the Wilkins theory.

The data reduction employed a sequential formulation of the minimum variance filter which estimated the following 213 parameters: (1) coordinates (ϕ, λ, h) of each control point; (2) three ellipsoid axes a, b, c which define the mean surface; (3) three TV pointing errors for each picture; and (4) three libration angles for each picture. It was assumed that the spacecraft trajectory and orbit of Phobos were perfectly known. TV camera

pointing errors and libration angles were assumed to be independent from picture to picture, reducing the number of parameters to be estimated at any single time to 159. The data was iterated five times to obtain convergence. Data residuals of 0.5 of a picture element (1σ) were obtained after convergence.

4. Geodesy Results

Results of the data processing verified that Phobos is in a synchronous rotation about Mars and that it is in a dynamically stable orientation with its longest axis toward Mars, its intermediate axis in the orbit plane of Phobos, and its smallest axis normal to the orbit plane. As expected, the axes of the ellipsoid defining the mean surface were determined to be slightly smaller than those determined using overlays.

It was found that surface height variations of as much as 10 percent of the radius occur. The base of the long linear feature (Kepler Ridge) is at least 1.5 km below the peak. A libration-amplitude of about 5 deg in the Phobos orbit plane was suggested by the data processing. Libration periods were not determined because of the time separation between pictures (days to weeks) and because the pictures were taken in a limited region of the Phobos orbit. Therefore, this angle represents the largest angle observed and may not be the libration amplitude.

5. Concluding Remarks

The major errors limiting the reduction of the Mariner 9 imaging data of the satellites for cartography were TV pointing errors and relative spacecraft-satellite position errors. Also, the limited coverage and overlap of the Mariner 9 pictures restricted a complete separation of mean surface, feature heights, and libration parameters.

REFERENCES

1. Aksnes, K., "On the Use of Hill Variables in Artificial Satellite Theory: Brouwer's Theory", Journal of Astron. and Astrophys., 17, 70, 1972.
2. Wilkins, G. A., Orbits of the Satellites of Mars, Tech. Note No. 1, H. M. Nautical Almanac Office, Aug. 1965.
3. Born, G. H., Christensen, E. J., Ferrari, A. J., Jordan, J. F., and Reinbold, S. J., "Determination of the Satellite Orbit of Mariner 9" Paper No. 72-928 AIAA/AAS Astrodynamics Conference, Palo Alto, Ca., Sept. 1972, to be published in Celestial Mechanics, Vol. 9, No. 2, 1974 (in press).
4. Sinclair, A. T., "The Motions of the Satellites of Mars", Mon. Not. R. Astr. Soc. 155, 249-274, 1972.
5. Thorpe, T. E., Star Photography With the MM'71 Prototype Camera, JPL internal document IOM 821, Jet Propulsion Laboratory, Pasadena, California, May 10, 1971.
6. Ferrari, A. J., and Christensen, E. J., "Mars Gravity Derived From the Long-Period Motion of Mariner 9," AAS/AIAA Astrodynamics Conference, Vail, Colorado, July 16 - 18, 1973.

APPENDIX A

A SPACECRAFT-BASED NAVIGATION INSTRUMENT
FOR OUTER PLANET MISSIONS

A Spacecraft-Based Navigation Instrument for Outer Planet Missions

THOMAS C. DUXBURY*
Jet Propulsion Laboratory, Pasadena, Calif.

This article presents the results of an analytical study of various spacecraft-based data that could be used to improve solely Earth-based navigational accuracies when approaching or orbiting outer planets. Measuring the celestial directions to outer planet natural satellites can supply the needed navigation data. The satellite motion can define the celestial direction to the center-of-mass of the outer planet-satellite system more accurately than can be determined from viewing the planet itself. An instrument similar to science television cameras used on the Mariner Mars missions would be suited to produce this spacecraft-based data by viewing satellites and reference stars simultaneously. A description of an instrument producing these measurements (accurate to better than 5 arc-sec) and the applicability of these spacecraft-based data to a Grand Tour mission are also presented.

Introduction

THE positions of the outer planets during the 1970's and 1980's make various multiple-outer planet missions possible within the expected launch vehicle capabilities.^{1,2} Of particular interest among possible future missions is the rare opportunity (once every 171 years) to launch spacecraft which would encounter Jupiter, Saturn, Uranus, and Neptune during a 9-13 year mission lifetime. Such outer planet missions require multiple trajectory correction maneuvers to insure the desired planet encounters. Limitations of Earth-based radio navigation capabilities at the great distances involved have led to an emphasis on developing a spacecraft-based navigation data source.^{3,4} Spacecraft-based data in conjunction with Earth-based radio tracking allow more accurate control of the planet approach trajectory which significantly decreases the amount of spacecraft weight needed for trajectory correction purposes, increases mission performance, and increases the probability of mission success over that obtainable using Earth-based radio navigation only.

Radio tracking data combined with Earth ephemeris data would be used to determine the heliocentric state (position and velocity) of a spacecraft. Earth ephemeris uncer-

tainties, tracking station location uncertainties, uncalibrated charged particle effects, and other data noise would be the major sources of error degrading the determination of the heliocentric spacecraft state when using only the Earth-based data. The determination of the target-centered spacecraft state would be degraded by this heliocentric state uncertainty and the target ephemeris uncertainty when outside the target sphere-of-influence. It is expected that Earth-based radio navigation in the mid-1970's would have the capability of determining the target-centered spacecraft state during planet approach to 0.1 arc-sec (3σ) in geocentric right ascension and declination. These uncertainties map to a spacecraft position uncertainty of 500 km at Jupiter and 3000 km at Neptune. Augmenting the Earth-based navigation data with spacecraft-based data could reduce the target-centered, spacecraft position uncertainty to ~400-1000 km (3σ) during the approach to these same planets.

This article discusses the desired information content of the spacecraft-based data and the difficulties associated with obtaining the data. Spacecraft-centered measurements of the direction to the planet center-of-mass supplies the needed trajectory information lacking from the Earth-based radio tracking data. The gaseousness of the outer planets, and the rings of Saturn makes the accuracy of planet center determination from planet limb measurements questionable. Fortunately, these gaseous planets have many natural satellites whose orbital motion can be related directly to the center-of-mass of the planet-satellite system. A television type instrument which would image these natural satellites and reference stars simultaneously to produce the desired navigation data is discussed together with the application of this data to the Grand Tour mission. The instrument re-

Presented as Paper 69-902 at the AIAA/AAS Astrodynamics Conference, Princeton, N.J., August 20-22, 1969; submitted September 8, 1969; revision received April 9, 1970. This article presents the results of one phase of research carried out at the Jet Propulsion Laboratory, California Institute of Technology, under Contract NAS 7-100, sponsored by NASA.

* Group Leader, Guidance and Control Division.

quires a refinement of existing capabilities rather than an advance in the state-of-the-art.

Instrument Concept

Expected Earth-based radio tracking data would provide an accurate determination of the spacecraft heliocentric state, whereas ephemeris data would provide an accurate determination of the target planet velocity. Lacking from these two data sources are accurate data on the target-centered position of the spacecraft. Additional data that could provide the desired position information are spacecraft-based measurements of the target planet direction. Planet direction measurements contain information that defines the spacecraft motion in its trajectory plane and also the orientation of the trajectory plane.

Determination of this direction requires an instrument or instruments to measure the individual directions to the target planet and reference bodies. The individual direction measurements would then be related to each other by using measured instrument calibration characteristics, and measured alignments between the instruments when more than one instrument is used. Viewing the target planet and/or its natural satellites could yield planet direction; stars (including the sun) could be used as celestial references for the measurement of planet direction.

Measured Planet Direction

The illuminated (lit) limb (apparent edge) of a planet can be used in determining the direction to the optical center of a planet. Instruments that view the planet lit limb to yield planet direction information could process the planet image aboard the spacecraft to derive the location of planet center^{5,6} or produce a planet image for transmission to Earth, e.g., a science television camera, where ground-based software could operate on the image to derive the planet center. For processing planet image data either aboard the spacecraft or on the earth, an algorithm based on image intensity would be used to define the lit limb of a planet image, and then a curve fitting technique would be used to determine the center of the image from measured points on the lit limb. The measured image center location would be converted into planet direction in an instrument coordinate system using instrument calibration data.

Major sources of error degrading the measured direction to the planet center-of-mass are 1) limb darkening, 2) marked

albedo variations near the lit limb, 3) atmosphere, 4) algorithm defining lit limb, 5) uncertainties in the target planet figure and spin axis orientation with respect to the instrument coordinate system, 6) differences between the planet optical center and center-of-mass, 7) electrical and optical geometric distortion of the image, 8) photometric distortion of the image due to image plane sensitivity nonuniformities, and 9) instrument calibration errors.

Figure 1 illustrates the aforementioned error sources 1, 2, 3, and 4. The darkening of the lit limb of Jupiter near its poles tends to exaggerate its oblateness. A simple limb algorithm (the type that could be used aboard the spacecraft) based on a fixed level of intensity would not be able to accurately distinguish the effects of limb darkening, dark surface features, or regions of less dense atmospheres from dark space. A more complex limb algorithm would undoubtedly require the aid of a computer. The rings of Saturn (Fig. 2) mask a significant portion of the limb and increase the complexity of a suitable limb algorithm.

Relating limb measurements to the center-of-mass of the planet requires a model of the planet figure. Ideally, the planets would be homogeneous solid or fluid bodies and the limb measurements would be on the edge of the body surface. A homogeneous solid or liquid spinning body is constrained dynamically to be ellipsoidal with the center-of-mass at the ellipsoid center; therefore, fitting the limb measurements with an ellipse could yield the planet center. Unfortunately, the outer planets exist in very gaseous states or possibly completely gaseous states, particularly the planets Jupiter and Saturn. A spinning gaseous body does not have to exhibit the dynamically constrained shape or center-of-mass characteristics of a liquid or solid planet. An example of observed peculiarities for these gaseous planets is the measured differences in spin rate of Jupiter at different latitudes. Outer planet limb measurements may be in the planet atmospheres and not at the edge of a solid or liquid surface since these surfaces may not exist or are hidden by the thick atmospheres. These limb measurements would be subject, then, to composition and density variations in the atmosphere and may deviate significantly from simple limb and planet figure models.

A study has been performed to determine the effect of error source 5 on determining the optical center of a planet. Center-finding errors from 300 to 2000 km (3σ) can be expected for the planets Jupiter through Neptune if the planet center is found without improving the accuracy of Earth-based estimates of planet figure and spin axis orientation; therefore, spacecraft-based data must improve the accuracy of these parameters when used to determine the optical center. Uncorrected image distortion of $\frac{1}{2}\%$ would produce center-finding errors of similar magnitude. An uncertainty in the difference between the optical and dynamical planet centers would map directly into a center-finding error. This center-finding error together with the previously mentioned center-finding errors could not be separated from the planet direction data until the discrepancy was revealed by the gravitational effect of the planet. Unfortunately, the tra-

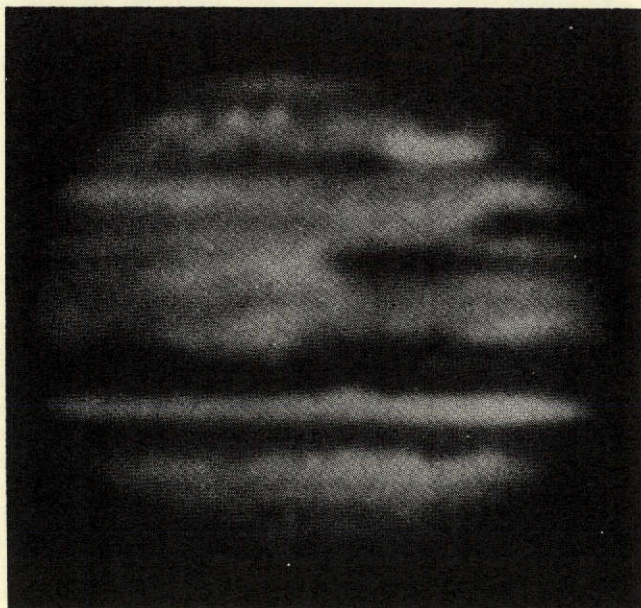


Fig. 1 Jupiter.

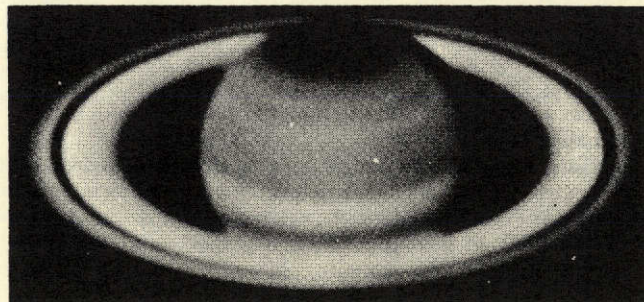


Fig. 2 Saturn.

jectory correction maneuvers to be performed on multiple outer planet missions are calculated before the pull of the planet is sufficient to enable these errors to be determined; therefore, these errors would corrupt the maneuver in addition to errors in executing the maneuver.

The problems of planet limb sensing to determine the planet center can be eliminated by viewing natural satellites of the planet. Satellite motion is related directly to the planet center-of-mass rather than the optical center. Also the rings of Saturn would not obscure from sight the natural satellites of Saturn as it would a portion of the limb of Saturn. A time history of measured directions to satellites would contain data from which orbital parameters of the satellites including the location of their common primary (planet center-of-mass) could be determined. As with the planets, satellite limb measurements would be used to determine the centers of the satellites. However, because of the small size of the satellites and the sparseness of satellite atmosphere as compared to the planets, the centers of the satellites could be determined from one to three orders of magnitude more accurately than the planet centers. The major error sources in determining the planet direction would be the accuracy of the satellite direction data and the accuracy of modeling the satellite equations of motion. Integration of the satellite equations of motion would be required at Jupiter because of the interactions of the Galilean satellites. Conic approximations of the orbits of the other outer planet natural satellites would introduce small model errors but significantly reduce the complexity of computations.

Planet Direction References

Studies^{7,8} of spacecraft-based navigation measurements indicate that significant trajectory estimation errors would be incurred if multiple instruments were used to view the planet-satellite system and reference bodies. Constant misalignments of the instruments could be accurately determined in a trajectory estimation process; but slowly varying misalignments due to electrical and mechanical drifts would be difficult to separate from the slow changes in planet direction resulting from spacecraft motion along its trajectory.

Instruments viewing one body at a time would require precision electrical, optical, or mechanical gimbaling to view all of the pertinent bodies. Instruments having the capability of viewing more than one body simultaneously would require precision gimbaling or an instantaneous field-of-view (FOV) sufficient to view all pertinent bodies simultaneously. An instrument with sufficient FOV would offer more accurate relative direction information by eliminating uncalibrated, nonrepeatable gimbal errors.

The sun would be undesirable as a reference body for outer planet missions because of its brightness as compared to the other bodies of interest, and because of the large angular separation of the spacecraft-planet direction and spacecraft-sun direction during planet approach ($\sim 160.0^\circ$). The use of stars in the direction of the target planet or in the direction of selected natural satellites would be desirable to reduce the total FOV required to detect all pertinent bodies. An instrument using stars within 5° of the planet or satellites for references would need to detect 6th magnitude stars for the variety of multiplanet missions possible in the late 1970's. Detecting dim stars near the target planet direction poses a problem because stray light from the planet would tend to mask the stars.

In summarizing the major spacecraft-based instrument requirements, it is concluded that an instrument viewing the planet must produce data, based on a sophisticated limb model, that yield a solution for the planet center including a solution for the planet figure and spin axis. Instruments viewing the planet or satellites should be able to view reference stars in a single FOV, or have precision gimbaling to

yield relative direction accurately. It is proposed that a TV type instrument viewing natural satellites of a target planet against a star field would meet these requirements. This type of instrument would have the capability of producing the required navigation data during planet approach, planet departure, or when orbiting a planet.

Instrument Description

The spacecraft-based instrument would obtain information on outer planet satellite directions in a star field by imaging these bodies on a vidicon tube. The instrument would have a $3^\circ \times 3^\circ$ FOV and would be mounted on a two-axis gimballed platform to provide a large total FOV capability. The instrument FOV would enable the satellites and reference stars to be viewed simultaneously. The gimballed platform would allow the instrument to view these bodies for the various planet approach directions and for the range of satellite motion.

Vidicon target raster resolution would be 1000 scan lines with 1000 picture elements (pixels) per scan line. The shutter speed of the instrument would be controllable to insure the detection of the satellites and 6th magnitude stars. To minimize stray light problems, the planet would not be within the instrument FOV during observations. An 11×11 grid of reseau would be placed on the vidicon face to yield in-flight geometric distortion data. The instrument, essentially viewing dark space, would require a white reseau grid.

Since the information content of each vidicon data frame is mostly of the dark space background, the video information from the vidicon target raster could be processed selectively aboard the spacecraft to separate and store only information (pixel location and intensity) on the bright images (satellites, stars, and reseau). Selective processing would consist of comparing the video intensity level of each picture element in the data frame with a reference video level. The reference level, brighter than the space background, would be controlled by a ground command or by information stored or calculated in a spacecraft computer to add flexibility to the selecting processing. The location and brightness of about 500 pixels out of a total of one million pixels would be stored per data frame during planet approach. At selected times, the stored data would be transmitted to earth where it would be combined with Earth-based radio tracking data. The video levels associated with the pixel locations would be used in identifying the images.

Spacecraft-Based Observables

The spacecraft-based observables would be the image coordinates of the satellites, stars and reseau, grid. A general expression for the measured image coordinates of stars and satellites with respect to the instrument principal point (intersection of optical axis with the target raster) is obtained from the colinearity equations of photogrammetry⁹ and is given by

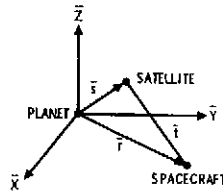
$$\begin{bmatrix} x_m \\ y_m \end{bmatrix} = -\frac{f}{w} \begin{bmatrix} 1 & 0 & 0 \\ 0 & 1 & 0 \end{bmatrix} (I - E)Mi + \begin{bmatrix} x_0 \\ y_0 \end{bmatrix} + \begin{bmatrix} x_r \\ y_r \end{bmatrix} + \begin{bmatrix} \eta_x \\ \eta_y \end{bmatrix} \quad (1)$$

and an expression for the measured image coordinate of a reseau grid point is given by

$$\begin{bmatrix} x_m \\ y_m \end{bmatrix} = \begin{bmatrix} x_r \\ y_r \end{bmatrix} + \begin{bmatrix} x_s \\ y_s \end{bmatrix} + \begin{bmatrix} \eta_x \\ \eta_y \end{bmatrix} \quad (2)$$

where (x_m, y_m) = measured pixel and line coordinate of an object's image; (x_r, y_r) = physical location of a reseau grid

Fig. 3 Spacecraft-planet-satellite geometry.



point measured before launch; f = instrument focal length; (x_0, y_0) = optical distortion function; (x_s, y_s) = electrical distortion function; (η_x, η_y) = measurement noise due to vidicon tube resolution; M = transformation from an inertial reference system to a nominal instrument reference system; \hat{i} = spacecraft-centered inertial direction to object; w = third component of the unit vector \hat{p} with $\hat{p} = Mi$. The functions representing electrical and optical geometric distortion could be modeled as a power series with the distance between the principal point and image location as the independent variable, and the coefficients of the series as parameters to be estimated from in-flight star and reseau grid data. A detailed discussion of modeling geometric distortion is given in Ref. 10. The term $(I - E)$ is a small angle rotation matrix that defines the deviation of the actual instrument orientation from a nominal reference system. For small angles, the rotation matrix is approximated by

$$(I - E) = \begin{bmatrix} 1 & \epsilon_3 & -\epsilon_2 \\ -\epsilon_3 & 1 & \epsilon_1 \\ \epsilon_2 & -\epsilon_1 & 1 \end{bmatrix} \quad (3)$$

The spacecraft-centered inertial direction to a satellite is expressed as

$$\hat{i} = (\vec{s} - \vec{r}) / |\vec{s} - \vec{r}| \quad (4)$$

where \vec{s} is the planet-satellite vector, \vec{r} is the planet-spacecraft vector, and $(\hat{X}\hat{Y}\hat{Z})$ is an inertial reference system (Fig. 3). The directions to stars are accurately known from Earth observations and are not a function of spacecraft trajectory or satellite orbits for the outer planet missions. The reseau locations on the vidicon target, accurately known from pre-launch calibration, do not change during flight.

During a measurement time period when the gimballed platform is not commanded to move, the errors between the actual and nominal instrument inertial orientation would be of the form

$$\vec{\epsilon} = \begin{bmatrix} \epsilon_1 \\ \epsilon_2 \\ \epsilon_3 \end{bmatrix} = \begin{bmatrix} l_1 + m_1 + n_1 \\ l_2 + m_2 + n_2 \\ l_3 + m_3 + n_3 \end{bmatrix} \quad (5)$$

where l = constant biases that are perfectly correlated between data frames, m = slow random variations that are neither constant nor uncorrelated between data frames, n = random biases that are uncorrelated between data frames. The constant biases (l) would be associated with fixed mount-

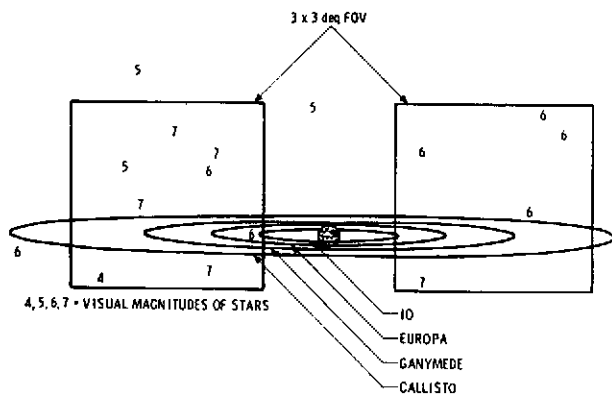


Fig. 4 10 days from Jupiter encounter.

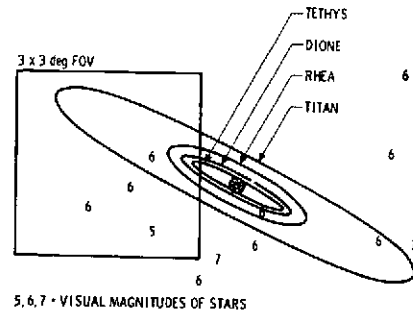


Fig. 5 10 days from Saturn encounter.

ing offsets between the instrument and the spacecraft structure (~ 3.0 mr); the slow random variations (m) would be associated with sensor electrical null drift and structural bending (~ 0.1 mr); and the random biases (n) would be associated with the telemetry resolution of the measured platform pointing direction and spacecraft attitude (~ 0.3 mr). When the gimballed platform is moved, the uncertainty of the constant biases would be degraded due to the uncertainty of the platform movement.

Data Content of Images

The reseau grid image data [Eq. (2)] would contain information from which the coefficients of the electrical distortion function could be estimated for each data frame. The 11×11 reseau grid data would be sufficient to allow electrical distortion to be removed from the star and satellite data to within 2 arc-sec (1σ). Star image data [Eq. (1)] would contain information from which the optical system parameters and the inertial pointing direction of the instrument could be estimated. Selected star clusters could be viewed for the specific purpose of calibrating the optical system before viewing the satellites and reference stars. Proper design and environmental control of the instrument optical system to insure its stability over the entire measurement interval could allow the errors due to the optical system to be removed from the satellite data to within 4 arc-sec (1σ). With the measurement errors essentially removed by the reseau grid and star data, the distortion corrected satellite data (accurate to better than 5 arc-sec) would be used primarily for estimating the spacecraft trajectory \vec{r} (time) and satellite orbits \vec{s} (time).

Table 1 Natural satellites

Planet and satellite	Semimajor axis, 10^3 km	Eccentricity	Period, days
Jupiter			
I Io	423.	0	1.769
II Europa	673.5	0.0003	3.551
III Ganymede	1074.	0.0015	7.154
IV Callisto	1888.5	0.0075	16.689
V	181.5	0.0030	0.498
Saturn			
I Mimas	186.	0.0201	0.942
II Enceladus	238.5	0.0044	1.370
III Tethys	295.	0	1.887
IV Dione	378.	0.0022	2.737
V Rhea	528.	0.0010	4.517
VI Titan	1225.5	0.0291	15.950
Uranus			
I Ariel	192	0	2.520
II Umbriel	268.5	0	4.144
III Titania	439.5	0	8.706
IV Oberon	588.	0	13.460
V Miranda	127.5	0	1.414
Neptune			
I Triton	353.	0	5.877

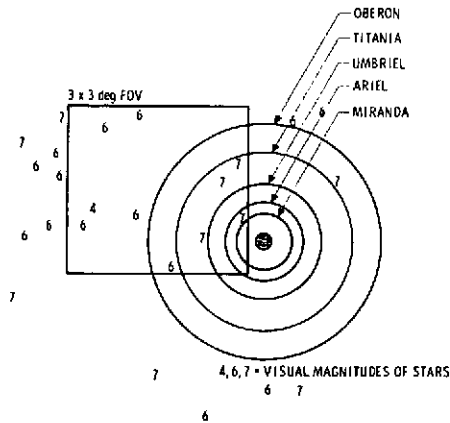


Fig. 6 10 days from Uranus encounter.

Grand Tour Navigation

The applicability of this instrument to a Grand Tour mission with an inner ring passage at Saturn has been investigated. This mission has the most demanding navigation requirements of any of the proposed outer planet missions; therefore, meeting the navigation requirements for this mission would guarantee that the navigation requirements of any of the proposed outer planet missions could be met.

Table 1 lists the satellites that could be viewed during the approaches to the outer planets.¹¹ Figures 4-6 illustrate the celestial geometry during the approach to Jupiter, Saturn, and Uranus for this Grand Tour mission. Measurements could be timed to obtain one or more satellite images with the star images. Measurements would begin about 20 days before encountering each planet and would be used to determine a pre-encounter maneuver for correcting the estimated trajectory deviation from the nominal approach trajectory. These trajectory deviations could be kept small by performing small trajectory correction maneuvers during the interplanetary cruise portions of the trajectory. Long arcs of Earth-based radio tracking data should be capable of reducing these trajectory deviations to within the limiting uncertainty of the target planet ephemeris at the time the spacecraft begins to approach the target planet. Figure 7 shows the rms pre-encounter velocity magnitudes required to correct these expected approach trajectory deviations.

Errors in a pre-encounter maneuver would have to be corrected by performing a postencounter maneuver to insure an accurate arrival at the next planet. These errors would result primarily from pre-encounter trajectory estimation errors which corrupt the calculation of the maneuver. Execution errors in pre-encounter maneuvers would be small relative to the maneuver-calculation errors. The spacecraft-based measurements would control the accuracy of the pre-

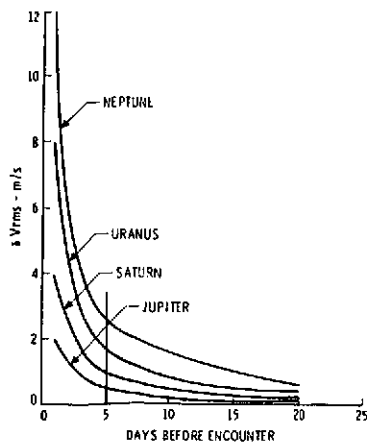


Fig. 7 Pre-encounter maneuver magnitude.

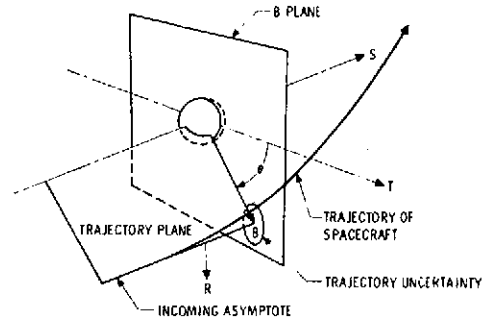


Fig. 8 \overline{RST} coordinate system.

encounter maneuver because the Earth-based tracking would have reached its limiting accuracy before the spacecraft-based measurements were taken. Sufficient measurements of satellite, star, and reseau grid positions would be taken to reduce errors in estimating the trajectory to a level commensurate with the instrument accuracy of approximately 5 arc-sec, and to have the trajectory accuracy essentially independent of the a priori satellite orbit uncertainties. The satellites would be viewed over major portions of their orbits (except near the planet) allowing this level of trajectory accuracy to be reached. A study⁸ of a Mars mission using the natural satellites Phobos and Deimos and a similar type of instrument showed that the instrument error limited the accuracy of the spacecraft trajectory estimate, even with large a priori satellite orbit uncertainties.

A convenient coordinate system for describing a fly-by trajectory and errors in that trajectory is the \overline{RST} system (Fig. 8), where \overline{S} is parallel to the approach asymptote of the trajectory, \overline{T} is parallel to the ecliptic plane, and \overline{R} , completing the orthogonal system, is in the southern hemisphere. Trajectory errors can be expressed in terms of uncertainties of the approach asymptote direction \overline{S} , approach velocity V_∞ , time of flight, and the impact parameter \overline{B} .

Earth-based data could determine the approach direction and approach velocity with sufficient accuracy so that the uncertainty in these parameters would map to negligible errors in the departure trajectory, as would time-of-flight errors. The major sources of error affecting the departure trajectory are uncertainties in \overline{B} . The rms magnitude of the expected postencounter maneuver as a function of errors in \overline{B} is given by⁹

$$\delta V_{rms} = V_\infty \sin \psi [\delta B^2 + B^2 \delta \theta^2]^{1/2} / B \quad (6)$$

where $B = |\overline{B}|$, $\theta = \tan^{-1}(\overline{B} \cdot \overline{R} / \overline{B} \cdot \overline{T})$, and ψ is the angle between the incoming and outgoing asymptotes.

The \overline{B} -plane uncertainty during planet approach can be approximated by the following function of instrument

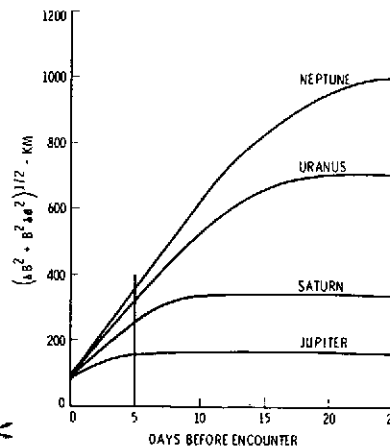


Fig. 9 \overline{B} -plane uncertainty using Earth-based and spacecraft-based data.

Table 2 Grand Tour maneuver magnitudes

Maneuver	δV_{rms} , m/sec	$V_{\infty} \sin \psi / B$, m/sec-km
Post-Earth ^a	18.00	...
Pre-Jupiter	0.40	...
Post-Jupiter	2.56	0.016
Pre-Saturn	0.80	...
Post-Saturn	29.38	0.113
Pre-Uranus	1.60	...
Post-Uranus	50.53	0.163
Pre-Neptune	2.40	...
Total velocity, m/sec	178.82	...

^a See Ref. 4.accuracy (α) per axis:

$$(\delta B^2 + B^2 \delta \theta^2)^{1/2} \approx (2)^{1/2} r \alpha \quad (7)$$

where r is the spacecraft range from the planet at the time of the pre-encounter maneuver. This \bar{B} -plane uncertainty (Fig. 9), using Earth-based and spacecraft-based data, would have an upper limit corresponding to the target ephemeris uncertainty and a lower limit corresponding to the satellite center finding accuracy (tens of km).

Minimizing the sum of the pre- and postencounter maneuvers at each planet would require pre-encounter maneuvers to be performed within a few days from encounter. Performing the detailed data processing, maneuver computations, and command sequencing at these times would be undesirable because of high activity and complexity of mission operations in support of the near-encounter science sequence. Therefore, it is assumed that the pre-encounter maneuvers would be performed at 5 days before encounter to ease mission operations at the expense of an off-optimum maneuver policy.

Table 2 lists the expected rms maneuver sizes at each planet and the total velocity magnitude (99 percentile) based on a Rayleigh distribution. The small trajectory correction maneuvers performed during interplanetary cruise were neglected. Even with the nonoptimum maneuver policy, only 180 m/sec velocity correction capability is required to meet (99% probability) the Grand Tour navigation requirements.

Conclusions

Viewing the natural satellites of an outer planet could yield more accurate spacecraft navigation data than could be obtained from viewing the target planet itself. Satellite data would not be degraded by the large planet center-

finding errors associated with viewing the gaseous outer planets. Viewing the satellites against a star background could be performed while approaching, orbiting, or departing a target planet. The satellite data would not be degraded by the rings of Saturn.

The instrumentation required to produce the satellite data essentially exists in the form of science television cameras being used on interplanetary missions to Mars. Simple data compression algorithms could be used to reduce the amount of navigation data transmitted to Earth to a low level when compared with the expected science data to be transmitted to earth. This navigation data, when combined with Earth-based data, would allow any of the possible multi-planet missions to be flown with less than 180-m/sec velocity correction capability.

References

- Long, J. E., "To the Outer Planets," *Aeronautics and Astronautics*, Vol. 7, No. 6, June 1969, pp. 32-47.
- Flanders, J. H., Fraser, D. C., and Lawson, J. R., "Technology for Guidance and Navigation of Unmanned Deep Space Missions in the 1970's," AIAA Paper 68-1104, Philadelphia, Pa., 1968.
- Friedlander, A. L., "Guidance Analysis of the Multiple Outer Planet (Grand Tour) Mission," Paper 68-109, Sept. 1968, American Astronautical Society.
- Kingsland, L., "Trajectory Analysis of a Grand Tour Mission to the outer Planets," AIAA Paper 68-1055, Philadelphia, Pa., 1968.
- Fraser, D. C. et al., "Final Report on Guidance and Navigation Requirements to the Outer Planets—Vol. II, Impulsive High Thrust Missions," NASA Contract NAS 2-5043, 1970, Massachusetts Institute of Technology Instrumentation Lab.
- Chamberlain, F. R., "Development of an Approach Guidance Optical Planet Tracker," *Space Program Summary 37-52*, Vol. III, Jet Propulsion Lab., Pasadena, Calif., Aug. 31, 1968, pp. 49-52.
- Breckenridge, W. G. and Duxbury, T. C., "Investigation of Planetary Navigation Using Spacecraft-Based Measurements," *Proceedings of the Institute of Navigation National Space Meeting on Space Navigation—Present and Future*, Institute of Navigation, 1969, pp. 18-30.
- Duxbury, T. C., "Spacecraft Navigation Using Science Television Data," Paper G60, April 1969, American Institute of Astronautics and Aeronautics/American Geophysical Union.
- Thompson, M. M., ed., *Manual of Photogrammetry*, 3rd ed., Vol. 1, American Society of Photogrammetry, Falls Church, Va., 1966, pp. 461-490.
- Wong, K. W., "Geometric Calibration of Television Systems for Photogrammetric Applications," paper presented at the 11th International Congress of Photogrammetry, International Society for Photogrammetry, Lusanne, Switzerland, July 1968.
- Melbourne, W. G. et al., "Constants and Related Information for Astrodynamical Calculations, 1968," TR 32-1306, July 15, 1968, Jet Propulsion Lab., Pasadena, Calif.

APPENDIX B
IN-FLIGHT CALIBRATION OF AN INTERPLANETARY
NAVIGATION INSTRUMENT

In-Flight Calibration of an Interplanetary Navigation Instrument

THOMAS C. DUXBURY* AND HIROSHI OHTAKAY†
Jet Propulsion Laboratory, Pasadena, Calif.

This paper presents the results of an analytical investigation which demonstrates the feasibility of geometrically calibrating a navigation instrument during interplanetary flight to arc-sec accuracy. The instrument, similar to a television camera, would view selected natural satellites and reference stars simultaneously for navigating to the outer planets. An 11×11 reseau grid, etched onto the target raster of a vidicon tube, would be used to remove electromagnetic distortion from the satellite and reference star data to less than 1.2 arc-sec (1σ) in each and every data frame, independent of reseau data from any other data frame. Taking advantage of expected optical distortion stability, a total of fifty star images obtained from many data frames would be used to determine optical distortion to less than 4.3 arc-sec (1σ). Therefore, the use of the reseau grid and star images could enable the navigation measurements to be geometrically calibrated to an accuracy of 5 arc-sec (1σ).

Introduction

LIMITATIONS of Earth-based radio navigation capabilities for proposed multiple-outer planet missions¹ motivated the development of a spacecraft-based navigation data source. Spacecraft-based data would be used to augment Earth-based radio tracking data during the approach to a target planet so as to obtain an accurate estimate of the spacecraft trajectory relative to the target planet. Increased approach trajectory accuracy would permit a more accurate control of the flyby trajectory, which would significantly decrease the amount of spacecraft weight needed for trajectory correction purposes and increase the probability of successfully performing the multiple-outer planet missions.

The most useful information that the spacecraft-based data could supply to the navigation process would be the celestially referenced direction to the center-of-mass of the outer planet-satellite system.² An instrument³ capable of producing this information is a television camera designed to view selected natural satellites and reference stars simultaneously during planet approach. Star data would be used to celestially reference the satellite directions, and satellite data would be used to determine the locations of the center-of-mass of the planet-satellite system.

Since the positions of the outer planet natural satellites are not known to many thousands of km, the orbital elements of these natural satellites would have to be estimated together with the spacecraft trajectory in the navigation process. Sufficient satellite/star data would be taken during planet approach to allow the determination of the natural satellite/spacecraft trajectory parameters to an accuracy limited only by the instrument measurement accuracy.

The instrument, producing optical measurements while many millions of kilometers from the target planet, is required to produce the direction information to an accuracy of 5 arc-sec (1σ) to obtain trajectory estimation accuracies of a few hundred kilometers.⁴ The trajectory correction capability required for a variety of multiple-outer planet missions is shown in Fig. 1 as a function of optical measurement accuracy.⁴ The missions considered were the Jupiter-Saturn-Uranus-Neptune missions with inner ring (GTA) and outer ring (GTB) passages at Saturn, the 1978 and 1979 Jupiter-Uranus-Neptune missions, and the 1977 Jupiter-Saturn-Pluto mission. Accuracies of 5 arc-sec (1σ) are possible

Received Sept. 9, 1970; revision received July 15, 1971. This paper presents the results of one phase of research carried out at Jet Propulsion Laboratory, California Institute of Technology, under Contract 7-100, sponsored by the NASA.

* Task Leader, Mission Analysis Division. Member of AIAA.

† Senior Engineer, Guidance and Control Division.

with the use of calibration markings (reseau grid) on the face of the image tube of the instrument and by imaging star clusters. This article discusses the error sources associated with the instrument, the modeling of these errors, and the use of a reseau grid and star clusters to remove these errors from the flight data. The expected calibration accuracy together with the sensitivity of this accuracy to error parameters and the number of points in the reseau grid and stars used for calibration are also discussed.

Instrument Description

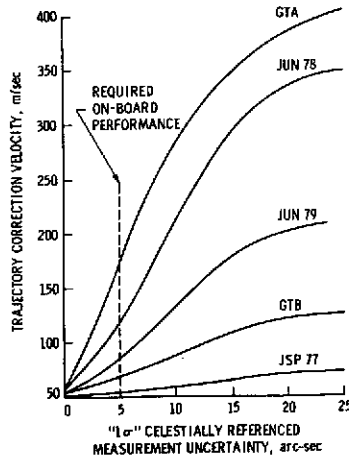
The proposed instrument, having a 3×3 -deg field-of-view (FOV), would image selected natural satellites and reference stars simultaneously on an active target raster of a vidicon tube. The target raster would be scanned at 1000 lines with 1000 picture elements (pixels) per scan line giving an angular resolution of ± 5 arc-sec per pixel. The instrument would be mounted on a two-axis gimballed platform allowing a large total viewing capability.

The instrument would provide information of electromagnetic deflection voltages controlling the location at which the electron-scanning beam samples the target raster and also information of image intensity of the pixel being sampled. The deflection voltages would give a measure of the pixel location being sampled while the measure of pixel intensity would aid in identifying the image. The measured locations of images combined with instrument transfer characteristics would be used to determine the directions of objects. Geometric distortion of the image relationships occurring in the electron beam scanning circuitry (electromagnetic distortion) and in the telescope of the instrument (optical distortion) corrupts the direction measurement. Errors in instrument parameters (e.g., focal length) also corrupt the measured direction.

Sources of electromagnetic distortion include:⁵ 1) nonuniform magnetic deflection field; 2) fringe field outside the deflection region of a vidicon tube; 3) interaction between the focusing and deflection fields; 4) nonuniform electric deceleration field; 5) electromagnetic bias shifts; 6) a common rotation of the scan deflection fields with respect to the target raster; and 7) a nonorthogonality of the scan line and pixel deflection fields.

The effect of the target planet magnetic field can be neglected since the spacecraft would be about 100 to 1000 planet radii away when the navigation data would be taken. Sources 1 and 2 cause symmetric radial distortions about the electromagnetic null point. Source 5 causes a shift (null-offset) of the null point. Error sources 5, 6, and 7 are illustrated in Fig. 2 where x_0 represents the offset of the electromagnetic null point from the center of the target raster, ξ_1 represents

Fig. 1 Navigation system performance as a function of onboard instrument measurement uncertainty.



the common rotation of the deflection fields, and ξ_2 represents the nonorthogonality between the deflection fields. The symbols X_1 and X_2 define an orthogonal, absolute reference system determined from pre-launch measurement and ξ_1 and ξ_2 would be small angles.

Sources of optical distortion include⁶: 1) imperfect design and/or development of the telescope lens; 2) misalignment (nonorthogonality) of the lens optical axis with the target raster; and 3) decentering of the lens optical axis with respect to the center of the target raster.

Source 1 causes symmetric radial distortions about the optical principal point (intersection of the optical axis with the target raster). Source 2 causes asymmetric radial and tangential distortion about the principal point. Also, sources 2 and 3 cause a null-offset of the principal point from the center of the target raster.

An error in the value of focal length used to describe the instrument transfer function causes a symmetric radial distortion about the principal point. Errors in the values of pointing direction used to describe the instrument transfer function have a similar effect as errors in the values used for the location of the principal point on the target raster.

Instrument Measurement Model

The instrument will provide measurements of scanning beam deflection voltages which can be related to a physical location on the target raster. An arbitrary coordinate system in which to define image location measurements is an $x_1x_2x_3$ system (Fig. 3), where x_1 is in the plane of the target raster and in the direction of increasing pixel, x_2 is in the plane of the target raster and in the direction of increasing scan line, and x_3 is normal to x_1x_2 . The origin of $x_1x_2x_3$ is chosen to be at the measured center (from flight data) of the target raster which is the nominal location of the electromagnetic null and also the optical principal point. The coordinate axis x_3 is in the direction of the nominal optical axis (outward from the instrument).

A general expression for the measured image location of an object (i.e., star or satellite) in front of the optics, based on the colinearity equation of photogrammetry,⁸ is given by

$$\mathbf{x}_m = (f/w)C(I - E)Mt + \mathbf{x}_{op} + \mathbf{x}_{em} + \mathbf{n} \quad (1)$$

Fig. 2 Electromagnetic errors.

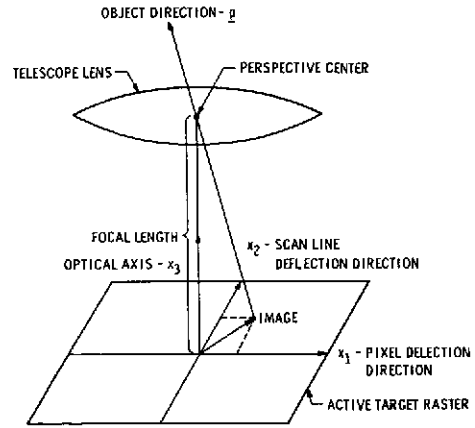
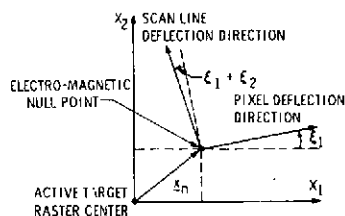


Fig. 3 Image geometry.

and a general expression for the measured image location of an object (reseau) on the target raster is given by

$$\mathbf{x}_m = \mathbf{x}_a + \mathbf{x}_{em} + \mathbf{n} \quad (2)$$

where the lower case boldface letters denote 2×1 vectors, unless otherwise mentioned, the upper case letters designate matrices and, f is the effective optical focal length of the instrument; M is the transformation matrix from an inertial reference system to a nominal instrument reference system calculated from telemetered measurements (which contain errors) of instrument pointing direction;

$$C = \begin{bmatrix} 1 & 0 & 0 \\ 0 & 1 & 0 \end{bmatrix}$$

\mathbf{t} is the spacecraft-centered inertial unit direction to an object; w is the third component of the 3×1 unit vector; $\mathbf{p} = Mt$, \mathbf{n} is measurement noise vector due to pixel and scan line resolution; \mathbf{x}_a is the absolute physical location of a reseau on the target raster determined precisely in X_1X_2 from pre-launch measurements.

The term $(I - E)$ is a rotation matrix that defines the deviation of the actual instrument orientation from the measured orientation. For small deviation angles ϵ_1 , ϵ_2 , and ϵ_3 , $(I - E)$ is approximated by

$$(I - E) = \begin{bmatrix} 1 & \epsilon_3 & -\epsilon_2 \\ -\epsilon_3 & 1 & \epsilon_1 \\ \epsilon_2 & -\epsilon_1 & 1 \end{bmatrix} \quad (3)$$

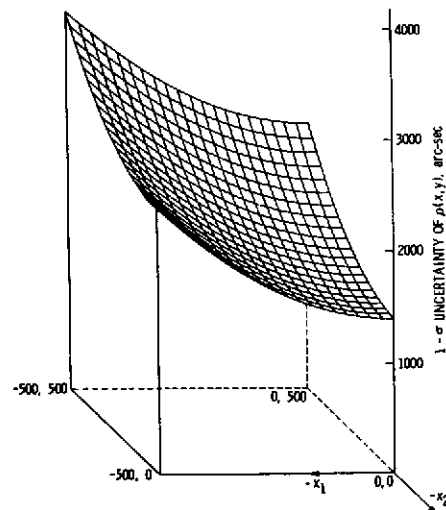


Fig. 4 Electromagnetic a priori uncertainty.

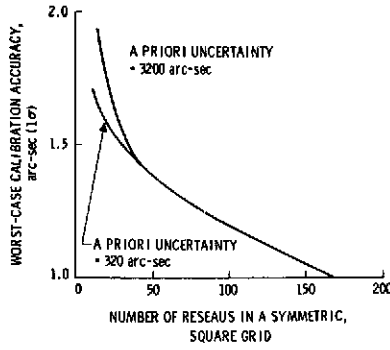


Fig. 5 Calibration accuracy of electromagnetic distortion as a function of reseau in the grid.

The terms \mathbf{x}_{em} and \mathbf{x}_{op} represent electromagnetic and optical distortions, respectively. The electromagnetic distortion, containing a null-offset, symmetric radial distortion Δ_{sr} , symmetric tangential distortion Δ_{st} , and common and non-orthogonal rotations, is given by $\mathbf{x}_{em} = \mathbf{x}_0 + A\mathbf{x}_a + B\mathbf{x}$ where

$$A = \begin{bmatrix} 0 & -(\xi_1 + \xi_2) \\ \xi_1 & 0 \end{bmatrix} \quad (4)$$

$$B = \begin{bmatrix} \Delta_{sr} & -\Delta_{st} \\ \Delta_{st} & \Delta_{sr} \end{bmatrix}$$

$$\Delta_{sr} = \sum_{i=1}^{M_1} \alpha_{2i-2} r^{2i-2} \quad (5)$$

$$\Delta_{st} = \sum_{i=1}^{M_2} \alpha_{2i-1} r^{2i-1} \quad (6)$$

α_i are electromagnetic distortion coefficients; r is the distance between image and electromagnetic null point in x_1x_2

$$r = (\mathbf{x}^T \mathbf{x})^{1/2}$$

$$\mathbf{x} = \mathbf{x}_i - \mathbf{x}_n$$

\mathbf{x} is the absolute location of image in X_1X_2 ; \mathbf{x}_n is the offset between arbitrary and absolute coordinate system origins; \mathbf{x}_i is the offset of electromagnetic null from origin of X_1X_2 .

The optical distortion, containing a null offset, a symmetric radial distortion δ_{sr} , an asymmetric radial and tangential distortion δ_{sp} , and a lens misalignment distortion δ_m , is given by

$$\mathbf{x}_{op} = \delta_{sr}\mathbf{x} + \delta_p + \delta_m \quad (7)$$

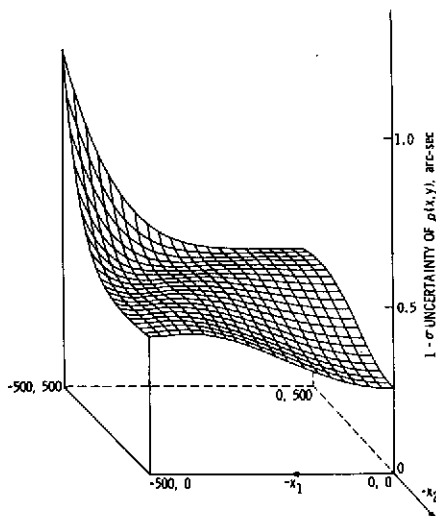


Fig. 6 Calibration accuracy of electromagnetic distortion using an 11 × 11 reseau grid.

where

$$\delta_{sr} = \sum_{i=1}^{M_2} \beta_{2i-2} r^{2i-2}$$

$$\delta_p = \delta_a \text{col}(-\sin\theta, \cos\theta) \quad (8)$$

$$\delta_a = \sum_{i=1}^{M_1} \beta_{2i-1} r^{2i} \quad (9)$$

$$\delta_m = \mathbf{x}d^T\mathbf{x} + \gamma_3 H\mathbf{x} \quad (10)$$

$$d = \text{col}(\gamma_1, \gamma_2)$$

$$H = \begin{bmatrix} 0 & -1 \\ 1 & 0 \end{bmatrix}$$

β_i are symmetric and asymmetric optical distortion coefficients; γ_i are lens misalignment distortion coefficients; r is the distance between image and principal point in X_1X_2 ;

$$r = (\mathbf{x}^T \mathbf{x})^{1/2}$$

$$\mathbf{x} = \mathbf{x}_i - \mathbf{x}_p$$

\mathbf{x} is the absolute location of the image in X_1X_2 ; \mathbf{x}_p is the offset of principal point from origin of X_1X_2 ; and θ is the distortion orientation.

From Eq. (1), it can be seen that the direction \mathbf{t} to an object can be reconstructed using the measured image location, the instrument focal length, and the instrument-pointing direction. The accuracy of this reconstructed direction is determined by the accuracy with which the parameter set $\mathbf{q} = \text{col}(f, \epsilon_1, \epsilon_2, \epsilon_3, \mathbf{x}_0, \mathbf{x}_n, \mathbf{x}_p, \alpha_0, \alpha_1, \alpha_2, \dots, \xi_1, \xi_2, \beta_0, \beta_1, \beta_2, \dots, \gamma_1, \gamma_2, \gamma_3, \theta)$ is known at the time of the measurement. Therefore, the object of an instrument geometric calibration is to determine \mathbf{q} from inflight data to an accuracy such that the uncertainty in \mathbf{t} is less than 5 arc-sec (1σ).

A reseau grid etched onto the target raster is commonly used for calibrating the electromagnetic distortion. The absolute locations of each reseau in the grid would be measured precisely on Earth. Differences between inflight measurements of reseau locations from their absolute locations would be used in an estimation process to determine the coefficients of electromagnetic distortion (Eq. 2).

Clusters of stars would be imaged to calibrate the optical parameters. The instrument would be moved by exercising the gimbaled platform to image the star cluster at various locations on the target raster. Since calibration of optical distortion is in reference to cluster of stars, the process also involves the calibration of instrument-pointing direction.

When the gimbaled platform is not commanded to move, the errors between the actual and measured instrument orientation are characterized by

$$\epsilon^T = \left(\sum_{i=1}^3 e_{1i}, \sum_{i=1}^3 e_{2i}, \sum_{i=1}^3 e_{3i} \right) \quad (11)$$

where e_{j1} are constant biases that are perfectly correlated between picture frames; e_{j2} are slowly varying biases that are

Table 1 Electromagnetic parameter uncertainty— 1σ

Parameter	Unit	Standard deviation	
		A priori	A posteriori
\mathbf{x}_0	arc-sec	1000	1.3×10^1
\mathbf{x}_n	arc-sec	1000	9.7
α_0	arc-sec/pixel	2.0	5.0×10^{-3}
α_1	arc-sec/pixel ²	2.8×10^{-8}	7.3×10^{-5}
α_2	arc-sec/pixel ³	4.0×10^{-8}	3.7×10^{-8}
α_3	arc-sec/pixel ⁴	5.6×10^{-9}	2.7×10^{-11}
α_4	arc-sec/pixel ⁵	8.0×10^{-12}	6.3×10^{-14}
α_6	arc-sec/pixel ⁶	1.1×10^{-14}	2.5×10^{-16}
ξ_1	arc-sec/pixel	2.0×10^{-1}	2.0×10^{-4}
ξ_2	arc-sec/pixel	2.0×10^{-1}	1.7×10^{-2}

correlated but not perfectly correlated between picture frames; e_{ji} are random biases that are uncorrelated between picture frames; and $j = 1,2,3$.

These instrument pointing errors can be modeled by the following linear stochastic differential equation:

$$\dot{e}_{ij}(t) = -e_{ij}(t)/T_{ij} + \xi_{ij} \tag{12}$$

where ξ_{ij} is a Gaussian white noise process with zero-mean and variance σ_{ij} ; T_{ij} is a correlation time; and $i,j = 1,2,3$.

Constant and random bias noise processes are conveniently represented by the limit processes of $T_{i1} \rightarrow +\infty$ and $T_{i3} \rightarrow +0$, respectively.

Calibration of Electromagnetic Distortion

A calibration philosophy was chosen such that sufficient reseau data would be available in each data frame to allow the calibration of electromagnetic distortion in that data frame to arc-sec accuracy independent of data from any other data frame. This philosophy was chosen because of the time varying nature of electromagnetic distortion from frame to frame due to deflection field interferences from other instruments and image charges on the vidicon tube. No attempt was made to determine possible accuracy improvements when electromagnetic distortion information from one data frame is used in the determination of distortion in another data frame.

A minimum variance sequential estimation process⁷ was used in performing a covariance analysis of the expected accuracy of calibrating electromagnetic distortion using a reseau grid. A symmetric reseau grid was investigated where for each reseau at location (x_{a1}, x_{a2}) , reseaux were also located at $(x_{a1}, -x_{a2})$, $(-x_{a1}, x_{a2})$, and $(-x_{a1}, -x_{a2})$. A reseau was also located at the center of the target raster (0,0). The reseaux were evenly spaced and spanned the target raster.

The accuracy of calibrating the parameter set $q_{em} = \text{col}(x_n, x_i, \xi_1, \xi_2, \alpha_0, \alpha_1, \alpha_2, \alpha_3, \dots)$ was determined as a function of the number of reseaux in the grid and the a priori uncertainty of q_{em} . The location uncertainty of a point x on the target raster is described by the (2×2) covariance matrix

$$\Gamma_x = [\partial x_m / \partial q_{em}] \Gamma_{q_{em}} [\partial x_m / \partial q_{em}]^T \tag{13}$$

where $\Gamma_{q_{em}}$ is the covariance matrix of q_{em} generated by the estimation process after processing the measured locations of the reseaux. The calibration accuracy of a point on the target raster is defined by

$$\rho(x) = [\text{Trace} \Gamma_x]^{1/2} \tag{14}$$

The a priori uncertainty of q_{em} used in this investigation is listed in Table 1. These values chosen were such that each parameter caused a 1000 arc-sec uncertainty at the corners of the target raster, except ξ_1 and ξ_2 which caused 100 arc-sec uncertainties at the corners. Experience with the narrow-

Table 2 Optical parameter uncertainty— 1σ

Parameter	Unit	Standard deviation	
		A priori	A posteriori
f	mm	9.5×10^{-1}	9.2×10^{-1}
e_{j1}	mrاد	3.0	1.2
e_{j2}	mrاد	1.0×10^{-1}	4.2×10^{-2}
e_{j3}	mrاد	3.0×10^{-1}	2.2×10^{-1}
x_p	arc-sec	1.0×10^2	5.3×10^1
θ	rad	1.0	2.0×10^{-1}
γ_1	arc-sec/pixel ²	4.0×10^{-4}	3.0×10^{-6}
γ_2	arc-sec/pixel ²	4.0×10^{-4}	3.4×10^{-6}
γ_3	arc-sec/pixel	2.0×10^{-1}	6.6×10^{-4}
β_0	arc-sec/pixel	2.0×10^{-1}	4.8×10^{-2}
β_1	arc-sec/pixel ²	2.0×10^{-4}	2.4×10^{-6}
β_2	arc-sec/pixel ³	4.0×10^{-7}	6.1×10^{-9}
β_3	arc-sec/pixel ⁴	4.0×10^{-10}	2.3×10^{-10}

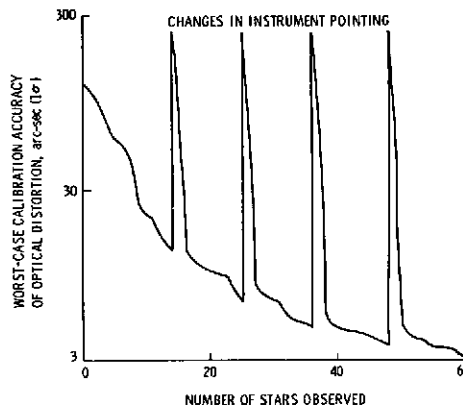


Fig. 7 Calibration of optical distortion.

angle Mariner Mars TV cameras, where the total distortion from all sources was less than 100 arc-sec, indicates that the uncertainties used in this investigation are conservative. Also, coefficients through α_3 are generally sufficient to fit the Mariner TV distortions. A contour which shows the a priori uncertainty mapped over a quadrant of the target raster is shown in Fig. 4.

Figure 5 shows the worst-case calibration accuracy, $\rho(500, 500)$, as a function of the number of reseaux in the grid. Also shown in the figure is the worst-case calibration accuracy with the a priori uncertainty reduced an order of magnitude. The figure shows that the calibration accuracy becomes essentially independent of a priori uncertainty when more than 50 reseaux are in the grid. Figure 6 shows the expected calibrated accuracy over a quadrant of the target raster when data from an 11×11 reseau grid are used. Table 1 also lists the a posteriori uncertainty of q_{em} for an 11×11 grid.

The conclusions derived from the investigation of electromagnetic distortion were: 1) with a symmetric reseau grid and the electromagnetic null point at the center of the reseau grid, calibration accuracy is symmetric about the null point; 2) the calibration accuracy within 500 pixels of the electromagnetic null point is better than 0.5 arc-sec (1σ) when using an 11×11 reseau grid; 3) an 11×11 reseau grid enables a worst-case calibration accuracy of 1.2 arc-sec (1σ) for each frame of data, essentially independent of a priori uncertainty and data from any other data frame.

Calibration of the Optical System

Normally, the optical distortion of a narrow angle camera is less than the scan resolution of its vidicon and exhibits long term stability (repeatability). The major uncertainty associated with the optics is in the pointing direction of the optical axis at shutter time. Imaging star clusters whose directions are essentially perfectly known is an ideal source data for calibrating the optical system. Following the conservative philosophy associated with electromagnetic distortion calibration, it will be assumed that the optical system will be calibrated during each planet approach and that the

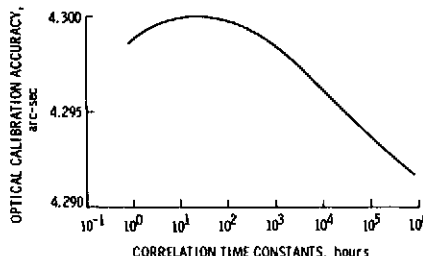


Fig. 8 Calibration accuracy as a function of correlation time constants using 50 star images.

optical distortion is repeatable during a 20 to 30 day navigation measurement period.

A cluster of stars was selected in the neighborhood of "Coma Berenices" to investigate the calibration of the optical parameters and instrument pointing direction. Stars brighter than seventh visual magnitude were assumed to be observable by using long exposure times (5 sec). The number of stars observed in one data frame would range from ten to fourteen. The instrument, mounted on a gimballed platform would be moved several times (at 15 min intervals) to obtain calibration information throughout the instrument FOV.

The a priori parameter uncertainties used in the investigation of optical distortion are listed in Table 2. The uncertainty values of optical distortion were chosen such that each parameter contributed a 100 arc-sec uncertainty at the edge of the target raster. The uncertainty values for the pointing error parameters were based on present accuracies associated with the Mariner spacecraft. Experience with Mariner narrow-angle science TV cameras, which have negligible optical distortion, indicates that the uncertainty values used in the investigation were conservative.

Figure 7 illustrates the expected worst-case calibrated accuracy of the optical system as a function of star images. The significant degradations in the figure resulted from movement uncertainty of the gimballed platform. Calibration accuracy is quickly restored by processing a few stars in a new data frame. To accomplish 4.3 arc-sec calibration accuracy for optical distortions and instrument pointing direction uncertainty, observations of approximately 50 star images were needed. Table 2 lists the a posteriori uncertainty of the optical system parameters when 50 star images were studied.

A parametric study determining the effect of the bias correlation times (Fig. 8) showed that calibrated accuracy was very insensitive to correlation times. From these results, it is concluded that: 1) observations of approximately 50 stars facilitates the calibration accuracy of optical distortions to better than 5 arc-sec (1σ); 2) changes in correlation times of sequentially correlated biases representing instrument pointing direction errors have little effect on the calibrated accuracy; and 3) many stars (>10) can be imaged simultaneously within the instrument FOV with the capability of detecting stars brighter than 7th magnitude.

Conclusions

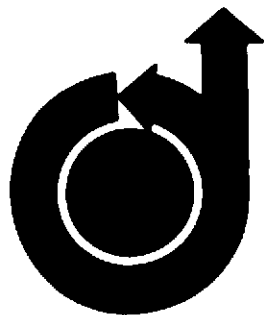
The worst-case uncertainty in reconstructed object direction would be less than 5 arc-sec (1σ) when using an 11×11 reseau grid and star clusters to perform an inflight calibration. The uncertainty in reconstructed object direction of an image within 500 pixels from the center of the target raster would be less than 2.5 arc-sec (1σ). Approximately 50 star images are needed to obtain this level of accuracy.

A significant developmental effort is still required before this type of instrument is flight worthy. The 9 to 12 yr outer planet missions require long life time instruments. Dynamic range and sensitivity is a problem area due to the brightness of the satellites as compared to the dim reference stars. Also, since optical measurements are only an element of the navigation system, additional effort is needed in the areas of Earth-based radio tracking measurements and planetary and natural satellite ephemeris development to yield a highly accurate, reliable and complementary system.

References

- ¹ Long, J. E., "Missions to the Outer Planets," *Aeronautics and Astronautics*, Vol. 7, No. 6, June 1969, pp. 32-47.
- ² Breckenridge, W. G. and Duxbury, T. C., "Defining a Spacecraft-Based Navigation Measurement System," *Aeronautics and Astronautics*, Vol. 8, No. 6, May 1970, pp. 44-49.
- ³ Duxbury, T. C., "A Spacecraft-Based Navigation Instrument for Outer Planet Missions," *Journal of Spacecraft and Rockets*, Vol. 7, No. 8, Aug. 1970, pp. 928-933.
- ⁴ Ball, J. E. and Duxbury, T. C., "Navigating the Grand Tours," *Aeronautics and Astronautics*, Vol. 8, No. 9, Sept. 1970, pp. 73-76.
- ⁵ Wong, K. W., "Geometric Calibration of Television Systems," paper presented at the 11th International Congress of Photogrammetry, International Society of Photogrammetry, Lusanne, Switzerland, July 1968.
- ⁶ *Manual of Photogrammetry*, edited by M. M. Thompson, American Society of Photogrammetry, Falls Church, Va., 1968, pp. 461-490.
- ⁷ Griffin, R. E. and Sage, A. P., "Sensitivity Analysis of Discrete Filtering and Smoothing Algorithms," *AIAA Journal*, Vol. 7, No. 10, Oct. 1969, pp. 1890-1897.

APPENDIX C
ENCOUNTER TRAJECTORY ACCURACY FOR A 1971
MARS ORBITER MISSION



**AIAA Paper
No. 71-189**

**ENCOUNTER TRAJECTORY ACCURACY FOR A
1971 MARS ORBITER MISSION**

by
THOMAS C. DUXBURY, S. KUEN WONG, GEORGE H. BORN
Jet Propulsion Laboratory
Pasadena, California

AIAA 9th Aerospace Sciences Meeting

NEW YORK, NEW YORK / JANUARY 25-27, 1971

First publication rights reserved by American Institute of Aeronautics and Astronautics,
1290 Avenue of the Americas, New York, N. Y. 10019. Abstracts may be published without
permission if credit is given to author and to AIAA. (Price: AIAA Member \$1.50. Nonmember \$2.00).

Note: This paper available at AIAA New York office for six months;
thereafter, photoprint copies are available at photocopy prices from
Technical Information Service, 750 3rd Ave., New York, N. Y. 10017

Thomas C. Duxbury**
 S. Kuen Wong†
 George H. Born‡
 Jet Propulsion Laboratory

Abstract

This paper presents the results of an investigation of the expected orbit determination accuracy during the approach phase of a 1971 Mars orbiter mission. This expected accuracy was determined for Earth-based doppler tracking data with and without the addition of ranging or on-board optical tracking data. The sensitivity of this expected accuracy to errors effecting the radio and optical data also was examined. It was found that unless planetary ephemeris errors are reduced below their anticipated levels, the addition of ranging data does not significantly improve the estimate of the spacecraft's state near encounter. However, the addition of optical data could make a significant improvement in the encounter accuracy when the spacecraft is outside the sphere of influence of Mars. This improvement diminished as the spacecraft deeply penetrated the sphere of influence.

Introduction

The planet Mars, still in the limelight for future space exploration, is to be investigated by the 1971 Mariner Mars and 1975 Viking missions. Both of these missions insert spacecraft into orbits about Mars with the Viking mission also placing a lander on Mars surface. The orbit insertion accuracy requirements of these types of missions place a major importance on the accuracy of the trajectory estimate at the time of insertion maneuver computation. To better understand the characteristics of this problem, a study was performed to determine the expected trajectory estimation accuracy during Mars approach and to identify the parameters which most significantly influence this accuracy.

A 30 day period prior to a 1971 Mars encounter was investigated. A data cutoff of encounter minus 7 hours (E-7h) was used to allow time for orbit insertion strategy evaluation, the insertion maneuver to be calculated, and spacecraft commands to be determined, transmitted, verified, and executed. A long and short arc of two-way doppler and two-way doppler plus range was investigated. A two day arc of optical data, assumed to be obtained during a normal science data sequence from science and engineering instruments of the types used on interplanetary spacecraft, also was investigated.

Analyses revealed that accuracies of 50 km(1σ) in trajectory parameters which significantly affect the spacecraft orbit about Mars could be obtained from expected radio data only. The major benefit of optical data would be to relax the time critically of mission operations in support orbit insertion operations by allowing trajectory accuracies comparable to radio data only at E-7h to be obtained at E-18h. Optical data could have an even greater significance if a data sequence, type of data taken during the sequence, and instrumentation were developed to satisfy a navigation function.

Radio Tracking System

For this study, it was assumed that Earth-based radio tracking data would be obtained from the Deep Space Station at Goldstone, California and at Woomera, Australia. These stations provide near continuous tracking of a spacecraft. A detailed description of the radio tracking system is given in reference 1. A detailed description of radio tracking data including its errors sources is given in references 1 and 2.

As discussed in reference 2, there are three major types of errors which affect the radio tracking data. These are: observer related errors, spacecraft-related errors, and planetary ephemeris errors. The first of these occurs through the use of insufficiently accurate models to locate the observer relative to the spacecraft and to calibrate out the effect of the transmission media. The second type of error occurs through a lack of precision in modeling all of the forces on a spacecraft. The last type of error is due to an imprecise model for the position of the target planet relative to the earth.

Errors result from uncertainties in the tracking station locations, in the direction of Earth's axis of figure with respect to its spin axis, in timing, and in inadequate modeling of charged particle and troposphere effects on the radio signal traveling between the tracking station and the spacecraft. These parameters were combined and expressed in terms of an equivalent station location uncertainty. A 1σ uncertainty of 3 meters was assumed for the station's distance from the Earth's spin axis and a 1σ uncertainty of 0.00005 deg. was assumed for station longitude (~5m on the Earth's surface).

*This paper presents the results of one phase of research carried out at the Jet Propulsion Laboratory, California Institute of Technology, under Contract No. NAS 7-100, sponsored by the National Aeronautics and Space Administration.

**Group Leader

† Orbit Determination Group Head

‡ Senior Research Engineer, Mission Analysis Division

Spacecraft related acceleration errors are due to uncertainties in the masses of bodies of attractions and non-gravitational forces resulting from gas leaks and solar pressure. A 1σ uncertainty of 1.4×10^{-12} km/sec² was assumed for the non-gravitational forces.

In addition, a 1σ uncertainty of 0.1 km³/sec² in the gravitational constant of Mars was assumed. A 1σ uncertainty of 1.0×10^{-7} in Brouwer's set III orbital elements³ was used. This corresponds to approximately 30 km in each of the cartesian coordinates of Mars measured in mean of 1950 ecliptic coordinate system.

A 0.003 m/sec (1σ) uncertainty was used for the random noise on the two-way doppler data for a 60 second sample. Finally, the standard deviation of the ranging data was assumed to be 100 m.

Optical Navigation System

For the purpose of this study, it was assumed that optical navigation data would be obtained from instruments of the types to be used on the Mariner Mars 1971 spacecraft (Fig. 1). These instruments include a narrow angle science television camera, a two-degree-of-freedom scan platform on which the TV is mounted, and the attitude control celestial sensors. The use of these instruments for interplanetary navigation was demonstrated successfully on the Mariner Mars 1969 mission⁴.

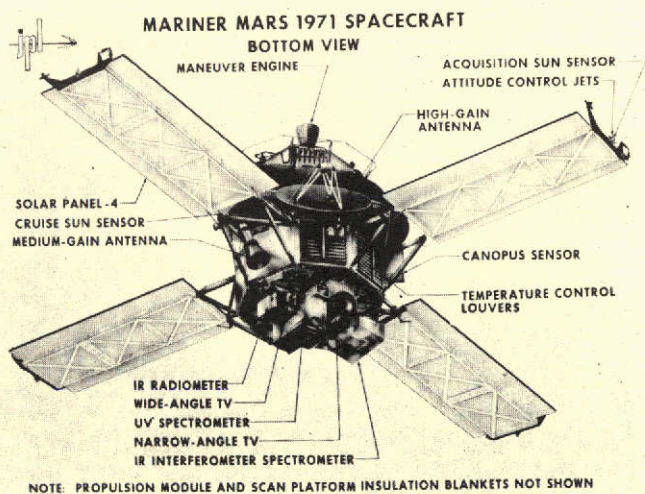


Figure 1

Celestially referenced measurements of the spacecraft - Mars direction can be reconstructed from telemetered science and engineering data. The direction to the optical center of Mars can be determined in TV coordinates by curve fitting the lit limb of Mars image in a TV picture^{5, 6}. Center-finding errors would result from geometric distortion of the Mars image, errors in identifying the lit limb of Mars, and errors in the mathematical model of Mars figure. The celestially referenced pointing direction of the TV at the time a picture was taken would be determined from body fixed measurements of the scan platform pointing direction and the spacecraft attitude position. TV pointing errors would result from instrument alignment uncertainties and telemetry resolution of the scan platform and attitude control measurements.

Mars center-finding errors were modeled as two proportionality constants (k_1, k_2) of Mars linear diameter Φ ⁵. The constant k_2 was defined to act in a direction along a line between the horns of Mars lit limb. The constant k_1 was defined to be orthogonal to k_2 . Center-finding errors due to image distortion can be reduced by geometrically correcting the lit limb data using reseau information in the TV picture. (A reseau grid is the pattern of black dots or "+" signs commonly seen on lunar and planetary TV pictures taken aboard a spacecraft.) Measurement and modeling errors can be reduced by also estimating Mars figure and orientation when determining the center of Mars.

The TV pointing errors were modeled as three orthogonal small angle rotations ($\epsilon_1, \epsilon_2, \epsilon_3$) where ϵ_1 and ϵ_2 change the pointing direction of the TV and ϵ_3 is a rotation about the TV optical axis. Each of the three rotations were composed of constant biases (e_{11}, e_{21}, e_{31}), exponentially correlated biases (e_{12}, e_{22}, e_{32}), and random biases (e_{13}, e_{23}, e_{33}) as expressed in the following equation

$$\begin{bmatrix} \epsilon_1 \\ \epsilon_2 \\ \epsilon_3 \end{bmatrix} = \begin{bmatrix} e_{11} + e_{12} + e_{13} \\ e_{21} + e_{22} + e_{23} \\ e_{31} + e_{32} + e_{33} \end{bmatrix} \quad (1)$$

These biases were modeled by the following linear stochastic differential equation

$$\dot{e}_{ij}(t) = -e_{ij}(t)/T_{ij} + N_{ij} \quad (2)$$

where N_{ij} is the Gaussian white noise with zero mean, T_{ij} is the correlation time of the bias, and $(i, j) \rightarrow (1, 2, 3)$. The constant and random biases are represented by the limit processes of $T_{i1} \rightarrow +\infty$ and $T_{i3} \rightarrow +0$, respectively.⁷

The constant biases represent fixed mounting misalignments and null offsets of the instruments. The exponentially correlated biases represent non-random, non-repeatable errors such as instrument null drifts, spacecraft structural bending and scan platform gimbal nonlinearities. The random biases represent random instrument noise and telemetry resolution. The constant biases can be determined partially during flight by imaging stars whose directions are well known. The random biases can be reduced by filtering a series of attitude control measurements about the picture time to lessen the effect of telemetry resolution.

The a priori uncertainty of the optical errors are listed in Table 1. The table includes a range for these uncertainties plus the nominal values used in the study. The table also includes the expected performance of an inflight calibration of the constant biases using stars and a geometric calibration of the center-finding errors using reseau data.

Navigation Study

The approach position of four 1971 Earth-Mars trajectories with launches in May or June, 1971 and arrivals in November 1971 were investigated using covariance analysis. The uncertainty of the encounter parameters for each of these trajectories differed by less than 10%; consequently, only a typical set of results will be presented.

PARAMETERS	Units	Uncertainty		
		Min	Nom	Max
Constant Biases	mrad			
Star Calibration		2.00	3.00	4.00
No Calibration		0.50		1.00
Correlated Biases	mrad	0.01	0.10	0.15
Random Biases	mrad	0.15	0.30	0.40
Center Finding - $k_2 \Phi$	km			
Calibrated TV Data		40.00	50.00	60.00
Uncalibrated TV Data		70.00		100.00
$(\sigma_{k_1} = 1.4 \sigma_{k_2})$				

Table 1. A Priori Optical Parameter Uncertainties - 1r

It was assumed that the final trajectory correction maneuver before orbit insertion occurred at encounter minus 30 days (E-30d). Encounter is defined to be periapsis passage of the approach hyperbola. Radio tracking data arcs of two-way doppler and two-way doppler plus range were investigated in order to determine the trajectory estimation accuracy at the time of orbit insertion maneuver computation. The data arc provides continuous doppler coverage between E-30d and E-7h. For the doppler plus range arc, a range point was taken every 24 hours from E-30d to E-5d.

An optical data arc length from E-72h to E-24h was investigated. It was assumed that 30 TV pictures of Mars would be taken per day during this time period and stored aboard the spacecraft. It was assumed that the data taken during a 24 hour period would be played back to earth beginning at E-48h and E-24h, and would be available for processing at E-44h and E-20h. It was further assumed that only 80 percent of these pictures could be used for navigation since the lit limb of Mars may not appear in all of the pictures due to TV pointing errors.

For investigating the combined data, optical data was used with the long arc of doppler data. An optical data sensitivity analysis was performed by a covariance analysis where the radio data performance was kept at nominal and the a priori uncertainties of the optical errors were varied within the ranges in Table 1.

The major error sources for the encounter phase of the trajectory were studied via covariance analysis with a parameter consider option. The assumption was made that the observation data are unbiased, and uncorrelated with known variances. It was assumed that the filter only estimates the state of the spacecraft and does not account for model errors. Since the filter is not optimal and the filter covariance does not represent the true state estimation errors, the consider covariance which does represent the true state estimation error is computed.

Briefly, the derivation of the consider covariance matrix is as follows. Assume that the state and observation relationships have been linearized about known nominal values. Let x_0 be the epoch state vector to be estimated, $z(t_i)$ the i^{th} observation vector, $\eta(t_i)$ the Gaussian observation noise vector and y a vector of unknown dynamic and observation model parameters. It is assumed that y is a random vector with mean zero and known covariance Γ_y . The true observation relationship is

$$z(t_i) = h(t_i) U(t_i, t_0) x_0 + b(t_i) y + \eta(t_i) \quad (3)$$

By definition, the consider parameters are not estimated. Since the y parameters are ignored in the formation of the state estimate, the assumed data equation becomes

$$z(t_i) = h(t_i) U(t_i, t_0) x_0 + \eta(t_i) \quad (4)$$

Using equation (2) the weighted least squares filter for x_0 is

$$\hat{x}_0 = (H^T R^{-1} H)^{-1} H^T R^{-1} z \quad (5)$$

where

$$H = \begin{bmatrix} \eta_0 \\ \eta_1 U(t_1, t_0) \\ \vdots \\ \eta_N U(t_N, t_0) \end{bmatrix}, \quad z = \begin{bmatrix} z(t_0) \\ z(t_1) \\ \vdots \\ z(t_N) \end{bmatrix}$$

and

$$R = E \left\{ \begin{bmatrix} \eta(t_0) \\ \eta(t_1) \\ \vdots \\ \eta(t_N) \end{bmatrix} \begin{bmatrix} \eta(t_0) & \eta(t_1) & \dots & \eta(t_N) \end{bmatrix} \right\}$$

Using equations (3) and (5) and assuming that $E[y \eta^T] = 0$ it can be shown that the actual or consider covariance of \hat{x}_0 is given by

$$\Gamma_c = \Gamma_p + \Gamma_p A^T R^{-1} B \Gamma_y B^T R^{-1} A \Gamma_p \quad (6)$$

where the filter covariance, Γ_p , is given by

$$\Gamma_p = (H^T R^{-1} H)^{-1}$$

and

$$B = \begin{bmatrix} b_0 \\ b_1 \\ \vdots \\ b_N \end{bmatrix}$$

If a priori statistics, P_0 , are available for \hat{x}_0 , Γ_p in equation (6) becomes

$$\Gamma_p = (H^T R^{-1} H + P_0^{-1})^{-1}$$

Equation (6) and its attendant mapping relationships were used to generate all results for this paper.

Table 2 summarizes the a priori statistics used for the X_0 and y vector in this study.

Parameter	Standard Deviation
A priori Cartesian position coordinates at E-30d	10,000 km
A priori Cartesian Velocity coordinates at E-30d	100 m/sec
Ephemeris elements of Mars (Brouwer Set III)	1.0×10^{-7}
Martian GM	$0.1 \text{ km}^3/\text{sec}^2$
Constant non-gravitational forces	$10^{-12} \text{ km}/\text{sec}^2$ in each component
Error in station distance off spin axis	3 m
Error in station longitude	5 m

Table 2. A Priori Standard Deviations

The target parameters chosen for accuracy analysis are the \underline{B} plane parameters⁸ defined in Figure 2. The uncertainty in these parameters is mapped into the 1σ aim plane dispersion ellipse shown in Figure 3.

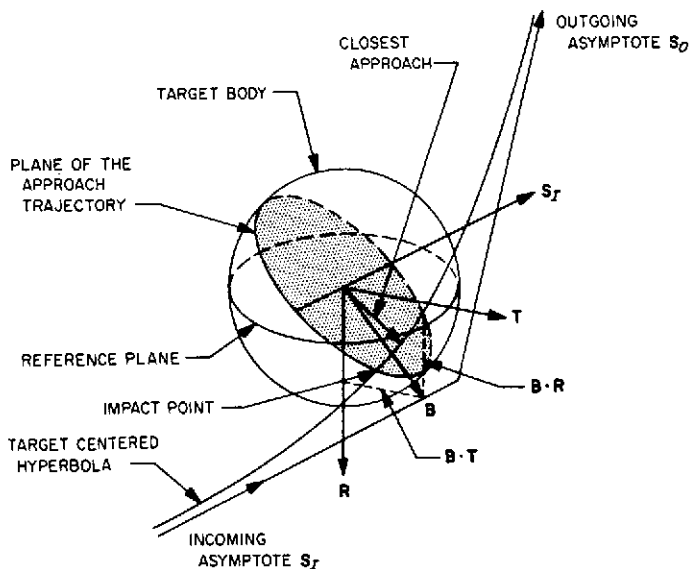


Figure 2. \underline{B} Plane Target Parameters

The following definitions refer to Figures 2 and 3.

Parameter	Definition
\underline{B}	The vector from the center of the target body directed perpendicular to the incoming asymptote of the target centered approach hyperbola.
\underline{T}	Unit vector from the center of the target body, defined by the intersection of the plane normal to the

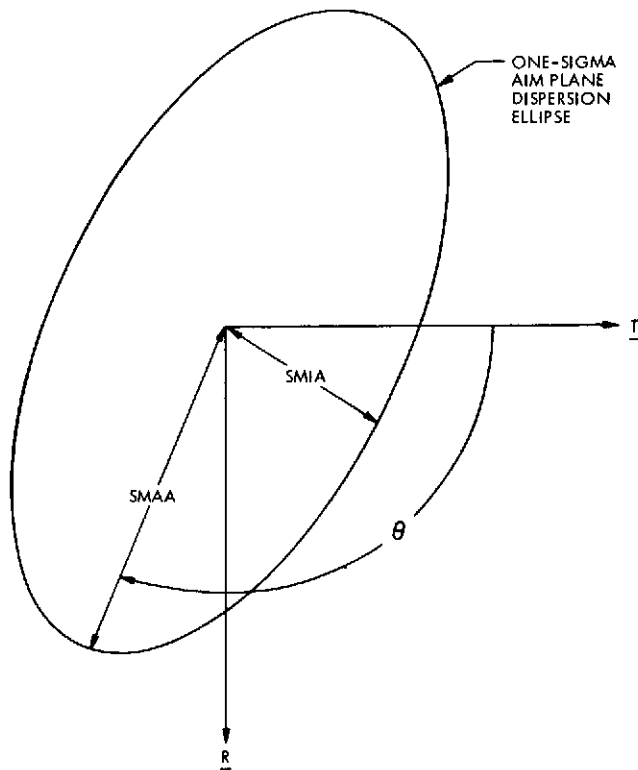


Figure 3. Definition of Aim Plane Dispersion Ellipse Nomenclature

Parameter	Definition
	incoming asymptote with a reference plane (usually the true ecliptic of date) centered at the target body
\underline{R}	Unit vector perpendicular to \underline{T} in the \underline{B} , \underline{T} plane, positive toward the -z direction of the reference plane
$\underline{B} \cdot \underline{R}$	The component of \underline{B} along \underline{R}
$\underline{B} \cdot \underline{T}$	The component of \underline{B} along \underline{T}
SMAA	The semi-major axis of the one-sigma uncertainty ellipse in the \underline{R} , \underline{T} plane
SMIA	The semi-minor axis of the one-sigma uncertainty ellipse
θ	The orientation angle of SMAA measured positive clockwise from \underline{T} to \underline{R}
t	The time of closest approach to the target

Encounter Accuracy Results

The results of a sensitivity analysis of data type to various error sources is shown in Figures (4) through (9). The sensitivity of the semimajor axis and the semiminor axis of the dispersion ellipse as well as the time of flight are shown. The statistics of these quantities are not greatly effected by approach geometry hence they are typical of all four trajectories examined. The standard deviations for the consider parameters of the nominal case shown on these figures are given in Table 2.

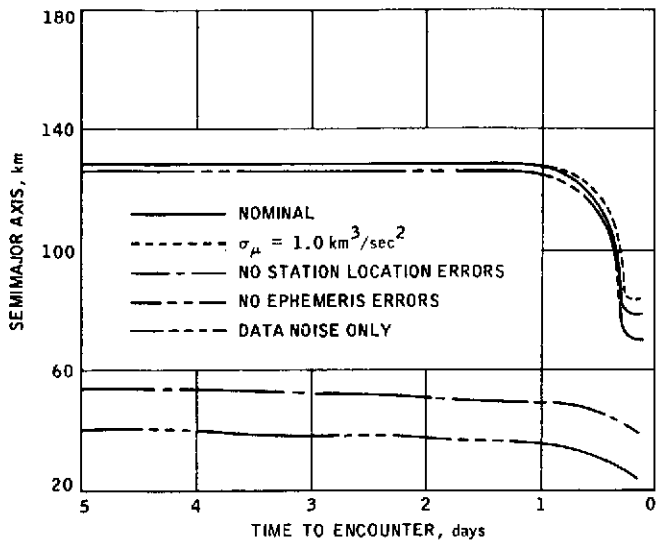


Figure 4. Encounter Accuracy for Doppler Only

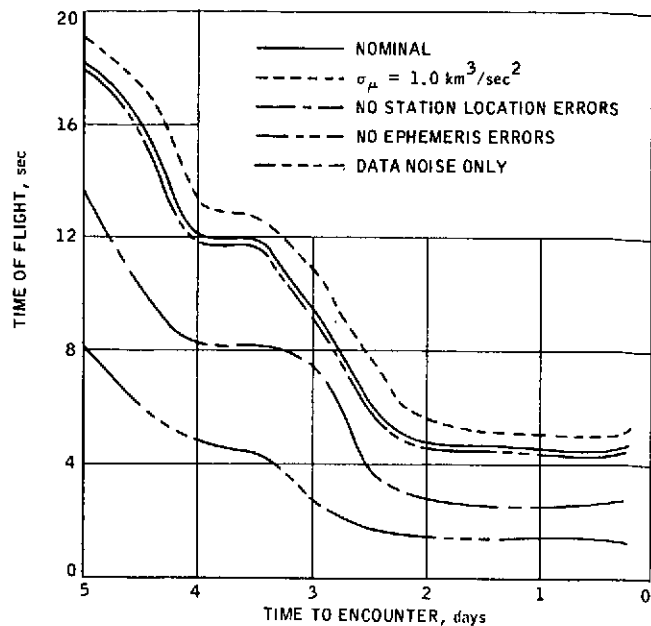


Figure 6. Encounter Accuracy for Doppler Only

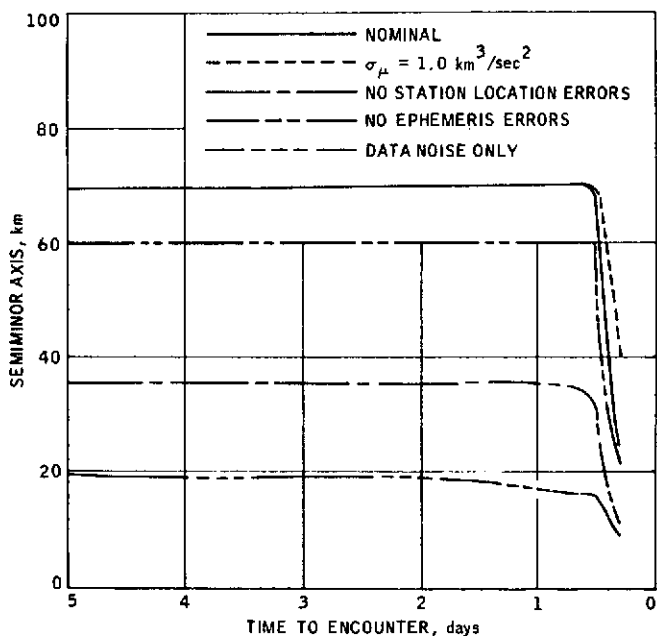


Figure 5. Encounter Accuracy for Doppler Only

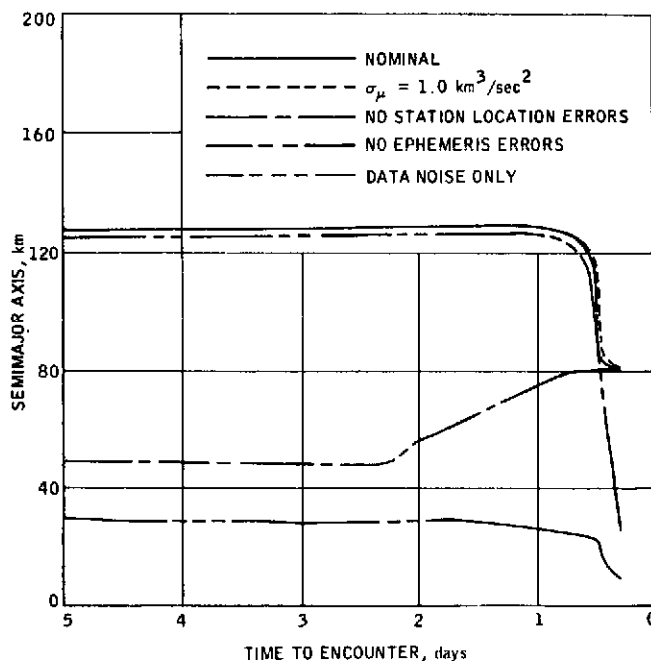


Figure 7. Encounter Accuracy for Doppler plus Range

As indicated by Figures 4, 5 and 6 the major error source for doppler tracking is the error in the location of the station. Ephemeris errors have little influence on the doppler accuracy at encounter since the range rate is not sensitive to ephemeris errors. Figure 5 indicates some sensitivity at E-7h of the semiminor axis to errors in the gravitational constant of Mars. This is because the minor axis at this time lies along the \bar{B} vector and the planet-asymptote distance is sensitive to the mass of the target planet.

In the case of doppler plus range, shown in Figures (7) through (9), the dominant error source at E-7h is the error in the ephemeris. In fact,

if the ephemeris errors are removed, the estimate uncertainties due to other consider parameters are only slightly greater than those due to only the data noise. The combination of range plus doppler is very effective in the absence of ephemeris errors since the probe-planet range is determined.

In addition to the long arc of tracking, a short data arc from E-5d to E-7h was examined. It was found that the uncertainty of all encounter parameters differed by less than 10 percent at E-7h from the results shown in the figures. Consequently, if another maneuver at E-5d was necessary there would be sufficient time to reacquire the orbit.

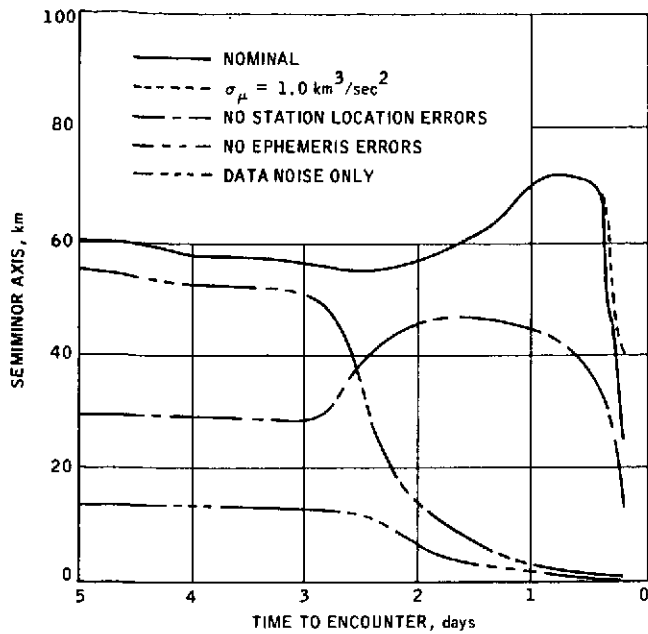


Figure 8. Encounter Accuracy for Doppler plus Range

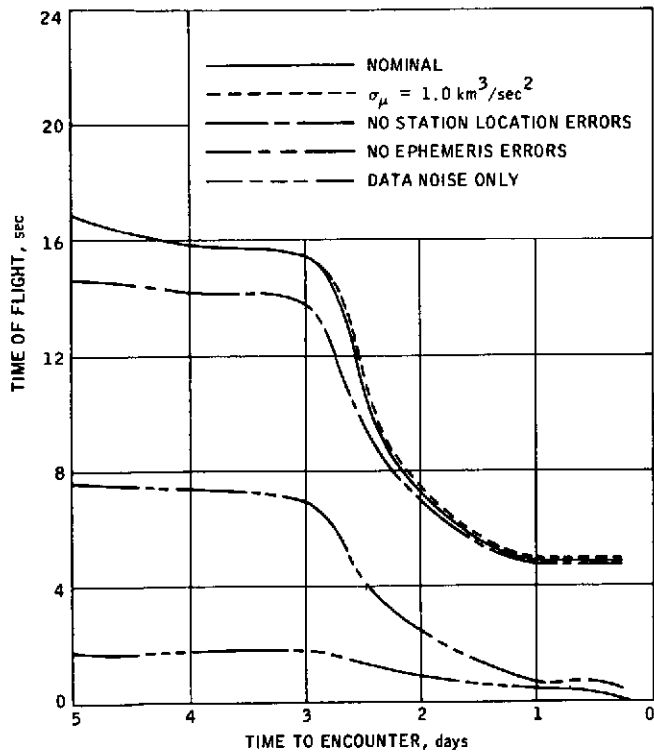


Figure 9. Encounter Accuracy for Doppler plus Range

Figure 10 presents the aim plane dispersion ellipse at E-1d and E-7h. This figure shows how the dispersion ellipse reorients itself as planetary forces become dominant.

The nominal nongravitational force of 10^{-12} km/sec² used for this study had a negligible effect on encounter accuracy. However, accuracy is greatly impaired for forces an order of magnitude larger than this. In fact, a nongravitational force of 10^{-11} km/sec² would be the dominant

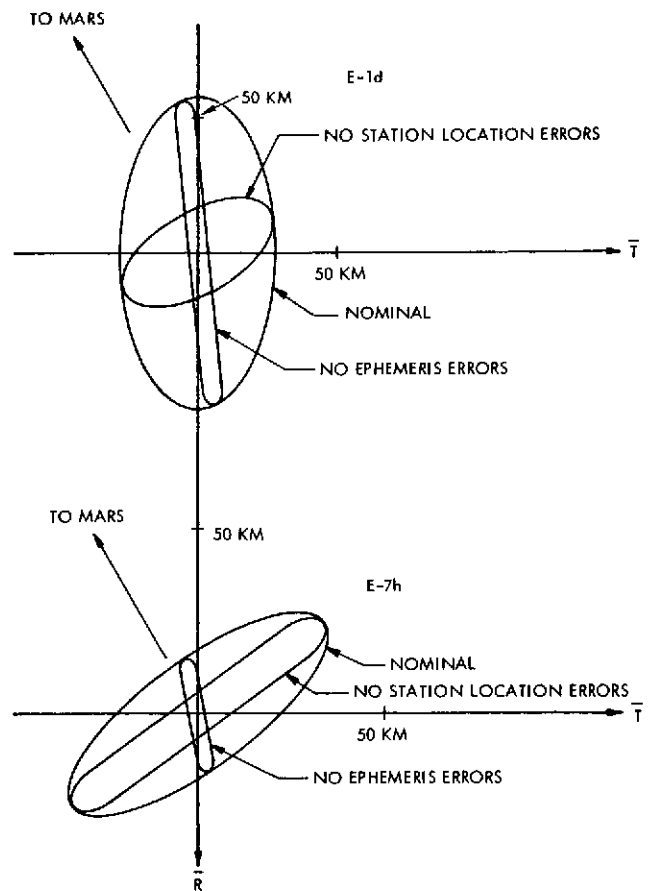


Figure 10. 1 Aim Plane Dispersion Ellipse at E-1d and E-7h for Doppler plus Range

error source throughout the tracking interval. At E-7h the uncertainty in the major axis is increased from the nominal by 20 percent and the uncertainty to the minor axis by 250 percent. The uncertainty in time of flight is increased by 5 percent for the case of doppler plus range and by 25 percent for doppler only. It should be noted that the orbit uncertainty which the nongravitational forces introduce is a function of the length of the data arc. For the short data arc of 5 days a nongravitational force as large as 10^{-11} has negligible influence on encounter accuracy.

Since the encounter parameters are a measure of how well the coordinates of the probe relative to the target planet are known, their accuracy is greatly improved as the probe approaches the planet. This characteristic is demonstrated by all the figures. In fact, if the spacecraft is tracked to encounter the uncertainties shown in the figures at E-7h will decrease by more than an order of magnitude. The encounter accuracies for the nominal cases presented in the figures represent RSS position and velocity errors of 60 km and 30 m/sec when mapped to hyperbolic periapsis.

For the study of optical data, the correlation times of the exponentially correlated biases were not known because the behavior of instruments and spacecraft structure during flight were not known. Therefore, the worse case correlation time was determined and used as nominal to give conservative results. The worst case correlation time was defined to give the largest SMAA after processing the optical data combined with radio tracking to

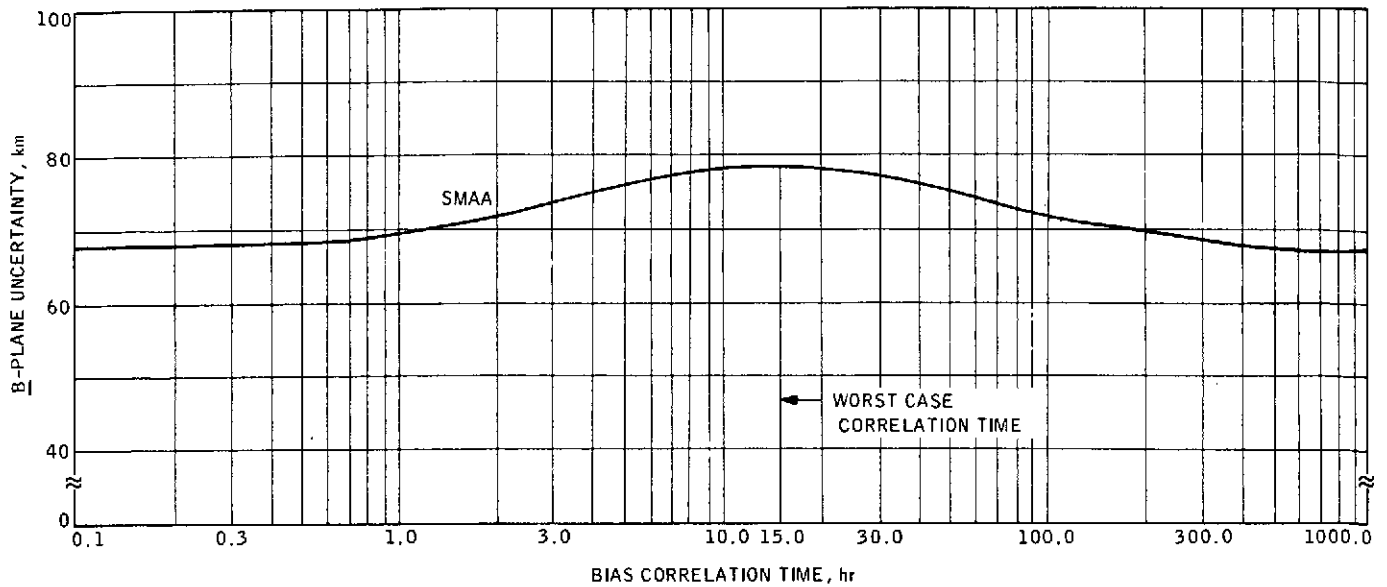


Figure 11. Encounter Accuracy vrs. Bias Correlation Time

E-24 hours. Using the nominal a priori uncertainties of the optical error parameters, the B-plane uncertainties were determined as a function of correlation time (Figure 11). A worst case correlation time of 15 hours was found and used as nominal for the remainder of the study.

The expected encounter accuracy using radio and optical data is shown on Figures 12 through 13. It can be seen that the addition of optical data can make a significant improvement in accuracy at E-1d; however, only a limited improvement is made at E-7h due to the planet center finding errors. Optical data gives little improvement in time of flight.

The sensitivity of this accuracy at E-24h to variations in the a priori uncertainty of optical error sources is shown in Figures 14 through 17. It was found that the expected trajectory accuracy is most sensitive to uncertainty variations within the expected ranges of correlated and random biases. The correlated bias uncertainties are not

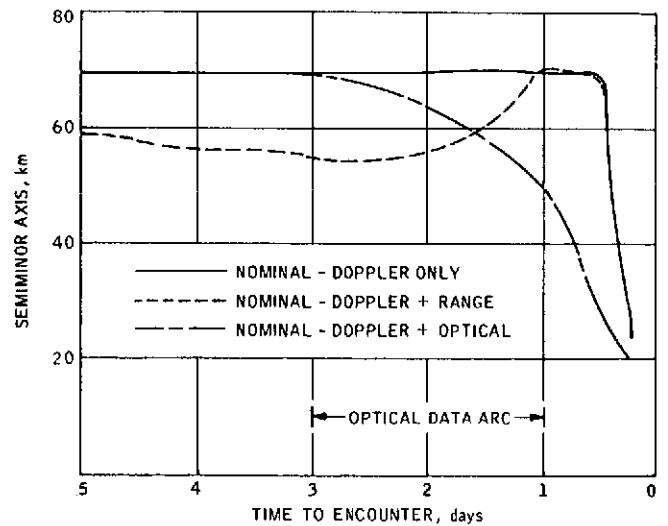


Figure 13. Comparison of Encounter Accuracy for Radio and Optical Data

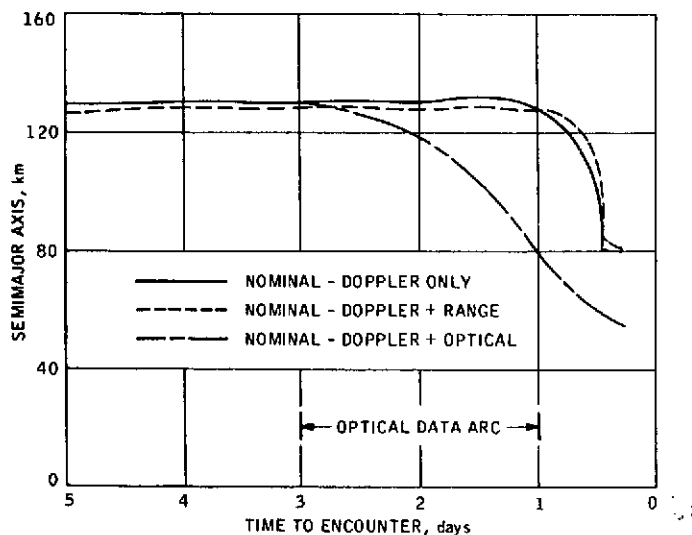


Figure 12. Comparison of Encounter Accuracy for Radio and Optical Data

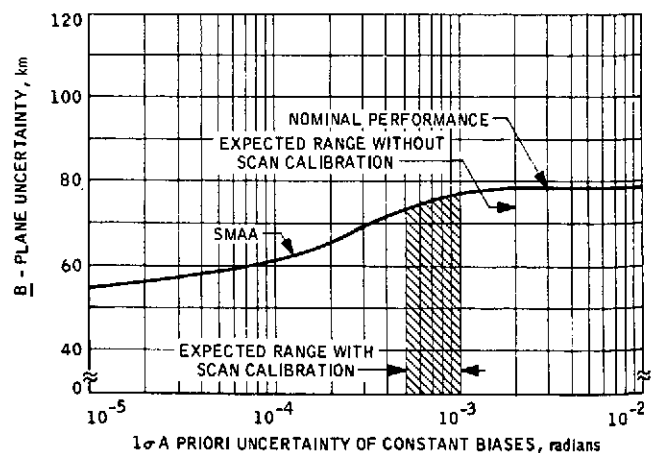


Figure 14. Encounter Accuracy at E-1d Sensitivity to Constant Bias

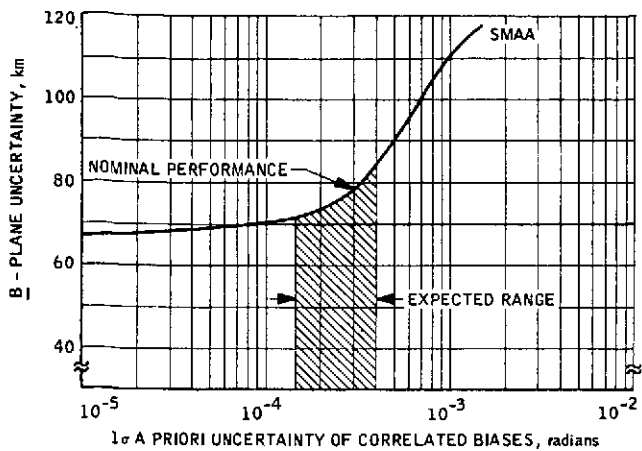


Figure 15. Encounter Accuracy at E-1d Sensitivity to Correlated Bias

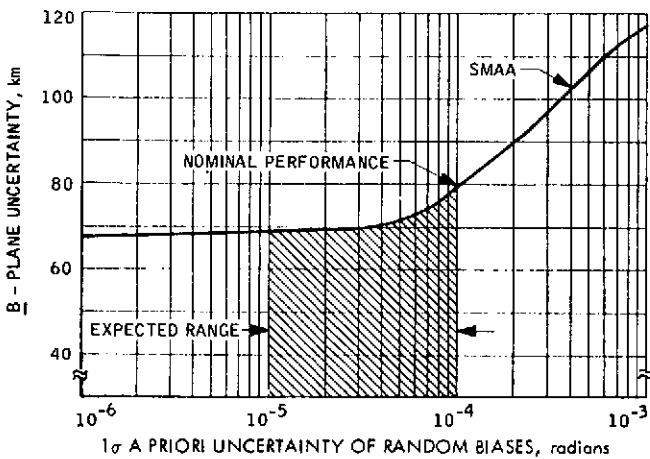


Figure 16. Encounter Accuracy at E-1d Sensitivity to Random Bias

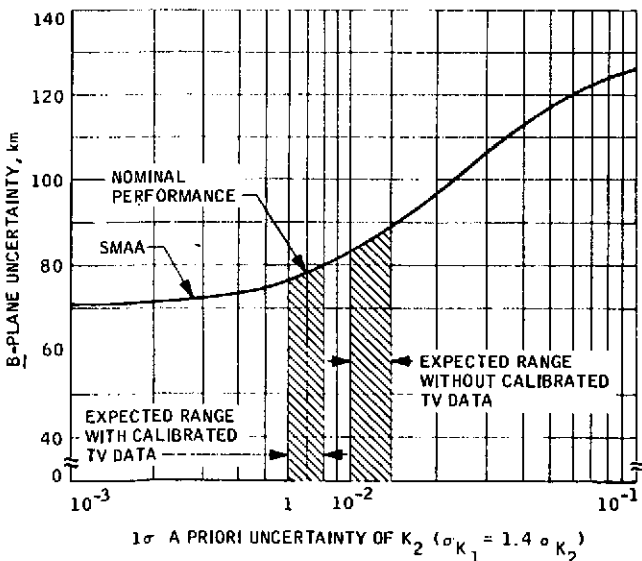


Figure 17. Encounter Accuracy at E-1d Sensitivity to Center Finding Error

reduced because of the worse case correlation time used. The significant effect of the random biases is due to the limited number of pictures assumed available over the two day picture sequence. The use of calibrated TV pictures over uncalibrated TV pictures can give a noticeable improvement in trajectory accuracy. This improvement can be even more significant if the effects of correlated and random biases are reduced. Little improvement in trajectory accuracy can be gained from an in-flight calibration of the constant biases for this application of optical data.

Conclusions

Highly sophisticated earth-based radio tracking to within 7 hours of encounter can provide Mars encounter accuracies on the order of 60 km and 30 m/sec with current tracking error magnitudes. Major radio data error sources are station location errors in the case of doppler tracking and Mars ephemeris errors whenever doppler and range data are combined. If Mars ephemeris errors can be reduced below current levels, (perhaps by planetary radar bouncing prior to encounter) the combination of range data with doppler can significantly decrease encounter uncertainties. Likewise, if station location errors were reduced, doppler tracking would be much more effective.

The addition of optical data to radio data would only slightly improve expected radio tracking accuracy at E-7h because of inaccuracies due to center finding errors in the optical data. However, the addition of optical data would provide encounter accuracies at E-1d comparable to those obtained at E-7h with radio tracking only thus benefiting mission operations by providing an additional 12 to 18 hours to determine the insertion maneuver strategy. In addition, added credence would be given to the navigation process at E-7h since optical data is redundant to and independent of radio data. Moreover, since nongravitational forces on the order of 10^{-11} km/sec² seriously degrade the expected accuracy of long arc radio tracking, optical data could be used as a prime data type because it is not very sensitive to this type of error.

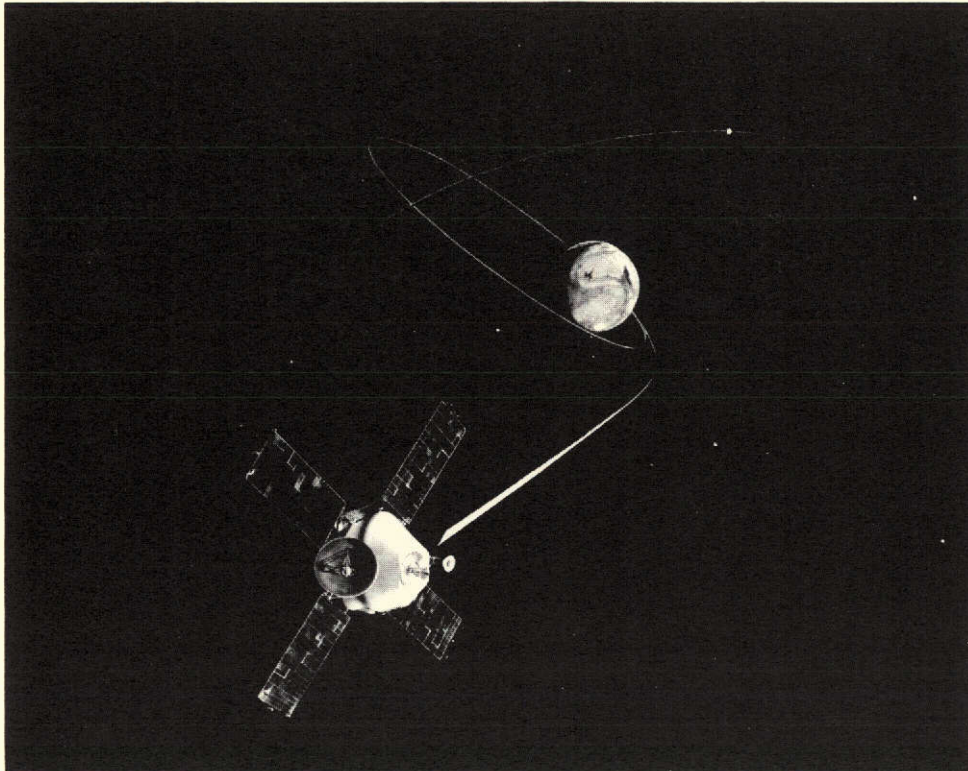
References

1. Curkendall, D. W., et al, "Planetary Navigation", *Astronautics and Aeronautics*, July 1969.
2. Jordan, J. F., et al, "The Effects of Major Error Sources on Planetary Spacecraft Navigation Accuracies, AIAA paper 70-1077, Aug. 1970.
3. Brower, D., and Clemence, G. M., *Methods of Celestial Mechanics*, Academic Press Inc., New York, 1961.
4. Duxbury, T. C., and Breckenridge, W. G., "Mariner Mars 1969 Optical Navigation Demonstration", AIAA paper 70-70, Jan. 1970
5. Duxbury, T. C., "Navigation Data from Mariner Mars 1969 TV Pictures", *Navigation*, Vol. 17, No. 3, Fall 1970.

6. Acton, C. H., "Television Image Processing for Navigation," Space Program Summary, 37-63, Vol. III, June 30, 1970.
7. Jordan, J. F., "Optical Stochastic Control Theory Applied to Interplanetary Guidance," Phd Dissertation, University of Texas at Austin, Aug. 1966.
8. Kizner, W. A., "A Method of Describing Miss Distance for Lunar and Interplanetary Trajectories," External Publication No. 674, Jet Propulsion Laboratory, Pasadena, California, 1 August 1969.
9. Duxbury, T. C. and Ohtakay, H., "In Flight Calibration of a Navigation Instrument," AIAA Paper No. 70-1023, August 1970.

APPENDIX D

TRACKING PHOBOS AND DEIMOS ABOARD AN ORBITING SPACECRAFT



TRACKING PHOBOS AND DEIMOS ABOARD AN ORBITING SPACECRAFT

T.C. Duxbury and G.H. Born

Jet Propulsion Laboratory
Pasadena, California

AAS/AIAA

ASTRODYNAMICS SPECIALISTS CONFERENCE 1971

Ft. Lauderdale, Florida

August 17-19, 1971

65<

D-1

TRACKING PHOBOS AND DEIMOS ABOARD AN ORBITING SPACECRAFT *

Thomas C. Duxbury and George H. Born

Jet Propulsion Laboratory

ABSTRACT

This paper presents the results of an investigation of determining the trajectory of a spacecraft orbiting Mars from spacecraft-based optical data in conjunction with earth-based radio tracking data. The on-board optical data was assumed to consist of TV pictures of the Martian satellites Phobos and Deimos while the radio tracking data consisted of two way doppler. The results of the investigation revealed that the addition of optical data to the radio data could reduce the spacecraft position uncertainty by a factor of 2 to 10 depending on optical data accuracy assumptions. Optical data was found to be especially valuable when star images were assumed to be within the same TV picture as a natural satellite image. Without star images, the improvements from natural satellite tracking were significantly reduced.

* This paper presents the results of one phase of research carried out at the Jet Propulsion Laboratory, California Institute of Technology, under Contract No. NAS 7-100, sponsored by the National Aeronautics and Space Administration.

Introduction

The use of spacecraft-based optical data for interplanetary navigation has become an accepted concept with a significant importance placed on the role of this data for outer planet missions. During planet approach, measurements of planet and/or natural satellite directions would be obtained and used to relate the spacecraft trajectory to the target planet. This same concept of optical data also can be applied to an orbiting spacecraft. Because of the close proximity of orbiting spacecraft to the target planet, planet limb measurements become difficult because of the large angular size of the planet as viewed from the spacecraft. Two promising optical data types for an orbiter are natural satellite and landmark tracking. This paper deals with tracking natural satellites from an orbiting spacecraft.

The motivation for this effort was to gain insight into the application of natural satellite data to estimating the trajectory of an orbiting spacecraft. For this study, a 1971 Mars orbiter was investigated. On-board optical data and earth based radio data, taken during a 24 hour period prior to an orbit trim maneuver, were combined to estimate the spacecraft trajectory at the time of the orbit trim maneuver. The on-board data consisted of Phobos and Deimos sightings obtained from a science TV camera. The objective of this effort was to determine the sensitivity of expected trajectory accuracy with the addition of optical data to a nominal radio tracking data arc.

Data Description

A spacecraft orbit with a period of 12 hours was used for this study. Table 1 gives the mean orbital elements of the spacecraft, Phobos, and Deimos referred to the Mars equator and equinox of 1971 Nov 19 3h 4m 0s GMT. It was assumed that a trim maneuver would be performed two orbits later (1971 Nov 20 3h 1m 17s GMT). The spacecraft trajectory and associated

Table 1. Mean Orbital Elements Referenced to Mars Equator and Equinox of Date

Symbol	Definition	Units	Value		
			Spacecraft	Phobos	Deimos
a	Semi-major axis	km	12633.2	9378.6	23459.0
e	Eccentricity		0.6287	0.0170	0.0031
M	Mean anomaly	deg	0.000	84.075	183.237
Ω	Longitude of ascending node	deg	44.550	52.091	11.374
ω	Argument of periapsis	deg	334.584	358.321	82.551
i	Inclination	deg	65.000	0.891	2.662
P	Period	hours	11.98	7.65	30.30

variational equations with respect to the state of the spacecraft at P_0 and Mars gravitational constant and harmonic coefficients were generated by the JPL Double Precision Trajectory Program (Ref. 1). The natural satellite trajectories and associated variational equations with respect to mean orbital elements at P_0 and Mars GM and J_2 were generated by a first order general perturbation theory (Ref. 2).

It was assumed that two-way doppler tracking data was obtained from Goldstone, Woomera, and Johannesburg to give continuous spacecraft coverage. A data span was chosen which began one hour after the first periapsis and terminated one hour before the third periapsis.

Optical navigation observations were assumed to be obtained from a combination of science and engineering instruments similar to those aboard the MM'71 spacecraft. These instruments include the narrow angle (1.1 x 1.4 deg) TV camera, the two axis gimballed scan platform which is used to point the TV camera, and the 3 axis attitude control sensors which measure and control the spacecraft attitude. The TV vidicon is scanned in 700 lines with 832 picture elements (pixels) per scan line. Also, the vidicon has a 7 x 9 reseau grid which is used in calibrating TV distortion.

The celestially referenced directions to Phobos and Deimos are reconstructed from satellite image locations (pixel and scan line number) combined with measurements of TV pointing and spacecraft attitude data or combined with star image locations within the same TV picture (Ref. 3). Satellite viewing opportunities are restricted by various instrumentation and geometric constraint. The scan platform/TV is mounted on the shaded side of the spacecraft and is physically restricted to view approximately one third of a hemisphere, essentially away from the Sun direction. Geometric restriction include natural satellite occultations and solar eclipses by Mars. Even when none of the above restrictions are violated, TV data storage capacity aboard the spacecraft and periods when the spacecraft is in Earth occultation (spacecraft cannot be commanded) may limit picture taking.

Applying these constraints, satellite viewing opportunities were determined for a 24 hour period (2 orbits) before the trim maneuver and are shown in Figure 1. The solid lines represent the viewing opportunities and the vertical lines on the solid lines represent times at which pictures were assumed to be taken. The P_i denotes the i th periapsis. Pictures were taken at a minimum of 7.5 minute intervals within the viewing opportunities to allow sufficient time for the scan platform to slew to the proper pointing direction. TV data storage capacity of 30 pictures was split between 11 pictures of Phobos and 19 pictures of Deimos. It is noted that the constraints restrict satellite viewing to within a few hours of spacecraft periapsis and the spacecraft-satellite range is generally from 10 to 30 thousand km. Figure 2 shows the motion of Deimos against a star background for the first Deimos viewing opportunity (10 pictures).

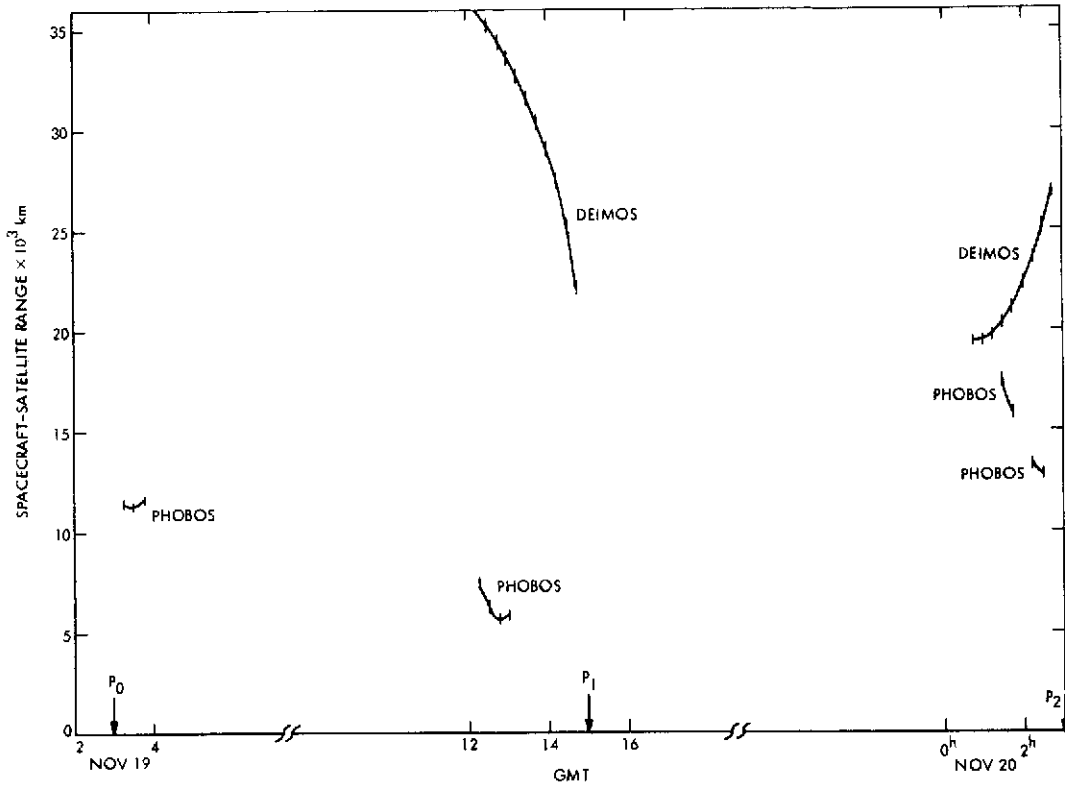


Figure 1. Satellite Viewing Opportunities

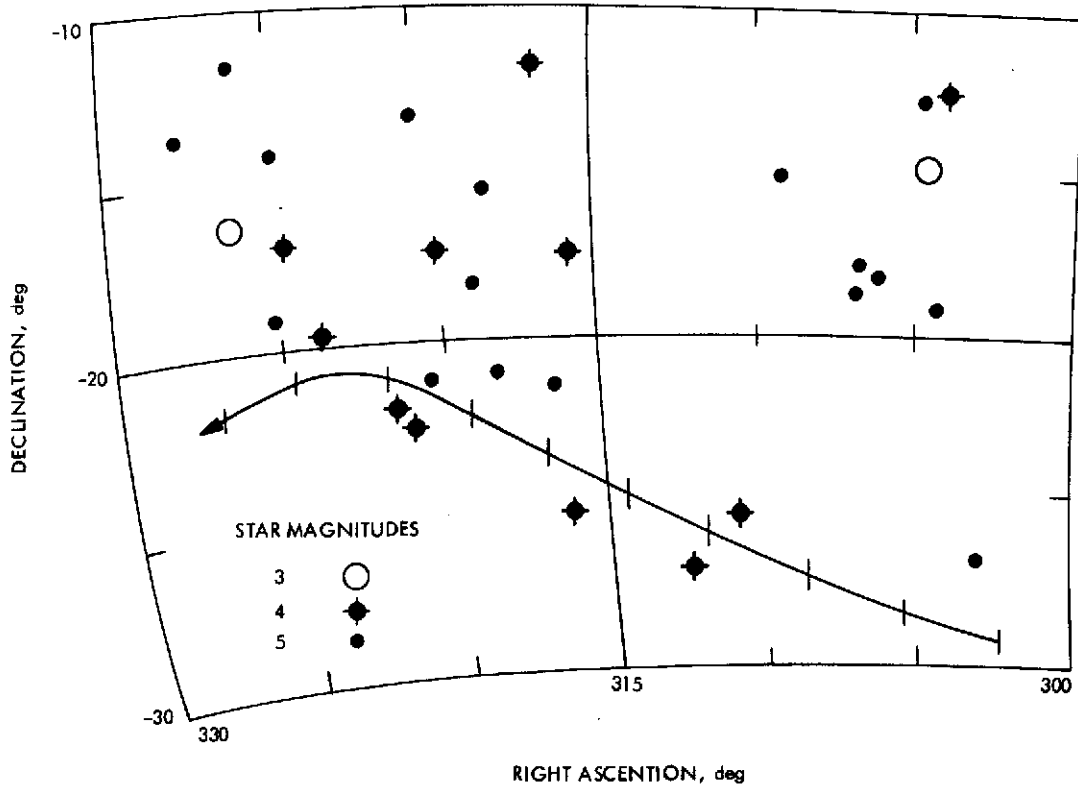


Figure 2. Deimos Path Against a Star Field

Consider Covariance Formulation

A sequential formulation of the minimum variance filter having a generalized consider option was used in performing the covariance analyses. The sequential version was required to properly handle optical measurement errors which were modeled as first order Gauss-Markov sequences (Ref. 4). A general discussion of this filter is as follows:

The observable equation is of the form

$$\bar{z}_i = H_i \bar{x}_i + G_i \bar{y}_i + \bar{q}_i \quad (1)$$

where \bar{z}_i is the observable; \bar{x}_i contains the parameters being estimated; \bar{y}_i , the consider parameters, contains parameters which affect the data but are not estimated; and \bar{q}_i is data noise.

The actual statistics of the estimated and consider parameters are given by

$$P_o = E \left\{ \begin{array}{c} \left[\begin{array}{c} \bar{x}_o \\ \bar{y}_o \end{array} \right] \left[\begin{array}{cc} \bar{x}_o^T & \bar{y}_o^T \end{array} \right] \end{array} \right\} = \begin{bmatrix} P_{xx_o} & P_{xy_o} \\ P_{yx_o} & P_{yy_o} \end{bmatrix} \quad (2)$$

and the actual statistics of the data noise is given by

$$Q \delta_{ij} = E \left\{ \bar{q}_i \bar{q}_j^T \right\} \quad (3)$$

where δ_{ij} is the Kronecker Delta.

If, however, one assumes that the statistics of the estimated parameters are given by

$$X_o = E \left\{ \bar{x}_o \bar{x}_o^T \right\} \quad (4)$$

which is not constrained to equal P_{xx_o} and that the statistics of the data noise is given by

$$Q' \delta_{ij} = E \left\{ \bar{q}_i \bar{q}_j^T \right\} \quad (5)$$

which is not constrained to equal $Q \delta_{ij}$, then the estimate of \bar{x} ignoring the presence of \bar{y} is given by

$$\begin{bmatrix} \Delta \\ \bar{x}_i \\ \Delta \\ \bar{y}_i \end{bmatrix} = \begin{bmatrix} 1 & 0 \\ 0 & 1 \end{bmatrix} \begin{bmatrix} \bar{x}_i \\ \bar{y}_i \end{bmatrix} + \begin{bmatrix} K_i \\ 0 \end{bmatrix} \left[\bar{z}_{m_i} - H_i \bar{x}_i \right] \quad (6)$$

where \bar{z}_{m_i} is the observed data and

$$K_i = \bar{X}_i H_i^T \left[H_i \bar{X}_i H_i^T + Q' \right]^{-1} \quad (7)$$

The covariance of $\Delta \bar{x}_i$ assuming K_i is optimal is given by

$$X_i = \bar{X}_i - K_i H_i \bar{X}_i \quad (8)$$

Mapping the parameter estimate and covariance matrix to the next measurement epoch (or any other time of interest) is given by

$$\bar{x}_{i+1} = \Phi \bar{x}_i \quad (9)$$

$$\bar{X}_{i+1} = \Phi X_i \Phi^T + \delta X_i \quad (10)$$

where Φ is the state transition matrix from time i to $i+1$, and δX_i is due to correlated process noise.

The optical errors modeled as Gauss-Markov sequences are propagated by the following relationship

$$\eta_{i+1} = \rho \eta_i + \sigma(1 - \rho^2)^{1/2} u_i \quad (11)$$

where η is part of the parameter set \bar{x} , $\rho = \exp(-\Delta t/\tau)$, τ is the process noise correlation time, u is a zero mean random process of unit variance, Δt is the time interval between samples, and σ is the standard deviation of the zero mean process η . For constant and correlated parameters Eqn. 10 is of the form

$$\bar{X}_{i+1} = \begin{bmatrix} I & 0 & 0 \\ 0 & \rho & 0 \\ 0 & 0 & I \end{bmatrix} X_i \begin{bmatrix} I & 0 & 0 \\ 0 & \rho & 0 \\ 0 & 0 & I \end{bmatrix}^T + \begin{bmatrix} 0 & 0 & 0 \\ 0 & (1 - \rho^2)\sigma^2 & 0 \\ 0 & 0 & 0 \end{bmatrix} \quad (12)$$

X_{i+1} represents the calculated covariance of the estimated parameters \bar{x}_{i+1} assuming that K_i was optimal. Since the parameter set \bar{y} was ignored and the statistical assumptions on \bar{x}_0 and \bar{q} were incorrect, K_i was suboptimal. The actual performance of the suboptimal filter K_i can be evaluated from the following relationship

$$P_i = \begin{bmatrix} (I - K_i H_i) & -K_i G_i \\ 0 & I \end{bmatrix} \bar{P}_i \begin{bmatrix} (I - K_i H_i) & -K_i G_i \\ 0 & I \end{bmatrix}^T + \begin{bmatrix} K_i \\ 0 \end{bmatrix} Q \begin{bmatrix} K_i^T & 0 \end{bmatrix} \quad (13)$$

where P_i is referred to as the consider covariance. The consider covariance mapping equation is of the form

$$\bar{P}_{i+1} = \begin{bmatrix} I & 0 & 0 \\ 0 & \rho & 0 \\ 0 & 0 & I \end{bmatrix} P_i \begin{bmatrix} I & 0 & 0 \\ 0 & \rho & 0 \\ 0 & 0 & I \end{bmatrix}^T + \begin{bmatrix} 0 & 0 & 0 \\ 0 & (1-\rho^2)\sigma^2 & 0 \\ 0 & 0 & 0 \end{bmatrix} \quad (14)$$

The accuracies discussed in the remainder of this paper were obtained from the consider covariance matrices.

Assumptions

The radio tracking data was used to generate a nominal set of statistics for the spacecraft trajectory and harmonic coefficients of Mars gravity potential. For this nominal case, it was assumed that the spacecraft state, the mass of Mars, and second order harmonics were estimated and that third order harmonics were considered. It was found in simulation studies that station location errors and planetary ephemeris errors were small in comparison to second and third order harmonics, hence, they were not estimated or considered. Also, it was assumed that doppler noise was 1 mm/sec for a 60 second sample time.

The model used to estimate the size of the uncertainties of the Mars harmonic coefficients is described in Ref. 5. Table 2 gives the uncertainties in the second and third order harmonics used in this study. It is also shown in Ref. 5 that acceleration errors due to an incomplete gravitational model of Mars are several orders of magnitude greater than acceleration errors due to other sources such as atmospheric drag, solar radiation pressure and gas leaks from the propellant-engine system. Consequently, the only parameters included in this study which dynamically perturb the spacecraft state are the

Table 2. Standard Deviations for Mars Harmonics Based on Dimensional Analysis

Zonal Harmonic	One-Sigma Uncertainty	Tesseral Harmonic	One-Sigma Uncertainty
J ₂	0.22 × 10 ⁻⁴	C ₂₁ , S ₂₁	0.233 × 10 ⁻⁴
		C ₂₂ , S ₂₂	0.111 × 10 ⁻⁴
J ₃	0.202 × 10 ⁻⁴	C ₃₁ , S ₃₁	0.828 × 10 ⁻⁵
		C ₃₂ , S ₃₂	0.260 × 10 ⁻⁵
		C ₃₃ , S ₃₃	0.107 × 10 ⁻⁵

gravity harmonics, and the mass of Mars. Because of software constraints the number of harmonics which were included was limited to third order to allow additional parameters associated with optical data to be processed. However, it is felt that the trends demonstrated here will be valid for any harmonic model.

In performing the analysis to include optical data, the estimated and considered parameters included the spacecraft state-x, the mass of Mars-GM, Mars second order harmonics - H₂, Mars third order harmonics - H₃, Phobos and Deimos mean orbital elements - OE, TV pointing biases - B, and TV distortion D. It is noted that the results of processing optical data after processing radio data can be made equivalent to simultaneously processing both radio and optical data under the following constraints: 1) the a posteriori calculated and consider radio covariances be used as the a priori calculated and consider covariances for optical data; 2) X, GM, and H₂ be in the estimated

parameter list; 3) H_3 be in the consider parameter list; 4) the optical data and radio data be uncorrelated; and 5) radio data be insensitive to additional parameters added to the estimated or consider parameter lists.

Table 3 defines the various combinations of estimated and consider parameters investigated when optical data was added to radio data. All combinations meet the equivalence constraints of simultaneous data processing. For all cases, it was assumed that reseau data was available to reduce TV distortion to a level of 1-1/2 pixels (0.003 deg) 1σ . The a priori uncertainty of the satellite mean orbital elements yielded 1σ rms position uncertainties of 60 km for Phobos and 50 km for Deimos. The satellite orbital element uncertainties reflected assumed improvements from data taken during Mars approach.

For the cases (A, B, C) where stars were assumed in the pictures with the natural satellites, the TV pointing biases were assumed to be reduced to the level of TV distortion and were not estimated or considered. When star images were assumed not available, a set of seven biases due to attitude control sensor, scan platform gimbal axes, and TV electrical and mechanical offsets will exist. The a priori uncertainty of each of the biases was assumed to be 0.07 deg 1σ which gave a total rms TV pointing uncertainty of 0.17 deg.

The image diameters would vary from 40 pixels to 120 pixels for Phobos and from 10 to 20 pixels for Deimos. It was assumed that the data noise for determining the image center location was 3.0 pixels 1σ for Phobos and 1.0 pixel 1σ for Deimos. For the cases when stars were not available additional noise of 40 pixels 1σ on both the Phobos and Deimos data would result from telemetry resolution of the spacecraft and TV attitude data.

77<

Table 3. Optical Data Cases

Case	Estimated Parameters	Considered Parameters
Nominal (Radio Only)	\underline{x} , GM, H_2	H_3
A	\underline{x} , GM, H_2	H_3 , D
B	\underline{x} , GM, H_2	H_3 , D, OE
C	\underline{x} , GM, H_2 , OE	H_3 , D
D	\underline{x} , GM, H_2 , OE	H_3 , D, B
E	\underline{x} , GM, H_2 , OE, B	H_3 , D

Results

As discussed in Ref. 5 and 6, radio data is insensitive to the orbit element node, measured, in the plane of the sky. Radio tracking data must rely on relative Earth-Mars motion to determine this element, hence several days of tracking are required to determine this element accurately. Figure 3 depicts the Keplerian elements referenced to the plane of the sky. The plane of the sky is defined to be a plane normal to the Earth-Mars line.

It was found that optical data of Phobos and Deimos were sensitive to this element as shown by Figure 4. The initial point represents the accuracy of the 22 hour radio data arc. After processing the 30 pictures of Phobos and Deimos the accuracy of node in the plane of the sky was found to increase by a factor of 2 to 10. It was noted also that the accuracy of all other Keplerian elements remained approximately the same as for the radio tracking results.

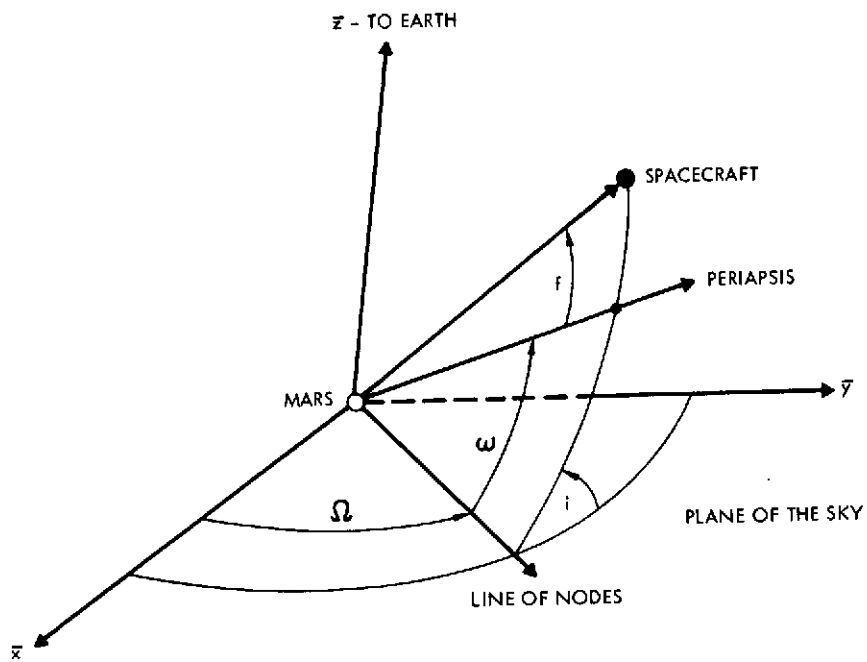


Figure 3. Plane of the Sky Geometry

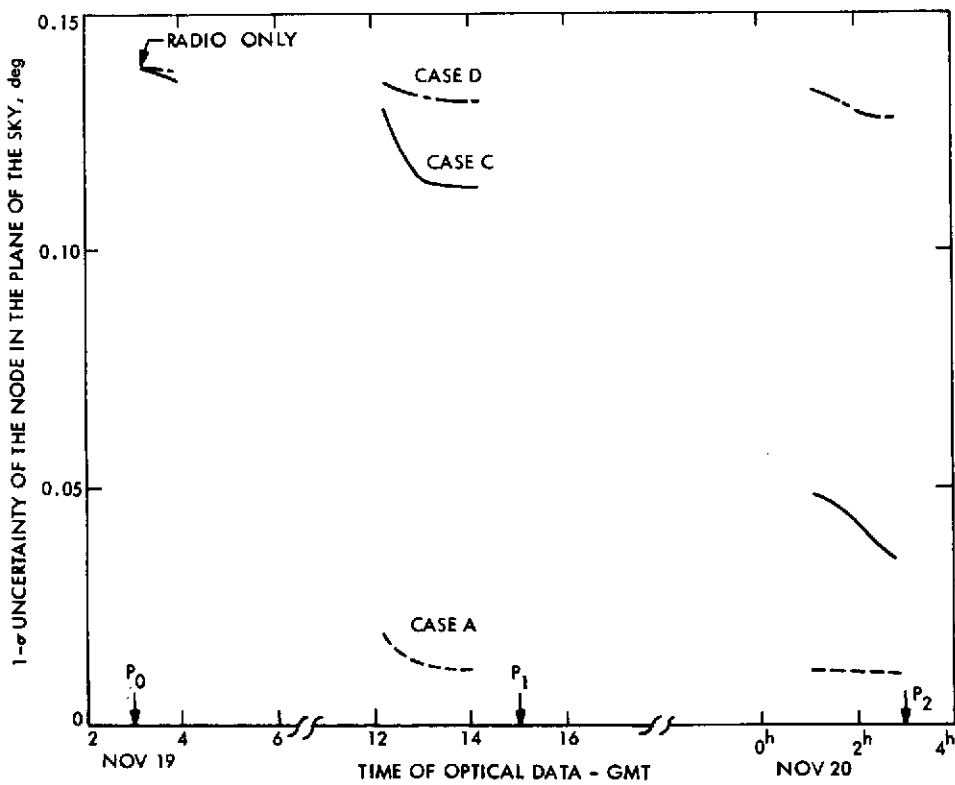


Figure 4. Line of Node Uncertainty

79<

A comparison of expected accuracies expressed in terms of rss position uncertainty at the time of the trim maneuver for various cases of optical data is depicted in Figure 5. It can be seen that when stars are available, optical data can give a factor of 2 to 10 improvement over radio data only. However, without star data, optical data gives little improvement over radio data only. The degradation of the optical data when stars are absent is essentially due to the increase of data noise rather than the presence of biases. The sensitivity of case E to data noise is shown in Figure 6. Also, case D' in Figure 5 shows the results of reducing the data noise in case D to the level when stars are available.

Figure 7 shows the tradeoff for case B when only Phobos or Deimos are viewed rather than both Phobos and Deimos. It is noted that the accuracy behavior is highly correlated with the spacecraft-natural satellite range when the satellite orbital elements are considered rather than estimated. The errors in assuming Deimos orbital elements are known corrupted the navigation process when Phobos data was added. However, even assuming that the orbital elements of Phobos and Deimos are known, improvements of 2 to 3 over radio data only are still possible.

It was found that little improvement in the uncertainty of the natural satellite orbital elements and Mars second order harmonics were obtained from the short arc of optical data. Longer data arcs of 2 to 5 days would begin to give improvements in these parameters.

CONCLUSIONS

Earth-based doppler is a very powerful data type for tracking a spacecraft orbiting Mars in 1971. Doppler data is sufficient to accurately determine the spacecraft orbit with the exception of the ambiguity in

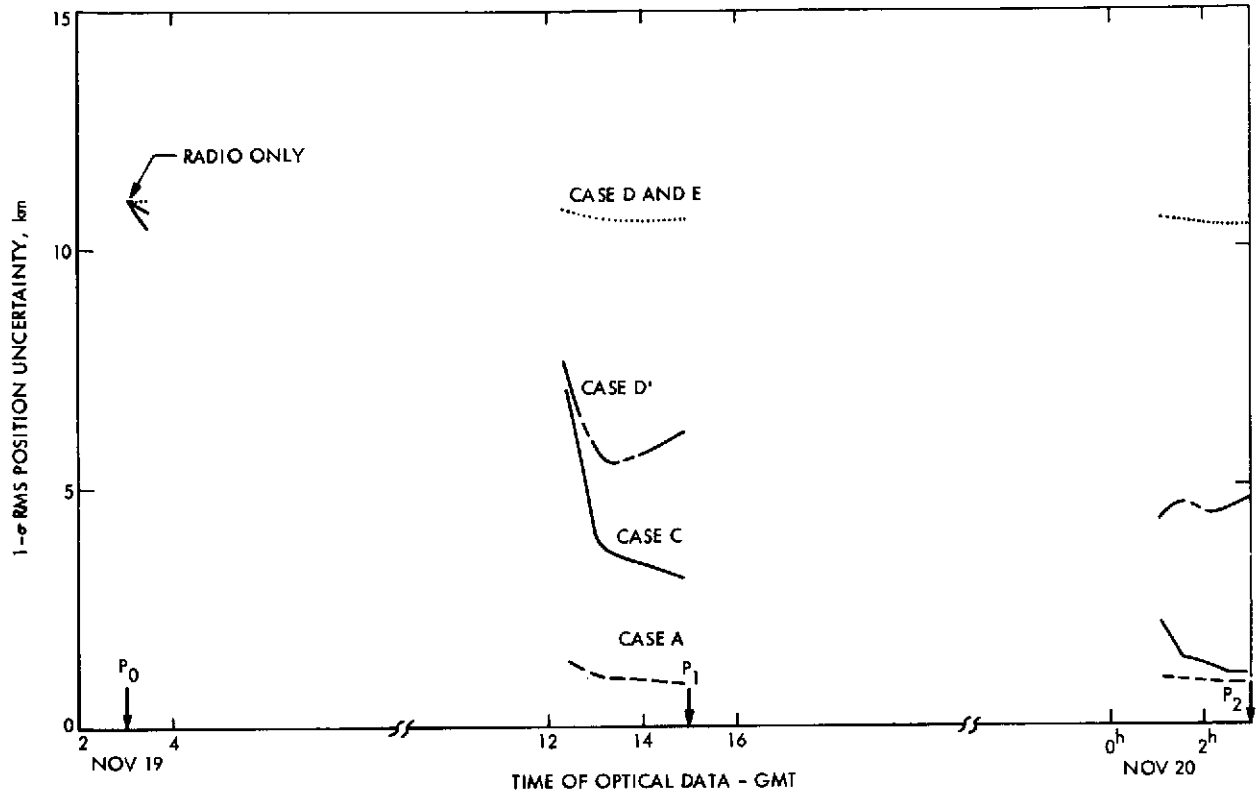


Figure 5. Position Uncertainty at Maneuver Time

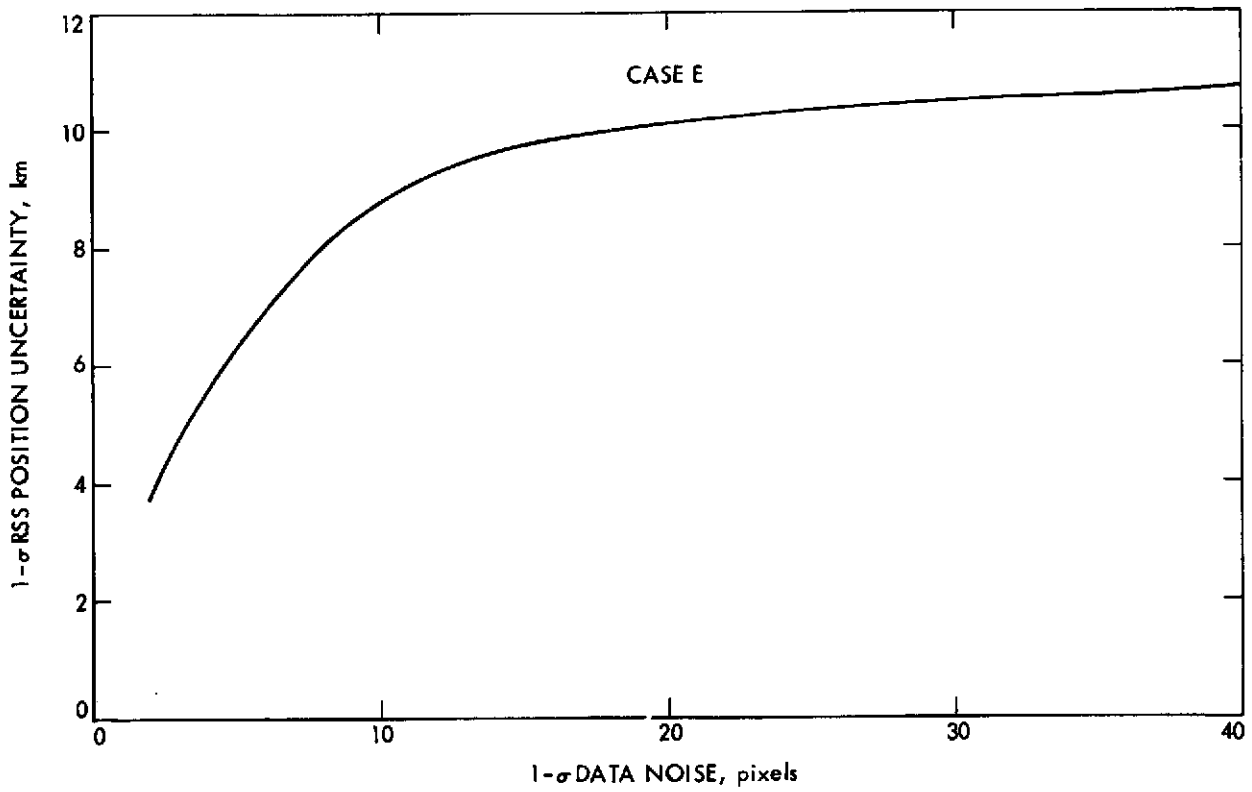


Figure 6. Effect of Data Noise

81<

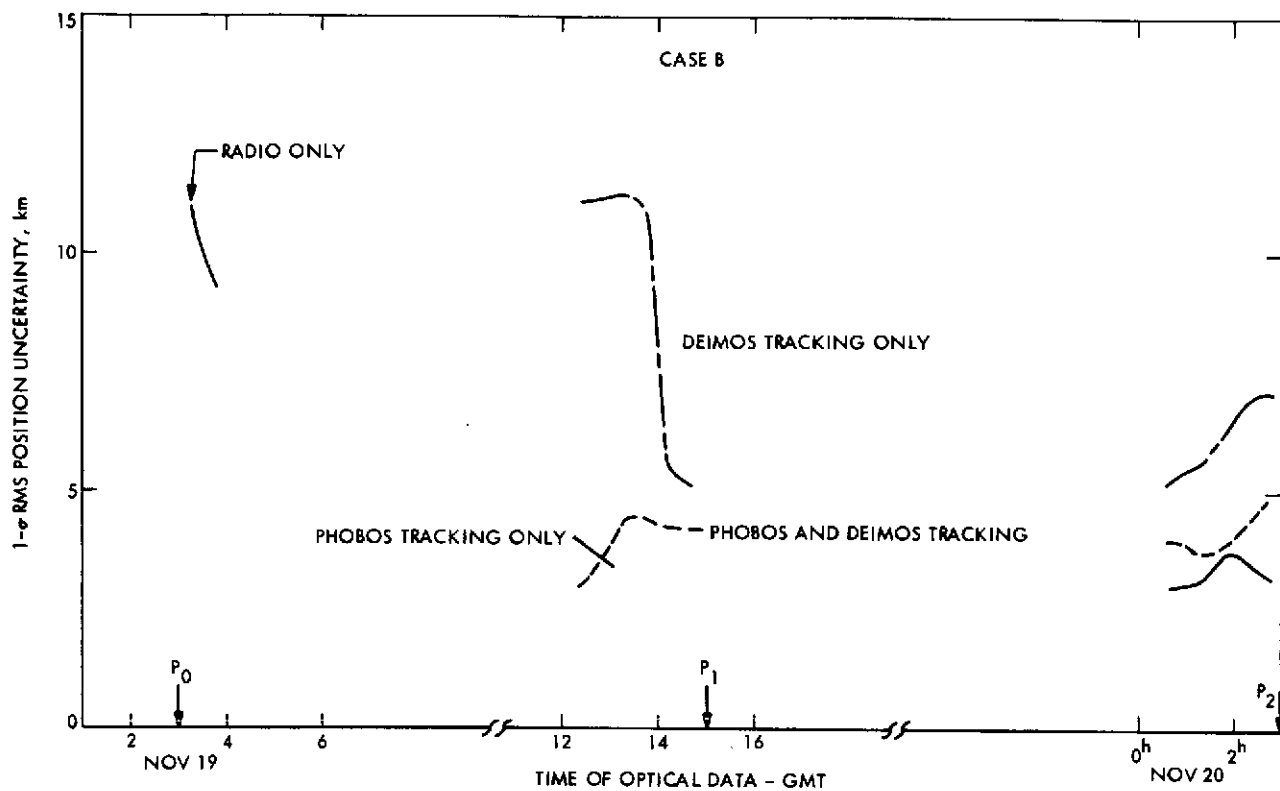


Figure 7. Tracking Phobos or Deimos Only

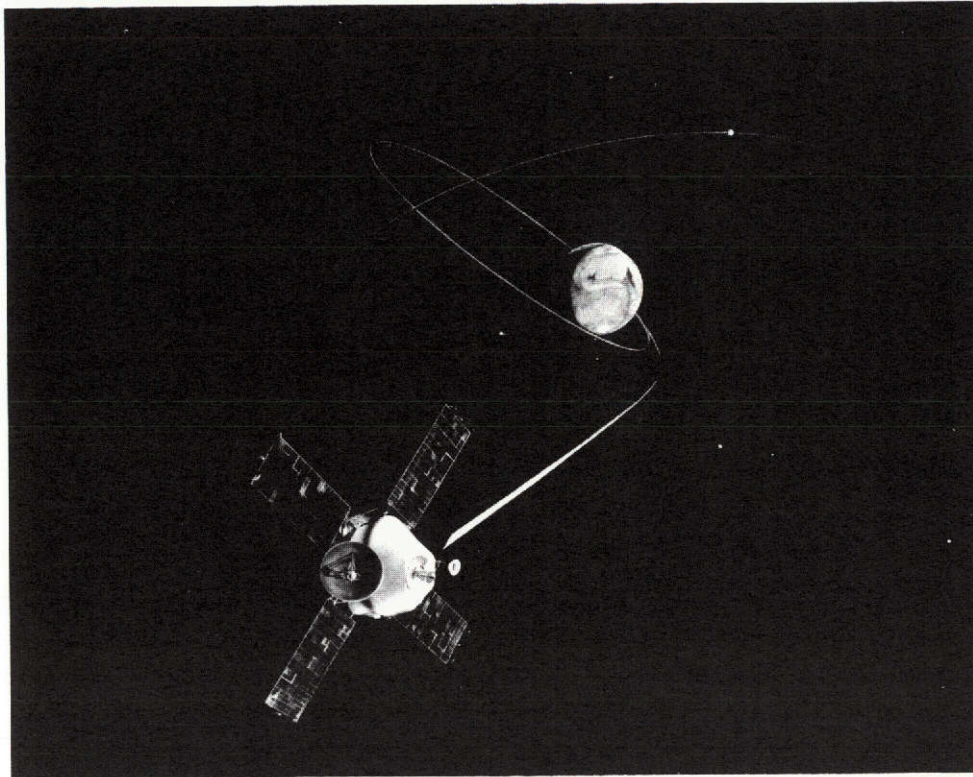
determining the node in the plane of sky. Optical tracking of Phobos and Deimos complements the radio data by allowing up to a factor of 10 improvement in the determination of the node when stars are imaged with the satellites. Without star images, improvements over radio data only were significantly reduced for the specific optical data arc investigated.

REFERENCES

1. Warner, M.R., et al., "Double Precision Orbit Determination Program", 900-56, EPD 426, Jet Propulsion Laboratory, Pasadena, Calif., June, 1967.
2. Aksnes, Kaare, "A Second-Order Artificial Satellite Theory Based on an Intermediate Orbit", Jet Propulsion Laboratory Technical Report No. 32-1507, Nov. 1, 1970.
3. Duxbury, T.C., and Ohtakay, H., "In-Flight Calibration of a Navigation Instrument", Presented at the AIAA Guidance, Control and Flight Mechanics Conference, Santa Barbara, Calif., Aug. 1970, AIAA Paper No. 70-1023.
4. Bryson, A.E. and Y.C. Ho, Applied Optimal Control Blaisdell, 1969.
5. Reynolds, G.W., et al, "Earth Based Orbit Determination for a Mars Orbiting Spacecraft", Presented at the AIAA 9th Aerospace Sciences Meeting, New York, N.Y., Jan. 1971, AIAA Paper No. 71-119.
6. Lovell, J., "Orbit Determination for a Lunar Satellite, Journal of Astronautical Sciences, V 11, No. 1, Spring 1964.

APPENDIX E

CARTOGRAPHY AND ORBIT DETERMINATION FROM A
MARS ORBITING SPACECRAFT



CARTOGRAPHY AND ORBIT DETERMINATION FROM A MARS ORBITING SPACECRAFT

S.N. Mohan and G.A. Ransford

Jet Propulsion Laboratory
Pasadena, California

AAS/AIAA

ASTRODYNAMICS SPECIALISTS CONFERENCE 1971

Ft. Lauderdale, Florida

85<

August 17-19, 1971

E-1

CARTOGRAPHY AND ORBIT DETERMINATION USING TV DATA
FROM A MARS ORBITING SPACECRAFT*

BY

Srinivas N. Mohan

Gary A. Ransford

ABSTRACT

TV pictures of the surface features of the planet Mars taken from a Mars orbiting spacecraft, when used in conjunction with earth-based tracking data, constitute an onboard observable which can, in principle, improve knowledge uncertainties of both the spacecraft state and of the landmark positions. The benefits of such TV data, for orbit determination, both in the orbiter and approach phases is presented as the results of covariance analysis. Simultaneous with solutions for the spacecraft state, solutions for the landmark positions in topocentric coordinates, the pole location of Mars in inertial space, and the TV pointing direction are also investigated. It is shown that while some improvement in the spacecraft state is possible both in the approach and orbiter phases of orbit determination, it is possible to get good solutions for landmark locations and the local radius of Mars at hitherto unknown landmarks. This information is of value to establishing a cartographic control point network.

* This paper represents one phase of research carried out at the Jet Propulsion Laboratory, California Institute of Technology, under NASA Contract NAS 7-100.

1. Introduction

The optical on-board observable is a measure of the orientation of the line of sight from the spacecraft to the object viewed, as seen in the TV frame of reference. It essentially ties the relative orientation of the spacecraft and the object sighted. Hence, the problem of processing this information must be viewed as a combined problem involving both the instantaneous position of the spacecraft and of the object sighted, in the present case, the landmark or landmarks. In the past, the two aspects of spacecraft state estimation and solutions to landmark locations have been treated separately. Landmark tracking data has been used in the Apollo program to determine landing site positions in the presence of assumed spacecraft state uncertainties as determined by earth-based radio tracking. (Ref. 1) TV pictures relayed during MM'69 encounter were processed by M. Davies (Ref. 2) to get relative latitude, longitude solutions of landmarks, referred to some convenient landmark. No solutions to the spin axis were attempted owing to the exceedingly small rotation of the planet (1.5°) over the entire picture sequence. Solutions to the spacecraft state were attempted using the same data by J. Campbell (Ref. 3) ignoring landmark location uncertainties. The current approach (cf. Ref. 10 for a baseline description) is different from the above in that the solution vector consists of all the physical parameters involved, namely, the spacecraft state, the gravitational model (employed in accord with the assumptions on the model used for processing earth-based radio data), the inertial location of the pole of Mars, the latitudes, longitudes and radii of the landmarks sighted, and the pointing errors associated with the television camera. The problem is therefore of increased

complexity both as regards computation and analysis. The object of this paper is to reveal the character of landmark tracking data using the results of covariance analysis. As will be shown in this paper, landmark tracking data can influence navigational accuracies; and, in an independent aspect, it can help to establish a cartographic control point network using both previously sighted and unsighted landmarks (the extent of previous mapping of Mars is very small - about 20% in comparison to the unmapped regions of the planet.) Solutions to the local radius of the target planet show potential in obtaining terrain heights for both mapping purposes and for determining elevations of future landing sites on Mars. The only alternate method available to obtain elevation information, is through the use of planetary radar ranging data (cf. Ref. 3 for detailed information and additional references).

Topographic information of Mars extracted from planetary radar ranging data is, however, restricted to a latitude band of 25°S to 25°N , approximately. The limits are dictated by available scanning of the latitude bands on Mars by the sub-earth point. Whereas planetary ranging yields results on a macroscopic scale, the orbiter photography yields highly localized information on terrain heights. The only restriction on latitude bands covered in the orbiter TV imaging system, is that imposed by lighting conditions, and ability to take sightings from the orbiter. As will be seen later, the accuracy of terrain height determination using TV imaging from an orbiter is comparable to that obtained by planetary radar ranging methods.

The discussion to follow, applies both to the approach aspects of navigation, and orbiter phase, using approach and orbit trajectories similar to the current course of Mariner 9.

2. Onboard Landmark Observable

The basic observable for TV imaging consists of (measured - calculated) differences in the image location as seen in the TV raster along two mutually orthogonal (nominally) directions, namely, the scan lines and picture elements. The location of the image in the TV raster coordinates can be calculated at any instant by projecting the instantaneous S/C-landmark vector into the TV coordinates by use of appropriate coordinate transformations, taking into account the sidereal rotation of Mars. The sensitivity of the observable to the S/C state, landmark latitude, longitude and radius of Mars at the landmark, right ascension and declination of the Martian pole, and TV pointing direction is essentially reflected as a variation of the S/C-landmark direction as seen in target raster coordinates.

This can be symbolically stated as:

$$\begin{bmatrix} \delta x \\ \delta y \end{bmatrix} = \frac{f}{w^2} \begin{bmatrix} k_x w & 0 & -k_x u \\ 0 & k_y w & -k_y v \end{bmatrix} T_{TV/I} \left\{ \delta \vec{r}_{LM} - \delta \vec{r}_{S/C} \right\}_I \quad (1)$$

the rotation $T_{TV/I}$ is made up of

$$T_{TV/Cel} T_{cel/I} \quad (2)$$

and involves orientation angles (clock, cone) referred to a celestial reference. Also,

$$\left\{ \vec{r}_{LM} \right\} = T_{I/B} \begin{bmatrix} r \cos\varphi \cos\lambda \\ r \cos\varphi \sin\lambda \\ r \sin\varphi \end{bmatrix} \quad (3)$$

The transformation $T_{I/B}$ depends upon the inertial orientation of the pole of the target planet Mars. Equations 1, 2 and 3 form the basis for obtaining data partials.

3. Filter Formulation

In the present context of both approach and orbital motion of the spacecraft, the perturbations of the spacecraft due to process noise such as solar radiation pressure and, in the orbiter phases, due to atmospheric drag are found

to be at least an order of magnitude smaller than the perturbations due to an unknown gravitational model for Mars. (cf. Ref. 5)

It is, therefore, sufficient to estimate the state of the spacecraft at some epoch. This is explained below.

Let z be the observable related to the state x and dynamic consider parameters y linearly as follows:

$$z = Ax + By + v$$

where v is a measurement noise vector of known covariance R , and x is the current S/C state evolved from the state x_0 at some epoch t_0 , according to,

$$\dot{x} = Fx + Jy$$

If the parameters y are associated with such parameters as gravity harmonic coefficients, it is reasonable to assume that y is a vector of constants; and, that their values are obtained as the result of sampling random variables of known variances. The observable equation in z can then be rewritten as

$$z = Hx_0 + Gy + v$$

where

$$H = A\Phi(t, t_0)$$

$$G = \int_{t_0}^t \Phi(t, \tau) J(\tau) d\tau$$

and

$$\frac{d}{dt} \Phi(t, t_0) = F(t) \Phi(t, t_0)$$

x_0 can have a more general interpretation of representing the S/C state as well as all constants associated with the system.

A Kalman filter with a consider effect can be implemented as follows:

$$\begin{aligned} \text{Define } P &\triangleq E \{ (x-\hat{x}) (x-\hat{x})^T \} \\ R &\triangleq E \{ v v^T \} \\ C_{xv} &\triangleq E \{ (x-\hat{x}) y^T \} \\ W &\triangleq E \{ y y^T \} \\ S &\triangleq -C_{xv} W^{-1} \end{aligned}$$

then it can be shown that P can be decomposed as

$$P = P_c + SWS^T$$

where P_c is the computed covariance, which is the resulting uncertainty due to measurement noise, given an a priori covariance and a set of measurements. The effect of acknowledging the existence of parameters y is an additive term to the computed covariance P_c resulting in the true covariance P , in the light of model and filter assumptions. It can be further shown that P_c and S are governed by, (Cf. Refs 7 & 8)

$$\begin{aligned} P_c^+ &= P_c^- - P_c^- H^T (H P_c^- H^T + R)^{-1} H P_c^- \\ K &= P_c^- H^T (H P_c^- H^T + R)^{-1} \\ S^+ &= (I - KH) S^- + KG \\ \hat{x}^+ &= \hat{x}^- + K(y - H\hat{x}^-) \end{aligned}$$

The results to follow are based upon the above filter formulation.

4. Observations

The Kalman filter and parameter models previously described were mechanized on a digital computer, and, covariances were propagated to observation times, with a view to studying the data characteristics. In both the

orbital and approach phases, to be described below, the apriori information for the filter was obtained from the results of representative earth-based radio tracking analyses. The main characteristics of earth-based radio tracking are best displayed in the earth's plane-of-sky coordinates. The results of landmark tracking, are similarly better seen in a Martian locally[‡] level reference frame (definitions of coordinate systems at the end of paper). The approach statistics will be presented in the B-plane in the conventional manner.

4.1 Cartography and Orbit Determination

In the planned sequence of photographing the planet Mars after the orbit insertion of MM'71, there are three different types of photographic passes that can be used for present purposes. These are, the Areodesy, the TV mapping and TV calibration sequences. Of these, the most interesting for the present discussion is the TV calibration sequence during which the wide angle TV camera will be trained on a fixed area of the planet as the spacecraft approaches periapsis. The current study enlarges upon the sequence to yield some insight into the error propagation as a function of geometry. The sub-spacecraft points at shuttering times, and the landmark positions are marked on a latitude, longitude grid in Figure 1. The data arcs were selected within constraints of lighting angles and pointing angles on the first, third and fifth revolutions. During these passes the same group of three landmarks were sighted in each picture. The pictures were taken at an interval of 4 min 12 secs, starting at 37 min from the first periapsis and repeating every 24 hours at the same interval thereafter for subsequent passes.

4.1.1 Apriori Assumptions

The apriori statistics on the S/C state and the gravitational model including second and third harmonics were obtained by processing one pass of

[‡] Martian Locally Level Frame will hereafter be abbreviated as LLF.

earth based radio tracking data. The expected limits of performance on the TV pointing direction of 0.2 deg maximum value were introduced. The spin axis uncertainty was set at 1 deg maximum based upon the one degree difference in numbers currently in use (cf. Michaux - Physical Properties of Mars). The landmark uncertainties were set large, giving no information to the filter about their positions.

The temporal behavior of the various uncertainties is shown in Figures 1 thru 7, plotted over the three passes of 7, 6 and 5 pictures each of the same set of three landmarks. In addition to a plot of the maximum value of the σ uncertainty, the semi-major and minor axis of the projection of the error ellipsoid on a plane consisting of the first two orthogonal directions in each set of three coordinates are also plotted. The orientation of the error in this plane and out of this plane are also indicated to assist in visualizing the error ellipsoid and its orientation associated with each group of parameters.

4.1.2 OD Characteristics

Figure 2 shows the best OD accuracy that can be achieved, if the TV pointing direction, the pole and LM[†] locations were known exactly. The effect of adding LM uncertainties is to shift the initial emphasis from determination of the S/C state to determination of landmark position and once these are determined the S/C state uncertainty is reduced to the best achievable. (cf. Figure 3)

Figure 4 shows the same spacecraft position uncertainties in the LLF reference. It can be seen that the errors in the p-o-s are tipped out of the plane of the sky as a result of adding landmark data while the orientation in the LLF frame appears to be such as to minimize

† LM - Landmark

errors along the local vertical. This feature appears to be consistent in all the LLF statistics of the spacecraft position, thereby suggesting that the strength of the IM data is on its ability to determine the distance of the spacecraft from the planet. In like manner, the spacecraft velocity error ellipsoid appears to be oriented almost entirely in a direction normal to the plane of the spacecraft orbit. It must be pointed out that the changes in velocity errors are to be interpreted as the reflection of spacecraft position errors into the spacecraft trajectory constraint, since the data has not information on the instantaneous velocity.

Figure 5 shows the effect of introducing spin axis uncertainty. The geometry appears to be such that the declination of spin axis is learned very well while the right ascension is rather poorly determined. The uncertainty in spin-axis orientation remains residual in the landmark location uncertainty which reflects in some worsening of OD characteristics. By comparison, the TV pointing direction uncertainty appears not so damaging to the OD characteristics (cf. Fig. 6). The complete solution to the problem is shown in (Figure 7.), with the previous Figure 1 thru Figure 6, serving to show the breakup of error contributions from various sources.

4.1.3 Characteristics of Landmark Solutions

Two groups of landmarks centered around 30°S latitude and 50°S latitude were tracked from identical camera stations at identical shuttering times. The landmark solutions in either case converged very rapidly. Table 1 shows terminal values of one sigma uncertainties as a function of assumptions on the various error sources.

It is noted from Figure 5, Figure 6, and Table 1 that the spin axis is responsible for the major degradation of landmark solutions. The solution to the spin axis is strongly geometry dependent; and, with suitable geometries, as for example by tracking two landmarks separated by 90° in longitude, it would be possible to construct two mutually orthogonal planes whose intersection may yield a good spin-axis solution. Figure

5 indicates that the separation between right ascension and declination is good and that the solution to the declination is almost an order of magnitude better than the same for right ascension.

Table 2 lists uncertainties when a landmark at 50°S latitude is tracked. Comparing figures in Tables 1 and 2 it can be seen that the overall solutions are much improved, when the landmark being tracked is closer to the plane of the spacecraft orbit.

4.2 Approach Orbit Determination

Application of landmark tracking data for cartography during the approach phases is limited by pointing errors. However, when it is used in conjunction with earth-based radio tracking, it can be of value to approach navigation.

This section will address itself to two questions, these are related to:
a) the contribution of each major error source mapped into the B-plane targeting statistics, and b) the overall navigation capability of the onboard data type.

A representative Mars approach trajectory was chosen for this study. Three sequences of photographs were taken every hour, starting at about three days before encounter giving coverage of every fifteen degrees of the planet in longitude. Figure 10 shows the spacecraft aerographic longitude and radius from the center of Mars at the shuttering times. It was

assumed that the photographs were taken with a camera similar to the narrow angle camera onboard the Mariner Mars '71 spacecraft (Figure 9). Several landmarks were picked for study from a list provided by Davies and Berg (Ref. 2). These landmarks are plotted in Figure 11 .

4.2.1 Apriori Assumptions

The apriori state covariance from radio tracking was generated by analyzing data taken on an arc which extended from thirty days before encounter to eight hours before encounter. During the studies, it was assumed that all parameters other than the ones discussed are perfectly known. A priori uncertainties on the various error sources are given in Table 3.

4.2.2 OD Characteristics

Using the observation sequence outlined above, the state covariance was propagated to the B-plane. Contribution of each of the major error sources, to the B-plane statistics is displayed in Figure 12. The control case, in which only the state is solved for, (curve 1-Fig. 12) illustrates that the information from these data appears to establish no "favored" direction. Figure 13 displays the temporal behavior of the error statistics. It can be seen that the effect of introducing the Martian pole location errors is felt more strongly as the spacecraft approaches the target planet. It was noticed in this situation that correlations between the spacecraft state and the right ascension and declination of the pole of Mars were fairly high.

The correlations with the state may be explained by the fact that there is linear dependence between the inertial direction of the pole and the

inclination to the martian equator of the incoming spacecraft trajectory.

The effects of the TV camera/scan platform biases (denoted as M, N, L biases) were investigated by a study which solved for the Mars centered vehicle state and the M, N, L biases. From the outset of the photographic sequence, it can be seen (Fig. 13), that all the information in the data is used to update the M,N,L biases. This is a result of the disparity in size between the effect of the biases and the effect of the state vector components on the landmark image position in a photograph at the beginning of the sequences. As the sequences progress, the uncertainties on the biases are reduced, allowing the information in the data to be used to update the vehicle state vector. The state vector uncertainties, by the sequence termination, are seen (Figures 12 and 13) to be smaller than the case which includes the Martian pole direction.

Landmark position effects on the B-plane uncertainties were studied in two cases: a) solve for the vehicle state vector and the latitudes, longitudes and the local radii of the landmarks, and b) solve for the vehicle state vector and the latitudes and longitudes of the landmarks and the equatorial radius and flattening of Mars. With regard to the B-plane ellipse parameters it is seen, from Figures 12 and 13, that the two different ways to study landmark position effects are equivalent. The effects on the semi-major axis of the B-plane error ellipse are regular and smaller in magnitude than the error sources which have been discussed to this point.

The second part of the study was completed by solving for all the major error sources listed above simultaneously. Figure 13 shows that the solution is dominated in the early sequence by the biases. The bias effects are replaced by the dominant effects of the Martian pole direction uncertainty in the latter portions of the sequences. The B-plane error ellipse is plotted

C-2

in Figure 12. Among the physical parameters included in the solution, it is noticed, from Table 3, that only the M and N biases are significantly decreased.

5. Summary and Conclusions

From the preceding observations there is good evidence that landmark data can influence navigational accuracies. Of significance is the fact, that addition of landmark data has the effect of leaving a residual orientation of the errors in state estimate such as to make it "visible" to further earth-based radio tracking, in addition to improving upon it.

On the approach phase, the TV/scan platform biases strongly effect the navigation accuracy at large distances from the planet. At the end of the sequence, however, the direction of the Martian north pole is the limiting error source in the approach landmark tracking navigation. The approach guidance results from landmark tracking are better than those obtained from processing the MM'69 Mars limb data (Ref. 9).

Solutions to the Martian pole are geometry dependent; and, indications are, that better solutions are achievable by tracking two landmarks which are separated by 90° in longitude.

The landmark solutions converge rapidly and the achievable limits of accuracy are dictated by ability to determine the Martian pole location. Solutions to terrain heights are comparable to those achievable by planetary radar ranging. This shows great promise for reconnaissance prior to lander operations on future Mars missions.

Future efforts will be directed at attempting combined radio and optical data solutions in real time mode. Alternate tracking schemes will be explored to better determine the location of the pole of Mars and thus improve upon landmark solutions and solutions to terrain heights.

References:

1. Ransford, G. A., Wollenhaupt, W. R., and Bizzell, R. M., "Lunar Landmark Locations - Apollo 8, 10, 11 and 12 Missions", NASA TN-D-6082, November 1970.
2. Davies, M. E. and Berg, R. A. "A Preliminary Control Net of Mars", Rand Corporation Report RM-6381-JPL, Nove. 1970.
3. Campbell, J. K., "A Method of Orbit Determination Using Overlapping Television Pictures", AIAA/AAS Paper presented at the Astrodynamics Conference, August 19-21, 1970, Santa Barbara, Calif.
4. O'Handley, D. A., et al., "Ephemeris, Radar Radius and Radar Topography of Mars", Paper presented at IAU Commission 7 Special Session, 18-27 August 1970, Brighton, England.
5. Reynolds, G. W., Russell, R. K. and Jordan, J. F., "Earth Based Orbit Determination for a Mars Orbiting Spacecraft" AIAA Paper 71-119 Presented at the 9th AIAA Aerospace Sciences Meeting, New York, January 25-27, 1971.
6. Michaux, C. M., Handbook of the Physical Properties of the Planet Mars, NASA Special Publication, SP-3030, 1967.
7. Kalman, R. E., "New Methods and Results in Linear Prediction and Filtering Theory", RIAS Tr 61- , Martin-Marietta Corp., Research Institute for Advanced Studies, Baltimore, Maryland, 1961.
8. McReynolds, S. R., Russell, R. K., "A Consider Option and a Consider Filter for a Sequential Estimation Program for a Planetary Orbiter", JPL TM 391-89, April 8, 1970.
9. Duxbury, T. C., "Navigation Data from Mariner Mars 1969 TV Pictures", Journal of the Institute of Navigation, Vol. 17, No. 3,
10. Mohan, S. N., "A Method of Combined Cartography and Orbit Determination Based on Expected TV Returns from MM'71", Jet Propulsion Laboratory Internal Report, TM391.2-107, Aug 12, 1970.

lc Values	Pass 1	Pass 2	Pass 3	Parameters Solved For
φ	.7073 deg	.1348	.0914	Spacecraft State TV Pointing Errors Pole Location of Mars Landmarks
λ	.7009 deg	.1364	.0933	
r	3.3358 km	2.3730	1.9743	
Max Val	58.2800 km	11.1200	7.5750	
RA	.9794 deg	.2026	.1329	
DEC	.8419 deg	.1205	.0710	
φ	.17409 deg	.06841	.042650	Spacecraft State TV Pointing Errors Landmarks
λ	.27220 deg	.04271	.031056	
r	6.18400 km	2.80560	2.677960	
Max Val	18.37700 km	4.16000	2.760000	
φ	.5851 deg	.3896	.229600	Spacecraft State Pole Location Landmarks
λ	.7022 deg	.4461	.284400	
r	2.7160 km	2.3920	1.981100	
Max Val	53.9300 km	34.9600	21.530000	
RA	.9775 deg	.6820	.416800	
DEC	.6301 deg	.1579	.103300	
φ	.06884 deg	.04782	.03517	Spacecraft State Landmarks
λ	.12220 deg	.03496	.02710	
r	2.70350 km	2.34798	1.90000	
Max Val	7.45000 km	3.44000	2.63000	

Table 1. $\varphi = -30^\circ$, $\lambda = 60^\circ$

Uncertainties in Landmark Location and Location of the Pole of Mars at the conclusion of each pass of landmark data

1σ Values	Pass 1	Pass 2	Pass 3	Parameters Solved For
φ	.6715 deg	.3185	.1781	Spacecraft State TV Pointing Errors Pole Location of Mars Landmarks
λ	.8986 deg	.3274	.2205	
r	5.1070 km	2.4050	1.9257	
Max Val	65.3400 km	26.8300	16.6000	
RA	.9821 deg	.6094	.3677	
DEC	.7807 deg	.1043	.0698	
φ	.07194 deg	.0531	.038	
λ	.17160 deg	.0419	.0295	
r	2.23000 km	1.3940	1.2480	
Max Val	10.36000 km	3.3800	2.6700	

Table 2. $\phi = -50^\circ$, $\lambda = 60^\circ$

Uncertainties in Landmark Location and Location of the Pole of Mars at the conclusion of each pass of landmark data

<u>Parameter</u>	<u>A priori Uncertainty</u>	<u>A Posteriori Uncertainty</u>
Right Ascension of Martian Pole	1.0 deg	.59 deg
Declination of Martian Pole	1.0 deg	.58 deg
M-Bias	0.2 deg	0.0035 deg
N-Bias	0.2 deg	0.0035 deg
L-Bias	0.2 deg	0.18 deg
Equatorial Radius of Mars	100 km	----
Flattening of Mars	.003	----
LMK Uncertainties	Uncertainties from Davies and Berg (Ref. 2)	----

Table 3
Effect on Uncertainties of Physical Parameters in
Solution Vector for Landmark Tracking Data

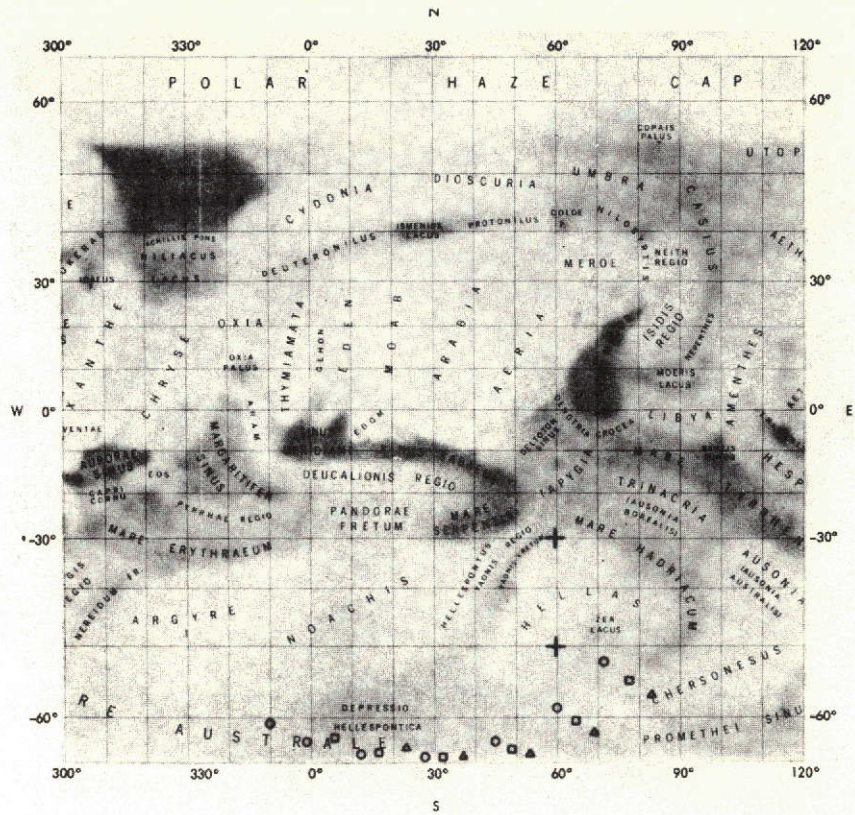


Figure 1. Landmarks and Sub-spacecraft Points at Shuttering Times.
 Symbols \circ \square \triangle indicate orbits 1, 3, and 5 respectively
 Symbol $+$ indicates landmarks tracked from the orbiter

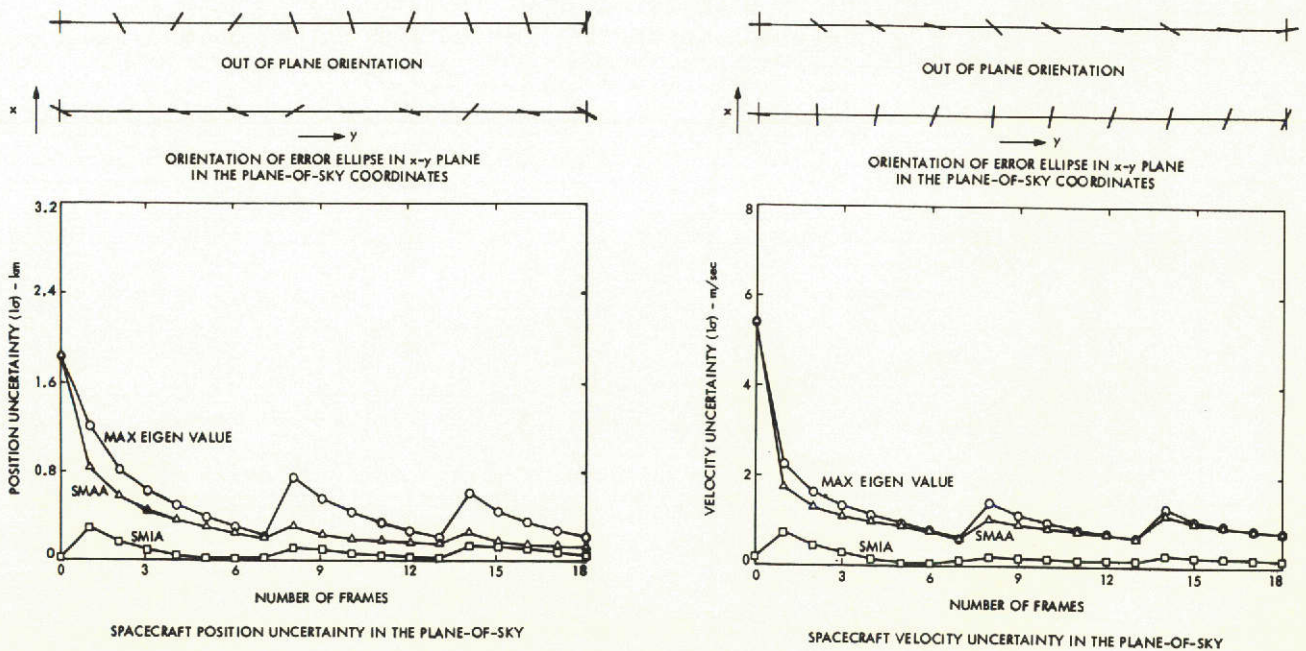


Figure 2. OD Statistics in the absence of all error sources

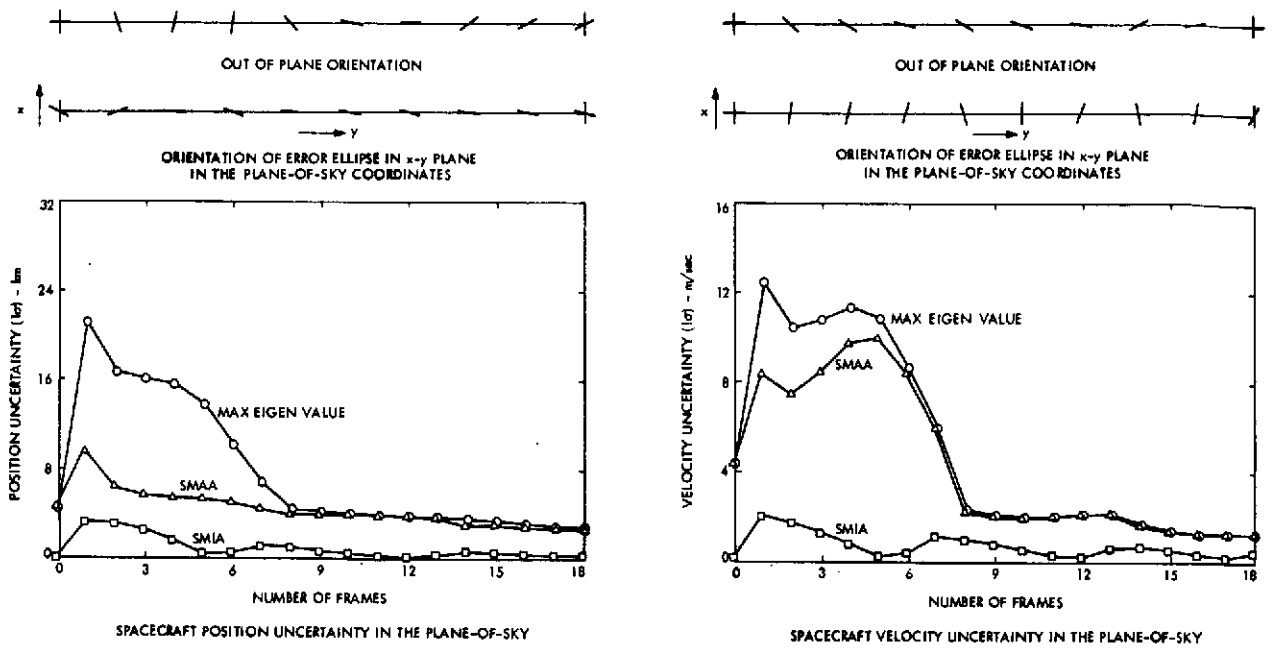


Figure 3. OD Statistics when Landmarks are Unknown

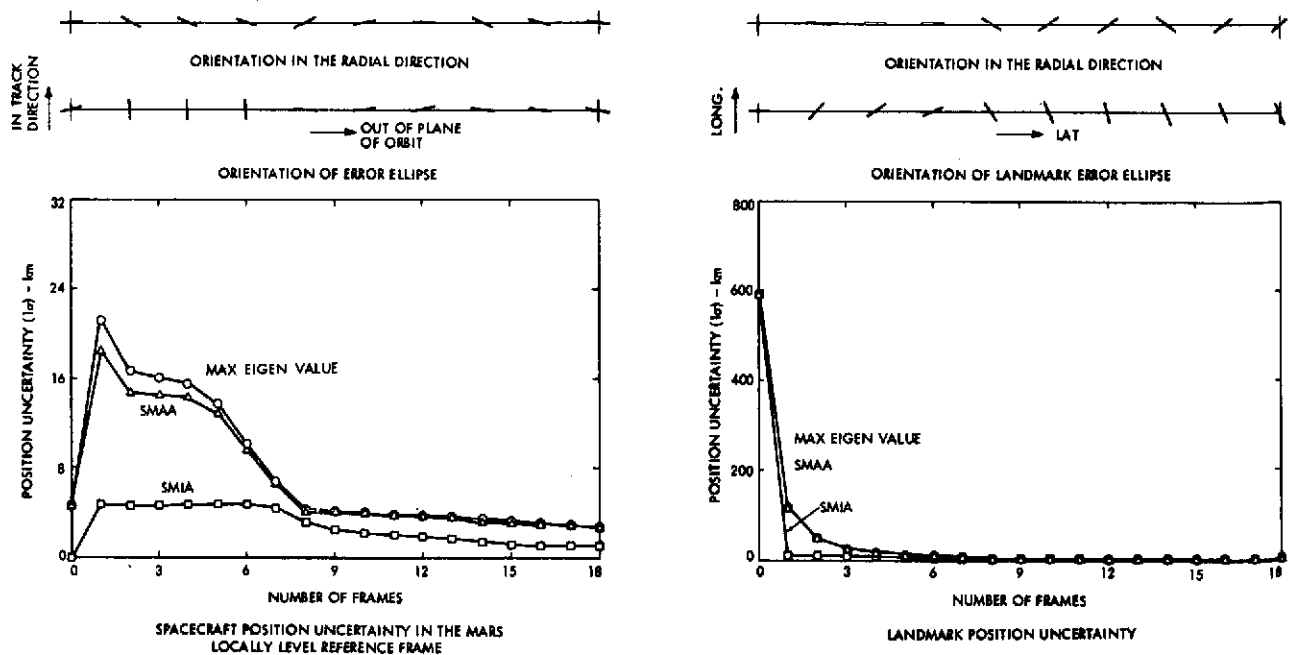


Figure 4. OD Statistics and Landmark Uncertainties when Landmark is Initially Unknown

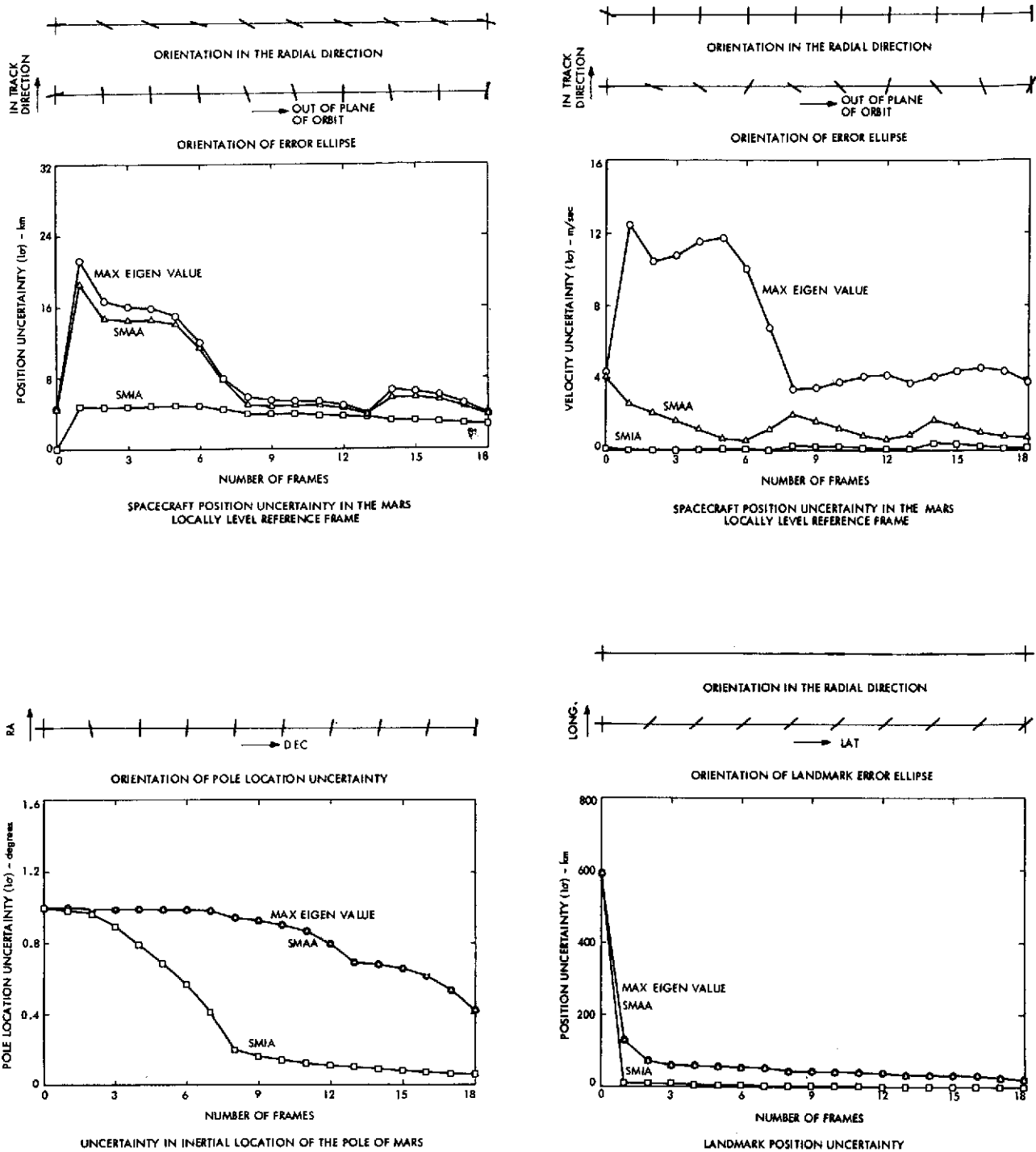


Figure 5. Combined Statistics of Spacecraft State, Spin Axis and Landmark

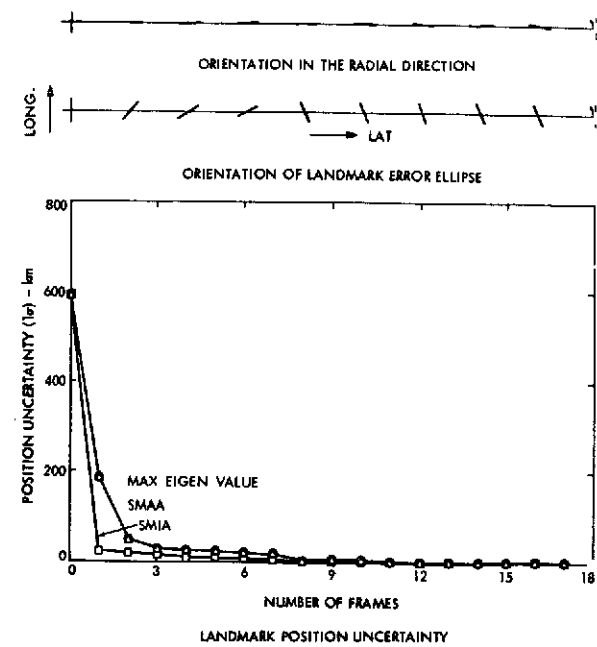
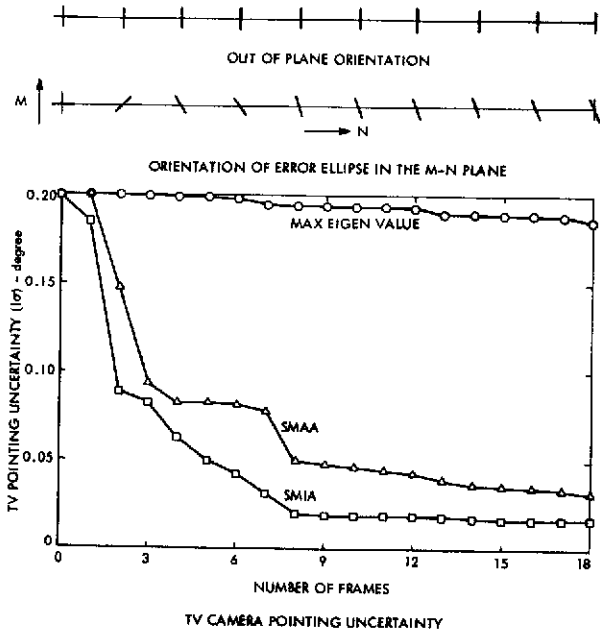
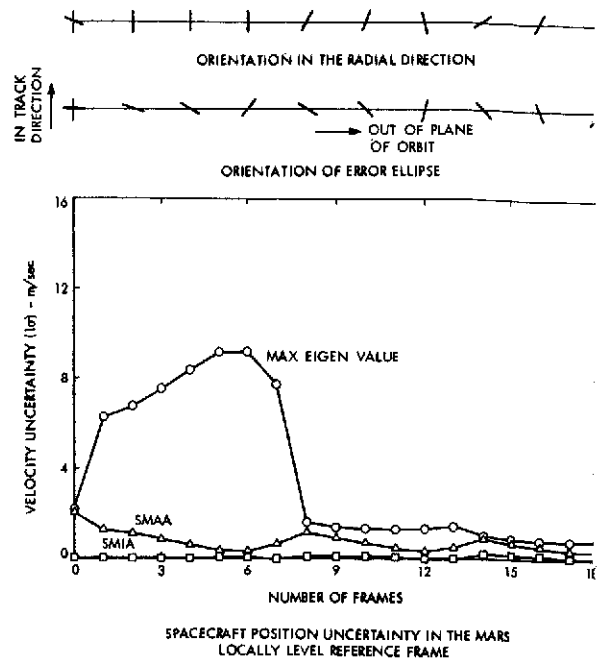
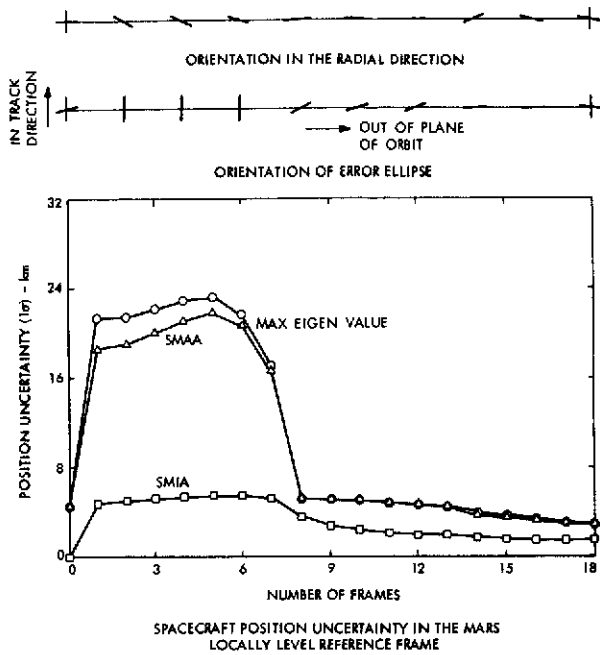


Figure 6. Combined Statistics of Spacecraft State, TV Pointing Direction, and Landmarks.

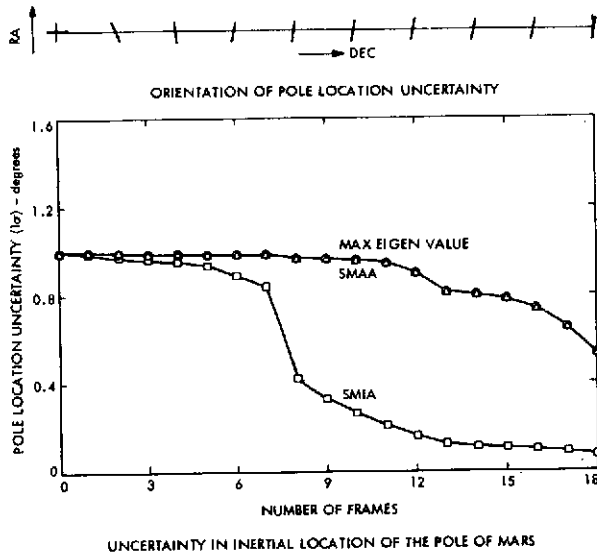
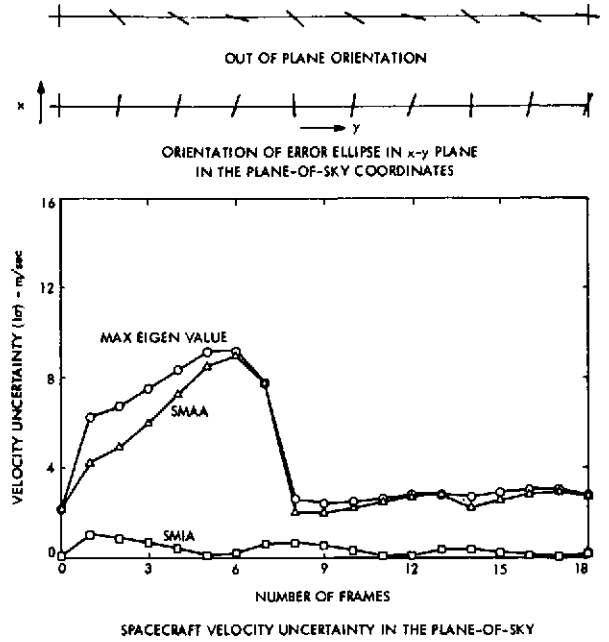
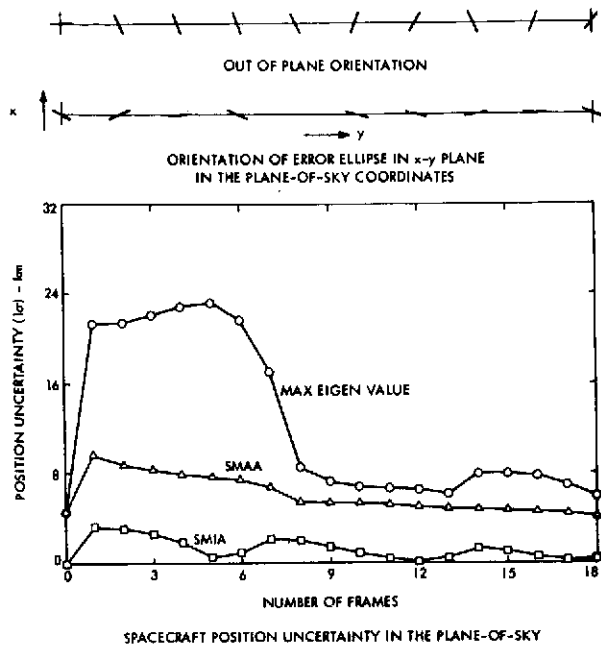
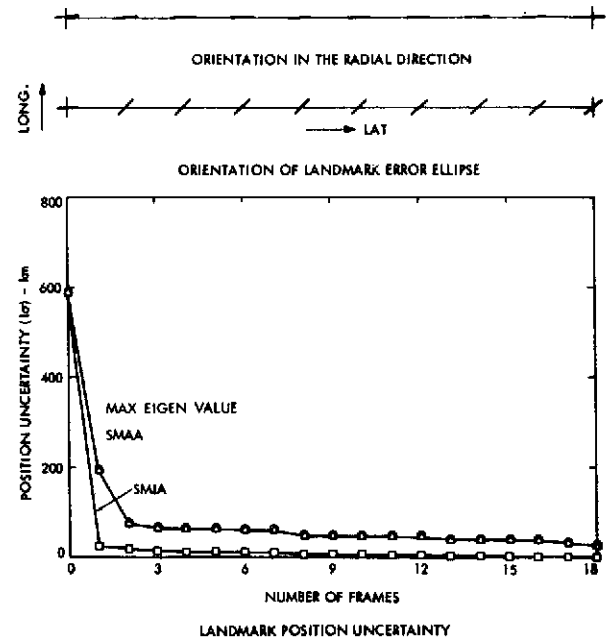
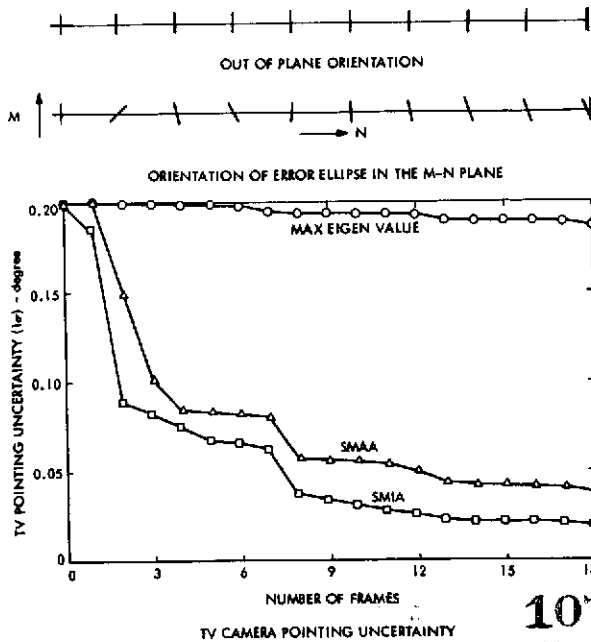


Figure 7. The Complete Solution.



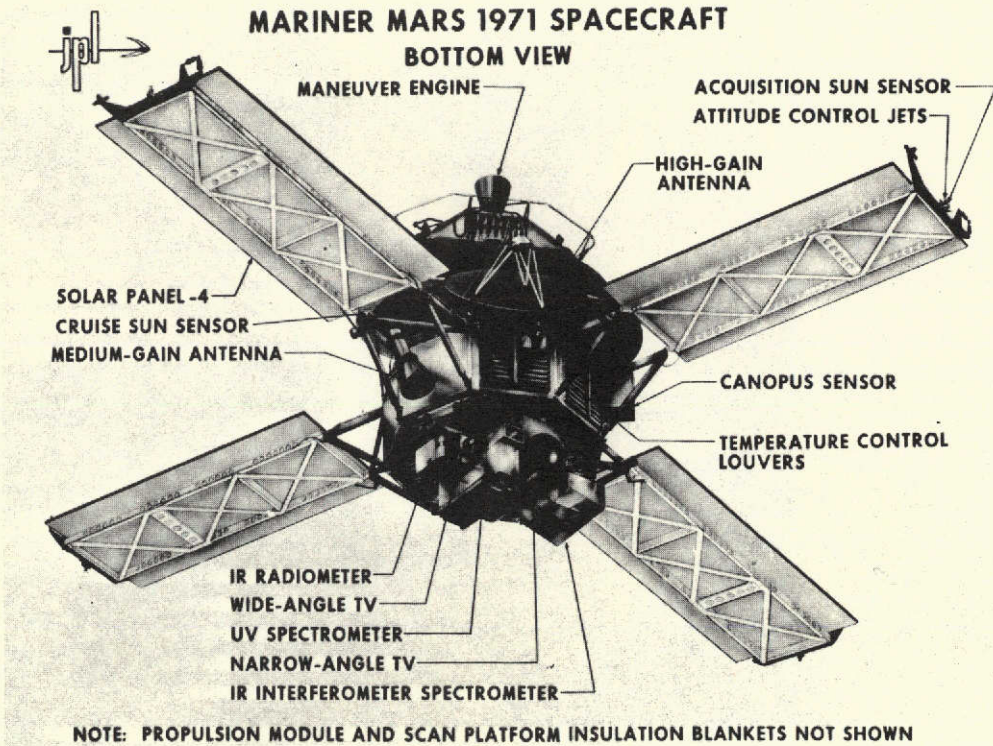


Figure 9

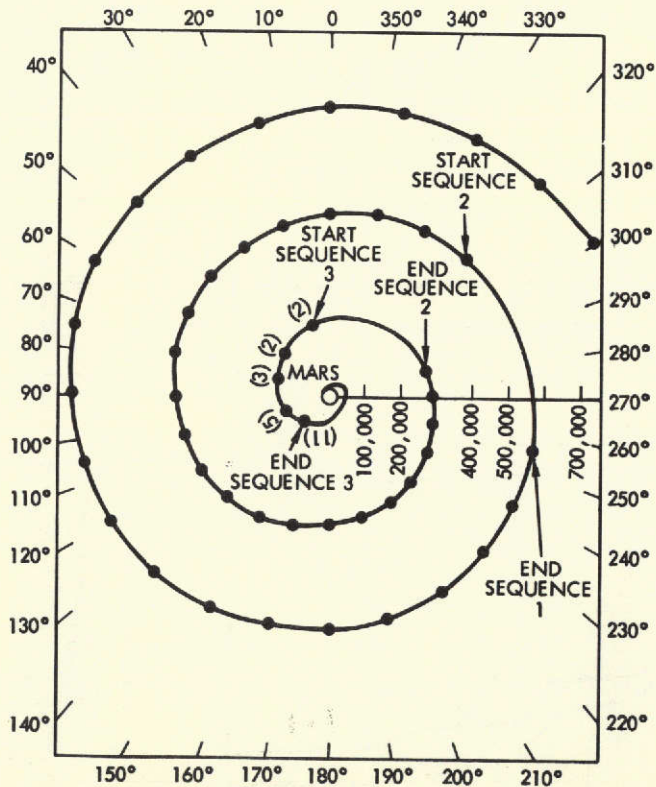


Figure 10. APPROACH PHOTOGRAPHIC SEQUENCE

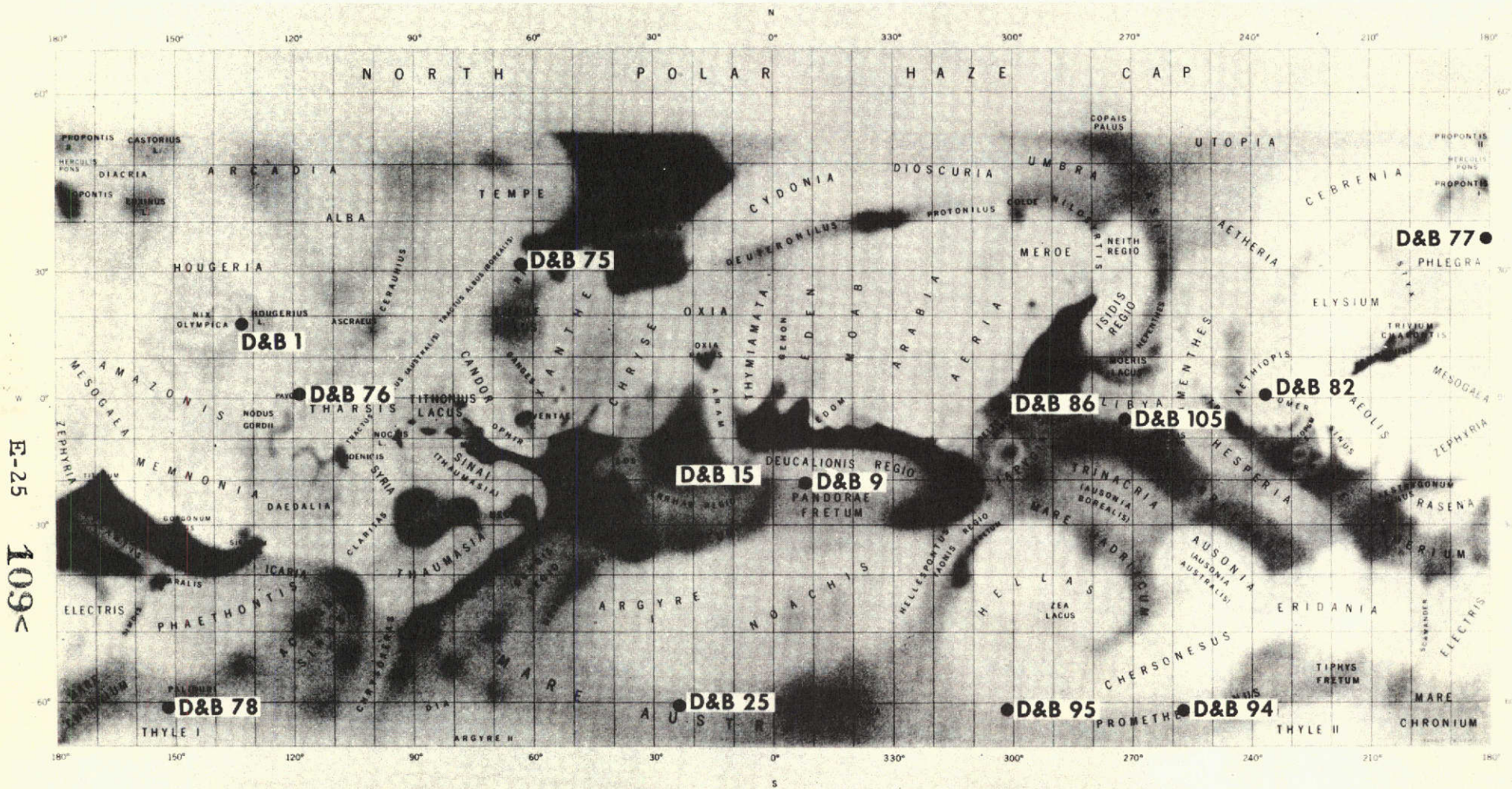


Figure 11. LANDMARKS USED IN APPROACH LANDMARK TRACKING STUDY
 SOURCE OF LANDMARKS - DAVIES AND BERG (Ref. 2)

E-25
 109<

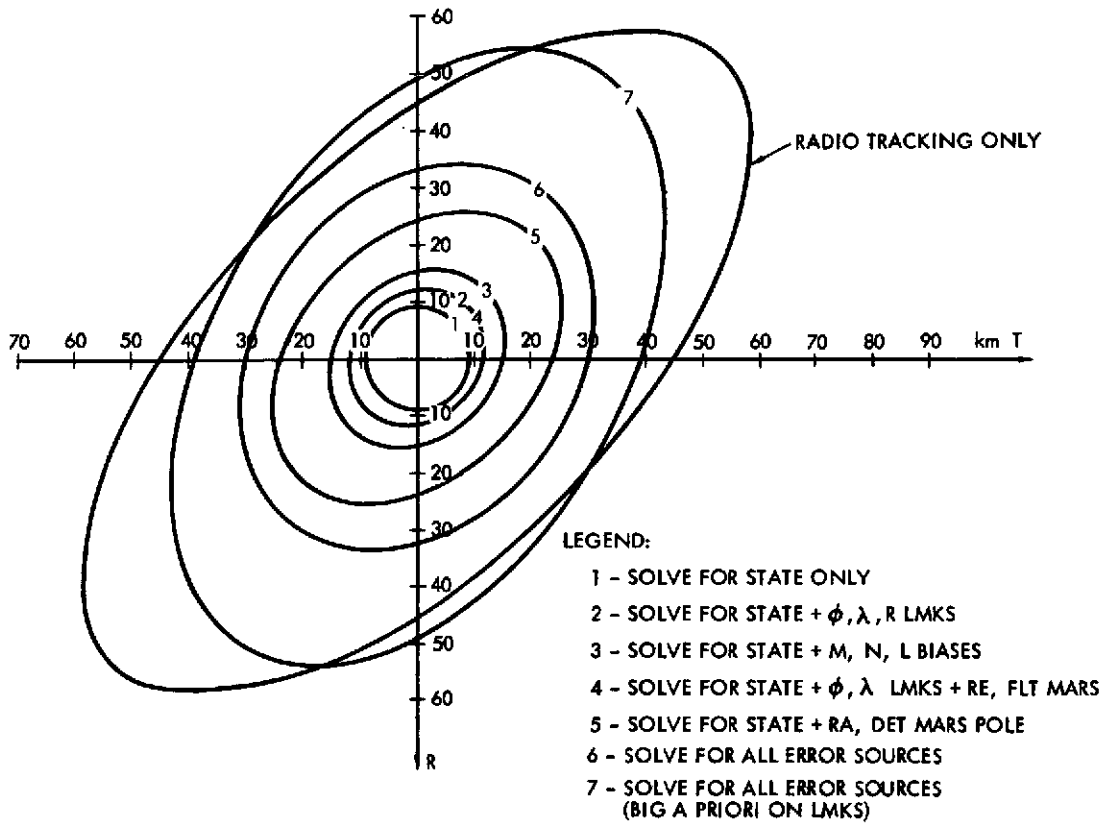


Figure 12. B-PLANE ERROR ELLISPES

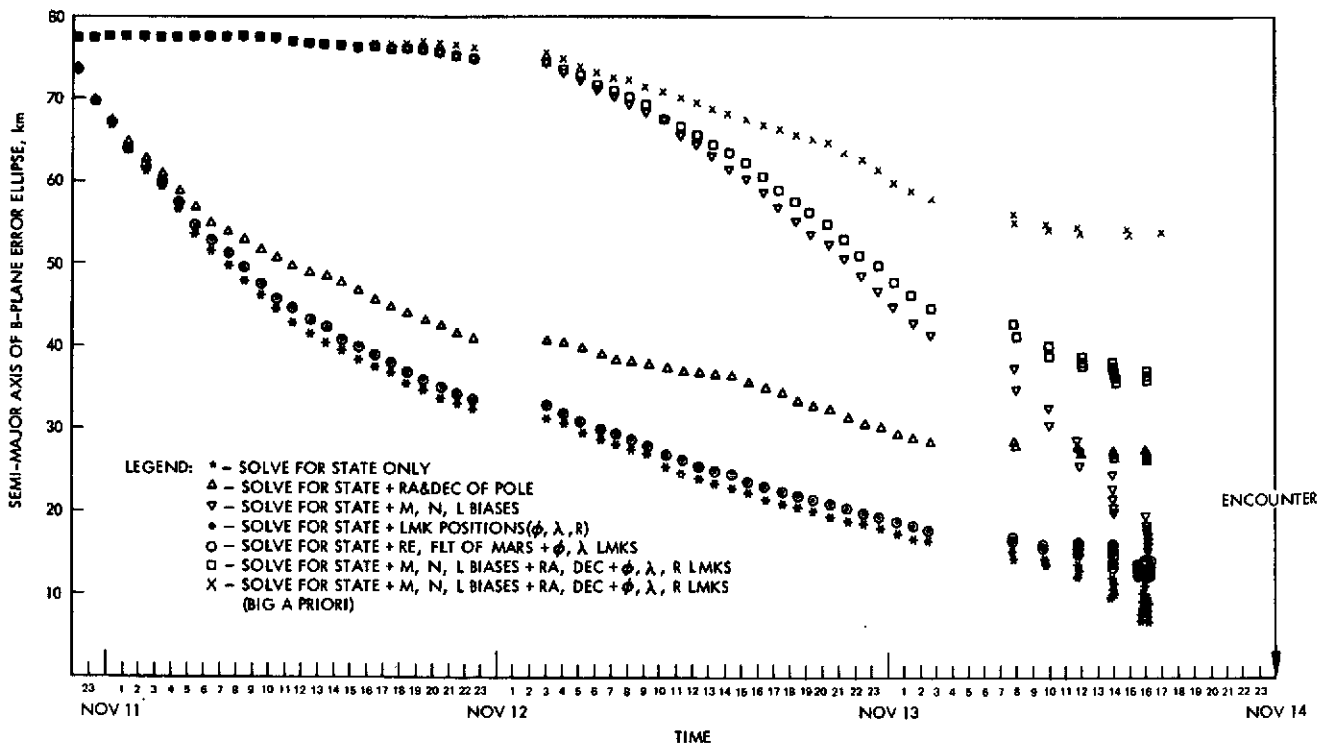


Figure 13. SEMI-MAJOR AXIS OF THE B-PLANE ERROR ELLIPSE VS. TIME FOR COMBINATION OF ERROR SOURCES

Symbols	Definitions
δx	Variation in pixel (picture element) location
δy	Variation in Line location
k_x	Pixels/mm
k_y	Lines/mm
f^y	TV Camera focal length in mm
u, v, w	Coordinates of s/c - LM vector in the TV reference frame
$T_{TV/I}$	Transformation from inertial frame to the TV reference
$T_{I/B}$	Transformation from Planet fixed reference frame to the Inertial reference frame
r	Local radius of the planet
ϕ	Areographic latitude
λ	Areographic longitude
$r_{s/c}$	Mars - spacecraft vector
r_{LM}	Mars - landmark vector
Φ	State Transition Matrix

Definition of the Plane-of-Sky Coordinate system:

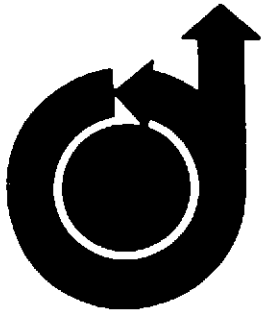
z	is a unit vector along the spacecraft/planet - Earth direction
y	is orthogonal to z and is parallel to the Earth Equatorial plane
x	completes the triad

Definition of the Mars Locally Level Reference: (LLF)

z	is a unit vector along the planet - spacecraft direction
y	is orthogonal to z and lies along the instantaneous angular momentum vector of the orbit of the spacecraft
x	completes the triad

APPENDIX F

A DETAILED ANALYSIS OF MARINER NINE TV NAVIGATION DATA



AIAA Paper No. 72-866

A DETAILED ANALYSIS OF MARINER NINE TV NAVIGATION DATA

by
W. G. BRECKENRIDGE and C. H. ACTON JR.
Jet Propulsion Laboratory
Pasadena, California

AIAA Guidance and Control Conference

STANFORD UNIVERSITY, STANFORD, CALIF./AUGUST 14-16, 1972

First publication rights reserved by American Institute of Aeronautics and Astronautics.
1290 Avenue of the Americas, New York, N. Y. 10019. Abstracts may be published without
permission if credit is given to author and to AIAA. (Price: AIAA Member \$1.50. Nonmember \$2.00).

Note: This paper available at AIAA New York office for six months;
thereafter, photoprint copies are available at photocopy prices from
AIAA Library, 750 3rd Avenue, New York, New York 10017

W. G. Breckenridge and C. H. Acton, Jr.
 Jet Propulsion Laboratory
 Pasadena, California

Abstract

The Mariner Mars 1971 Optical Navigation Demonstration used television pictures from Mariner 9 to successfully verify the star-satellite optical data concept for planetary approach navigation. This analysis of the data is to verify the models used and the measurement noise predictions as well as to identify those areas where changes and improvements are needed. The results indicate that the observed performance was in good agreement with predictions, but there are some areas where improved performance is possible.

Introduction

The Mariner Mars 1971 Optical Navigation Demonstration^{1, 2} was designed to demonstrate the capability to perform navigation, in near-real time during a planetary approach, using star-satellite optical measurements from the spacecraft. This mission offered a unique opportunity to test this method without requiring its success for mission success. The demonstration, however, was very successful. All operations were completed on time and the accuracy achieved was even better than expected. This accuracy was due to two factors, the observation of more stars than expected and the calibration of the instruments used to make the measurements. The principal instrument was the science television camera used for taking pictures of the satellites against a star background.

This paper discusses the accuracy of the measurements made by these instruments, and the accuracy of the optical navigation system calibrations based on those measurements. The evaluation of performance is based on the data collected and processed during several phases of the mission and is compared to the preflight predictions of performance. The four major topics discussed are the error models for optical navigation system elements, calibration of the scan platform pointing of the television camera, geometric calibration of the television camera, and image detection and location.

Models

Those subsystems of the Mariner 9 spacecraft, shown in Figure 1, that are of primary importance to optical navigation, are the sun and star sensors, the scan platform, and the television (TV) cameras. The principal data used in the Mariner Mars '71 Optical Navigation Demonstration were TV pictures of the Martian satellites, Phobos and Deimos, against a background of stars. To obtain and use these pictures, it was necessary to point the TV camera in the proper direction and then be able to interpret the resulting picture in terms of relative directions to the imaged objects.

The spacecraft orientation with respect to the Sun and reference star is controlled and measured by the attitude control system, using the sun and star sensors. The scan control system, which

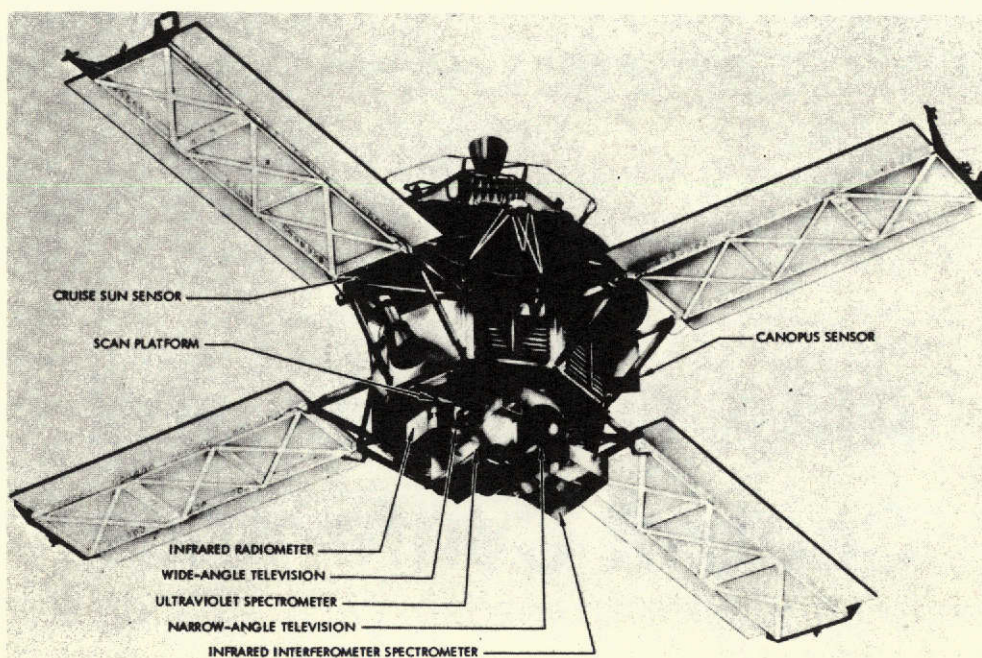


Figure 1. Mariner Mars 1971 Spacecraft, Showing Scan Platform, Science Instruments, and Sensors

* This paper presents the results of one phase of research carried out at the Jet Propulsion Laboratory, California Institute of Technology, under Contract No. NAS-7-100, Sponsored by the National Aeronautics and Space Administration.

controls and measures the clock and cone gimbal actuator angles, determines the orientation of the TV camera with respect to the spacecraft as shown in Figure 2. The relative positions of images in the TV pictures depend on the geometric characteristics of the camera optics and image scanning.

The orientation of the TV camera and the directions to the imaged objects are reconstructed using the telemetered measurements from the sun and star sensors, gimbal actuator potentiometers, and the TV video signal and knowledge of non-telemetered, fixed parameters. These sensors were calibrated and the fixed parameters measured before launch, but they are subject to variation between this pre-flight calibration and their use for optical navigation, many months and millions of kilometers later. Hence, the calibration models of the spacecraft must be augmented with an error model which would account for these variations. In-flight calibrations were performed to determine the parameters of that model.

Attitude Control Sensors

The error model for each attitude control sensor (pitch and yaw sun sensors and roll star sensor) consists of two parameters, a null offset and scale factor change. These two parameters are adequate to model the sensor since all normal measurements are near null and well within the range of linearity of the sensor.

In addition to the error model, a model for the measurement noise is needed as a measure of the value of the telemetered measurements. For the attitude control sensors, the dominant noise source is quantization of the sensor outputs into digital form for telemetry, where one digital number (DN) increment is about 0.015° for pitch and yaw and 0.03° for roll.

Scan Platform

The scan platform error model covers the alignment errors between the spacecraft body and the narrow angle TV camera (TV-B). It consists

of seven distinguishable error parameters: two-axis offset of the clock gimbal, null offset of the clock gimbal actuator, nonorthogonality of the clock and cone gimbal axes, null offset of the cone gimbal actuator, nonorthogonality of the cone gimbal axis and TV-B line-of-sight (LOS), and a rotation of TV-B about its LOS.

The alignment on the scan platform of the wide-angle TV camera (TV-A) with respect to TV-B is defined by three rotations, sequentially about the \hat{N} , $-\hat{M}$, and \hat{L} axes of the TV coordinate system shown in Figure 2.

The telemetry measurements from the scan platform are the gimbal actuator potentiometer resistance ratios. The noise model for these measurements consists of the telemetry quantization error ($1DN \approx 0.035^\circ$) plus residual pot calibration error for a total of about 0.02° , 1σ .

Television Cameras

The total calibration model of the TV geometric characteristics was used as the error model, permitting complete recalibration of the TV from in-flight measurements. This was done because of pre-flight uncertainty of the stability of the calibration. The model parameters³ include optical focal length; center, scale factors, orthogonality, and rotation of the scan line and pixel (sample) coordinates; and center and six coefficients of electromagnetic distortion. Optical distortion parameters are included in the model but were not used because of the low optical distortion of TV-B (narrow angle) and the minimal amount of data obtained from TV-A (wide angle).

The measurements obtained from the TV pictures are primarily the line and pixel coordinates of the center of an image. The noise model consists of the image location errors, which can be different for each image, and are discussed in later sections of this paper.

Scan Calibration

The in-flight calibration of the attitude control and scan platform error models was necessary to be able to point scan platform mounted science instruments, including the TV cameras, and to determine their pointing directions from telemetry to the accuracy required for the science experiments and optical navigation. The in-flight calibration⁴ was performed using TV pictures of stars. The expected locations of the star images were computed from the attitude sensor and gimbal telemetry, the sensor's calibration models, and the spacecraft trajectory. The differences between the expected and observed image locations depend upon the error model parameters and measurement noise and are the 'measurements' used in the estimation process for the error model parameters.

The raw telemetry was preprocessed, using both computer programs and an analyst, to get sensor and gimbal angles (in engineering units, e.g., degrees, rather than DN) and their estimated 1σ measurement noises and to locate and identify the star image in the TV pictures. The parameter estimation program first used this data to compute the expected star image locations and the expected

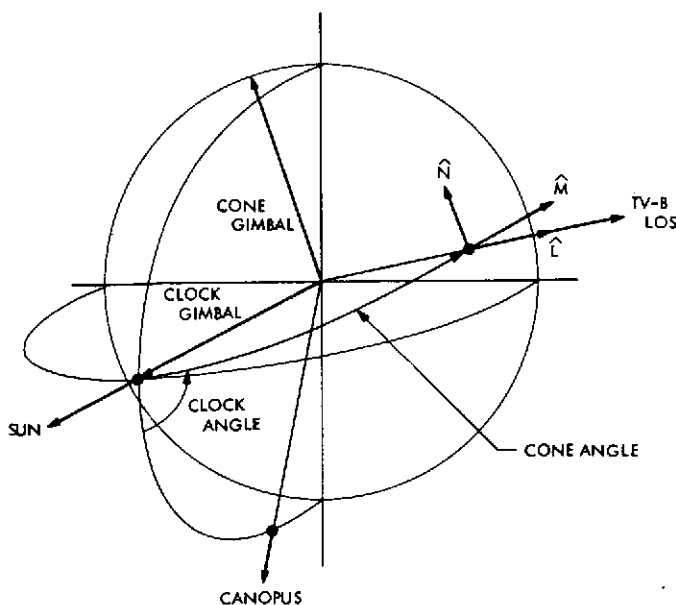


Figure 2. Clock-Cone, Scan Platform Gimbal, and TV Coordinate Systems

1σ variation due to measurement noise and image location errors. The estimation process used was a batch form of a minimum variance estimate in a two-stage process. The first stage estimates the error model parameters and their covariance matrix, and the second estimates the pointing error of each picture and the residual star image location errors.

The resulting estimates and variances are shown in Table 1 with their 1σ uncertainties. The a posteriori covariance matrix has some high correlations, so to evaluate the effect of this residual calibration error on TV pointing, the matrix was mapped to the pointing error coordinates for each picture. These averaged about 0.005° , 1σ , about axes \hat{M} and \hat{N} , and 0.020° about \hat{L} for the narrow angle camera, and 0.015° and 0.17° respectively for the wide-angle camera (TV-A has 1/10 the focal length of TV-B).

Table 1. Error Model Parameter Estimates

Parameters	Scan Cal. Value/ σ	Orbit 72 Change/ σ
Sensor Null Offset:		
pitch	.133%/.045°	N. E.
yaw	-.237%/.045°	N. E.
roll	N. E.	N. E.
Sensor Scale Factor:		
pitch	-18.5%/2.7%	-.3%/3.7%
yaw	-21.5%/2.7%	+4.4%/4.1%
roll	-3.1%/2.8%	+2.0%/4.2%
Clock Gimbal:		
misalign. #1	-.085%/.045°	+0.010°/.022°
misalign. #2	-.005%/.045°	-.024°/.020°
null offset	-.084%/.026°	-.072°/.021°
Cone Gimbal:		
nonorthog. to clock	-.028%/.021°	+0.041°/.036°
null offset	-.494%/.004°	-.018°/.021°
TV-B:		
nonorthog. to cone	.037%/.031°	+0.006°/.036°
rotation about LOS	.088%/.026°	-.012°/.045°
TV-A:		
N axis rotation	-.175%/.018°	+0.034°/.020°
-M axis rotation	-.474%/.018°	-.064°/.018°
L axis rotation	30.509%/.182°	N. E.

N. E. = Not Estimated

Pointing Error Evaluation

Picture pointing error, the difference between the star referenced orientation and that obtained from engineering telemetry after correction for the estimated error model parameters, is due to measurement noise and residual error parameter uncertainty. The statistics of the pointing errors of all the scan calibration pictures can be compared to the a priori assumptions of the measurement noise to evaluate the performance of the sensor measurements. The results are shown in Table 2. The variation in a priori values is due to the variation in cone angle for the various pictures. The observed values are averaged over the whole cone angle range.

Table 2. Comparison of A Priori and Observed Pointing Error

Error Axis	A Priori 1σ Value	Observed 1σ Value
cross cone, $-\hat{M}$.010° - .023°	.019°
cone, \hat{N}	.021°	.026°
rotation, \hat{L}	.006° - .022°	.012°

Plots of these pointing errors vs. clock angle of the picture are given in Figure 3. Also shown on the figure are the sizes of the telemetry quantization increments (IDN), the major measurement noise sources. Several features of these plots are worthy of comment. The cross-cone (M-axis) plot shows residuals after removal of a systematic error (about 0.1° peak to peak) not included in the original error model. This error was of the form $C_1 \sin \alpha + C_2 \cos \alpha$ (α = clock angle). Errors of this form are in the actuator calibration model and model gear train errors, but external to the actuator represent offset and misalignment of the actuator axis with respect to the gimbal axis. It was expected that this kind of error would not be significant.

Hysteresis in the gimbal measurements becomes observable when the points are identified by direction of motion prior to the picture. The magnitude is generally about $\pm 0.015^\circ$; however, in one region it is considerably more. This exception is a clock angle dependent, cone angle hysteresis. Below 140° of clock angle, the cone angle hysteresis increases to about $\pm 0.04^\circ$ and is easily seen in the plot. No cause for this has been isolated, but appears like a clock angle dependent mechanical interference to platform cone motion since the actuator readout leads the platform position rather than lagging as would a gear train/potentiometer hysteresis or backlash. When the points below 140° clock are deleted, the 1σ cone pointing error changes from the 0.026° in Table 2 to 0.018° , closer to the cross-cone value.

The overall conclusion regarding the performance of the telemetry measurements of camera pointing is that the observed pointing errors were slightly better than the a priori assumptions except for the two anomalies previously mentioned, the unmodeled systematic clock error and the region of high cone hysteresis

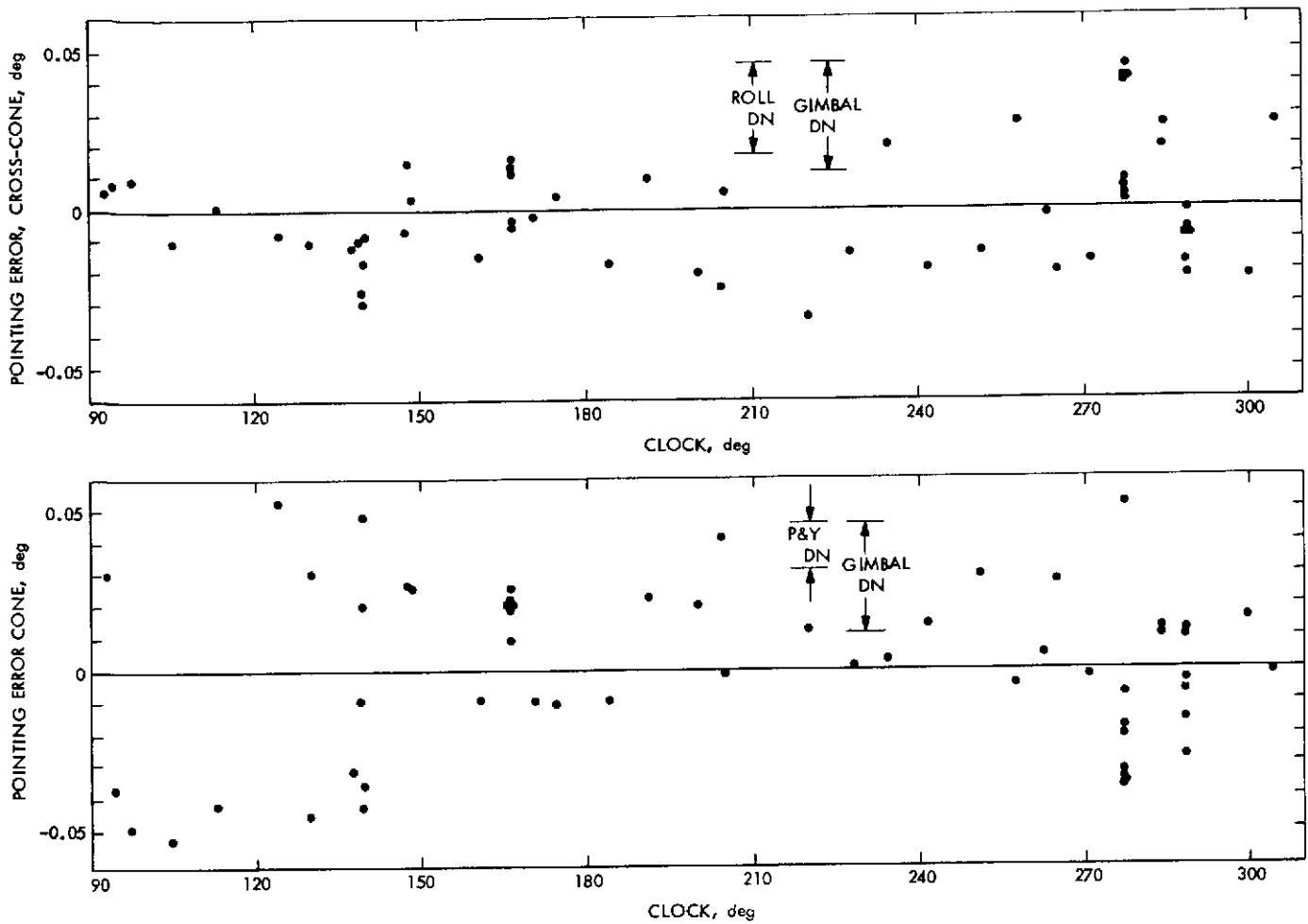


Figure 3. Cone and Cross-Cone Pointing Error Residuals vs. Platform Clock Angle

Recalibration

The scan calibration results shown in Table 1 were used for optical navigation real-time operations, but the calibration has been periodically checked by using other data sets. One such check used the star data from the optical navigation star-satellite pictures. The platform pointing direction varied very little, so only three components of pointing error were separable. The three mean offsets found were $(-0.001^\circ, -0.005^\circ, \text{ and } -0.038^\circ)$ with standard deviations of $(0.005^\circ, 0.005^\circ, 0.031^\circ)$. These offsets are in agreement with their uncertainties and the residual pointing error uncertainties from the scan calibration.

A second check was made using star pictures taken in Orbit 72, after the orbit insertion and the first orbit trim maneuvers. The changes from scan calibration values are also shown in Table 1. As for the scan calibration, the parameter estimates are highly correlated. Comparison of the mapped results indicate that the only statistically significant change was in the cross-cone (M-axis) offset of the wide-angle camera (TV-A). When separated from other correlated errors, it amounts to about a 0.08° shift.

Separation of Noises

For scan calibration, the camera pointing was changed for each picture and the measurement noises of the attitude control and gimbal sensors

could not be separated. However, during the approach picture sequence, groups of pictures of Mars were taken without moving the scan platform gimbals. After encounter, the spacecraft approach trajectory with respect to Mars was known, and the Mars images in the TV pictures were used to evaluate the TV pointing error. A sample of the pointing errors is shown in Figure 4, having three groups of Mars pictures. The variations within a group are primarily due to attitude control measurement errors, with some effect of small, random image location errors. The variations (steps) between groups are due to changes in gimbal angle measurement errors. Using this data to separate the attitude control and gimbal noise effects gives the results shown in Table 3. The uncertainty in

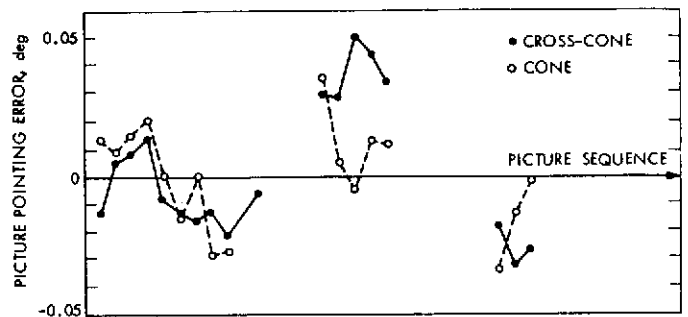


Figure 4. Typical Groups of Pointing Errors at Fixed Gimbal Angles

the observed values is 20 percent. The larger cone (N-axis) errors are partly attributable to the higher hysteresis since the cone angle for these pictures was 120°.

Table 3. Expected and Observed 1σ Measurement Noise

Pointing Error Axis	Attitude Control		Gimbal Angle	
	Expected	Observed	Expected	Observed
M	.007°	.006°	.023°	.021°
N	.004°	.006°	.020°	.026°

TV Geometric Calibration

Calibration of the television camera geometric distortion was necessary to be able to establish the relative directions of imaged objects to the accuracy required for optical navigation. If used only for scan calibration, the uncalibrated television distortion of 10 pixels (0.016°) 1σ would be acceptable as an additional measurement noise.

The calibration of the television camera geometric distortion is done using the locations of the images of a pattern of objects with known geometric relationships. Two kinds of objects have been used, reseau marks at measured positions on the face of the vidicon and clusters of stars. The use of reseau limits the calibration to the internal distortions of the camera, excluding optical distortion, while star clusters include both. The optical navigation data is from the narrow angle camera which has very low optical distortion so that there should be little basic difference between the results using the two types of objects.

The same process is used for calibrating the television geometric model as described for scan calibration. The parameters of all models can be estimated simultaneously if necessary but the TV calibration was done separately, prior to the scan calibration, to limit the number of parameters used and the computer time required.

Pre-flight calibration of the TV-B model was done using reseau images. The calibration accuracy, as indicated by the residual reseau image location differences, was 0.46 line and 0.69 pixel (sample), 1σ . A pixel, as the unit of measure in the TV picture, is the distance between adjacent lines or samples (pixel, as a coordinate) and is approximately 6 arc sec for the narrow angle camera (TV-B).

The first picture of the scan calibration sequence was a TV-B dark-current-buildup picture in which the reseau could be seen. These reseau images were used for the primary in-flight calibration, having a residual 1σ error of 0.51 line and 0.72 pixel which includes both the residual distortion error and the random reseau location errors. The results of this calibration, compared to the pre-flight calibration in Figure 5, showed that there was a 2 pixel shift and 0.2° rotation of the scanning pattern, but no significant change in the electromagnetic distortion.

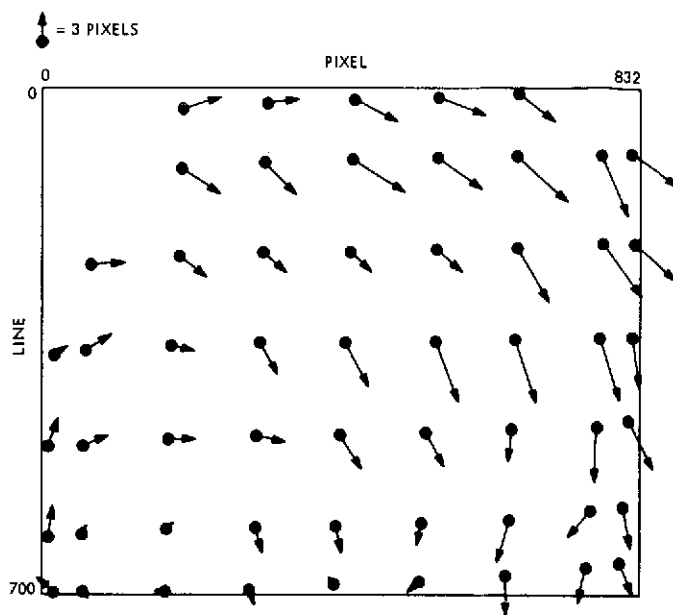


Figure 5. Change in Observed Reseau Locations

The residual reseau location errors are not random, but are systematic, as shown in Figure 6, indicating that further model development could reduce the calibration error, possibly to 0.1 to 0.2 pixels, 1σ .

Calibration Evaluation

The calibration of the TV distortion was evaluated by looking at the residual star image location errors from the scan calibration pictures. Histograms of the line and pixel residuals for 225 stars in 59 pictures are shown in Figure 7. The standard deviations are 0.42 lines and 0.52 pixels. These statistics are lowered by pictures having few stars. A more representative sample, the 24 pictures having 3 or more stars, has average standard deviations of 0.63 lines and 0.78 pixels. These residuals contain the residual calibration error, and the image location error. If the residual calibration error, as measured by reseau residuals, is removed (subtract variances) that part attributed to random image location error is 0.38 line and 0.31 pixel, 1σ . Image locations were specified to the nearest line and pixel so a 1σ error of 0.29 was expected because of the quantization. The a priori value assumed for image location and residual calibration errors was 1 line and 1 pixel, 1σ . Some of the factors affecting image location accuracy are discussed in a later section of this paper.

One other factor influencing the star residuals is the nonlinearity (sixth order) of the distortion model. The calibration program was designed to be compatible with the orbit determination software which requires raw observed image location data and the expected image location, given the attitude control and scan platform telemetry data. Because the pointing error uncertainty (~0.02°/axis) maps to 12 pixels, 1σ , the linear correction of image locations over this range can introduce error due to the nonlinearity of the distortion

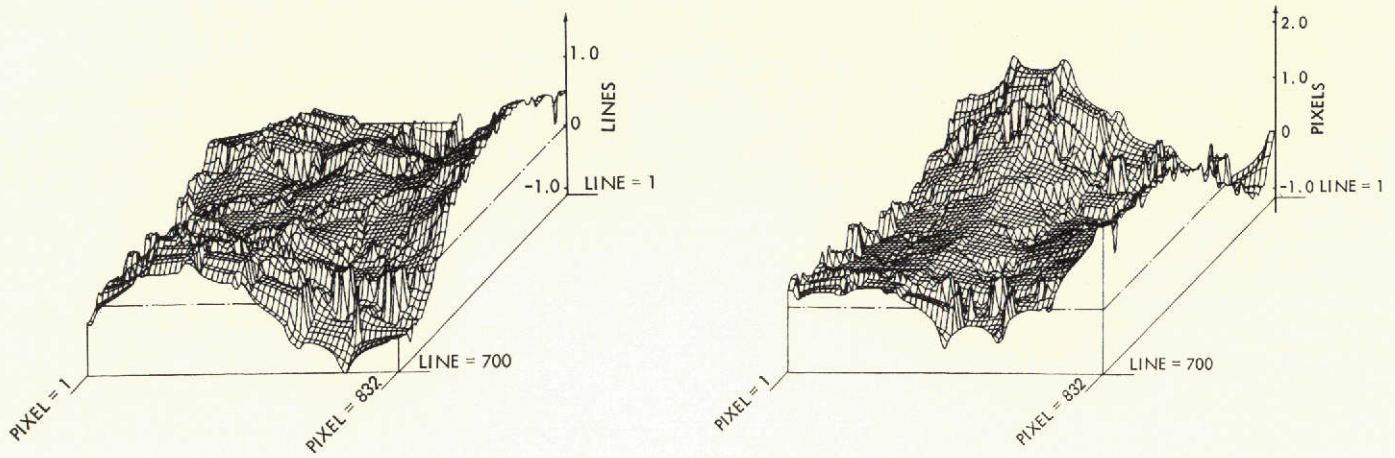


Figure 6. Post Calibration Line and Pixel Residuals

model, particularly near the edges and corners of the picture. A more accurate method of processing (object space) partials are linear over a much wider angle range than the TV distortion (image space) partials. This would also provide more accurate partials for estimating the TV distortion model parameters.

Recalibration

The in-flight stability of the TV distortion was checked by recalibrating using reseaux from a series of pictures taken over a 250 day period including orbit insertion and two orbit trim maneuvers and the solar occultation period. These recalibrations show no significant variations in the model parameters after the scan calibration dark-current picture, the first of the series.

The TV model was also calibrated using a cluster of stars (the Pleiades). The picture, like the one shown in Figure 8 from the scan calibration series, contained 30 star images. The star image residual error after calibration was 0.65 line and 0.55 pixel, 1σ . When the estimated parameters were used to process reseau images, their residuals went up to 3 pixels, 1σ . This occurred because the star images were concentrated in the lower-right two-thirds of the picture, while the

reseaux were distributed uniformly throughout the picture. The star picture did not calibrate the whole frame. If stars are to be used for primary calibration of the picture, they should cover the whole field of view, or several pictures could be used which jointly provide total coverage.

Image Analysis

Video images used for scan calibration and optical approach navigation include satellites, stars and reseaux. Stars, which are point-source stimuli, appear as somewhat gaussian charge distributions on the vidicon's photoconductor, but these distributions may be trailed as a result of spacecraft attitude motion during exposure. Deimos and Phobos were generally 2 to 5 magnitudes brighter than the background stars and consequently resulted in more severely bloomed images. Reseau marks are visible against the lighted planet surface and in pictures where the vidicon's dark current was integrated over several minutes before being read out. These marks appear as "depressions" in the local video signal, covering an area of about 2 pixels by 2 pixels.

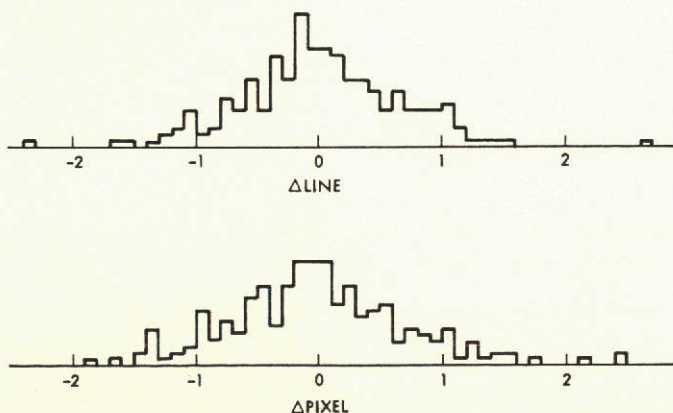


Figure 7. Histograms of Scan Calibration Star Residuals

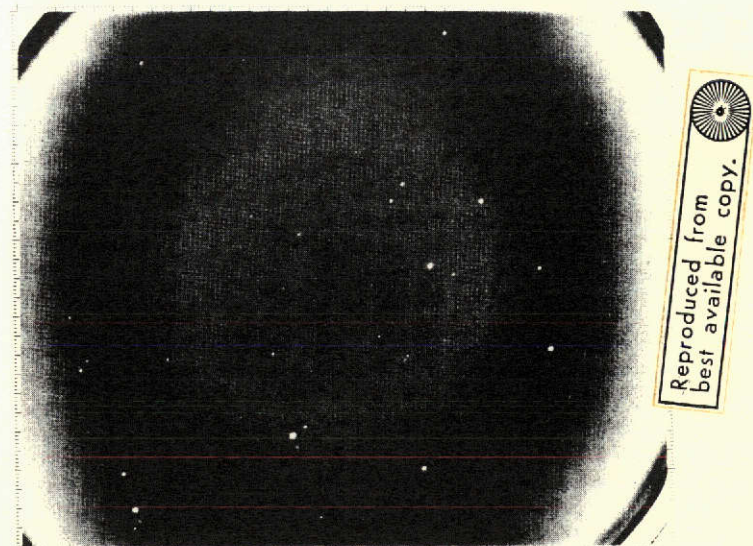


Figure 8. Typical TV Picture of the Pleiades

Images detected by the vidicon are converted on the spacecraft to 9 bit data numbers (DN), allowing a range from 0 to 511, although the average noise level of 2.3 DN effectively reduced by one bit the inherent signal detection sensitivity. Excepting the dark current integration and Mars pictures, the stars and satellites appeared against an average vidicon dark current level of 17.5 DN. Some peculiarities of the vidicon, the occasional presence of stray light, blemishes on the vidicon target, coherent noise from other spacecraft electronics and bit errors during transmission to earth all added to the dynamics of the scene being viewed, Figure 8 and Figure 9.

Image Detection

Star detection was done semi-automatically on the ground by computer processing of the digitized video data.² Each picture was scanned by the computer for multi-pixel signals with significant local signal to noise ratios ($S/N \approx 2.5$). Visual examination of the digital data for each candidate image was used to eliminate those signals with a signature uncharacteristic of a star, Figure 10. Correlation of easily detected stars with their expected positions allowed detection of additional stars with near unity signal to noise. Success in detecting a given star depended primarily on its magnitude. Spacecraft attitude motion and low and high frequency noise became significant factors when searching for stars of magnitude eight or greater. Existing data has revealed no conclusive correlation between detectability and star spectral class, suggesting the greater relative importance of system noise. Detection of the satellite image in each picture was easily accomplished in the process of searching for stars.

Image Location

The task of selecting the correct center location for each image is hindered by attitude rate, image spreading and scanning beam readout characteristics. Energy from a star may be trailed across several pixels as the spacecraft attitude changes.

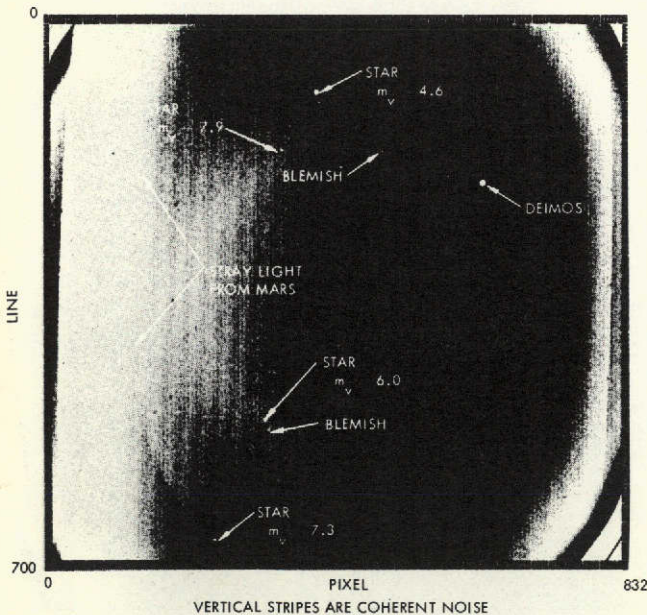


Figure 9. Star-Satellite Picture Showing Scene Dynamics and Noise

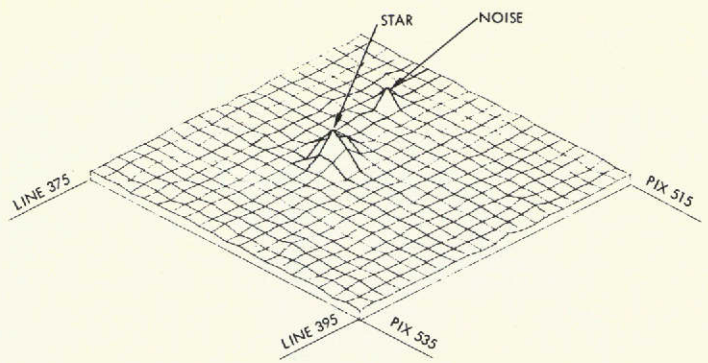


Figure 10. Signatures of Typical Star and Noise Signals

Additionally, the charge produced by a star or satellite signal tends to "bloom" over two or more pixels, depending on the brightness of the object and local properties of the photoconductor. This results in the somewhat gaussian shaped charge distribution seen in the digital data. While the image stored on the photoconductor is being sampled, the scanning beam tends to bend toward regions of higher charge. As a result, charge stored on line number $L + 1$ may be read out when the TV control electronics are logically sampling line L . An additional effect, scanning spot overlap, results in more apparent charge migration. Figure 11 shows the relative sizes of the scanning spot and pixel separation. The video level measured at pixel P on Line L , (L, P) , is supplemented by charge stored at locations $(L, P+1)$, $(L+1, P-1)$, $(L+1, P)$ and $(L+1, P+1)$. Pixels on the preceding line and the previous pixel $(L, P-1)$ have already been sampled ("erased") and thus contribute little to the signal measured at (L, P) . This overlap, as much as 26 percent, shifts the apparent location of an image to a lesser line and pixel. The combined effects of beam bending and spot overlap have a random component on the order of $0.3 \text{ pixels } (1\sigma)$ when star locations are selected to the nearest pixel. The fixed component of the combined error for other than the brightest images is probably

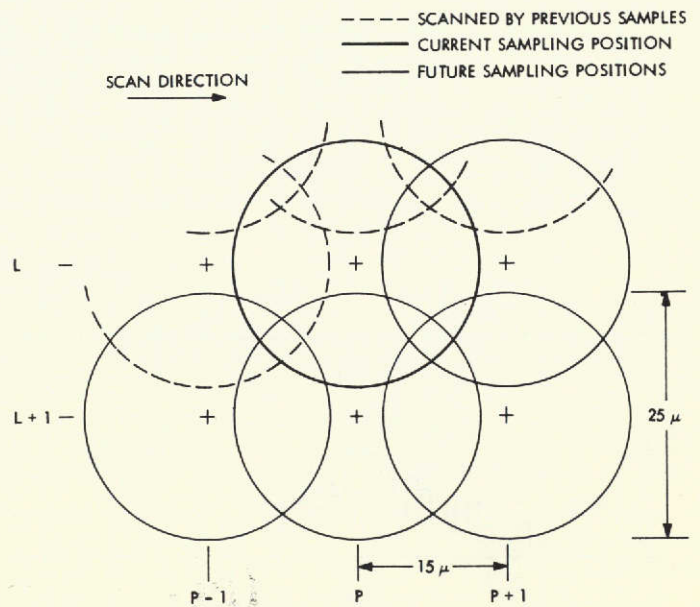


Figure 11. Scanning Spot Geometry

somewhat less than the observed 0.6 pixel (1σ) residual electromagnetic distortion error. Improvement of the distortion error model to reduce the distortion residuals from 0.6 pixels to near 0.2 pixels must be accompanied by appropriate models to account for the effects of these readout errors and image trailing if the overall system performance is to be improved.

Estimates of satellite image locations are more strongly affected by beam bending, where image energy density is close to ten times that of a typical star. Image blooming (up to 20 pixels for a 3 pixel object) and image trailing further degrade the center finding estimate. Compensation for the 60 degree phase angle while estimating the location of the center of mass was not attempted due to the comparatively small magnitude of this correction.

Acknowledgement

The authors wish to acknowledge the efforts of H. Ohtakay and James A. Miller in support of this

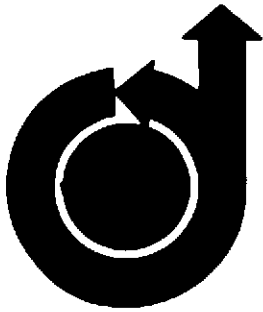
analysis, and JPL's Image Processing Laboratory for providing photographs and reseau locations.

References

1. Duxbury, T.C., and Acton, C.H., "On-board Optical Navigation Data from Mariner '71", Presented at Institute of Navigation National Space Meeting, Orlando, Florida, March 1972.
2. Acton, C.H., "Processing On-board Optical Data for Planetary Approach Navigation", AIAA Paper No. 72-53, January 1972.
3. Duxbury, T.C., and Ohtakay, H., "In-Flight Calibration of an Interplanetary Navigation Instrument", Journal of Spacecraft and Rockets, Vol. 8, No. 10, October 1971.
4. Pace, G.D., Jaivin, G.I. and Virzi, R.A., "Mariner Mars 1971 Scan Platform Pointing Calibration", Jet Propulsion Laboratory Quarterly Technical Review, Vol. 2, No. 1, April 1972.

APPENDIX G

PROCESSING ON-BOARD OPTICAL DATA FOR PLANETARY
APPROACH NAVIGATION



**AIAA Paper
No. 72-53**

PROCESSING ON-BOARD OPTICAL DATA FOR PLANETARY
APPROACH NAVIGATION

by
C. H. ACTON JR.
Jet Propulsion Laboratory
Pasadena, California

AIAA 10th Aerospace Sciences Meeting

SAN DIEGO, CALIFORNIA / JANUARY 17-19, 1972

First publication rights reserved by American Institute of Aeronautics and Astronautics.
1290 Avenue of the Americas, New York, N. Y. 10019. Abstracts may be published without
permission if credit is given to author and to AIAA. (Price: AIAA Member \$1.50. Nonmember \$2.00).

Note: This paper available at AIAA New York office for six months;
thereafter, photoprint copies are available at photocopy prices from
AIAA Library, 750 3rd Avenue, New York, New York 10017

Charles H. Acton, Jr.†
 Jet Propulsion Laboratory
 Pasadena, California

Abstract

Table 1. Optical Navigation
 Experiment Objective

The Mariner 9 spacecraft's science television camera provided an optical navigation experiment with TV pictures containing images of Mars' natural satellites against star backgrounds. Required TV image data and spacecraft engineering data were extracted from the spacecraft telemetry stream in this near-real time experiment designed to validate the navigation content of spacecraft-based optical data. This paper discusses the computer programs developed to prepare optical data for use in a navigation filter. Ground and in-flight calibration allowed pointing knowledge of better than 6 arc seconds. System performance during Mars approach was excellent, leading to extremely accurate trajectory estimates. The experiment provides a basis for the design of equivalent systems for future missions.

Introduction

Current Earth-based radio tracking techniques have been shown^{1,2,3} to be marginal or inadequate for many future missions to the outer planets. The additional navigation accuracy required may be achieved within spacecraft design fuel loading constraints by combining spacecraft-based optical measurements with Earth-based radio ranging and doppler data during planetary approach. Images of the target planet's natural satellites against a background of stars may be used to obtain an estimate of the spacecraft trajectory substantially better and earlier than that available using only radio data⁴, allowing significant reductions in fuel requirements. The Mariner Mars 1971 mission provided a timely opportunity to test this optical navigation concept with real data. The objective of the optical navigation experiment (Table 1) was chosen to formally demonstrate the navigational quality of optical data obtained from a TV camera and processed in a real mission environment.

Error Model

The extraction of data useful for navigation from the spacecraft telemetry stream and the rectification of this data for known errors are significant tasks leading to the development of optical observables suitable for use in a navigation filter. Intrinsic to this process is the formulation and calibration of spacecraft and sensor error models.

Images of Phobos, Deimos and stars were obtained from the narrow angle science TV camera, the characteristics of which are listed in Table 2. The vidicon's active target raster of 9.6 x 12.5 mm is electronically scanned in 700 lines and sampled

<u>Objective</u>
Develop and document the computer programs, mission interfaces and procedures necessary to obtain, process and use star-satellite optical navigation data within the mission environment. Perform a near-real time system demonstration during Mars approach, making results available to the mission in a timely manner.
<u>Supporting Goals</u>
1. Plan and schedule <ul style="list-style-type: none"> a) Pictures used for in-flight calibration of spacecraft and camera. b) Simultaneous imaging of a satellite and star(s) in a series of pictures taken during Mars approach. c) In-orbit satellite pictures.
2. Perform an in-flight calibration of the TV and spacecraft error models.
3. Extract engineering and video image data from the spacecraft telemetry stream in near-real time during Mars approach.
4. Identify and locate the satellite image and at least two star images in each approach picture in near-real time.
5. Using the calibrated math models and star images, rectify satellite image locations for known errors in near-real time.

at 832 picture elements (pixels) per scan line. The 500 mm focal length allows a 1.1 x 1.4 deg. field of view with an angular resolution of 6 arc seconds. Each video sample is digitized to 9 bits (512 intensity levels) prior to transmission to earth. A continuous, analytic error model developed for the camera⁵ contains terms for symmetric and asymmetric radial and tangential distortion, electromagnetic and optical principle point null-offsets and scan coordinate system scale factor, nonorthogonality and rotation. The TV is hard mounted to a two-degree of freedom scan platform, with TV mounting misalignments, scan platform gimbal errors and misalignments and pitch, yaw and roll sensor offsets and scale factor error comprising the remaining major components of the math model.

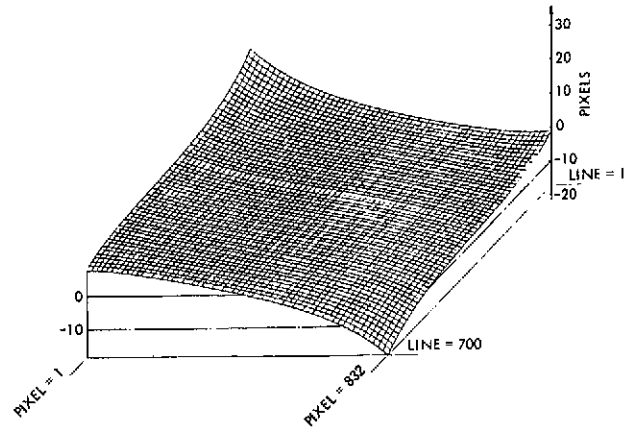
*This paper presents the results of one phase of research carried out at the Jet Propulsion Laboratory, California Institute of Technology, under Contract No. NAS 7-100, sponsored by the National Aeronautics and Space Administration.

†Team Leader, Optical Navigation Measurements Group, MM'71 Navigation Team.

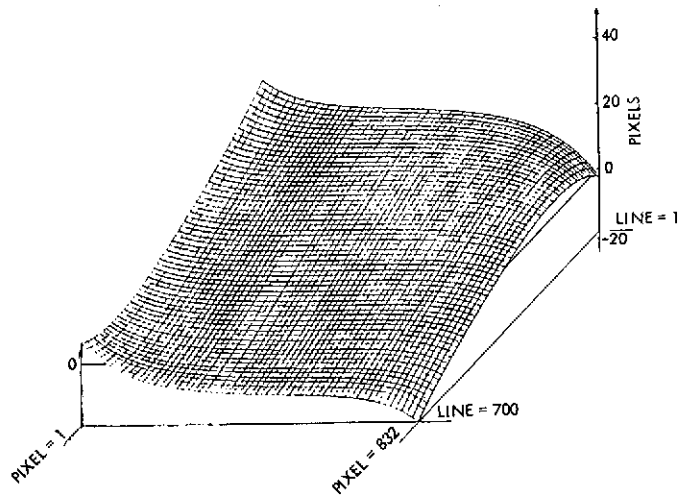
Table 2. Narrow Angle Camera Characteristics

Field of View	= 1.1 × 1.4 deg
Focal Length	= 500 mm
Target Dimensions	= 9.6 × 12.5 mm
No. of Scan Lines	= 700
No. Samples/Line	= 832
Shutter Speed	= Variable - 6 ms to 6.144 s
Resolution	= 6 arc seconds
Pixel Size	= 15 microns
Scanning Spot Size	= 25 microns
Readout Time	= 42 secs

Geometric ground calibration of the narrow angle camera revealed electromagnetic distortion as shown in Figure 1; optical distortion was found to be negligible. The electromagnetic distortion calibration was effected by observing the position changes of reseau marks etched at known locations on the vidicon target. A preliminary light transfer curve was developed for point sources by photographing stars with the prototype camera system. Signal level as a function of star magnitude is shown in Fig. 2⁶ for two values of limit cycle rate which bounded the expected spacecraft performance of about 20 microradians/sec. Each axis of the scan platform was individually ground calibrated to verify the associated math model and to serve as a priori for in-flight calibration sequences.



Geometric Distortion in Line Direction



Geometric Distortion in Pixel Direction

Figure 1. Ground Calibration

An in-flight calibration of the camera and scan platform pointing system was performed forty days prior to Mars encounter. Two sets of thirty-one pictures aimed at star clusters, single stars, Mars and Saturn provided a good set of data for redetermination of electromagnetic and optical distortion, vidicon light transfer and camera pointing in a flight environment. The first set of pictures was targeted at exceptionally bright stars, Saturn and a bright, compact star cluster to insure acquisition of an initial set of data independent of possible system degradation or bias during launch, maneuver, or cruise. These pictures indicated a 0.5 deg. post-launch pointing bias in one axis of the scan platform. A significant change of up to 6 pixels (36 arc seconds) in the electromagnetic distortion, shown in Figure 3, resulted from the absence of Earth's magnetic field and possible movement of the vidicon beam deflection coils. Residual distortion, after fitting the continuous, analytic error model, resulted in a 1σ error of 0.75 pixels with a maximum excursion of 1.8 pixels, Figure 4. Images observed in three areas exhibiting particularly large residual distortion were either ignored or received additional distortion correction using local linear interpolation.

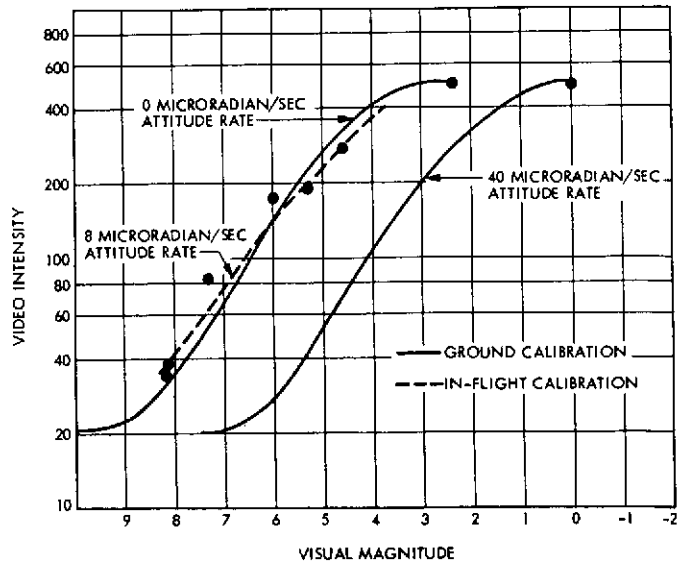


Figure 2. Stellar Light Transfer Curves

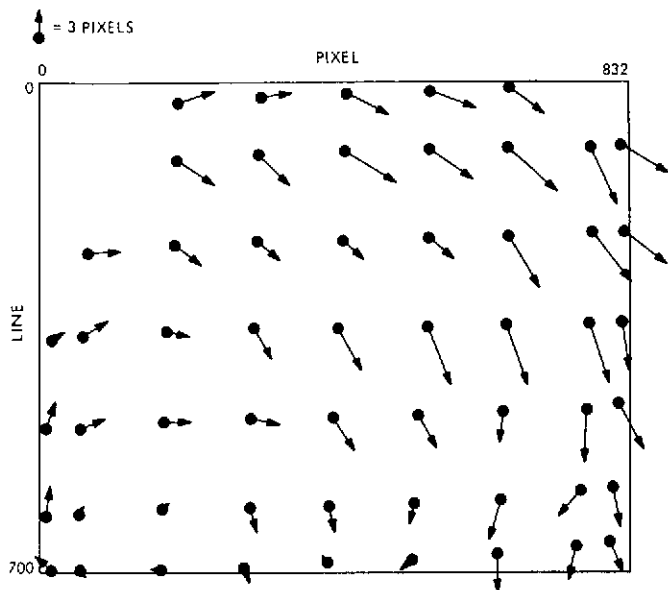
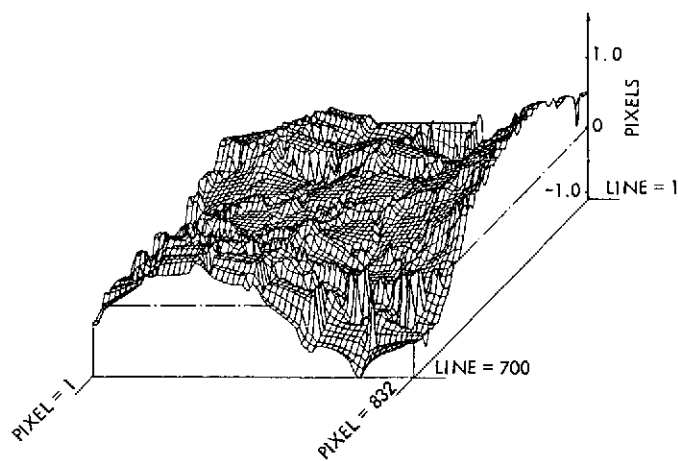
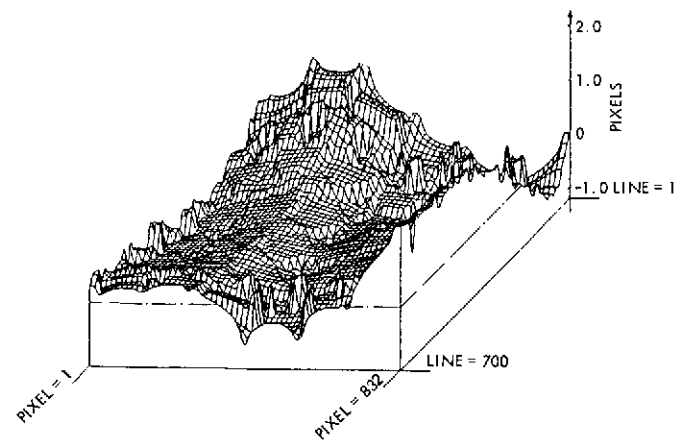


Figure 3. Change in Observed Reseaux Locations



LINE RESIDUALS



PIXEL RESIDUALS

Figure 4. Inflight Calibration

Vidicon sensitivity proved to be significantly greater than expected. Real time processing of video data resulted in detection of stars as dim as magnitude 7.8, while non-real time processing allowed detection of stars of magnitude 8.9. Observed video intensity was seen to be a function of image spot location relative to scanning beam geometry as well as spacecraft attitude rate. Stars of magnitude 0.9 (Altair) and 8.6 are shown in Figure 5 as three dimensional plots. Here, video intensity plotted as a function of location within a 20 x 20 picture element segment of a TV picture provides a visual representation of the dynamic range of star image data.

The initial pointing recalibration and excellent vidicon sensitivity observed in the first set of pictures permitted some retargeting to optimize the second calibration set. Targets for these 31 pictures were selected to require camera pointing over the entire dynamic range of scan platform motion. Two or more star images were detected in 28 of these pictures, while a single image was observed in the remaining 4.

Software Development

The ground based software system performed picture planning, data extraction and data rectification functions. Requirements to process a large volume of data from many sources in a short period of time using a heavily loaded time sharing system indicated a need for simple, flexible and highly automated computer programs.

Picture planning entailed consideration of:

- Spacecraft Trajectory
- Mars Ephemeris
- Phobos and Deimos Ephemerides
- Star Locations (from Smithsonian Star Catalogue)
- Mission Operations Constraints
- Spacecraft Limit Cycle Motion
- Vidicon Characteristics

Planning included pictures of stars for calibration sequences, pictures of Phobos and Deimos against star backgrounds during Mars approach and close range pictures of Phobos and Deimos while in Mars orbit. An example of one form of graphic output from the planning program is shown in Figure 6. This simulated TV picture, scaled to match the size of the mission produced photographs, shows the expected locations of Phobos and 8 stars with associated magnitudes in a picture taken at 14 hours before Mars encounter at a range of 176,752 km. Offsets in the observed positions of the stars result from spacecraft limit cycle motion, while limit cycle, ephemeris error and trajectory error cause offsets in the observed position of Deimos. Each such a priori plot was regenerated after the associated picture was shuttered, based on known camera pointing as obtained from spacecraft engineering telemetry. These overlays were used to help visually locate star images in photographic hard copy.

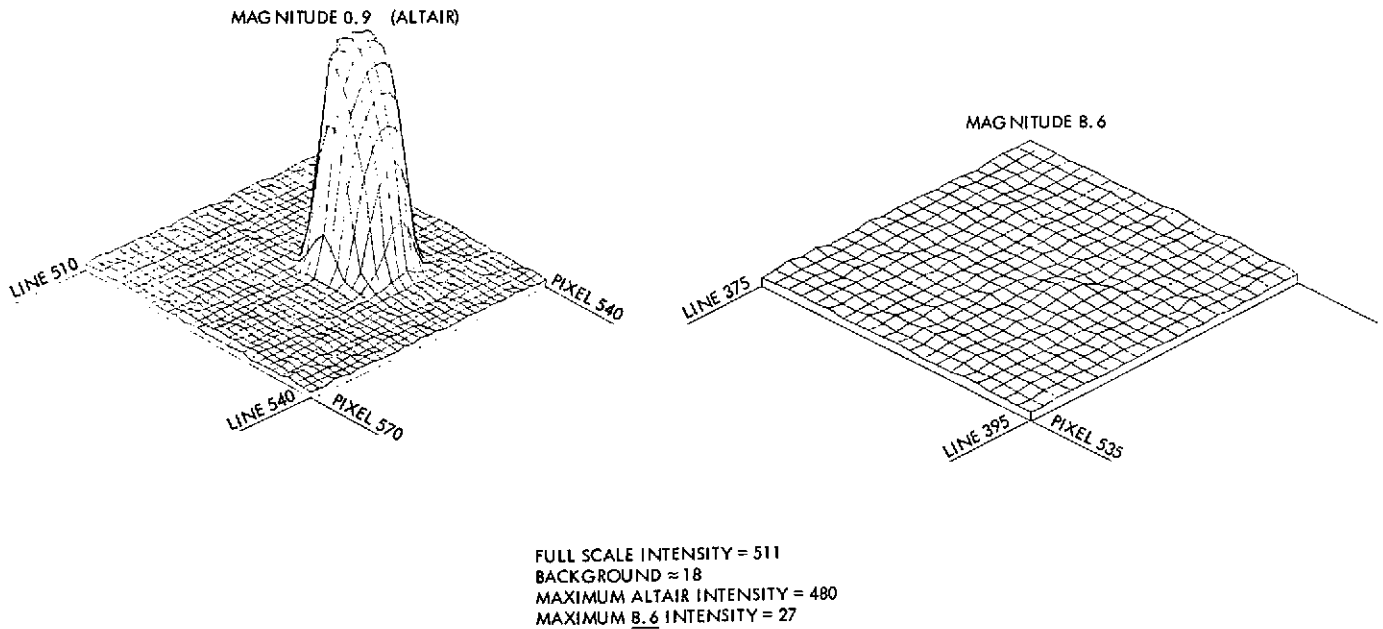


Figure 5. Dynamic Range of Observed Stars

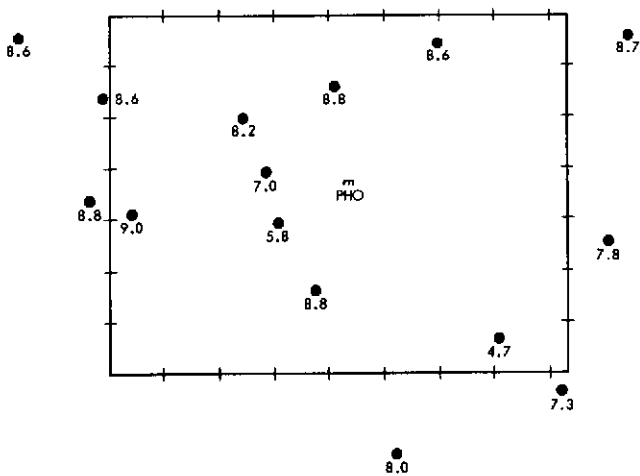


Figure 6. Simulated TV Picture Encounter - 14 Hours

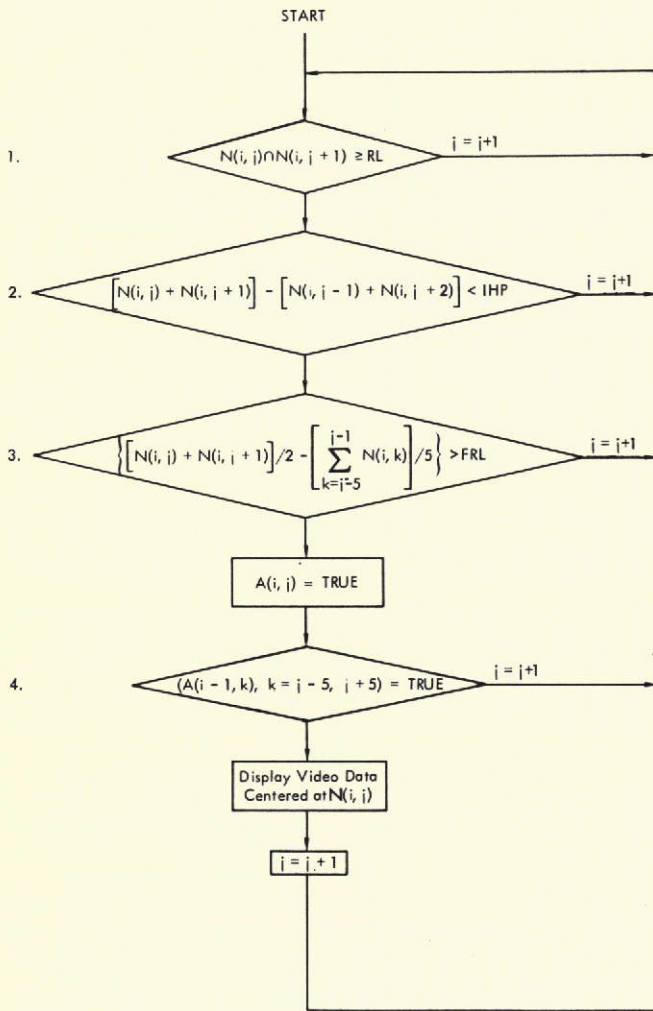
Video data returned from the spacecraft was intermixed with data from other science instruments in the telemetry stream. A two stage computer program comprised of editing and scanning sections was used to process this data. Each video "record" consisted of one line of TV data, preceded by appropriate identification and status tags. Validation and sequence ordering of video records to produce complete digital representations of each TV picture was complicated by missing or duplicated

records, bit errors in the TV line number and the occurrence of pseudo-valid video data inserted in the data stream as a result of the stop and start transients of the spacecraft's tape recorder.

Initial plans for image detection called for the scanning of relatively small (50 x 50 pixels) portions of each TV picture, centered at the expected image locations as calculated by the picture planning program. Experience with processing the calibration sequence pictures revealed the inordinate amount of time required to insure the detection of at least two validated star images in each picture. However, the characterization of video data as obtained from these pictures was used to develop a self-sufficient scanning algorithm.

Detection of a star based on the signal level of a single pixel as compared to the local noise would require a large signal to noise ratio. However, the occurrence of bit errors during transmission to earth causes hundreds of noise spikes exceeding 3σ statistics to occur in each picture, thus eliminating any consideration of dependable and efficient single pixel analysis. Stars as dim as magnitude 8.0 were seen to generally cause a noticeable signal level in two adjacent pixels; this became the basis for automatic image detection. Further signal processing would filter out more types of noise, but would substantially increase the computer time required to process the more than 500,000 video samples in each picture. The algorithms listed below were found to filter out most noise in an acceptable length of time.

Let $N(i, j)$ = the video intensity of the j^{th} video sample on the i^{th} TV line where $0 \leq N(i, j) \leq 511$.



RL, IHP and FRL are parameter values selected by the user. Algorithm No. 1 detects two adjacent pixels (on a given line) with video intensities greater than RL. No. 2 rejects high frequency noise caused by a series of bit errors spanning two adjacent nine bit data words (one data word per video sample). Algorithm No. 3 allows for the dynamic range of dark current (average video level in the absence of external signal) and stray light encountered within a given picture (Figure 8) or from picture to picture. This algorithm requires that the average signal level of the two adjacent pixels be greater than the average of the five previous pixels by an amount greater than FRL. No. 4 eliminates "re-detection" of a given signal when processing the next line of data. Values of RL=25, IHP=200 and FRL=9 were used during Mars approach with good results. Some additional filtering was required to eliminate false signals caused by other peculiarities inherent in the data.

Each signal not rejected triggered a display of the local video data, centered at the location of the "detected" signal (Figure 9). Each 20 x 20 pixel line printer display was visually examined by an analyst who, based on any available a priori information on expected star locations, an understanding of limit cycle motion and possible pointing errors and a knowledge of the general characterization of star images, noise spikes and vidicon target

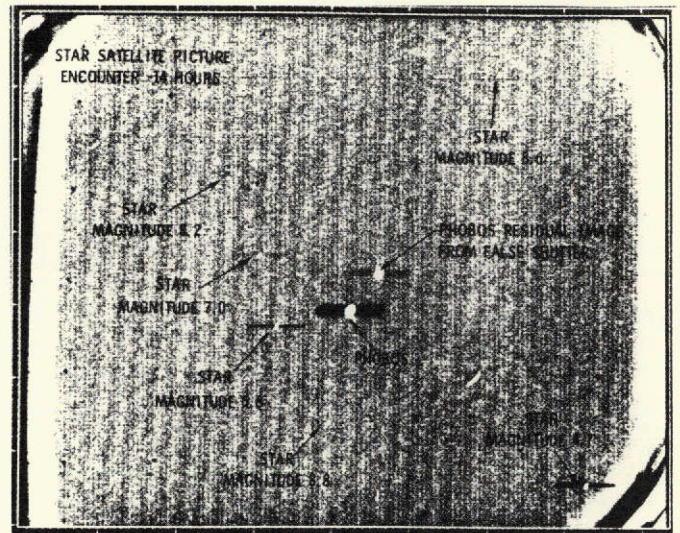


Figure 7. Star-Satellite Picture Encounter - 14 Hours

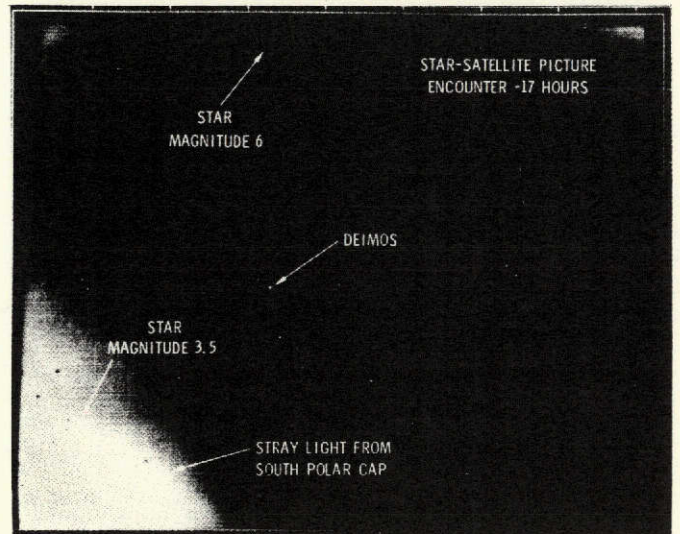


Figure 8. Star-Satellite Picture Encounter - 17 Hours

blemishes, would accept or reject each signal as representing a valid image. Figure 10 shows a video intensity plot corresponding to the data listed in Figure 9. The star of magnitude 8.1 produced a peak signal very nearly the same as that of the noise spike. Selection of this noise as corresponding to the near-by star image could lead to a pointing error of 48 arc seconds.

Image center location was degraded by image blooming, image trailing, vidicon beam deflection and point spread effects. Blooming of about 5 pixels was observed for a moderately bright star (magnitude 4.6), and an image of Phobos subtending 4 pixels produced a substantial signal in 20 pixels (Figure 11). Image trailing, caused by spacecraft limit cycle motion, was usually not noticeable. However, trailing of about 8 pixels was observed in one of the 21 approach sequence pictures, shown here in the image of a star of magnitude 6.2 (Figure 12). Beam deflection and point spread function tended to bias the peak output signal in the low

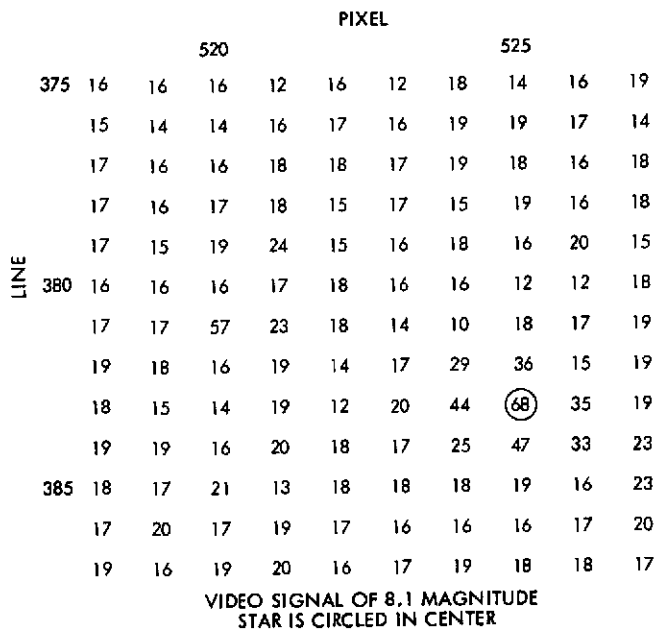


Figure 9. Line Printer Display of Video Data

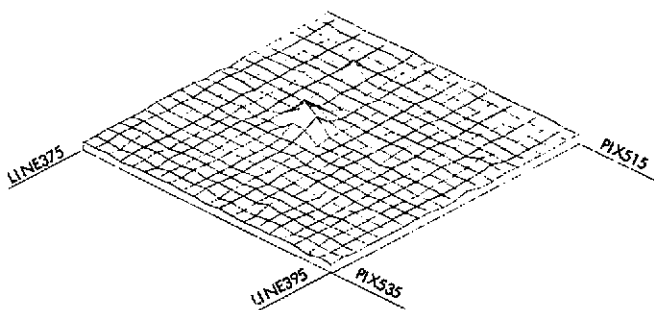


Figure 10. Star (Magnitude 8.1) and Noise Spike

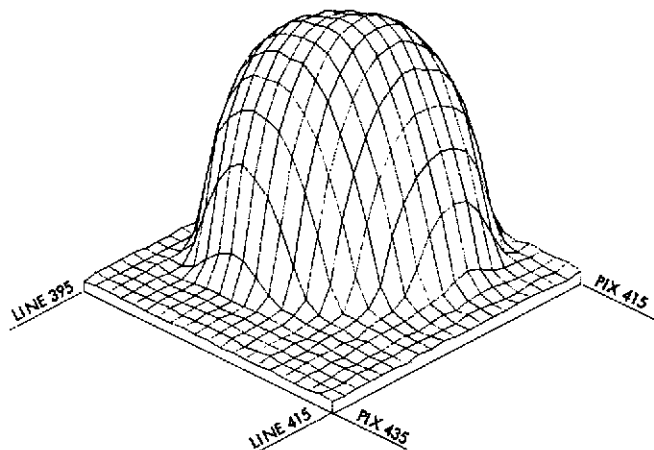


Figure 11. Phobos Image

line/low pixel direction. This effect is shown in Figure 13 where equal intensity contours are plotted for a star of magnitude 6.9. With practice obtained by processing the calibration sequence pictures, the analyst was able to account for these effects when selecting exact image locations; residual location errors were on the order of residual distortion error, 0.7 pixels (1σ).

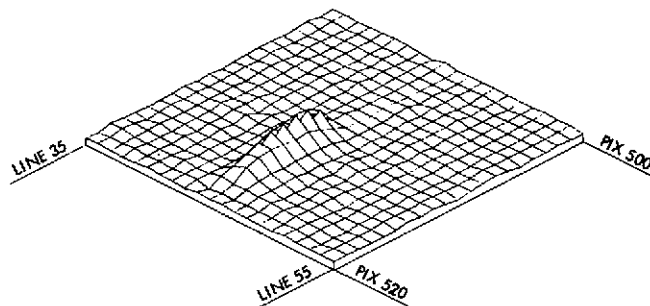
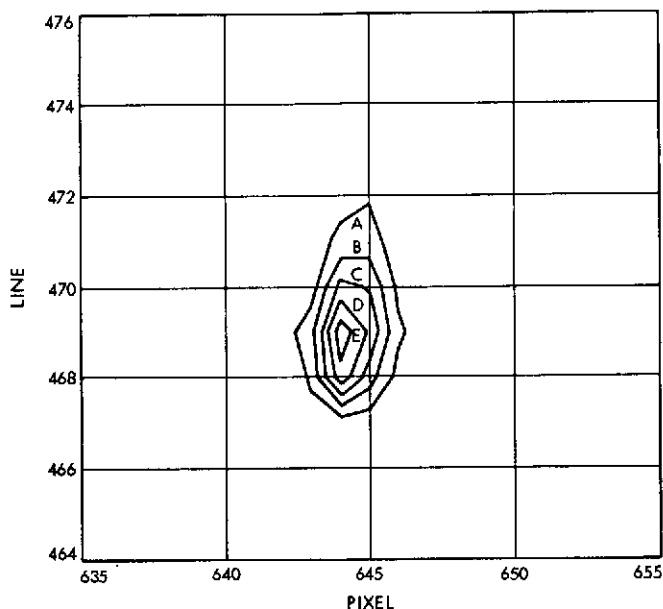


Figure 12. Star Image Showing Trailing



ARC LABEL	CONTOUR VALUE
A	20.000000
B	30.000000
C	40.000000
D	50.000000
E	60.000000

Figure 13. Video Contour Plot of 6.9 Magnitude Star

Optical data rectification could be performed once the required spacecraft engineering data and observed image locations were available. The engineering telemetry, containing limit cycle position and scan platform pointing, was used for a priori camera orientation in the correlation of observed star image locations with expected locations. Star images were used to complete the pointing estimation, and the image location of Deimos or Phobos was corrected for distortion errors. The corrected satellite image location and associated observation statistics, along with the associated partial derivatives, and the expected position of the satellite image based on the best estimate of the spacecraft state, were delivered to the mission navigation programs for combination with radio tracking data prior to trajectory estimation.

System Performance

Eighteen pictures of Deimos and three pictures of Phobos were obtained during Mars approach

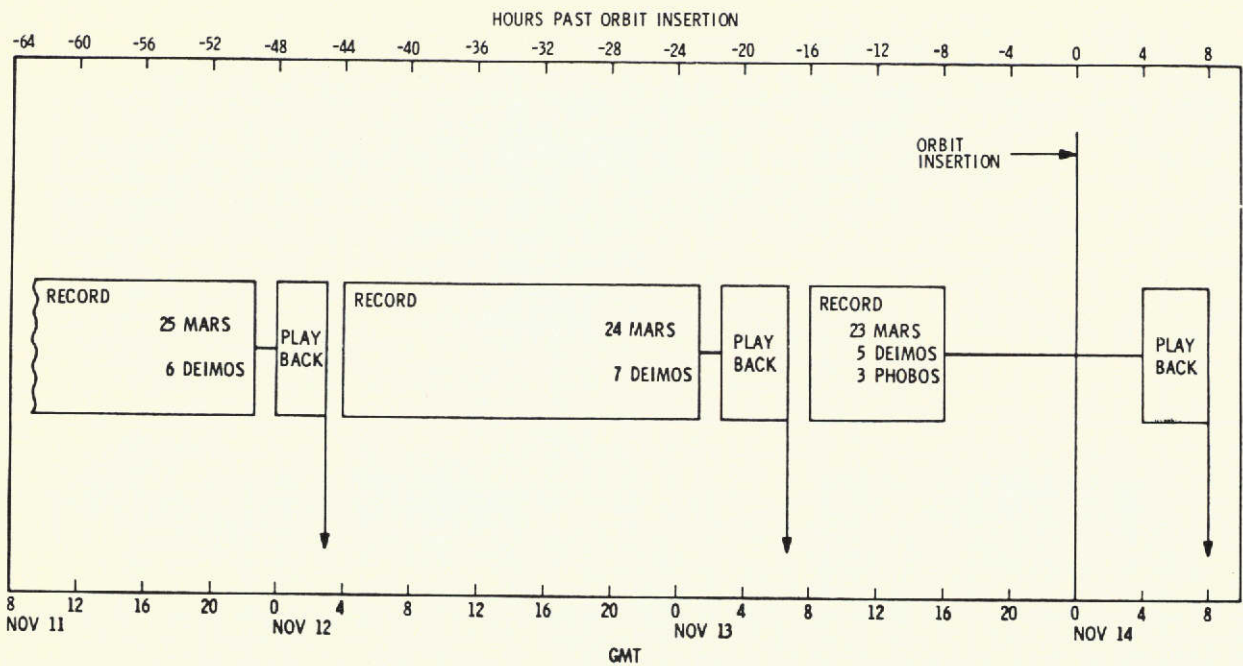


Figure 14. Optical Navigation Pre-Insertion Picture Sequence

(Figure 14). Using a 6 second exposure, the satellite image and at least two star images were found in each of nineteen pictures in near-real time (the remaining two showed Phobos in transit across Mars). The spacecraft trajectory estimates obtained using varying amounts of optical and radio data proved to be extremely accurate.

0.017 deg. (1σ) using the spacecraft celestial attitude sensors (Sun and Canopus) for reference.

Conclusions

The success of pre-insertion satellite pictures was instrumental in decisions to attempt in-orbit imaging of Phobos and Deimos. The planning program used during approach was used in an alternate mode to identify good viewing opportunities. The excellent camera pointing calibration effected prior to insertion was valuable in obtaining and analyzing the close range pictures, an example of which is shown in Figure 15. Aside from their scientific value, these pictures were used to update Phobos' and Deimos' ephemerides. Since no stars were visible (exposures were not more than 48 milliseconds), the calibrated spacecraft math models allowed a posteriori camera pointing accuracy of

The combination of vidicon sensitivity, camera field of view and spacecraft limit cycle rates obtained with the Mariner 9 spacecraft proved to be sufficient for obtaining the required images to produce reliable optical navigation observations. In-flight calibration of spacecraft and TV error models was an integral part of the experiment, allowing a high degree of accuracy and confidence in the results obtained and providing invaluable operational experience with real data. The software required during Mars encounter was considerably more complex than originally designed. Future systems must make extensive use of real-time, interactive programs and I/O devices. Complete or near-complete automation of data extraction, data editing and image identification will significantly reduce the time critical trajectory estimation process. New developments in vidicon and on-board computer technology may allow some amount of video data editing and/or compression prior to transmission to Earth. Such a capability may be essential for missions to the outer planets where data rates will be significantly less than the 16.2 kbs achieved on Mariner 9. Extensive analysis of the data obtained during this mission will conclusively validate the use of star-satellite optical measurements combined with earth based radio tracking for navigation of interplanetary spacecraft.

Acknowledgement

The author is indebted to W. G. Breckenridge, H. Ohtakay and M. H. Bantell of the Jet Propulsion Laboratory for their work in developing many of the computer programs used in the experiment.

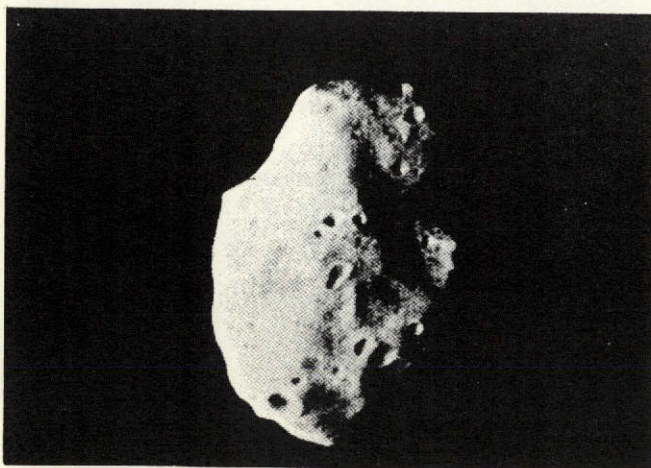


Figure 15. Phobos Picture Taken During Mars Orbit

References

1. Kingsland, Jr., Louis, "Trajectory Analysis of a Grand Tour Mission to the Outer Planets," Presented at AIAA 5th Annual Meeting and Technical Display, Philadelphia, Pa., Oct. 1968.
2. Ball, J. E. and Duxbury, T. C., "Navigating the Grand Tours," *Aeronautics and Astronautics*, Vol. 8, No. 9, Sept. 1970, pp. 73-76.
3. Friedman, L. D., Hamilton, T. W., and Stanton, R. H., "Estimating Trajectory Correction Requirements for the Outer Planets Grand Tour Missions," Paper Presented at the 10th Aerospace Sciences Meeting, San Diego, Calif., January, 1972.
4. Duxbury, T. C., "A Spacecraft-Based Navigation Instrument for Outer Planet Missions," *Journal of Spacecraft and Rockets*, Vol. 7, No. 8, August, 1970, pp. 928-933.
5. Duxbury, T. C. and Ohtakay, H., "In-Flight Calibration of an Interplanetary Navigation Instrument," *Journal of Spacecraft and Rockets*, Vol. 8, No. 10, October 1971.
6. Personal Communications with T. E. Thorpe, Jet Propulsion Laboratory, Pasadena, California.

APPENDIX H

ON-BOARD OPTICAL NAVIGATION DATA FROM MARINER 71

On-Board Optical Navigation Data from Mariner 71*

T. C. DUXBURY and C. H. ACTON, JR.

Abstract

SATELLITE-STAR OPTICAL NAVIGATION, a new spacecraft navigation technique has been successfully demonstrated during Mariner 9's approach to Mars in mid-November of 1971. As Mariner 9 approached Mars, 21 TV pictures of its satellites, Phobos and Deimos, were taken and transmitted to earth. On earth, these pictures were carefully processed in order to locate the positions of the bright satellites against the relatively faint star background. These position fixes were used to obtain more accurate knowledge of Mariner 9's path with respect to Mars and its satellites. The accuracy of the new navigation technique has been confirmed by comparison with the standard radio navigation results on Mariner 9. This successful demonstration of satellite-star optical navigation is the culmination of over 2 years of development work at JPL sponsored by NASA's Office of Aeronautics and Space Technology (OAST). NASA now has developed and demonstrated a prototype of a more accurate navigation system, using on-board measurements, which is essential to meeting the challenging requirements of future missions such as the multi-planet gravity-

assisted outer planet missions. This paper describes the objectives and performance of the pre-flight and real time activities leading to the successful demonstration of satellite-star navigation data.

Introduction

The stringent navigation requirements for proposed future missions make the projected capability of the earth-based radio tracking system marginal or inadequate. This, in turn, has emphasized the need for an on-board system to augment the earth-based system. The earth-based radio system, subject to uncertainties in planetary ephemeris, non-gravitational accelerations and tracking station locations, is expected to have navigational uncertainties of a thousand kilometers or more at the outer planets even with a projected order of magnitude improvement over present capability. Augmenting earth-based measurements with spacecraft-based optical measurements will substantially reduce the navigational uncertainties while giving a highly reliable navigation system.

Future missions with stringent navigational delivery accuracy requirements include the multiple-outer planet missions, the natural satellite rendezvous/orbiter missions, and the comet and asteroid rendezvous missions. Dependable delivery accuracy improvements will reduce mid-course fuel requirements and will make more payload weight available for scientific functions. For orbiter missions, this will increase fuel reserves for orbit trim maneuvers to increase mission coverage or flexibility. Increased orbit determination accuracy during flyby approaches to intermediate and final destination planets has the added potential for increasing the value of scien-

* This paper presents the results of one phase of research carried out at the Jet Propulsion Laboratory, California Institute of Technology, under Contract No. NAS 7-100, sponsored by the National Aeronautics and Space Administration.

The authors are with Jet Propulsion Laboratory, 4800 Oak Grove Drive, Pasadena, Calif. 91103. They presented this paper at The Institute's National Space Meeting in Orlando, Fla. on March 16, 1972.

tific data return by providing a more flexible choice in the selection of aiming zones. This can be realized by relaxing planetary quarantine trajectory constraints and by providing increased accuracy in the selection of pointing directions for scientific instruments.

Initially, on board planet limb measurements were considered as the prime mode for augmenting earth-based radio data to navigate the outer planet missions (Ref. 1). However, planet center finding errors were identified as a major navigation error source for the larger gaseous outer planets including Saturn with its rings (Ref. 2). A new concept of imagining the natural satellites of a target planet against a star field with a science TV camera was developed (Ref. 2) to overcome the planet centerfinding errors. Observations of the motion of the natural satellites are used to estimate the spacecraft trajectory relative to the planet/satellite system center of mass (Fig. 1). This spacecraft-center of mass relationship can be determined even when spacecraft motion is not influenced by the target planet.

Further study revealed that suitable navigation system performance for the outer planet

missions would require satellite/star measurement accuracies to an arc second level (Ref. 3). This level of accuracy was shown feasible (Ref. 4) with the use of a reseau grid to calibrate electromagnetic TV distortion and the use of stars to calibrate optical distortion and inertial TV pointing. Also, the TV would be required to produce identifiable images of stars as dim as 8th magnitude.

The Mariner Mars 1971 (MM'71) mission offered a unique opportunity to test and evaluate the new satellite-star data type prior to when a commitment would be needed to define the on-board data types for the outer planet missions. The Mariner 9 spacecraft carried a narrow angle TV camera (Table 1) capable of simultaneously imaging Phobos or Deimos and stars as dim as 9th magnitude during the approach to Mars. Early in 1970, an Optical Navigation Demonstration (OND) was formed to exploit this unique opportunity.

The OND was a NASA OAST funded R/AD activity which was allowed to operate within the MM'71 mission, but on a non-interference basis. The project was to assist the OND to its fullest

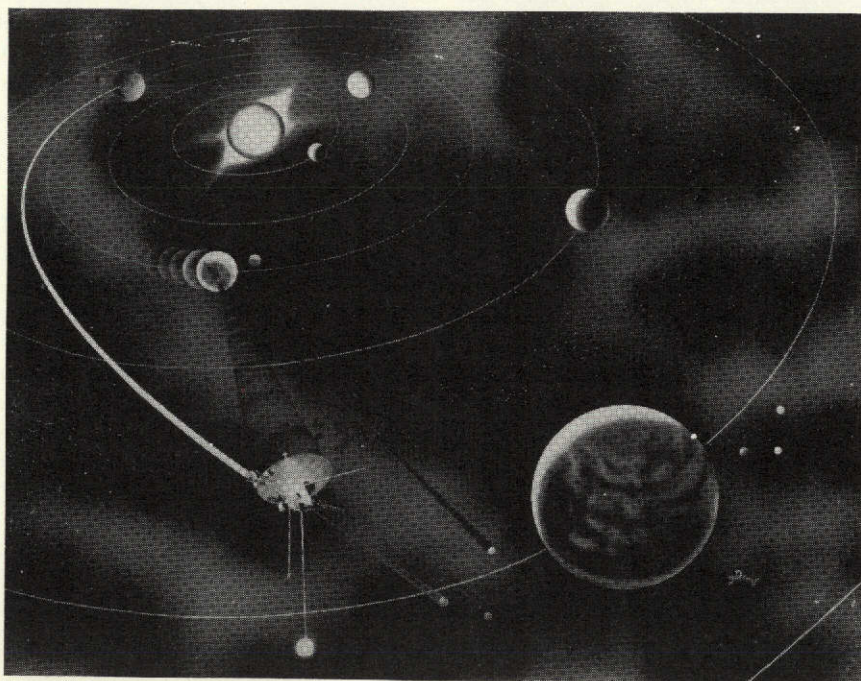


Fig. 1—Spacecraft Relative to Planet/Satellite Center of Mass.

Reproduced from
best available copy.

Table 1—MM'71 Narrow Angle TV Camera

Parameter	Value
Focal Length	500 mm
Angular Field of View	1.1 × 1.4 deg
Scan Lines	700
Pixels/Scan Lines	832
Pixel Resolution	±3 arc sec
Reseau Grid	7 × 9
Exposure Intervals	6 to 6144 ms

capabilities short of jeopardizing its prime objectives and responsibilities. MM'71 accepted the OND data processing software into the Mission Software System and also accepted the OND team as part of the Mission Navigation Team. The OND in turn had no commitment to MM'71 but was to supply information to MM'71 on a best effort basis.

In mid-November as Mariner 9 was inserted into orbit about Mars, the pre-flight and real-time activities of the OND had come to a successful conclusion. The satellite/star TV data concept, including the in-flight calibration (3 arc sec 1σ -Ref. 5), had been demonstrated successfully during real-time mission operations. TV pictures of Deimos with stars were processed and combined with earth-based radio tracking data to produce the most accurate real-time approach trajectory estimate in the history of interplanetary space flight. This estimate was used by MM'71 in the decision processes for the critical orbit insertion maneuver.

The success of the OND was due in part to the great amount of planning, analysis, and training that was performed prior to the real-time operations. The pre-flight activities were jointly formulated and reviewed by the Jet Propulsion Laboratory Navigation Planning Board (JNP). The review board included JPL management from 3 technical divisions, from the R/AD office and from the MM'71 project office. This paper described the objectives and performance of the OND relative to these pre-flight and real-time activities.

OND Objectives

The overall objective of the Optical Navigation Demonstration was to develop and demon-

strate the technology to understand and use on-board optical measurements of natural satellites and reference stars in the near real-time Mariner-Mars 1971 navigation process. This enabling technology will serve as a foundation for the development of navigation systems for future missions. The pre-flight objectives were to develop and document the software, mission interfaces, and analytical understanding needed to perform the near real-time gathering and processing of satellite/star navigation data in conjunction with Earth-based radio tracking data. The real-time approach objective was to use satellite/star data, in conjunction with radio data, to produce approach spacecraft trajectory estimates and associated statistics in a timely manner such that, if used by the Mariner-Mars 1971 Project, the estimates and statistics would be of value to the real-time encounter navigation function.

Software System

In support of the OND pre-flight objectives, a ground based software system (Fig. 2) was developed to gather and process on-board optical navigation data in a near real-time mission environment. This software system additionally supported navigation studies and mission planning and training in advance of obtaining the optical data. These computer programs, although not critical to the success of the mission, were documented, verified, and tested to the MM'71 standards and were placed within the mission controlled software system. The optical software

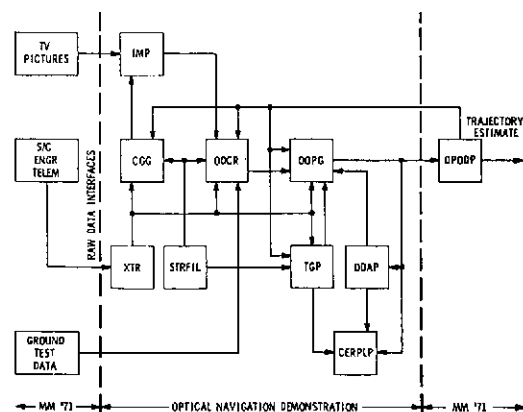


Fig. 2—OND Software System.

system was developed for processing data obtained from Mariner type spacecraft having three axes stabilized attitude, two degree of freedom scan platforms, and vidicon type television cameras. The software was developed to have general application to current and future missions with exceptions where specific raw data interfaces were constrained by MM'71 formats.

Optical navigation observables were developed in terms of an image location in TV picture coordinates, defined by the picture element (pixel) and scan line (line) number. Images of natural satellites, planets, landmarks, stars, and reseaux can be processed by the software system.

Raw data input to the software consists of telemetered TV picture data in digital and hard copy form and telemetered spacecraft engineering data. The software system processes the data and generates an output file which contains optical navigation observables and associated data for use in the JPL navigation program (Double Precision Orbit Determination Program-DPODP). The specific functions of the component programs in this software system are described in the following paragraphs.

The Reduced Star Catalogue Program (STRFIL) scans the 250,000 star Smithsonian Astrophysical Observatory (SAO) star catalogue, contained on magnetic tape, and creates a new catalogue, a subset of SAO, based on user supplied constraints placed on right ascension, declination and visual magnitude. Extractor (XTR) is used to compute the celestially referenced pointing direction of the scan platform at the time a TV picture is taken, based on telemetered spacecraft engineering data (pitch, yaw, roll and scan platform gimbal angles). Output on line printer and punched cards is used as a prior TV pointing data for camera pointing estimation and determination of expected image location. The Celestial Geometry Generator (CGG) combines spacecraft trajectory, satellite ephemeris, star catalogue and camera pointing data to compute a priori star and satellite image locations. Plotted output for each picture scaled to match near real-time hardcopy, assists in locating and identifying observed images.

The Image Processing Program (IMP) is used to search for and graphically display star, satellite, planet and reseaux images contained in the

telemetered TV video data. IMP will automatically scan an entire TV picture, producing a line printer "plot" of video intensity in a 20 line by 20 pixel portion of a picture, centered about each detected bright spot. The Optical Data Calibration and Rectification Program (ODCR) is used to estimate measurement errors and to compute expected image locations, rectified for known errors associated with the TV camera and spacecraft. Observed image locations, expected image locations and partial derivatives of image locations with respect to measurement errors and observation statistics are passed on to the Optical Observable and Partial Generator (OOPG).

The Trajectory Geometry Program (TGP) is used to generate geometric quantities necessary to plan TV picture sequences and process data from these sequences. TGP can operate in an interactive mode to expedite I/O during mission operations. The Optical Observable and Partial Generator (OOPG) Program produces a data file for input to the JPL navigation program DPODP which contains: observed and calculated image locations; time tags; image identification; data weight; and partial derivatives of the optical data with respect to the spacecraft trajectory satellite and planet ephemeris, planet physical parameters, and instrument parameters. The optical data files can be used in a near real or nonreal time navigation process or in a study process.

The Optical Data Analysis Program (ODAP) is an estimation program specifically developed to meet the needs of optical data. ODAP uses a sequential formulation of the minimum variance filter with a generalized consider option. The sequential formulation allows the evaluation of optical data errors which are modeled as exponentially time correlated processes. The generalized consider option allows the evaluation of filter performance in the presence of unmodeled or mismodeled parameters and errors in a priori parameters and data noise statistics. Correlated a priori statistics on parameters and data noise can be accommodated. \bar{B} -Plane and Plane-of-Sky mapping is available. The Celestial and Residual Plot Program (CERPLP) is used to plot optical data (pixel and line) residuals from OOPG and ODAP data files and trajectory (\bar{B} -Plane) estimates obtained from ODAP. CERPLP also plots

spacecraft centered and target centered celestial geometries of spacecraft, planets, natural satellites, stars and landmarks from TGP data files.

The Double Precision Orbit Determination Program capability was expanded to process the new optical data types being supplied by the OND Software System.

Approach Picture Selection

During the 3 day approach period prior to the insertion of Mariner 9 into orbit about Mars, three Pre-Orbital Science picture sequences (POS I, II, and III) were taken (Fig. 3). Each POS sequence covered a 24 hour period with 31 pictures being recorded aboard Mariner 9 and then transmitted to Earth during a 3 hour period near Goldstone (Deep Space Station 14) zenith. Since orbit insertion was performed early in the Goldstone tracking window, the POS III pictures were played back after orbit insertion.

The Mariner project required that a minimum of 24 of the 31 pictures in both POS I and II be used to obtain two full revolutions of Mars surface coverage at 15 deg surface longitude intervals. Also, a minimum of 23 of the 31 pictures in POS III were required for additional Mars surface coverage and for photometric calibration of the wide angle TV camera. Despite the non-interference and non-committal basis with the mission, all but one of the pictures beyond the mission minimum picture requirements were allocated to the OND.

The OND was given complete freedom in selecting the timing, targets, and exposures of its allocated pictures within the constraints that the timing could not interfere with either the Mars pictures (1 hour centers) or the 3 hour playback

periods. With only POS I and II pictures to be played back prior to insertion, it was decided to target all 13 OND pictures in these two sequences on Deimos in order to reduce its ephemeris uncertainty to a level which would not seriously degrade the approach spacecraft trajectory estimates produced during real-time operations. The small angular separation of Phobos and Mars during this period made Phobos an undesirable target because of possible Mars stray light interference. The 8 pictures in POS III were divided between 5 of Deimos and 3 of Phobos.

Criteria for POS I and II picture selection included: 1) obtain a wide coverage of Deimos mean anomaly; 2) minimize spacecraft-Deimos range; 3) include at least 1 star brighter than magnitude 7.8 in each picture; and 4) keep the edge of the TV field of view at least 0.5 deg from Mars lit limb to minimize stray light. Items 2, 3, and 4 generally conflict with item 1. Items 3 and 4 would insure the detection of at least 1 star/picture during real-time operations. Items 1 and 2 would allow the separation of Deimos ephemeris errors from spacecraft trajectory errors.

The inability to accurately control the TV pointing placed the greatest restrictions on the choice of timing and pointing navigation pictures. Spacecraft attitude control dead band limits of ± 0.25 deg in 3 axes and TV pointing step resolution of 0.25 deg in two axes gave a 0.5 deg (3σ) expected control accuracy. A contour showing the probability of actually imaging an object in various areas within the field of view due to the stochastic nature of the TV pointing control error is shown in Fig. 4. These control errors forced pictures to be taken when Deimos was within a few tenths of a degree from a star brighter than magnitude 7.8.

Criteria for POS III picture selection included: 1) fill in gaps of Deimos mean anomaly coverage; 2) have at least 1 star/picture brighter than magnitude 8.5; 3) have at least 1 Phobos transit picture; and 4) relax stray light constraints on camera pointing selection. The POS III pictures, obtained after insertion, were processed on a relaxed time scale allowing more time to find dim stars (item 2). Deimos pictures were still favored in the event of picture loss or data anomalies in the POS I and II sequences. Table II gives a summary of the picture selection.

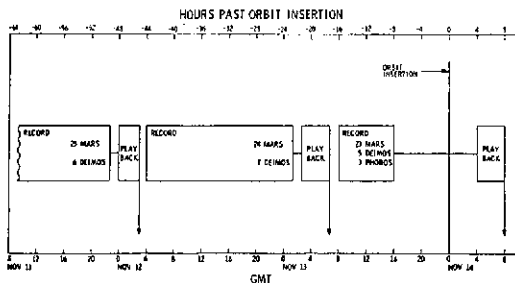


Fig. 3—Pre-Orbital Science Picture Sequence.

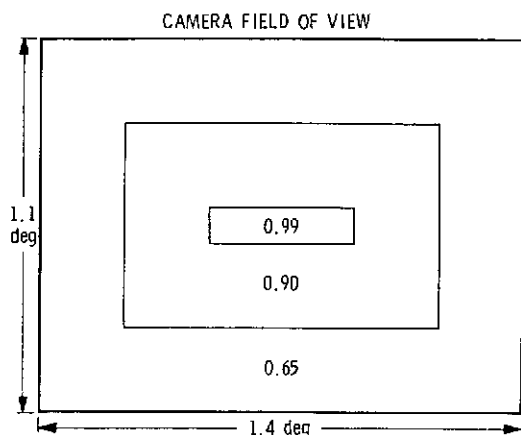


Fig. 4—Imaging Probability Areas.

Operational Activities

Basic to the generation of the trajectory estimates which were delivered to MM'71 in a timely manner were the detailed operational procedures carried out in the gathering and processing of the satellite/star data. The operational activities were centered around the playback periods (Fig. 5). An OND goal was to produce useful approach radio/optical trajectory estimates within 6 hours after the ends of playback. The OND computer programs were scheduled to be run commensurate with this goal, with sufficient time included to set up input/output files between programs, evaluate intermediate data products, and have 3 complete iterations of the data per playback.

Prior to the beginning of playback, TV pointing was determined for the OND pictures. Spacecraft attitude and scan platform telemetry had been transmitted to earth in real-time as each picture was taken. Extracted from teletype printouts, this data was processed by XTR within fifteen minutes to produce a priori camera pointing estimates for each picture. This process was repeated one half hour later, using equivalent data contained on magnetic tape, to verify pointing estimates and to produce a priori input data for ODCR.

The a priori pointing estimates were combined in CGG with the best available spacecraft trajectory and satellite ephemeris estimates to produce plots simulating each TV picture with expected image locations. These plots, produced

in the allotted half hour, were used to assist in identifying images seen on TV monitors during video playback. Also, within this same time interval, TGP produced an input file for OOPG.

During the playback, pictures were displayed on TV monitors in the Navigation Team area as they were received. Image location coordinates of satellites and stars were measured manually from the monitors for backup. These measurements were crude (30 arc sec 1σ) but were generally available 2 to 4 hours before good hardcopy and magnetic tapes with digital video data were available. These crude measurements were input to OOPG/ODAP/CERPLP within 30 minutes after playback to obtain a quick look at the data and resultant spacecraft trajectory and satellite

Table II—Approach Satellite Coverage

POS	Satellite	Hours Before Insertion	Mean Anomaly-deg
I	Deimos	66.0	95
I	Deimos	59.0	180
I	Deimos	57.0	204
I	Deimos	55.0	228
I	Deimos	54.0	243
I	Deimos	53.0	256
II	Deimos	36.0	92
II	Deimos	35.0	104
II	Deimos	34.0	116
II	Deimos	29.0	176
II	Deimos	28.0	190
II	Deimos	26.0	212
II	Deimos	22.0	271
III	Deimos	16.5	325
III	Deimos	16.4	327
III	Phobos	14.0	130
III	Phobos	12.6	186
III	Phobos	12.5	194
III	Deimos	12.0	18
III	Deimos	10.0	43
III	Deimos	9.0	59

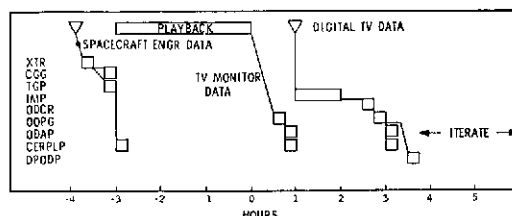


Fig. 5—Operational Sequence.

parameter estimates within 1 hour after playback.

After completion of playback, four magnetic tapes containing digital data for the 31 pictures were made available to the experiment. The image processing program was initially allotted one hour to locate an average of three images in each of the six to eight star/satellite pictures. Due to real-time changes in the mission plan and the ease in identifying images of stars brighter than magnitude 8.5, the optical navigation experimenters elected to allot more time to the location and identification of star images in order to improve the real-time trajectory estimate. Video processing was delayed by late delivery of the required tapes. Once available, an average of 4 images per picture for 7 pictures were located and identified within 84 minutes. This process involved accessing over 5 million bits per picture for an average of 18 pictures in order to locate the appropriate data, followed by actually scanning and comparing over 582,000 video samples in each of the star/satellite pictures.

Using XTR computations a priori, ODCR used all available star images to calculate the celestially referenced TV pointing for each picture. ODCR required 20 minutes to reduce pointing errors to less than 3 arc seconds for 7 pictures by including an accurate, analytic model of TV electromagnetic distortion. Included in ODCR's estimation was the updating of the measurement error model parameters.

The OOPG/ODAP/CERPLP combination produced a verified optical data file for input into DPODP within 20 minutes of receipt of the ODCR file. The verification included making a spacecraft trajectory and satellite ephemeris estimate and the evaluation of optical data residuals after the fit. No data anomalies or non-linearities were found, eliminating the need for additional iterations of the data. Various DPODP runs were made during the remainder of the six hour period. The results of processing POS I data were used to change the pointing of POS II and III pictures to maximize satellite/star data content.

Trajectory estimates using both radio and optical data were made available to the mission at 40 hours and 12 hours prior to orbit insertion. These estimates differed by only 50 km from the radio only estimate used in the computation of

the orbit insertion maneuver at 5 days prior to insertion. This closeness coupled with the radio only estimate moving to within 30 km of the radio/optical solution at 12 hours before insertion gave the mission the necessary confidence to go with the maneuver already stored in Mariner 9.

System Calibration

Considerable effort was expended to plan, obtain and process ground and inflight calibration data. These exercises served to verify program interfaces and provide operational training as well as fulfilling system calibration requirements. Ground calibration of TV distortion verified the analytic distortion model and served as a priori for the critical inflight calibration performed outside of earth's magnetic field. Ground calibration of the scan platform and attitude sensors provided enough pointing control to allow acquisition of inflight calibration targets. Pictures of stars taken from earth with a prototype camera provided initial stellar sensitivity information (Fig. 6). Predictions of the limiting star magnitude that could be detected during real-time operations, Table III, were based on this data and were used in initial Mars approach sequence picture planning.

Inflight calibration, performed one month prior to arrival at Mars, was conducted in two parts. An initial set of 31 pictures was targeted at five bright targets. Camera pointing control and vidicon sensitivity were verified. Large scan platform slews were seen to have little long term

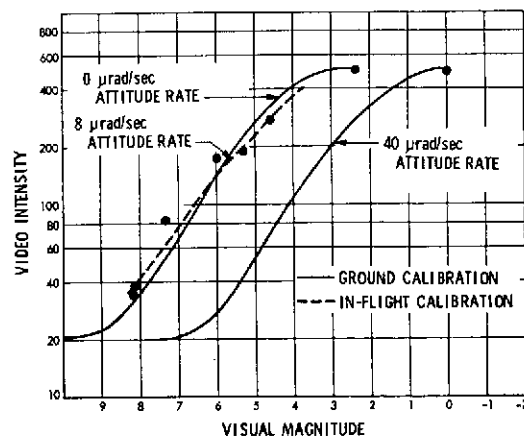


Fig. 6—Stellar Light Transfer Curves.

Table III—Predicted System Sensitivity to Stars

	Spacecraft Attitude Rate	Limiting Real Time System Sensitivity	Uncertainty (1σ)
Pre-scan calibration	20 μ r/sec	$V_m = 6.5$	0.3
Post-scan calibration	20	7.8	0.3
	15	8.0	0.4

effect on spacecraft attitude motion; rates of 8 microradians per second were average. Consequently, targets for the second set of 31 pictures covered the entire range of scan platform motion and included stars as dim as 6th magnitude. Mean pointing control was found to be 0.6 degrees, while mean pointing knowledge uncertainty when using celestial sensors for reference was reduced to 0.03 degree (1σ). Stars of magnitude 8 were easily found, while stars as dim as magnitude 9 could be seen in computer enhanced picture provided by JPL's Image Processing Laboratory. The calibration residuals had a sigma of 0.75 pixels (1 pixel = 6 arc sec) with a maximum deviation of 1.8 pixels (Fig. 7).

Real-time data processing results met or exceeded predicted performance. Pointing control, data noise and biases, image location residuals, satellite ephemeris uncertainties and spacecraft trajectory estimates were evaluated using in part, the approach satellite/star picture data listed in Table IV. Included in this table are:

1. Desired pointing (clock and cone, Fig. 8) for each picture
2. Pointing obtained, based on celestial sensor telemetry
3. Pointing obtained, based on observed star images
4. Pointing control (3. - 1.)
5. Pointing knowledge using celestial sensors (2. - 3.)
6. Statistics on best pointing knowledge (star location residuals)

The pointing control realized for the satellite/star pictures had a mean and sigma of $\mu = 0.0235^\circ$, $\sigma = 0.169^\circ$ in the clock axis and $\mu = -0.0013^\circ$, $\sigma = 0.155^\circ$ in the cone axis, meeting the mission requirement of 0.5° , 3σ . Although cone axis performance suffered from a hysteresis

effect observed in scan platform cone motion, all primary target images were successfully obtained as a result of the picture planning strategy.

Attitude sensor (pitch, yaw, roll) limit cycle noise, composed of sensor noise, calibration errors and telemetry quantization, was evaluated using blocks of Mars pictures taken at fixed scan platform settings, thus eliminating scan platform noise. The predicted 1σ values using no limit cycle fitting map into 0.0144 deg in cross-cone and 0.0060 deg in cone. The pointing error uncertainty was evaluated for each block. As shown in Table V, the predicted attitude uncertainty in both axes compares favorably with the mean observed error, the maximum excursion being 1.3σ .

Scan platform gimbal noise was observed in the pointing errors associated with the approach sequence satellite pictures, taken over a moderate range of scan platform gimbal angles. Attitude sensor noise is included in these measurements, but is from one to two orders of magnitude less. Observed 1σ cross-cone and cone noise values are compared in Table VI with predicted values obtained by mapping predicted pitch, yaw, roll and scan gimbal noise into cross-cone and cone. Cross-cone axis noise was a factor of two smaller than predicted, while cone axis noise was slightly larger than expected, due to the hysteresis effect.

Predicted scan platform bias uncertainty esti-

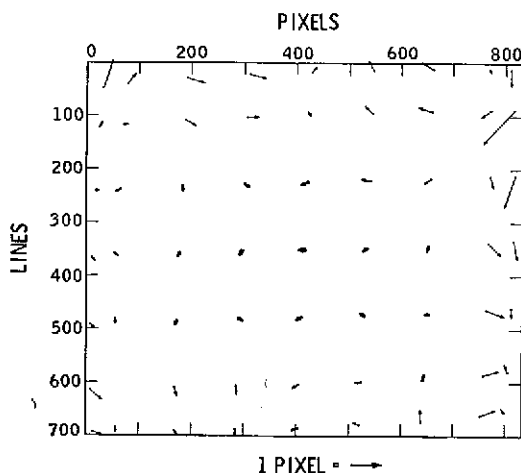


Fig. 7—Reseau Residuals after In-Flight Calibration.

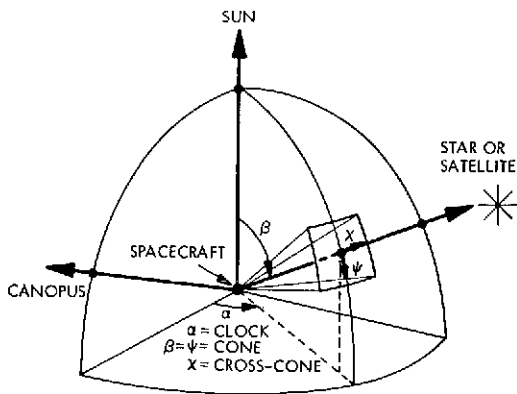
Table IV—Mars Approach Data Summary

Pic. No.	1.	2.	3.	4.	5.	6.	
	Desired (Clock Cone)	Obtained (Engineering Telemetry)	Obtained (Star Images)	Control (3. - 1.)	Inertial Knowledge (2. - 3.)	No. of Stars	Star Location Residuals
1	96.80 Degrees	96.635	96.641	-0.159	-0.006	2	0.50 pixels
	121.20 Degrees	121.331	121.306	+0.106	+0.025		0.48 pixels
2	97.90	97.966	97.985	+0.085	-0.019	2	0.31
	118.30	118.313	118.329	+0.029	-0.016		0.36
3	97.90	97.837	97.830	-0.070	+0.007	3	0.78
	118.00	117.729	117.738	-0.262	-0.009		0.86
4	97.80	97.956	97.963	+0.163	-0.007	4	0.16 0.13
	117.60	117.722	117.705	+0.105	+0.017		0.54 0.55
5	97.70	97.725	97.757	+0.057	-0.032	2	0.30
	117.50	117.295	117.281	-0.219	+0.014		0.24
6	97.60	97.382	97.385	-0.115	-0.003	4	0.66 0.18
	117.50	117.361	117.345	-0.155	+0.016		0.59 0.43
7	97.20	97.454	97.444	+0.244	+0.010	2	0.14
	121.15	121.338	121.348	+0.198	-0.010		0.16
8	97.40	97.634	97.625	+0.225	+0.009	4	0.75 0.59
	121.00	120.831	120.850	-0.150	-0.019		0.42 0.64
9	97.50	97.475	97.491	-0.009	-0.016	2	0.76
	120.80	120.636	120.650	-0.150	-0.014		0.83
10	99.20	99.025	99.023	-0.177	+0.002	2	1.16
	116.80	116.666	116.675	-0.125	-0.009		1.13
11	99.30	98.961	98.975	-0.325	-0.014	2	0.49
	116.30	116.286	116.289	-0.011	-0.003		0.43
12	99.20	99.160	99.201	+0.001	-0.041	2	0.59
	115.90	116.078	116.095	+0.195	-0.017		0.58
13	97.80	97.427	97.434	-0.366	-0.007	3	0.65 0.52
	115.60	115.823	115.876	+0.276	-0.053		0.45
14	96.35	96.300	96.318	-0.032	-0.018	2	1.42
	120.35	120.246	120.271	-0.079	-0.025		1.44
15	96.35	96.028	96.015	-0.335	+0.013	3	0.30 0.30
	120.60	120.523	120.529	-0.071	-0.006		0.02

Table IV—Continued

Pic. No.	1.	2.	3.	4.	5.	6.	
	Desired (Clock Cone)	Obtained (Engineering Telemetry)	Obtained (Star Images)	Control (3. - 1.)	Inertial Knowledge (2. - 3.)	No. of Stars	Star Location Residuals
16	98.40	98.296	98.279	-0.121	+0.017	4	0.30 1.27
	122.40	122.448	122.408	+0.008	+0.040		0.83 1.45
17*	99.70	99.542	—	—	—	—	—
	120.10	120.103	—	—	—		—
18*	99.70	99.361	—	—	—	—	—
	120.10	120.188	—	—	—		—
19	95.00	95.131	95.148	+0.148	-0.017	3	0.83 0.48
	126.60	126.827	126.780	+0.180	+0.047		0.96
20	96.00	96.100	96.104	+0.104	-0.004	1	0.12
	130.95	130.107	130.077	+0.127	+0.020		
21	96.75	96.962	96.985	+0.235	-0.023	1	0.10
	132.80	132.759	132.774	-0.026	-0.015		
				$\mu = -0.0235$ $\mu = -0.00126$ $\sigma = 0.169$ $\sigma = 0.155$	$\mu = -0.00784$ $\mu = -0.000895$ $\sigma = 0.0117$ $\sigma = 0.0247$	$\mu = 0$ $\sigma = 0.403$ pixels	

* Phobos Transit Across Mars
No Stars Visible



SCAN PLATFORM'S CLOCK/CONE SYSTEM REFERENCED TO SUN AND CANOPUS CROSS-CONE/CONE SYSTEM REFERENCED TO SCAN PLATFORM

Fig. 8—Clock and Cone Angle TV Pointing System.

Table V—1 σ Attitude Sensor Noise

	Predicted	Observed	
		Mean	Sigma
Cross-Cone	0.0144°	0.0064°	0.0063°
Cone	0.0060°	0.0060°	0.0048°

imates compared favorably with real-time estimates made during the spacecraft calibration sequence and the Mars approach sequence, Table VII. These estimates are seen to vary directly with the number of parameters estimated due to high correlation coefficients. Degradation of Mars approach a posteriori uncertainties relative to those obtained during the inflight calibration resulted from the limited amount of

Table VI—1 σ Scan Platform Gimbal Noise

	Predicted	Observed
Cross-Cone	0.021°	0.0117°
Cone	0.021°	0.0247°

Table VII—1 σ Scan Platform Bias Uncertainties

	Spacecraft Calibration		Mars Approach	
	Predicted	Observed	Predicted	Observed
Cross-Cone	0.003	0.003	0.005	0.005
Cone	0.003	0.0025	0.005	0.0046
Rotation	0.03	0.022	0.05	0.032

tude sensor and scan platform gimbal errors from camera pointing estimates; residual TV distortion and image center finding or readout error remained. Predicted 1 σ uncertainties mapped into 0.77 pixels per axis. Observed mean star image residuals for pictures containing 3 or more stars were 0.403 pixels per axis. This excellent real-time performance using the primary observable types led to highly accurate spacecraft trajectory estimates.

Navigation

Covariance analyses and data simulations were performed to develop a detailed understanding of the MM71 navigation system performance using satellite/star data and radio data. Results were used to minimize the operational activities needed to support the processing of the radio and optical data. The studies revealed that a short arc of radio data (within 5 days of orbit insertion) was sufficient to allow the combined radio/optical performance to obtain its full accuracy potential during the approach to Mars.

data obtained during the approach sequence and a decision to degrade the a priori estimates to allow for possible bias changes during the intervening month.

The observation of stars in the approach sequence satellite pictures, Fig. 9, eliminated atti-

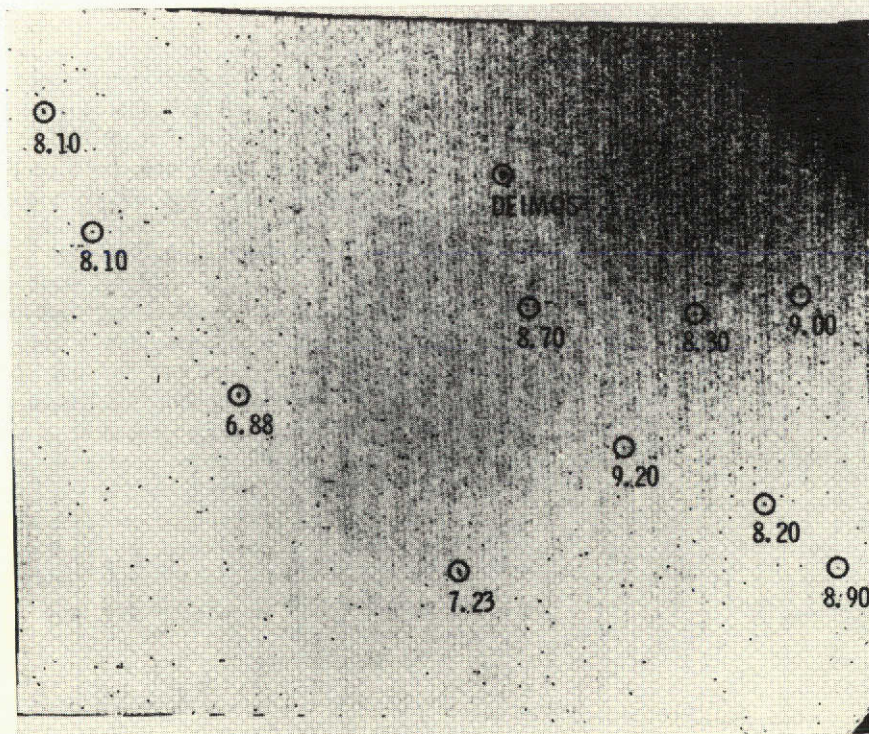


Fig. 9—Approach Deimos/Star Picture.

Reproduced from best available copy.

Using the short arc of radio data with the optical data eliminated the need to estimate earth-based tracking station locations, Mars ephemeris, and non-gravitational forces. It was found that a negligible degradation to the trajectory accuracy would be obtained by not estimating the longitude of ascending node and argument of periapsis of Deimos' orbit, which is near circular with a small inclination to Mars equator.

During real-time operation, therefore, only the spacecraft state, four Deimos orbital elements (a, e, M_0, i) Mars GM and J_2 , and three camera pointing errors were estimated. The behavior of the estimates of GM and J_2 , whose values were accurately known, were used to indicate the presence of unmodeled parameters or data anomalies. In determining the expected approach trajectory accuracy for the above parameter assumptions, it was assumed that: 1) only 9 of the 13 pictures in POS I and II would be processed in real-time; 2) only 1 star brighter than magnitude 7.8 per picture would be found during real-time operations; and 3) a measurement accuracy of 6 arc-sec (1σ) would be achieved. The anticipated loss of 4 pictures during real-time operations was based on a combination of TV pointing control errors, Deimos ephemeris uncertainties and operational difficulties in data interfaces. These assumptions resulted in an expected \bar{B} -Plane (Fig. 10) trajectory accuracy of 40×30 km 1σ (Fig. 11).

During real-time operations, 12.8 of the 13 POS I and II pictures were obtained and processed. Unfortunately, the 0.2 picture lost con-

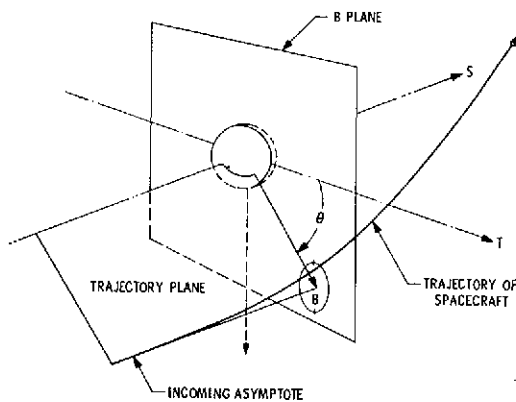


Fig. 10—B-Plane.

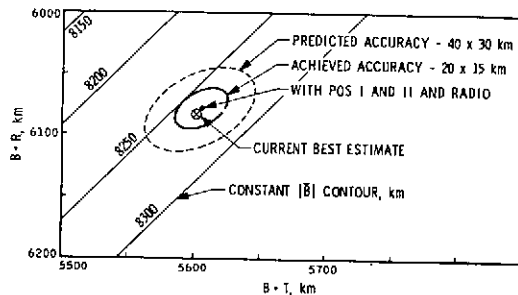


Fig. 11—Real-Time OND Results.

tained that picture's image of Deimos. An average of 2.5 stars/picture were found and a measurement accuracy of 3 arc-sec (1σ) was achieved. The real-time achieved \bar{B} -Plane accuracy of 20×15 km 1σ (Fig. 11) was comparable to the expected post flight accuracy when time for data processing was not a constraint. Also, a 400 km position correction was determined for Deimos. There were no data or model anomalies during real-time operation and the data residuals after the fit were 3 arc sec (1σ) for both the satellite and star data.

Conclusions

The OND has conclusively validated the new satellite/star navigation data in combination with radio data in the real-time MM'71 environment. The real-time performance of the combined radio/optical navigation process was more accurate than predicted. Continuous, analytic math models, calibrated with in-flight pictures of reseau and stars, provided excellent accuracy and operational simplicity in modeling error sources arising in the television, celestial sensors and spacecraft static and dynamic structures. Inflight calibration provided valuable operational training and procedures verification as well as the necessary math model parameter estimates. Three sigma pointing control of one half degree coupled with vidicon sensitivity sufficient to detect stars of magnitude 8.5 insured the real-time detection of at least one and generally several stars in each satellite picture.

Acknowledgement

The authors wish to recognize the outstanding efforts of the following OND team members: M. P. Anada, M. H. Bantell, G. H. Born, W. G.

Breckenridge, N. Jerath, H. Ohtakay, and G. A. Ransford. We would also like to express our appreciation to the MM'71 project for their complete cooperation, without which a meaningful OND would not have been possible.

References

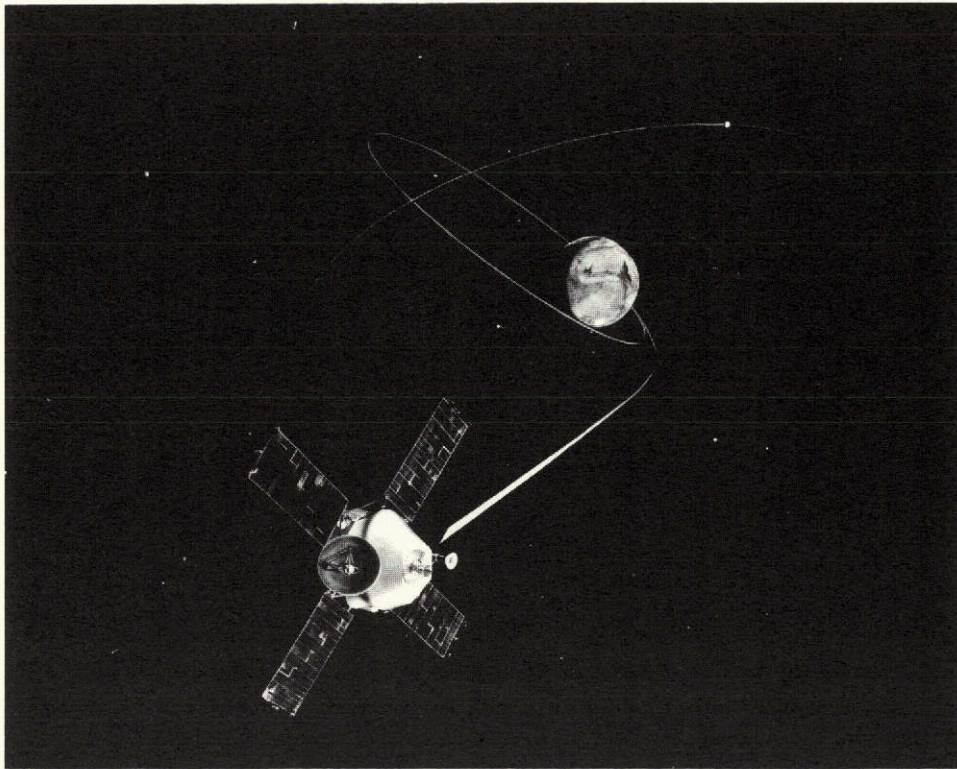
1. Kingsland, L., "Trajectory Analysis of a Grand Tour Mission," *Journal of Spacecraft and Rockets*, Aug. 1969, pp. 897-902.
2. Duxbury, T. C., "A Spacecraft Based Navigation Instrument for Outer Planet Missions," *Journal of Spacecraft and Rockets*, Vol. 7, No. 8, August 1970, pp. 928-933.
3. Ball, J. E. and Duxbury, T. C., "Navigating the Ground Tours," *Aeronautics and Astronautics*, Vol. 8, No. 9, Sept. 1970, pp. 73-76.
4. Duxbury, T. C., and Ohtakay, H., "In-Flight Calibration of an Interplanetary Navigation Instrument," *Journal of Spacecraft and Rockets*, Vol. 8, No. 10, October 1971, pp. 1038-1042.
5. Acton, C. H., "Processing On-Board Optical Data for Planetary Approach Navigation," *Journal of Spacecraft and Rockets*, Vol. 9, No. 10, October 1972, pp. 746-750.

APPENDIX I
VIEWING PHOBOS AND DEIMOS FOR NAVIGATING MARINER 9

146<

Sponsored by —
American Astronautical Society (AAS)
American Institute of Aeronautics and Astronautics (AIAA)

AIAA Paper
No. 72-927



VIEWING PHOBOS AND DEIMOS FOR NAVIGATING
MARINER 9

by
T. C. DUXBURY, G. H. BORN,
and
N. JERATH
Jet Propulsion Laboratory
Pasadena, California

AIAA/AAS Astrodynamics Conference

PALO ALTO, CALIFORNIA / SEPTEMBER 11-12, 1972

First publication rights reserved by American Institute of Aeronautics and Astronautics,
1290 Avenue of the Americas, New York, N. Y. 10019. Abstracts may be published without
permission if credit is given to author and to AIAA. (Price: AIAA Member \$1.50. Nonmember \$2.00).

Note: This paper available at AIAA New York office for six months;
thereafter, photoprint copies are available at photocopy prices from
Technical Information Service, 750 3rd Ave., New York, N. Y. 10017

Viewing Phobos and Deimos for Navigating Mariner 9*
T. C. Duxbury, G. H. Born and N. Jerath
Jet Propulsion Laboratory
Pasadena, California

Abstract

A new on-board optical navigation data technique has been successfully demonstrated on Mariner 9. Science TV pictures of Phobos and Deimos against star fields were used in the real time navigation process to insert Mariner 9 into orbit about Mars. Real time and post flight evaluation results have shown that the satellite/star data taken by Mariner 9 was more accurate than preflight analysis indicated. In fact the orbital insertion phase of the mission could have been achieved using only optical data to determine encounter parameters. The use of a science TV camera to obtain this data was successfully demonstrated. Stars as dim as 9th magnitude were detected and measurement accuracies of 3 arc sec (1σ) were achieved. The success of the optical navigation techniques developed for Mariner 9 has placed a new class of demanding missions (e. g., multiple outer planet, satellite tour, etc.) within realized navigation capability.

I. Introduction

A new on-board optical navigation data technique has been proposed for use on outer planet missions (Ref. 1). The technique uses a television camera to view natural satellites against a star background during planetary approach. An in-flight pointing and geometric calibration of the TV was proposed to obtain an optical data accuracy of 5 arc sec (1σ) (Ref. 2). Stars as dim as 8th magnitude must be detectable to insure star availability for any arrival geometry. The Mariner Mars 1971 mission offered a unique opportunity to demonstrate this new technique during flight operations before committing future missions to its use. Every aspect of this technique was demonstrated to be feasible during MM'71. This paper presents the results of the post flight evaluation of the satellite/star on-board optical navigation data taken during the approach phase of MM'71.

During Mars approach, Mariner 9 transmitted 13 pictures of Deimos and stars. Five approach pictures of satellite were transmitted after insertion. Before this time, the TV had been calibrated and furthermore had detected 9th magnitude stars. During real time mission operations, the Deimos/star data was combined with radio tracking data to produce the most accurate trajectory estimate ever obtained during interplanetary flight operations. An optical data accuracy of 3 arc-sec (1σ) was achieved. The proposed optical navigation

technique including instrumentation as successfully demonstrated beyond expectation during real time mission operations. Since then, a thorough evaluation of the optical data taken during approach has been performed. It was found that optical navigation alone would have been adequate to insert Mariner 9 into orbit about Mars within mission accuracy requirements. Post flight evaluation has shown that only one star per picture was required to yield the full accuracy potential of the optical data. A few days of radio doppler data combined with the optical data yielded the full accuracy potential of the combined optical/radio data. Satellite data, as expected, was found to be superior over Mars limb data for approach navigation. Also, star images in the flight picture were sufficient to perform the pointing and geometric calibration of the TV for navigation, independent of other ground or in-flight calibration data.

Details of the TV calibration for navigation are given in Refs. 3 and 4. Details of the data processing software and mission operations are given in Ref. 5.

II. Source of Optical Data

The narrow angle science television camera was the source of the optical navigation observations for MM'71. The narrow angle TV has a 500 mm focal length with $f/2.5$ Schmidt-Cassegrain optics. A selenium-sulfur vidicon tube with a 7 x 9 reseau grid was used. A 9.6 x 12.5 mm area on the vidicon target was scanned with a resolution of 700 scan lines and 832 picture elements (pixels) per scan line. The active area of the vidicon target gave a 1.1 x 1.4 deg field of view with a pixel resolution of ± 3 arc sec. The video intensity of each pixel was digitized to 9 bits. Each picture element, therefore, would be defined by its pixel number (1 to 832), its line number (1 to 700) and its intensity (0 to 511).

The narrow angle camera can be shuttered on increments of 84 seconds allowing sufficient time for a picture to be readout and recorded. Exposure may be ground commanded from 0.06 to 6.144 seconds enabling stars as dim as 9th magnitude to be detected.

III. Optical Data Errors

Optical data errors are classified as instrument and model errors. Instrument errors include TV distortions, TV pointing errors, image center-finding errors and random measurement errors.

* This paper presents the results of work carried out at the Jet Propulsion Laboratory, California Institute of Technology under Contract No. NAS 7-100, approved by the National Aeronautics and Space Administration.

TV distortion errors corrupt the relative geometry of images within a picture. It is caused by non-uniform deflection fields which in turn sweep the electron readout beam across the vidicon target non-uniformly. TV distortion causes image location errors in raw data of a few pixels near the center of the vidicon to tens of pixels near the edges of the vidicon. This distortion is accurately modeled as a 6th order polynomial of the radial distance from the center of the vidicon (Ref. 4). Either reseau or star images may be used to calibrate TV distortion. Distortion from the optics is negligible.

TV pointing errors cause a global shift of all images in a picture and also corrupt the relative image geometry within a picture due to the non-linearity of the TV distortion. TV pointing errors, which are caused by imperfect knowledge of TV pointing directions at shutter times, can be eliminated if stars with known directions are included in the picture. Prior to processing star images, preliminary knowledge of TV pointing can be obtained from reduced telemetry data of spacecraft and TV attitude. Reduced telemetry gives TV pointing errors of tens of pixels which are random in nature from picture to picture. Star data further reduces pointing errors to the pixel level.

Image center-finding errors result when dealing with finite size images such as those of Deimos and Phobos. Also, limit cycle motion during exposure, diffraction in the optics, and blooming of saturated images combine to yield finite size images. These center-finding errors are of pixel or sub-pixel magnitude for Phobos and Deimos. Random measurement errors result from random center-finding errors and TV resolution.

Model errors include satellite ephemeris errors as well as planet gravity and spin axis errors. For MM'71 the effects of these model errors was minimized by estimating Deimos and Phobos orbital elements, and the mass and spin axis direction of Mars simultaneously with the spacecraft trajectory.

IV. Data Types and Content

Optical navigation observables were defined as the image locations (pixel and line numbers) of Deimos, Phobos, stars and reseau. An approach picture is shown in Fig. 1 which has the images of Deimos, ten stars of magnitude 3.9 to 9.2, and the 9 x 7 reseau grid. The picture was enhanced to bring out the dim images. Figure 2 is a computer drawn version of the picture which is used to distinguish noise from dim stars.

Reseau images were used to compute the coefficients of the 6th order TV distortion polynomial to sub pixel accuracy. Star images were used to compute the TV pointing direction to an accuracy commensurate with the TV resolution of three arc sec (1σ). Star images were used instead of reseau post-flight to yield an equally accurate determination of TV distortion. Satellite images contained information on satellite ephemerides, the spacecraft trajectory, and Mars gravity potential and spin axis direction.

The reseau data used in TV distortion calibration for real time operations and a majority of post-flight evaluation was obtained from pictures

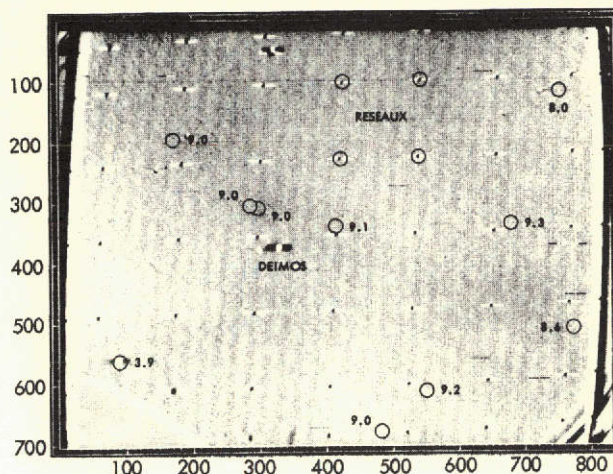


Fig. 1. Approach Deimos picture.

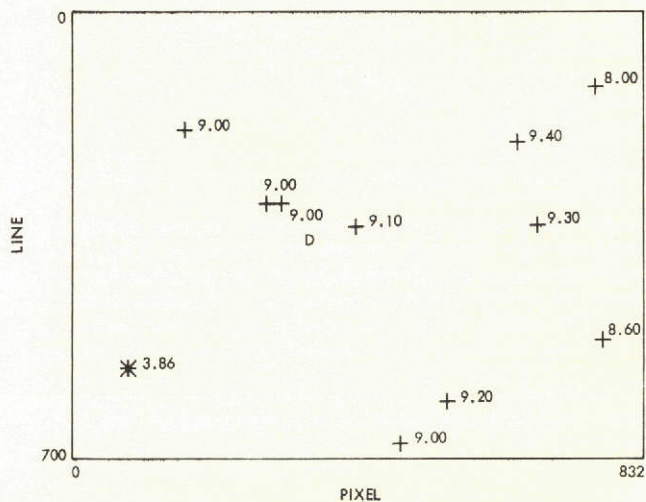


Fig. 2. Predicted approach Deimos picture.

taken about a month before orbit insertion. With the TV distortion being stable to a sub pixel level, no additional reseau data was needed for processing the optical navigation pictures. Star data, independent of spacecraft trajectory for this application, could be processed separately or combined with the satellite data processing.

V. Approach Pictures

During the 3 day approach period prior to the insertion of Mariner 9 into orbit about Mars, three Pre-Orbital Science picture sequences (POS I, II, and III) were taken (Fig. 3). Each POS sequence covered a 24 hour period with 31 pictures being recorded aboard Mariner 9 and then transmitted to Earth during a 3 hour period near Goldstone (Deep Space Station 14) zenith. Since orbit insertion was performed early in the Goldstone tracking window, the POS III pictures were played back after orbit insertion. With only POS I and II pictures to be played back prior to insertion, all 13 optical navigation pictures in

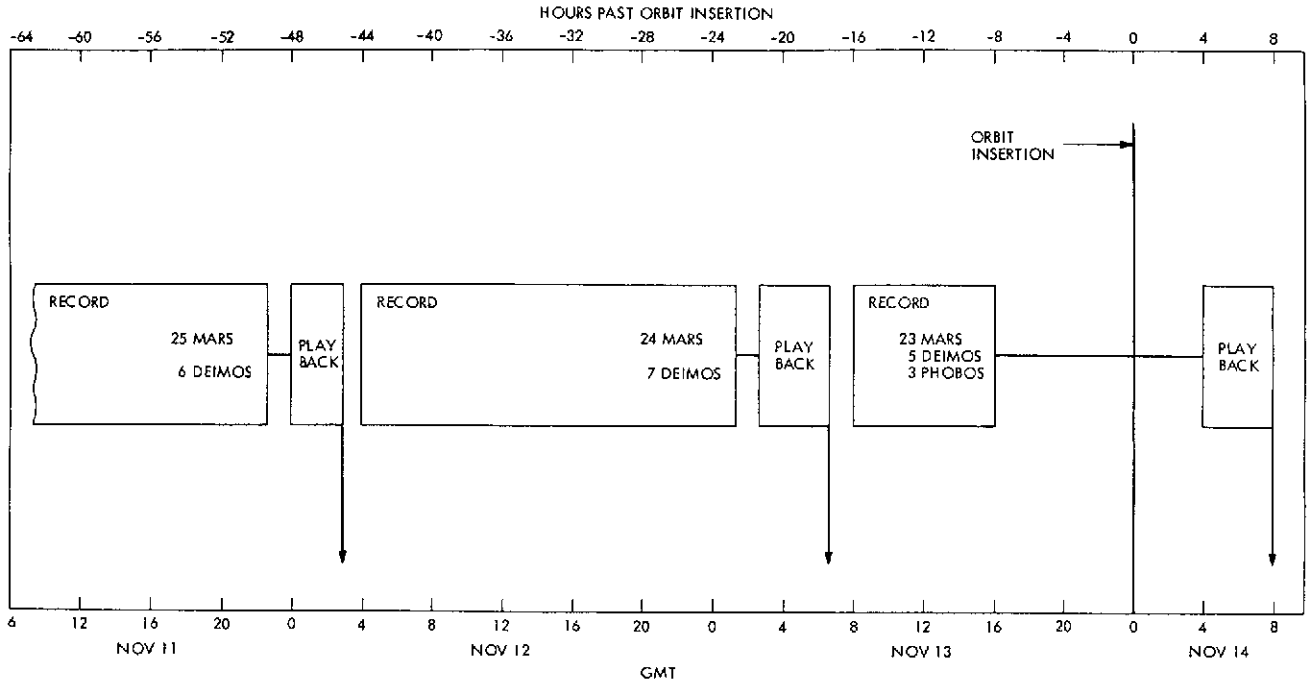


Fig. 3. Approach picture sequence.

these two sequences were targeted to Deimos. This reduced its ephemeris uncertainty to a level which would not seriously degrade the approach spacecraft trajectory estimates produced during real-time operations. The small angular separation of Phobos and Mars during this period made Phobos an undesirable target because of possible Mars stray light interference. The 8 pictures in POS III were divided between 5 of Deimos and 3 of Phobos.

The positions of Deimos as viewed from Mariner 9 against the star background are shown in Fig. 4. The orbital coverage of Deimos is listed in Table 1. During approach operations, the first Deimos picture was lost during transmission to JPL. Therefore, real time and post-flight data processing had only five POS I pictures. Also, one of the three Phobos pictures in POS II was missed because of improper pointing of the TV camera. With only two Phobos approach pictures

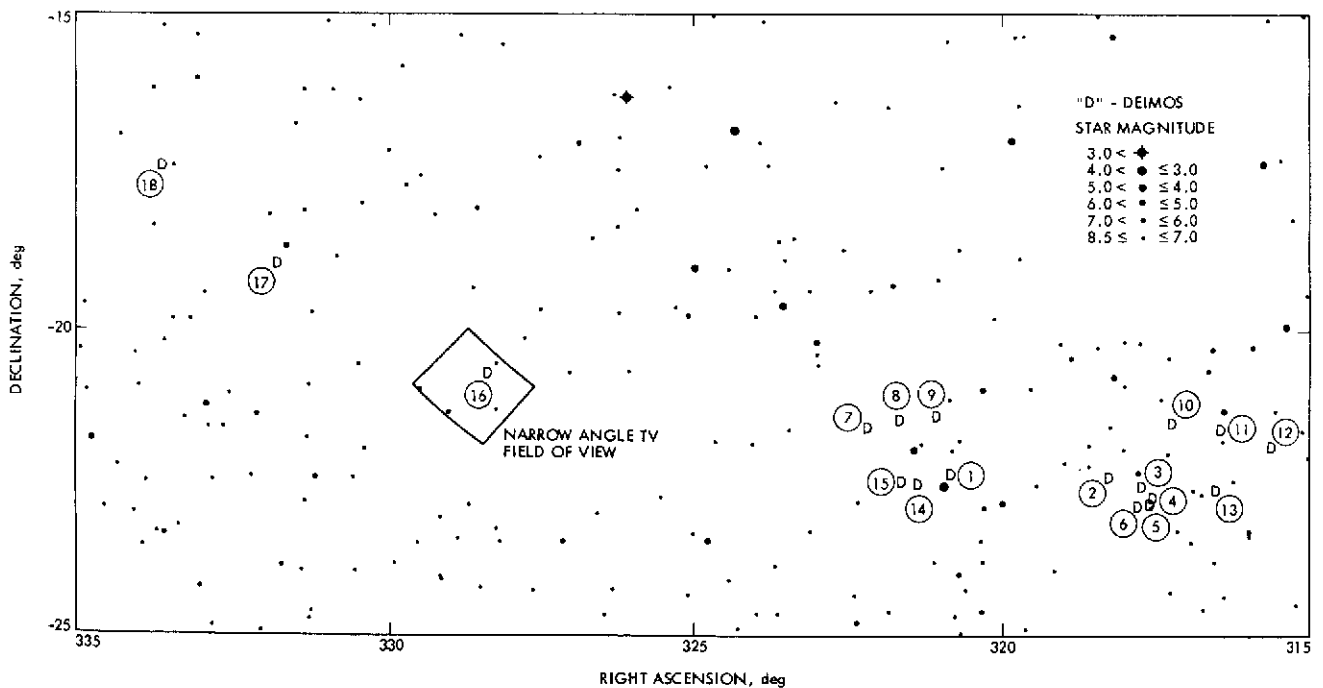


Fig. 4. Approach Deimos/star geometry.

Table 1. Deimos orbital coverage

POS	SATELLITE	HOURS BEFORE INSERTION	MEAN ANOMALY - deg
I	DEIMOS	66.0	95
I	DEIMOS	59.0	180
I	DEIMOS	57.0	204
I	DEIMOS	55.0	228
I	DEIMOS	54.0	243
I	DEIMOS	53.0	256
II	DEIMOS	36.0	92
II	DEIMOS	35.0	104
II	DEIMOS	34.0	116
II	DEIMOS	29.0	176
II	DEIMOS	28.0	190
II	DEIMOS	26.0	212
II	DEIMOS	22.0	271
III	DEIMOS	16.5	325
III	DEIMOS	16.4	327
III	DEIMOS	12.0	18
III	DEIMOS	10.0	43
III	DEIMOS	9.0	59

and large a priori Phobos ephemeris uncertainties, the Phobos data did not give any improvement of navigation accuracy over the Deimos data.

The pixel residuals (difference between observed and computed image locations) for Deimos (D) and stars (o) are shown in Fig. 5. The residuals at the top of the figure were obtained using an a priori Deimos ephemerides, a trajectory based on radio data to encounter minus 13 hours (E-13 hours), and TV pointing based on reduced spacecraft telemetry data. The star cluster residuals reflect the global offset of the images due to TV pointing errors. It is noted that the TV pointing errors become large at the end of POS II and throughout POS III. The line residuals for the approach pictures were small and random.

The residuals in the center of Fig. 5 were generated using the same conditions as those at the top with the exception that TV pointing errors have been removed by using the star images. Note that the star residuals which are only sensitive to TV pointing errors are practically zero. With TV pointing errors removed, the Deimos residuals reflect Deimos ephemeris errors (30 hour period) and spacecraft trajectory errors. The Deimos ephemeris errors are evident in the 30 hour period cycle seen in POS II and POS III residuals.

The residuals at the bottom of Fig. 5 were generated after solving for the spacecraft trajectory and Deimos ephemerides. Note that the residuals are zero mean and random having a standard deviation of less than 0.5 pixels (3 arc sec).

VI. Combined Doppler and Optical Solutions

Solutions which use a combination of doppler and optical data are of particular value during planetary approach phase since these data types complement one another. The primary error source prior to encounter in solutions using only doppler data is target planet ephemeris error. Optical data is insensitive to this error since it directly relates the planet and spacecraft positions. On the other hand, optical data suffers from the inability to determine time of flight and velocity (V_{∞}) of the spacecraft, quantities which are well determined by doppler data. Hence, the combination of radio and optical data yields extremely accurate solutions. In particular they may be combined to give a good estimate of encounter conditions much earlier than either data type taken separately. This is of primary importance if an additional corrective maneuver is contemplated. This section presents a simple analysis illustrating why combined solutions are useful.

No matter what type of optical observation is taken, either planet limb or natural satellites, what one attempts to measure is the angle between the target planet center of mass and a reference direction, e.g., a star direction. For the purposes of this analysis the error in this angular measurement represents the accumulation of all error sources such as center finding errors, satellite ephemeris errors, biases and camera pointing errors. These errors effectively result in a degradation of the observation angle.

Assume that the spacecraft is moving on trajectory No. 1 (Fig. 6). Let θ_1 and θ_2 represent two angular measurements of the direction between the reference star and center of mass of the target planet. For simplicity the reference star is assumed to lie along the V_{∞} vector. In general the observable equation is

$$\tan \theta_i = \frac{B}{V_{\infty} T_i} \tag{1}$$

where

$$T_i = T - t_i$$

and

$B \sim$ magnitude of B vector

$V_{\infty} \sim$ velocity on approach asymptote

$T \sim$ time of flight

$t_i \sim$ time of ith observation

From Eq (1) it is seen that the time of flight, T can be solved for from two perfect observations of θ . However, only the ratio B/V_{∞} can be determined from observations of θ . This is because the observation history for any parallel trajectory with the same value of B/V_{∞} (for example, trajectory No. 2) will be identical to the true trajectory. These parallel trajectories also will have the same time of flight as the true trajectory. Note also that two perfect direction observations determine the plane of motion.

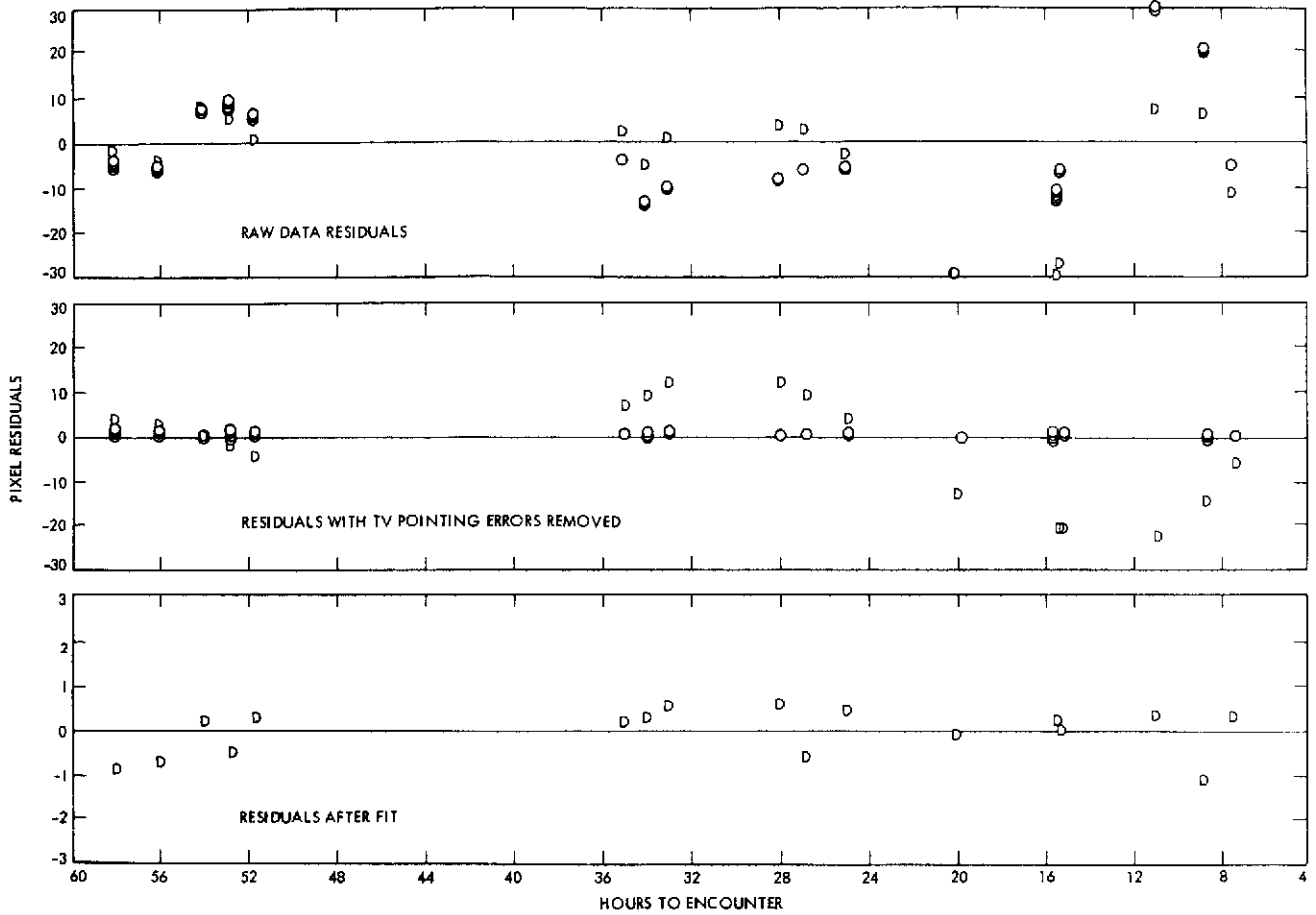


Fig. 5. Deimos observation residuals.

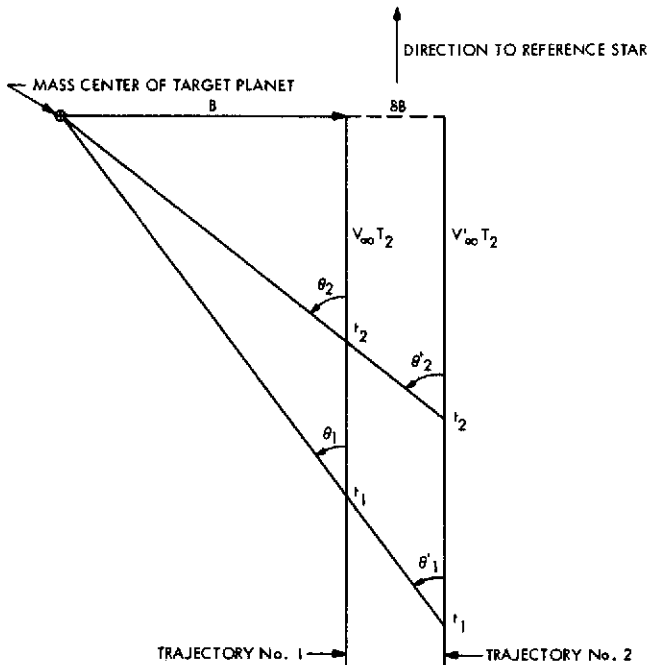


Fig. 6. Approach trajectory geometry.

From Eq (1)

$$\frac{\delta\theta}{\sin\theta \cos\theta} = \frac{\delta B}{B} - \frac{\delta V_\infty}{V_\infty} - \frac{\delta T}{T}$$

or for small values of θ

$$\frac{\delta B}{B} = \frac{\delta V_\infty}{V_\infty} + \frac{\delta T}{T} + \frac{\delta\theta}{\theta} \quad (2)$$

Consequently, even with perfect observations the limiting accuracy for B is determined by δV_∞ i.e.,

$$\frac{\delta B}{B} = \frac{\delta V_\infty}{V_\infty} \quad (3)$$

Even though in theory two perfect observations of θ uniquely determine time of flight, in practice this quantity is rather poorly determined by optical data since it is extremely sensitive to errors in θ . This can be illustrated by examining an expression for the time of flight uncertainty.

Assume that two observations of θ are taken, then solving Eq (1) for T yields

$$T = \frac{t_2 \tan \theta_2 - t_1 \tan \theta_1}{\tan \theta_2 - \tan \theta_1}$$

assuming θ_1 and θ_2 are small

$$T = \frac{t_2 \theta_2 - t_1 \theta_1}{\theta_2 - \theta_1}$$

and

$$\delta T = \frac{(t_2 - t_1) (\theta_2 \delta \theta_2 - \theta_1 \delta \theta_1)}{(\theta_2 - \theta_1)^2}$$

assuming independent observations the standard deviation of T becomes

$$\sigma_T = \left[\frac{(t_2 - t_1) \sqrt{\theta_1^2 + \theta_2^2}}{(\theta_2 - \theta_1)^2} \right] \sigma_\theta \quad (4)$$

From Eq (4) it is seen that the uncertainty in time of flight is very sensitive to uncertainty in pointing angle when the spacecraft is far from the target planet and decreases as the spacecraft approaches the planet. Equation (4) also emphasizes the importance of stars in the data since they minimize the contribution of pointing errors to σ_θ .

Equations (3) and (4) illustrate the quantities, V_∞ and T which are weakly determined by optical data. Since these same quantities are determined very well by earth-based doppler data the combination of the two data types can yield good solutions much sooner than either type used separately.

It is emphasized that the analysis presented here only applies far from encounter. As the spacecraft approaches the planet, parallax effects in the case of natural satellite observations allow one to solve for V_∞ . Also the time of flight solution becomes less sensitive to pointing errors. Furthermore, sufficient data will have been taken to estimate the natural satellite's ephemeris relative to the target planet thus reducing effects of this error source. In the case of planet limb observations V_∞ cannot be accurately determined until planetary bending of the approach trajectory occurs.

In the case of Deimos parallax effects are discernible long before planetary bending occurs. In addition, the small size of Deimos makes image center-finding errors negligible.

VII. Techniques for Combined Solutions

As shown in the previous section it is desirable to combine doppler and optical data for planetary encounter solutions. The technique used for MM'71 was to combine, as independent data types, a short arc (5 days) of doppler data with the optical data. A short arc of radio data is sufficient to determine the spacecraft velocity and time of flight without being corrupted by unmodeled accelerations. Since optical data is insensitive to Mars ephemeris errors, an accurate simultaneous solution for the state of the spacecraft and the ephemeris of Deimos relative to Mars can now be obtained.

In real time operations for MM'71 12 pictures containing Deimos and stars were available to the optical team 18 hours before encounter. These

pictures spanned 40 hours of real time or 1 1/3 Deimos orbits.

This optical data was combined with 4 1/2 days of doppler data which extended from Nov. 9 to E-19 hours. The solution list contained the spacecraft state plus 4 elements of Deimos orbit. Since Deimos is in a near circular, near equatorial orbit only two orientation angles, inclination and mean anomaly were included in the solution along with semimajor axis and eccentricity. This solution which was available at E-16 hours was within 7 km in B·R, 5 km in B·T and 2 km in B magnitude of the current best estimate of encounter parameters.

VIII. Real Time Results

During Mars approach, 12 Deimos pictures were included in the real time navigation process. Prior to obtaining these pictures, an insertion maneuver had been calculated and stored aboard Mariner at E-5 days. The maneuver would only be updated in the event that additional radio data and the optical data indicated an unacceptable trajectory error. Additional radio and optical data indicated a trajectory error of only 70 km; therefore, no update to the maneuver was required. However, if the decision to update the insertion maneuver had been made, a solution based on radio plus optical data was available and had an error of less than 10 km.

Figure 7 shows the B-plane trajectory estimates which were generated in real time. The radio only solution and its 1 σ error ellipse (Fig. 6) were based on data to E-13 hours. The radio plus optical iterated solution and 1 σ error ellipse (Fig. 6) were based on radio data to E-19 hours and optical data from POS I and II. The current best estimate is denoted as CBE (Ref. 6). Also, solutions denoted as optical were generated using a trajectory based on radio data but processing optical data only. These optical solutions were from the first pass of the iteration process to remove non-linearities.

Post flight evaluation of the data has given greater insight to the data but has made little improvement in the accuracy of the real time trajectory estimates.

IX. Sensitivity to Stars

The OD accuracy sensitivity to the number of stars per picture was investigated. The following three cases were studied: a) no stars/picture; b) one star/picture; and c) an average of five stars/picture. All three cases also had a priori TV pointing information from reduced spacecraft telemetry data. The OD accuracies for the three cases assuming infinite a priori variances are shown in Fig. 6 and the associated trajectory estimates are shown in Fig. 7. The case of one star/picture and 5 stars/picture resulted in the same OD accuracy history. The a priori trajectory was based on radio data only from E-30 days to E-16 hours.

Figure 7 shows that the first picture in POS I for cases b and c drive the trajectory estimate to within 15 km of the current best estimate (CBE). The time behavior of cases b and c are very similar with the trajectory estimates within 10 km

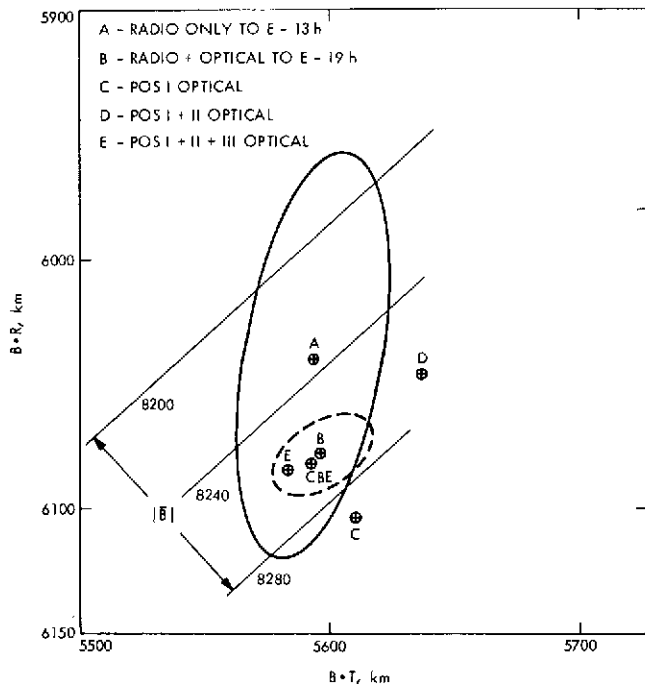


Fig. 7. Real time trajectory estimates.

agreement at the end of POS I and POS II data and within 2 km agreement at the end of POS III data. The expected accuracies of cases b and c (Fig. 6) are the same. It is seen, therefore, that the full accuracy potential of the optical data can be obtained with only one star/picture. This is also true if the desired TV pointing were used as a priori instead of reduced spacecraft telemetry data.

TV pointing derived from spacecraft telemetry is an order of magnitude less accurate than pointing derived from star images. This degradation is reflected in both the expected accuracy and the actual trajectory estimate of case a as compared to cases b and c. The case a trajectory estimate is well behaved when compared to its expected accuracy until the last picture in POS II (no. 12). Then the large non-random TV pointing errors (modeled as random errors) in the remaining pictures drove the trajectory estimate to a 3σ error. Improved trajectory accuracy may be possible by modeling the TV pointing errors as time correlated processes.

These star sensitivity results can be explained by examining the TV pointing errors. For a given picture, all sources of pointing errors can be modeled as three independent rotations about the axes of an orthogonal coordinate system (e.g., TV pointing has three degrees of rotational freedom). One star image (a pixel and line observation) yields two of the three degrees of rotational freedom. The third degree of freedom is obtained from a second star or from a priori TV pointing which has an accuracy of a few tenths of a degree. A priori TV pointing to this accuracy can be obtained from either reduced spacecraft telemetry data (0.15 deg - 1σ) or from the desired pointing (0.15 deg - 1σ). Additional stars, however, do not improve the Deimos-inertial reference information in a picture. Deimos image location measurement errors control this accuracy and are not affected by stars observations.

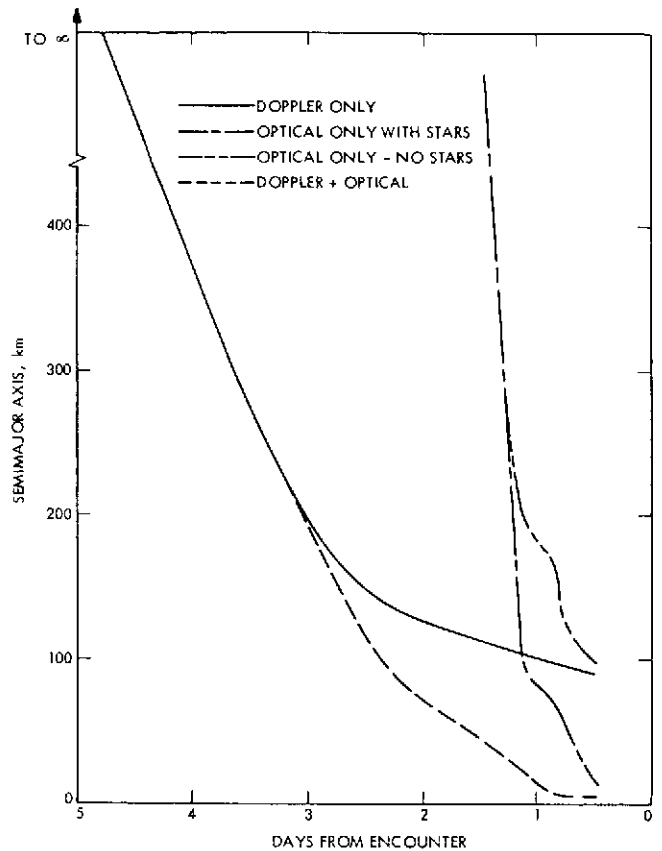


Fig. 8. Expected trajectory estimation accuracy.

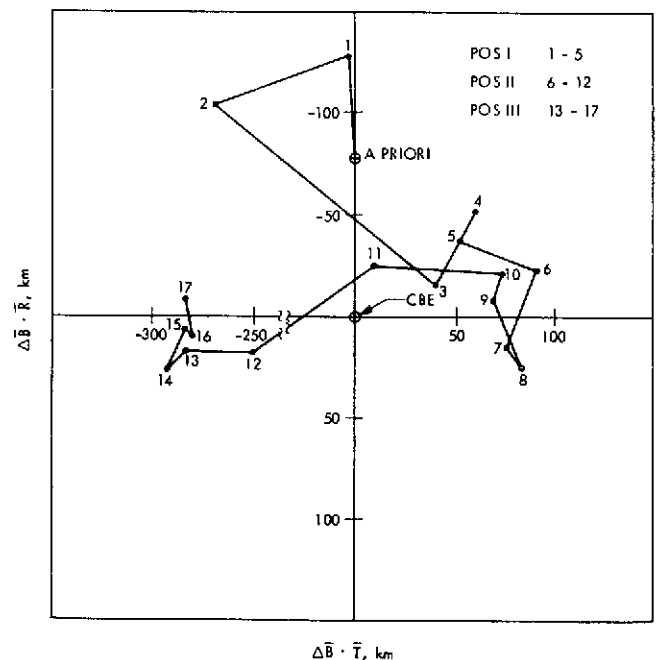


Fig. 9. Trajectory estimate using no stars.

Even though only one star/picture is needed, it is desirable to have many stars/picture. From a reliability standpoint, many stars/picture give independent checks on the TV pointing and also indicate the accuracy of the TV distortion model. Any discrepancy between image location residuals within a given picture would flag it for further evaluation.

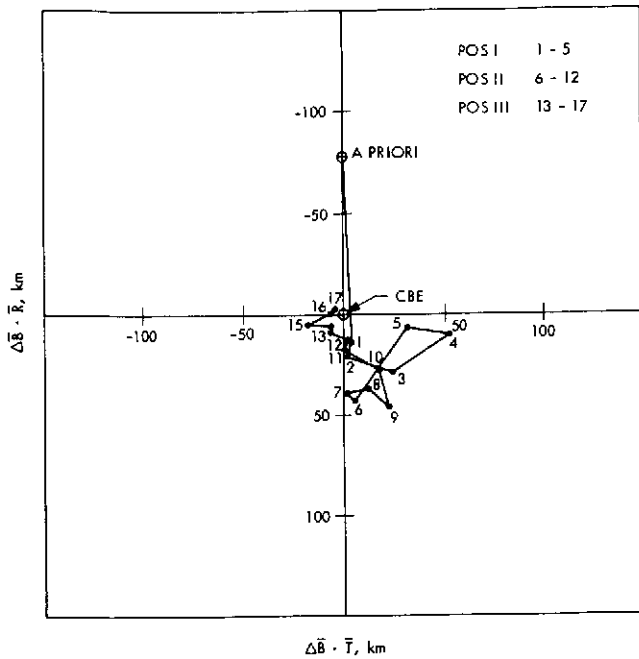


Fig. 10. Trajectory estimate using one star/picture.

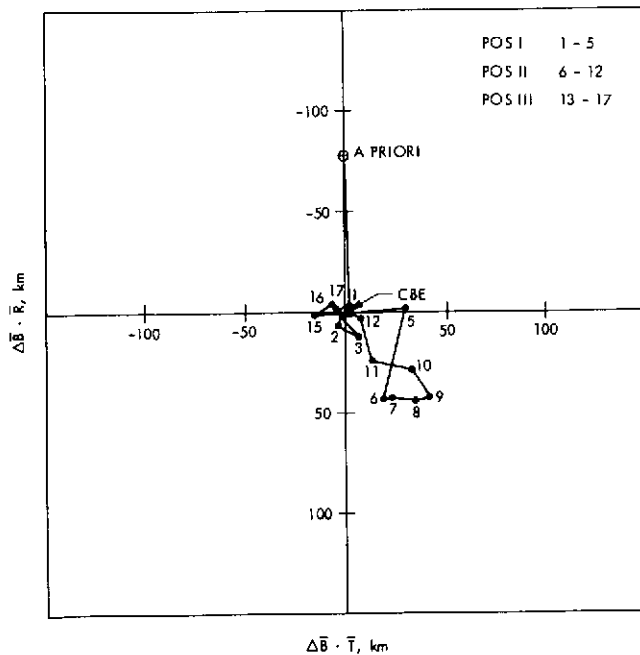


Fig. 11. Trajectory estimate using many stars/picture.

X. Evaluation - Sensitivity to TV Distortion

A comparison was made of OD performance as a function of the data type used to calibrate TV distortion and also the order of polynomial used to model distortion. Data used for distortion calibration included: 1) only reseau images from ground pictures; 2) only reseau images from flight pictures; and 3) only star images from flight data. Distortion polynomials of 2nd and 4th order, determined from flight reseau images, were compared to results from the 6th order polynomial.

In comparing calibration data, it was found that all three types gave equivalent trajectory estimation results. The difference between reseau images from ground and flight pictures was an offset and rotation common to all reseaux (Ref. 4). This difference was easily absorbed in the TV pointing error model. Approximately 200 star images from Pleiades pictures and optical navigation pictures were used to produce equivalent results as from reseau data. Stars are a more desirable data type for distortion calibration because they also enable the calibration of optical distortion in addition to electromagnetic distortion and are more easily detected than reseaux in pictures used for TV calibration and navigation.

A tradeoff for increased optical data linearity at the expense of reduced accuracy was evaluated. It was found that a 4th order distortion polynomial gave equivalent trajectory estimates to the nominal 6th order model. The increased linearity was accompanied with a noisier trajectory estimate behavior which, however, was well within the predicted accuracy. The trajectory estimate obtained using a 2nd order distortion model was in error by over 100 km. Therefore, it is concluded that a 4th order model would suffice if time constraints would not allow iteration of the optical data. If time is available, which will generally be the case, the 6th order model gives the full accuracy potential of the optical data with iteration of the data.

XI. Optical Only Solutions

In order to determine the potential of optical data and its sensitivity to the amount of radio data in combined radio-optical solutions, an "optical only" solution was made. For this optical-only solution no doppler data was assumed beyond the first mid-course correction maneuver, at launch (L) + 5 days. The spacecraft state estimate and covariance at that time were input as a priori to the optical data arc. The mapped B-plane uncertainties were very large at this point owing to large maneuver execution uncertainties being mapped several months forward. The analysis was conducted using only the photographs in POS I and POS II - that is, the pictures that could have been used for a real-time "optical only" solution before computing the Mars orbit insertion maneuver.

The results of the optical-only solution are shown in Fig. 12 which gives the time history of the B-plane estimate. The origin is at the current best estimate (CBE), and the a priori estimate is more than 2,500 km off in the B-plane. The first few pictures are observed to correct most of the errors and at the end of the first pass the estimate has moved to within 50 km of the CBE. The first iteration to remove trajectory nonlinearities moves the estimate to within 6 km of the CBE. This accuracy is well within the mission requirements for inserting Mariner 9 into orbit.

XII. Sensitivity to Mars Ephemeris

One major source of error in the use of doppler data for navigation estimates is planetary ephemeris errors. This results from the fact that the data is taken by stations on Earth and must be related to the target planet by using assumed station locations, and a planetary ephemeris.

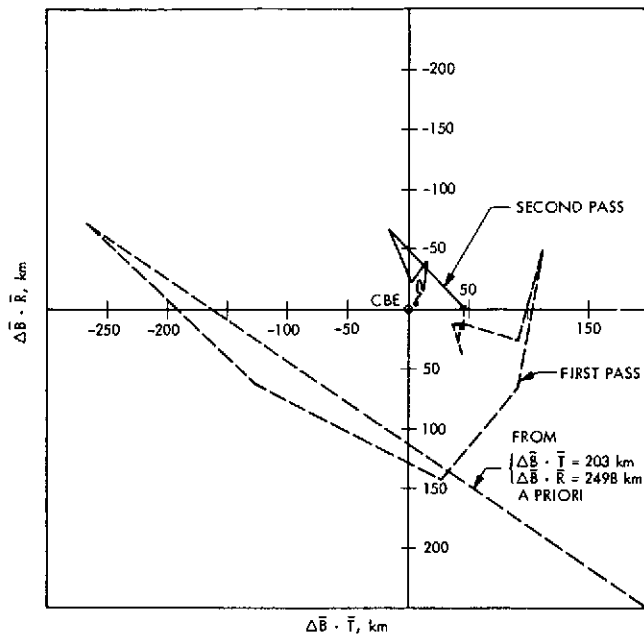


Fig. 12. Optical data solution.

However, from onboard optical data the spacecraft state is directly related to the target planet. After the insertion of Mariner 9 into Mars orbit there was an update to the planetary ephemeris affecting the position of Mars by about 40 km. The optical navigation estimates for the B-plane parameters remained essentially the same with this change in ephemeris.

To demonstrate the independence of optical navigation estimates from the planetary ephemeris more effectively a solution was made with a Mars ephemeris error of about 500 km. The results of processing the optical data with this ephemeris error are shown in Fig. 13, giving the B-plane solution history. The origin of the plot is at the current best estimate (CBE). The figure shows that the first pass through the data moves the estimate from an a priori more than 500 km away to within 10 km of the CBE. The final iteration moves the estimate to within 2 km of the CBE.

XIII. Conclusions

The doppler plus satellite/star trajectory estimate for Mariner 9 was the most accurate solution generated during any real time approach operations. The new optical data, navigation techniques and science TV camera were successfully demonstrated during real time and post-flight analysis. Star and reseau images were used to eliminate all systematic TV pointing and distortion errors to arc sec accuracy. Consequently, satellite image location errors were random having a measurement noise of 3.0 arc sec (1σ). These satellite images allowed Mariner 9's trajectory and the satellite's ephemeris to be determined independent of a priori uncertainty on satellite ephemerides. The addition of the optical data to a few days of radio data allows the approach navigation process to reach its full accuracy potential and become insensitive to planetary ephemeris errors, non-gravitational spacecraft accelerations and earth-based tracking station location errors. Thus a demonstrated navigation capability

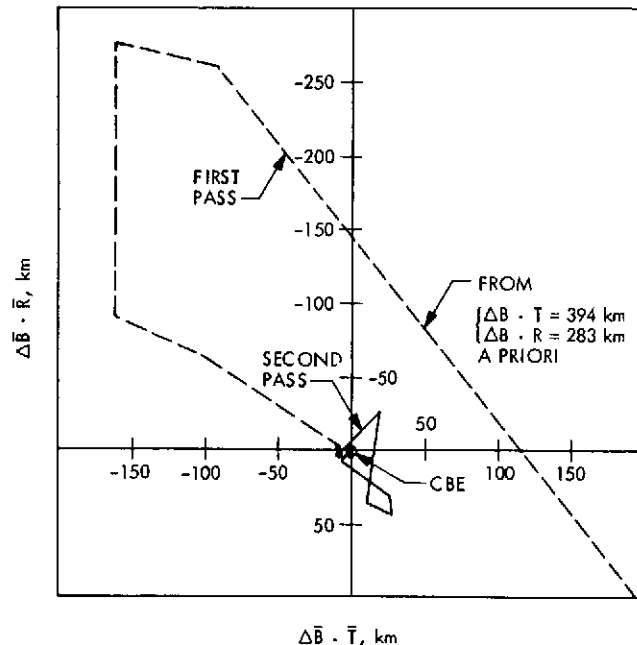


Fig. 13. Sensitivity to Mars ephemeris error.

now exists which can meet the demanding requirements of future missions such as outer planet or satellite tour missions.

XIV. References

1. Duxbury, T. C., "A Spacecraft-Based Navigation Instrument for Outer Planet Missions", *Journal of Spacecraft and Rockets*, Vol. 7, No. 8, August 1970, pp. 928-933.
2. Duxbury, T. C. and H. Ohtakay, "In-Flight Calibration of an Interplanetary Navigation Instrument", *Journal of Spacecraft and Rockets*, Vol. 8, No. 10, October 1971, pp. 1038-1042.
3. Acton, C. H., "Processing On-Board Optical Data for Planetary Approach Navigation", AIAA Paper No. 72-53, January 1972.
4. Breckenridge, W. G. and C. H. Acton, "A Detailed Analysis of Mariner 9 TV Navigation Data", AIAA Paper No. 72-866, August 1972.
5. Duxbury, T. C. and C. H. Acton, "On-Board Optical Navigation Data from Mariner '71", Institute of Navigation - National Space Meeting, March 1972.
6. Personal Communication with S. K. Wong of the Jet Propulsion Laboratory.

APPENDIX J

SUMMARY OF RESULTS OF MM'71 OND TV DATA ANALYSIS

SUMMARY OF RESULTS OF MM'71
OND TV DATA ANALYSIS

James A. Miller

January 16, 1974

The following information represents a summary of the results of investigations of factors relevant to the optical imaging process in the Mariner Mars 1971 (MM'71) Optical Navigation Demonstration (OND).

Areas of investigation included effects and/or characteristics of: (1) periodic noise ("stripes"), (2) differential location, local background and "rings," (3) attitude rates and detection thresholds, (4) correlations of various characteristics of image sources with measures of displayed image, and (5) notes on an auto-detection algorithm.

1. Periodic Noise

Examination of enhanced hard copy pictures of MM'71 TV data reveals thin vertical lines occurring at about 6-pixel intervals. These lines are attributed to periodic noise arising from resonance of the read-beam modulation with the on-board power supply.

Fifteen 20×20 picture-element search areas from four flight pictures served as the primary data source for the analysis of frequency, amplitude and phase of the periodic noise. Figure (1) illustrates graphically the average discrete periodic noise waveforms isolated from the data. For purposes of this analysis, all waveforms were divided into two categories; those whose peaks could be considered as falling on a pixel, and those whose peaks seemed to fall between pixels. In figure (1), graph (A) represents the average of the former while graph (B), plotted 1/2-pixel out of phase with graph (A) represents the average of the latter. Graph (C) is the average of both data types, and the vertical lines represent 6-pixel intervals.

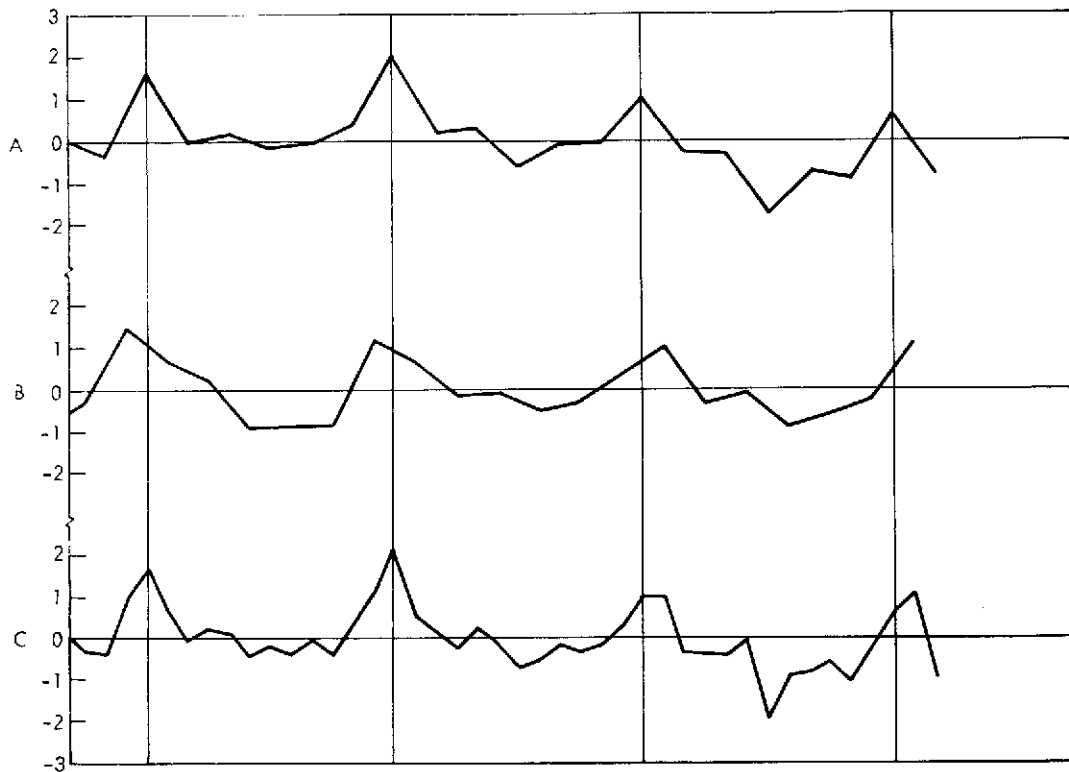


Figure 1. A, all pictures, single peak; B, all pictures, double peak; C, all pictures

The analysis resulted in the following conclusions:

- 1) The periodic noise varies from picture to picture.
- 2) The period of the horizontal noise responsible for the stripes is about 6.00 - 6.07 samples/cycle.
- 3) The vertical periodic noise varies largely from picture to picture.
- 4) The horizontal noise waveform is out of phase from line to line (vertically unaligned).
- 5) The phase differences vary from picture to picture.
- 6) The peak-to-peak horizontal periodic noise amplitude ranges from about 1.4 - 2.4 DN.
- 7) The RMS horizontal periodic noise amplitude ranges from about 0.48 - 0.72 DN.

These conclusions were in agreement with results of ground based tests by the TV Subsystems Group (Reference 1).

Removal of the periodic noise would involve either isolation of the periodic noise amplitude, phase and frequency and its subtraction from the data, or determination of the frequency and application of a digital filter for that frequency.

It is believed that the effects of the horizontal periodic noise, while detracting from the general quality of the pictures, is insignificant with respect to the identification of star images in the Mariner 9 TV data. It is probable that the periodic noise would contribute to the detection of as many marginally detectable images as it would hinder, and the expected number of images detected remains the same. Another factor contributing to the conclusion of the insignificance of the periodic noise with respect to detection of images is that the amplitude of the random noise is several times greater than the amplitude of the periodic noise. Also, the images automatically detected by the Image Processing Program (IMP) were those whose intensity was 6 DN or more greater than the mean background intensity, as compared to a peak periodic noise amplitude of about 1DN.

2. Differential Location, Local Background and "Rings"

Analysis of effects of differential location sensitivities upon image intensities was conducted using data from photometric mapping studies (Reference 1).

This data was collected using flatfield illumination at various exposure levels at system and subsystem levels in environmental and bench test conditions. To minimize effects of varying test conditions, data from the four bench tests at the subsystem level only was used.

Significant findings may be enumerated as follows:

- a) There is a significant difference in sensitivities of different areas of the picture.
- b) The relative sensitivity with respect to position is a function of the exposure level.

- c) The relative sensitivity with respect to position varied from test to test at the same exposure levels.
- d) From the data available, it is presently impossible to specify relative sensitivity differences as a function of position in a picture.

The magnitude of the sensitivity differences with respect to position is perhaps best expressed by the data in Table 1.

Table 1.

\overline{DN}	σ_1	σ_2	σ_3	CI	σ_4
15	2.5	1.5	2.9	±5.7	1.4
25	2.7	2.8	3.8	±7.5	2.3
50	3.3	6.5	7.1	±14.0	4.2
100	4.5	11.3	11.9	±23.3	7.9
200	7.2	18.8	19.7	±38.6	14.8
280	9.3	21.8	23.2	±45.5	20.1
360	8.6	24.9	25.8	±50.5	25.3
425	10.8	26.8	28.3	±55.4	29.4

\overline{DN} is the average intensity at a selected exposure of 20 100×100 picture-element sample areas from four pictures of five sample areas each, with the position of the samples held constant across pictures (as was the level of exposure). σ_1 represents the standard deviation within a 100×100 sample area. σ_2 represents the standard deviation of the means of the five sample areas. σ_3 represents the standard deviation of the distribution of individual element intensities within a picture. (σ_4 will be discussed with the attitude rate results.) If there were no differences in sensitivity between sample areas, it would be expected that

$$\sigma_2 \approx \frac{\sigma_1}{100} \quad (\text{for } 10,000 \text{ samples/sample area}). \quad (1)$$

It is thus obvious that there is a significant difference in sensitivities of different locations in the picture. σ_1 then represents location differences in sensitivity for small differences in location, while σ_2 represents sensitivity differences for different sample areas and σ_3 represents sensitivity differences for random differences in location. CI (Confidence Interval) represents the amount added to and subtracted from \overline{DN} to find the approximate range within which 95 percent of the samples (picture elements) in the picture would lie for that exposure level.

It was learned from the study of location differences in sensitivities, that the relative sensitivity of sample areas varied with exposure levels. Thus, knowledge of the background intensities of a given area is of little value in predicting the relative brightness of an image appearing in that area.

Plots of image intensity versus background intensity for images appearing in several pictures were constructed, using algorithmic estimates for attitude rate compensation. These plots showed no significant correlation between image intensity and background intensity. Also consistent with these findings were results of comparisons of plots of maximum image intensity versus attitude rates with plots of relative image intensities (maximum intensity minus background intensity) versus attitude rates. Such plots were similar. There is apparently no orderly relationship between background intensity and relative sensitivity.

It should be mentioned, however, that during the process of identifying the images in the various pictures, it was observed that a) a higher background intensity hindered visual identification of images due to lower contrast, and b) a higher background intensity aided automatic detection of images by IMP due to the higher relative signal.

Vidicon characteristics are such that background intensities vary radially from the center of the picture. The effect is more pronounced for the B camera. The center of the picture has a dark background and is surrounded by three concentric bands or rings, alternating from light to dark to light, with the contrast between rings increasing with increasing radius. These rings are due to several factors, including diffusion toward edges, secondary beams due to deflection of primary beams along the vidicon tube sides and electron optics.

These effects vary from one vidicon to another and are not well understood, consequently no attempt has been made to provide descriptive data for this phenomenon by the TV Subsystems group.

Differences in sensitivity between lighter and darker rings are identical to differences in sensitivity due to background intensity, while differences in sensitivity within the same or similar rings (i. e., similar background intensities) is equivalent to location differences mentioned above. Thus, previous remarks pertaining to location and background differences apply, and knowledge of an image's position in the picture relative to the rings and their brightness contributes little to our ability to predict an effect upon image intensity due to its position in the picture.

It should be restated here, that images located at the edge of the picture in the brightest (background) ring are very difficult to detect visually due to decreased contrast between the image and the background, although such images may be detected digitally with ease.

3. Attitude Rates and Detection Thresholds

Stars appearing in four or more Scan I and Rev. 72 pictures were used as the principal data source for studies of effects of spacecraft attitude rates upon image intensities. Intensities of single stars appearing in several pictures were plotted against the attitude rate of the pictures. The intensity of the images were found to decrease linearly with increasing attitude rates. The rate of reduction of intensity with increasing attitude rates ($dI/d\dot{\theta}$) was found to be a function of the zero-attitude-rate expected intensity for that image as found by extrapolation of the linear fit to zero attitude rate:

$$\frac{dI}{d\dot{\theta}} \approx \frac{-\sqrt{-28,800 - I_o(I_o - 760)}}{100} \quad (2)$$

The above relationship is applicable only to images with zero-attitude-rate intensities of 200 DN or less; roughly $M_v \geq 6$ (the majority of stars of concern to the optical guidance effort are dimmer than 6th magnitude). Brighter images showed little or no correlation between the rate of reduction of

intensity with increasing attitude rate ($dI/d\dot{\theta}$) and zero-attitude-rate expected intensities.

In general, for images of visual magnitude, 4.5 or brighter (>320 DN):

$$\frac{dI}{d\dot{\theta}} \approx -1.1 \pm 0.5 \quad \frac{\text{DN}}{\mu \text{ rad/sec}} \quad (3)$$

Thus, at 20 μ radians/second, it would be expected that the maximum intensity would decline approximately 22 ± 10 DN. Remembering the previous discussion of location effects, such images would show a standard deviation of about 25 DN from differential location effects alone (assuming a zero-attitude-rate intensity of 360 DN).

The expected intensity range would be 338 ± 60 DN for 95 percent of the samples. The uncertainty due to attitude rate for these brighter images is thus overshadowed by the uncertainty due to differential location sensitivity.

During the calculation of a least squares solution to the straight line approximation to attitude rate/intensity data, the standard deviation of the data points from the expected value for the linear fit was found to be related to the zero-attitude-rate expected intensity according to the following equation:

$$\ln \sigma_4 = \frac{\ln I_0 - 2.326 \pm 0.3474}{1.102 \pm 0.1510} \quad (4)$$

Computations of σ_4 using the central values of the constants in equation (4) are listed in Table 1. Comparison of σ_3 with σ_4 indicates agreement well within the uncertainties of the constants in equation (4), thus supporting both previous calculations of uncertainty due to position and the assumption of a linear relationship between image intensity decrement and attitude rate.

Using Scan I and Rev. 72 data, visual magnitudes of detected and undetected images in each picture were plotted against the attitude rate normal to the line of sight of the camera. Extrapolation of results yielded a zero-attitude-rate visual magnitude threshold of approximately 8.7.

The relationship between visual magnitude threshold and attitude rate was found to be:

$$M_{V_o} = 8.7(\pm 0.2) - 0.0154(\pm 0.006)\dot{\theta} \quad (5)$$

where

M_{V_o} = Visual Magnitude Threshold for detection

and

$\dot{\theta}$ = Spacecraft attitude rate component normal to the line of sight of the camera expressed in microradians per second

Scan I and Rev. 72 data were consistent with one another; however, similar treatment of POS data yielded a detection threshold of 9.2 with the relationship between M_{V_o} and $\dot{\theta}$ found to be

$$M_{V_o} = 9.2(\pm 0.4) - 0.035(+0.020 - 0.010)\dot{\theta} \quad (6)$$

The inconsistency between (5) and (6) is due in part to unknowns in POS data (no knowledge of undetected images or exposure time; uncertain attitude rates), however, greater sensitivity was evident in the POS pictures as witnessed by the detection of three 9th magnitude stars.

These rates of change of M_{V_o} with $\dot{\theta}$ disagree further with findings using an Earth-based MVM camera and 12 second exposure, and graphical data from Reference 2, both of which put

$$\frac{dM_{V_o}}{d\dot{\theta}} \approx 0.06 \quad (7)$$

These differences may be in part due to use of different cameras in Earth-based tests with different exposure times. No tolerances were available for (7), so the degree of disagreement remains unknown. Sufficient data is lacking to offer further explanation for these differences.

4. Correlations of Various Characteristics of Image Sources with Measures of Displayed Image

The effects of the following characteristics of image sources upon image intensity distribution were studied: Visual magnitude, photographic magnitude, relative magnitude, spectral class and color index.

An attempt was made to correlate the visual magnitude photographic magnitude, relative magnitude (a specially developed algorithm to partially compensate for vidicon spectral response), color index and spectral class with maximum and relative (to background) image intensities, and compare these to one another as predictors of image intensity.

Data for such a study was extremely limited. Visual magnitude data was available in abundance. However, the correlation with displayed image intensity was low. It was for this reason that other characteristics of image sources were explored as indicators of image intensity. Initially hopeful findings with the photographic magnitude were later found to be applicable only to the highly similar data at hand (all stars for which data was complete were between 7.4 and 8.5 in M_V and they were all class A stars). Other characteristics either failed to correlate significantly or lacked sufficient data.

A major contributor to the low correlation between visual magnitudes and image intensity is the variability due to differential location sensitivity. A second contributor is the spectral response of the vidicon. To obtain a measure of stellar magnitude which correlates more highly with image intensities, it is necessary to calculate the relationship between the detector system (i. e., MM71 Science Cameras A and B) and the Johnson-Morgan UBV system using this relationship to calculate M_A or M_B , the stellar magnitudes relative to the A or B camera (Reference 3). M_A or M_B with the best pointing, attitude rate and position estimates may enable greater predictive ability of a star's digital intensity and facilitate automatic identification of images based on magnitude as well as geometric patterns. Such an approach would necessitate calibration of cameras and filters, and is hampered by presently inadequate UBV data sources for the stars.

5. Notes on an Auto-Detection Algorithm

An algorithm improving distinction between images and blemishes was developed utilizing a data matrix encompassing the candidate image.

This matrix test involves determination of the total number of picture elements within a matrix that exceed a background level by a nominal amount with the total compared to a minimum value attributed to identification as a star. Using this criterion, it has been possible to remove 10 of the 12 blemishes in Scan I pictures 24, 25 and 26 with no loss of stars. Attempts to remove one or both of the remaining blemishes have resulted in the loss of several stars. Disadvantages of this method are increased computed processing time and costs.

Conclusions

The major obstacles hindering the ability to predict the intensity of a displayed image within small tolerances (and conversely, to match displayed images with possible sources with greater efficiency) is seen to be the effects of 1) differential position sensitivity 2) attitude rates and 3) low correlation between stellar magnitudes and detector system response. Attempts to compensate for differential position sensitivity (which may include random differences in response of the same area) would require extensive calibration processes which may not be justified by the results (random differences may be significant). Effects of attitude rates may be compensated for using algorithms mentioned previously. Further study could yield a significant improvement in bright-image attitude rate compensation algorithms. Calculation of detector system stellar magnitudes as previously discussed would also require a major effort.

It is the dimmer stars which are seen to play the most significant role in the optical guidance effort. For such stars, differential position sensitivity is much smaller and attitude rate compensation well described. Thus, a smaller uncertainty for the expected intensity of a given image may be calculated, and, knowledge of image intensities and positions along with preliminary pointing, attitude rate and S/C position data may permit image identification with greater efficiency.

References

1. Snyder, L. M., "Mariner 9 TV Subsystem Calibration Report," JPL Report 610-202, Nov. 15, 1971 (JPL internal document).
2. Duxbury, T. C., and Acton, C. H., Jr., "Onboard Optical Navigation Data from Mariner '71," Institute of Navigation paper presented at the National Space Meeting, Orlando, Florida, March 15-16, 1972.
3. Rhoads, J. W., "A Technique for Computation of Star Magnitudes Relative to an Optical Sensor," NASA TM 33-586, Dec. 30, 1972.

APPENDIX K
EPHEMERIS THEORY FOR PHOBOS AND DEIMOS

APPENDIX K
EPHEMERIS THEORY FOR PHOBOS AND DEIMOS

by
George H. Born

The purpose of this Appendix is to present the general perturbation theory for the motion of Phobos and Deimos which was used in processing the TV data of the natural satellites taken by the Mariner 9 spacecraft.

Phobos and Deimos, Mars' two natural satellites, are in close proximity to Mars and move in nearly circular orbits with small inclinations to Mars' equator. They have orbital periods of 7.7 and 30.3 hours respectively. They are quite small, being on the order of 10 km in diameter. Their orbits are strongly perturbed by Mars' oblateness and, in the case of Deimos, solar perturbations are significant. For a discussion of their dynamical characteristics, see Ref. 1.

Since Phobos and Deimos are in near-circular, low-inclination orbits, it is advantageous to use a non-singular set of orbital elements to describe their motion. Accordingly the following set of elements was chosen:

$$\left. \begin{aligned} a \\ h = \sin I \sin \Omega \\ k = \sin I \cos \Omega \\ A = e \sin (\omega + \Omega) \\ B = e \cos (\omega + \Omega) \\ \delta = \Omega + \omega + M \end{aligned} \right\} \quad (1)$$

where

- a = semimajor axis
- e = eccentricity
- I = inclination relative to Mars equator
- Ω = longitude of ascending node
- ω = argument of periapsis
- M = mean anomaly

The associated differential equations are obtained by differentiating the above expressions and substituting Lagrange's planetary equations (see Ref. 2). The equations are then solved by substituting the appropriate disturbing function and then analytically integrating the equations by assuming a secularly precessing ellipse as the reference solution.

DISTURBING FUNCTION

Kaula's form of the disturbing function for both the primary and third body effects is used here. The potential function for the primary body is given by (see Ref. 3)

$$\begin{aligned}
 V = \sum_{\ell=0}^{\infty} \sum_{m=0}^{\ell} \frac{\mu R^{\ell}}{a^{\ell+1}} \sum_{p=0}^{\ell} \sum_{q=-\infty}^{\infty} F_{\ell mp}^{(I)} G_{\ell pq}(e) \left\{ \begin{array}{l} \left[C_{\ell m} \right]_{\ell-m \text{ even}}^{\ell-m \text{ even}} \\ \left[-S_{\ell m} \right]_{\ell-m \text{ odd}}^{\ell-m \text{ odd}} \end{array} \right. \cos \Phi_{\ell mpq} \\
 + \left. \begin{array}{l} \left[S_{\ell m} \right]_{\ell-m \text{ even}}^{\ell-m \text{ even}} \\ \left[C_{\ell m} \right]_{\ell-m \text{ odd}}^{\ell-m \text{ odd}} \end{array} \right\} \sin \Phi_{\ell mpq} \quad (2)
 \end{aligned}$$

where

$$\Phi_{\ell mpq} = (\ell - 2p) \omega + (\ell - 2p + q) M + m(\Omega - \theta)$$

The quantities $F_{\ell mp}^{(I)}$ and $G_{\ell pq}(e)$ are the inclination and eccentricity functions respectively and are defined in Reference (3). The eccentricity function is of order e^q hence only a few terms need be carried in this expansion.

The third-body disturbing function is given by Kaula in Ref. (4) as

$$\begin{aligned}
 R = \sum_{\ell=2}^{\infty} \frac{\mu^* R^{\ell}}{a^{*\ell+1}} \sum_{m=0}^{\ell} K_m \frac{(\ell - m)!}{(\ell + m)!} \sum_{p=0}^{\ell} \sum_{q=-\infty}^{\infty} \sum_{s=0}^{\ell} \sum_{j=-\infty}^{\infty} \\
 F_{\ell mp}^{(I)} H_{\ell pq}(e) F_{\ell ms}^{(I^*)} G_{\ell sj}(e^*) \cos \gamma_{\ell mpsq} \quad (3)
 \end{aligned}$$

171<

where

$$Y_{\ell m p s q j} = (\ell - 2p)\omega + (\ell - 2p + q)M - (\ell - 2s)\omega^* - (\ell - 2s + j)M^* + m(\Omega - \Omega^*)$$

and

$$K_m = \begin{cases} 1, & m = 0 \\ 2, & m \neq 0 \end{cases}$$

where the quantities denoted by the asterisk refer to the sun's orbit relative to Mars. Once again only a few terms need be included in the infinite series since the eccentricities are small.

The disturbing functions given by Equations (2) and (3) may now be differentiated with respect to the orbital elements and substituted into the differential equations for the nonsingular elements. This system of equations may then be integrated directly under the assumption that the reference orbit is a secularly precessing ellipse, i. e., the quantities a , e , I , a^* , e^* , I^* , ω^* , Ω^* are constant and Ω , ω , M and M^* are linear functions of time. The resulting solution is given by (see Ref. 2 for details)

$$a = a_0 + \left(\sum_{\ell, m} \frac{2\bar{n}a_e^\ell}{\bar{a}^{-\ell-1}} \tilde{q}PE_6 + \sum_{\ell} \sum_{m} 2\alpha_{\ell}^* \frac{Y_m}{\bar{n}} \frac{\bar{a}^{-\ell-1}}{\bar{a}^{-\ell-1}} \tilde{q}CE_{12} \right) \Bigg|_{t_0}^t \quad (4)$$

$$h = \sin I_0 \sin(\Omega_0 + \dot{\Omega}_c \Delta t) + \sum_{\ell, m} \frac{\bar{n}a_e^\ell}{\bar{K}\bar{a}^{-\ell}} \left[\frac{\partial P}{\partial \bar{I}} E_1 + P \cot \bar{I} (\tilde{p} \cos \bar{I} - m) E_4 \right] \Bigg|_{t_0}^t + \sum_{\ell} \sum_{m} \alpha_{\ell}^* Y_m \frac{\bar{a}^{-\ell-2}}{\bar{n}\bar{K}} \left[\frac{\partial C}{\partial \bar{I}} E_7 + C \cot \bar{I} (\tilde{p} \cos \bar{I} - m) E_{10} \right] \Bigg|_{t_0}^t \quad (5)$$

172<

$$\begin{aligned}
k = & \sin I_0 \cos(\Omega_0 + \dot{\Omega}_c \Delta t) + \sum_{l, m} \frac{\bar{n} a_e^l}{\bar{K} a^l} \left[-\frac{\partial P}{\partial I} E_2 + P \cot \bar{I} (\tilde{p} \cos \bar{I} - m) E_3 \right] \Bigg|_{t_0}^t \\
& + \sum_l \sum_m \alpha_l^* \gamma_m \frac{\bar{a}^{\ell-2}}{\bar{n} \bar{K}} \left[-\frac{\partial C}{\partial I} E_8 + \cot \bar{I} (\tilde{p} \cos \bar{I} - m) C E_9 \right] \Bigg|_{t_0}^t \quad (6)
\end{aligned}$$

$$\begin{aligned}
A = & e_0 \sin(\omega_0 + \dot{\omega}_c \Delta t) + \sum_{l, m} \frac{\bar{n} a_e^l}{\bar{a}^l} \left\{ \left[\frac{\bar{e} \beta}{\bar{K}} \frac{\partial P}{\partial I} + \bar{K} \frac{\partial P}{\partial e} \right] E_1 \right. \\
& + \bar{K} P \left(\frac{-\bar{e} \tilde{p}}{1 + \bar{K}} + \frac{q \bar{K}}{\bar{e}} \right) E_4 \Bigg|_{t_0}^t + \sum_l \sum_m \frac{\alpha_l^* \bar{a}^{\ell-2}}{\bar{n}} \gamma_m \left\{ \left[\frac{\bar{e} \beta}{\bar{K}} \frac{\partial C}{\partial I} + \bar{K} \frac{\partial C}{\partial e} \right] E_7 \right. \\
& \left. \left. + \bar{K} C \left(\frac{-\tilde{p} \bar{e}}{1 + \bar{K}} + \frac{q \bar{K}}{\bar{e}} \right) E_{10} \right\} \Bigg|_{t_0}^t \quad (7)
\end{aligned}$$

$$\begin{aligned}
B = & e_0 \cos[\omega_0 + \dot{\omega}_c \Delta t] + \sum_{l, m} \frac{\bar{n} a_e^l}{\bar{a}^l} \left\{ \left[\frac{-\bar{e} \beta}{\bar{K}} \frac{\partial P}{\partial I} - \bar{K} \frac{\partial P}{\partial e} \right] E_2 \right. \\
& + \bar{K} P \left[\frac{-\bar{e} \tilde{p}}{1 + \bar{K}} + \frac{q \bar{K}}{\bar{e}} \right] E_3 \Bigg|_{t_0}^t + \sum_l \sum_m \frac{\alpha_l^* \bar{a}^{\ell-2}}{\bar{n}} \gamma_m \left\{ \left[\frac{-\bar{e} \beta}{\bar{K}} \frac{\partial C}{\partial I} \right. \right. \\
& \left. \left. - \bar{K} \frac{\partial C}{\partial e} \right] E_8 + \bar{K} C \left[\frac{-\tilde{p} \bar{e}}{1 + \bar{K}} + \frac{q \bar{K}}{\bar{e}} \right] E_9 \right\} \Bigg|_{t_0}^t \quad (8)
\end{aligned}$$

$$\begin{aligned}
\delta = & \delta_0 + \dot{\delta}_c \Delta t + \sum_{\ell, m} \frac{\bar{n} a_e^\ell}{\bar{a}^\ell} \left\{ \left[\frac{\beta}{\bar{K}} \frac{\partial P}{\partial I} + 2(\ell + 1)P \right. \right. \\
& \left. \left. + \frac{\bar{e} \bar{K}}{1 + \bar{K}} \frac{\partial P}{\partial e} - 3\bar{n}P \frac{\tilde{q}}{\dot{\Phi}_{\ell mpq}^-} \right] E_5 \right\} \Bigg|_{t_0}^t \\
& + \sum_{\ell} \sum_m \alpha_\ell^* \frac{\bar{a}^{\ell-2}}{\bar{n}} \gamma_m \left\{ \left[\frac{\beta}{\bar{K}} \frac{\partial C}{\partial I} \right. \right. \\
& \left. \left. - 2\ell C + \frac{\bar{e} \bar{K}}{1 + \bar{K}} \frac{\partial C}{\partial e} - 3\bar{n}C \frac{\tilde{q}}{\dot{\gamma}_{\ell mpsqj}^-} \right] E_{11} \right\} \Bigg|_{t_0}^t \quad (9)
\end{aligned}$$

where

$$\alpha_\ell^* = \frac{\mu^*}{a^{*\ell+1}}, \quad \beta = \frac{\sin \bar{I}}{1 + \cos \bar{I}}, \quad \gamma_m = K_m \frac{(\ell - m)!}{(\ell + m)!} \text{ and } (\dot{})_c$$

indicates constant rate and where the overbars indicate mean quantities.

For $\ell - m$ even, the E_i 's are

$$\left. \begin{aligned}
E_1 &= \frac{J_{\ell m}}{2} \left[\frac{\sin \Phi_{\ell mpq}^-}{\dot{\Phi}_{\ell mpq}^-} + \frac{\sin \Phi_{\ell mpq}^+}{\dot{\Phi}_{\ell mpq}^+} \right] \\
E_2 &= \frac{J_{\ell m}}{2} \left[\frac{\cos \Phi_{\ell mpq}^-}{\dot{\Phi}_{\ell mpq}^-} - \frac{\cos \Phi_{\ell mpq}^+}{\dot{\Phi}_{\ell mpq}^+} \right] \\
E_3 &= \frac{J_{\ell m}}{2} \left[\frac{\cos \Phi_{\ell mpq}^-}{\dot{\Phi}_{\ell mpq}^-} - \frac{\cos \Phi_{\ell mpq}^+}{\dot{\Phi}_{\ell mpq}^+} \right]
\end{aligned} \right\} \quad (10a)$$

$$\left. \begin{aligned}
E_4 &= -\frac{J_{\ell m}}{2} \left[\frac{\sin \Phi_{\ell mpq}^-}{\dot{\Phi}_{\ell mpq}^-} - \frac{\sin \Phi_{\ell mpq}^+}{\dot{\Phi}_{\ell mpq}^+} \right] \\
E_5 &= J_{\ell m} (\sin \Phi_{\ell mpq}) / \dot{\Phi}_{\ell mpq} \\
E_6 &= J_{\ell m} (\cos \Phi_{\ell mpq}) / \dot{\Phi}_{\ell mpq}
\end{aligned} \right\} \quad (10b)$$

If $\ell - m$ is odd, E_1 is replaced by $-E_3$, E_2 by $-E_4$, E_3 by E_1 , E_4 by E_2 , E_5 by $-E_6$, and E_6 by E_5 . The quantities E_7 through E_{12} are obtained by replacing $\Phi_{\ell mpq}$ with $\gamma_{\ell mpsqj}$ and omitting $J_{\ell m}$ in Eq. (10).

In addition,

$$\left. \begin{aligned}
K &= \sqrt{1 - e^2} \\
P &= \sum_{p=0}^{\ell} \sum_{q=-\infty}^{\infty} F_{\ell mp}^{(I)} G_{\ell pq}(e) \\
C &= \sum_{p=0}^{\ell} \sum_{q=-\infty}^{\infty} \sum_{s=0}^{\ell} \sum_{j=-\infty}^{\infty} F_{\ell mp}^{(I)} H_{\ell pq}(e) F_{\ell ms}^{(I*)} G_{\ell sj}(e^*)
\end{aligned} \right\} \quad (11)$$

The Φ and $\dot{\Phi}$ functions are defined by

$$\Phi_{\ell mpq} = \tilde{p}\omega + \tilde{q}M + m(\Omega - \theta - \lambda_{\ell m})$$

$$\dot{\Phi}_{\ell mpq} = \tilde{p}\dot{\omega}_c + \tilde{q}\dot{n} + m(\dot{\Omega}_c - \dot{\theta})$$

$$\Phi_{\ell mpq}^+ = (\tilde{p} + b)\omega + \tilde{q}M + (m + 1)\Omega - m(\theta + \lambda_{\ell m})$$

$$\dot{\Phi}_{\ell mpq}^+ = (\tilde{p} + b)\dot{\omega}_c + \tilde{q}\dot{n} + (m + 1)\dot{\Omega}_c - m\dot{\theta}$$

$$\Phi_{lmpq}^- = (\tilde{p} - b)\omega + \tilde{q}M + (m - 1)\Omega - m(\theta + \lambda_{lm})$$

$$\dot{\Phi}_{lmpq}^- = (\tilde{p} - b)\dot{\omega}_c + \tilde{q}\dot{n} + (m - 1)\dot{\Omega}_c - m\dot{\theta}$$

The γ and $\dot{\gamma}$ functions are defined by

$$\gamma_{lmpsqj}^- = \tilde{p}\omega + \tilde{q}M - \tilde{s}\omega^* - \tilde{j}M^* + m(\Omega - \Omega^*)$$

$$\dot{\gamma}_{lmpsqj}^- = \tilde{p}\dot{\omega}_c + \tilde{q}\dot{n} - \tilde{j}\dot{n}^* + m\dot{\Omega}_c$$

$$\gamma_{lmpsqj}^+ = (\tilde{p} - b)\omega + \tilde{q}M - \tilde{s}\omega^* - \tilde{j}M^* + (m - 1)\Omega - m\Omega^*$$

$$\dot{\gamma}_{lmpsqj}^+ = (\tilde{p} - b)\dot{\omega}_c + \tilde{q}\dot{n} - \tilde{j}\dot{n}^* + (m - \alpha)\dot{\Omega}_c$$

$$\gamma_{lmpsqj}^- = (\tilde{p} + b)\omega + \tilde{q}M - \tilde{s}\omega^* - \tilde{j}M^* + (m + 1)\Omega - m\Omega^*$$

$$\dot{\gamma}_{lmpsqj}^- = (\tilde{p} + b)\dot{\omega}_c + \tilde{q}\dot{n} - \tilde{j}\dot{n}^* + (m + 1)\dot{\Omega}_c$$

(12)

and

$$b = 0 \text{ for Eqs. (5) and (6)}$$

$$b = 1 \text{ for Eqs. (7) and (8)}$$

$$\tilde{p} = l - 2p$$

$$\tilde{q} = l - 2p + q$$

$$\tilde{s} = l - 2h$$

$$\tilde{j} = l - 2h + j$$

(13)

The secular rates of change of the elements are given by

$$\left. \begin{aligned}
 \dot{\Omega}_c &= \sum_{\ell} \frac{\mu a_e^{\ell}}{n a^{\ell+3} K} \csc I \frac{\partial P}{\partial I} J_{\ell 0} + \sum_{\ell} \frac{\mu^*}{a^{*\ell+1}} \frac{a^{\ell-2}}{n K} \csc I \frac{\partial C}{\partial I} \\
 \dot{\omega}_c &= \sum_{\ell} \frac{\mu a_e^{\ell} K}{n a^{\ell+3}} \left(\frac{\cot I}{K^2} \frac{\partial P}{\partial I} + \frac{1}{e} \frac{\partial P}{\partial e} \right) J_{\ell 0} \\
 &+ \sum_{\ell} \frac{\mu^* a^{\ell-2}}{n a^{*\ell+1}} K \left(-\frac{\cot I}{K^2} \frac{\partial C}{\partial I} + \frac{1}{e} \frac{\partial C}{\partial e} \right) \\
 \dot{M}_c &= n - \sum_{\ell} \frac{\mu a_e^{\ell}}{n a^{\ell+2}} \left[\left(\frac{K^2}{a e} \right) \frac{\partial P}{\partial e} - \frac{2(\ell+1)}{a} P \right] J_{\ell 0} \\
 &- \sum_{\ell} \frac{\mu^* a^{\ell-2}}{n a^{*\ell+1}} \left(\frac{K^2}{e} \frac{\partial C}{\partial e} + 2\ell c \right)
 \end{aligned} \right\} (14)$$

where

$$P = G_{\ell(\ell/2)0}^{(e)} F_{\ell 0(\ell/2)}^{(I)}$$

$$C = F_{\ell 0(\ell/2)}^{(I)} H_{\ell(\ell/2)0}^{(e)} F_{\ell 0(\ell/2)}^{(I^*)} G_{\ell(\ell/2)0}^{(e^*)}$$

The dummy index, ℓ , is summed over even values from 2 through the number of terms carried in the disturbing function.

The solutions given by Eqs. (4) through (9) are not complete through first order since they do not contain the first-order long-period terms in J_2 which result from a second-order solution. These terms may be obtained by substituting the first-order solutions into the right-hand side of the differential equations and integrating. The first-order terms are given by Brouwer in Ref. 5. The theory presented here has an accuracy potential of 0.5 km for periods of a few years.

In the case of Phobos there are additional significant first-order terms which result from interaction of the oblateness and solar effects. Solar gravity perturbations cause a long period variation in the inclination of Deimos orbit relative to Mars equator. This perturbation has an amplitude of 0.9° and a period of 54 years which corresponds to the period of the ascending node of Deimos orbit relative to Mars' equator. This change in inclination induces a variation in the secular rate of the mean longitude, δ , and a corresponding long-period variation in the mean longitude.

The interaction term between the solar and J_2 perturbations can be modeled with the following expression

$$\Delta \delta = \int \frac{\partial \dot{\delta}}{\partial I} \Delta I + \frac{1}{2} \int \frac{\partial^2 \dot{\delta}}{\partial I^2} \Delta I^2 \quad (15)$$

where for $I \simeq 0$ and $e \simeq 0$

$$\frac{\partial \dot{\delta}}{\partial I} = -\frac{7}{2} \dot{\omega}_c \sin I \quad (16)$$

$$\frac{\partial^2 \dot{\delta}}{\partial I^2} = \frac{\dot{\omega}_c}{2} \left[1 - \frac{8 \cos 2I}{\cos I} \right] \quad (17)$$

The second-order term in Eq. (15) must be retained since $\sin I$ is the same size as ΔI . Consequently, when Eqs. (16) and (17) are substituted into Eq. (15), both terms are the same order of magnitude. The long-period variation in mean longitude given by Eq. (15) has an amplitude of 0.3° and a period of 54 years for Deimos.

Although it is possible to reference the motion of Phobos and Deimos to the Laplacian plane (see Ref. 6) there seems to be no real advantage to doing so since it complicates considerably the formulation of the disturbing function and does not eliminate the long-period perturbation in mean longitude given by Eq. (15). Referencing to the Laplacian plane does eliminate large amplitude variations in inclination, node and argument of periapsis which occur relative

to Mars' equator; however, these are included in the general perturbation theory given here and present no problem.

The solutions for the orbital elements were differentiated with respect to the mean orbital elements as well as the harmonic coefficients so that differential corrections could be applied to these quantities. Hence, the program developed from this satellite theory was capable of processing optical data to determine the state of the satellites and the Mars gravity field, as well as TV parameters. Results obtained from this program are given in Ref. (7).

REFERENCES

1. Burns, Joseph A., "Dynamical Characteristics of Phobos and Deimos," Review of Geophysics and Space Physics, Vol. 10, No. 2, May, 1972.
2. Born, G. H. and Tapley, B. D., "An Approximate Solution for the Short Term Motion of a Lunar Satellite," Journal of Spacecraft and Rockets, May, 1969.
3. Kaula, W. M., Theory of Satellite Geodesy, Blaisdell Publishing Co., Waltham, Mass., 1966.
4. Kaula, W. M., "Development of the Lunar and Solar Disturbing Functions for a Close Satellite," Astronomical Journal, V. 67, No. 5, June, 1962.
5. Brouwer, D., "The Problem of Artificial Satellite Theory without Drag," Astronomical Journal, V. 64, No. 1274, Nov. 1959.
6. Sinclair, A. T., "The Motions of the Satellites of Mars," Mon. Not. R. Astr. Soc., 155, 249-274, 1972.
7. Born, G. H., "Mars Physical Parameters as Determined from Mariner 9 Observations of the Natural Satellites", AAS/AIAA Astrodynamics Conference, July 16-18, 1973, Vail, Colorado. To be published in the Journal of Geophysical Research. (Appendix 14 of this report.)

APPENDIX L
MM'71 ORBITAL SEQUENCE SATELLITE PICTURE SUMMARY

180<

MM'71 ORBITAL SEQUENCE SATELLITE PICTURE SUMMARY

C. H. Acton and W. G. Breckenridge

This appendix summarizes the camera pointing (clock, cone, twist) and line and pixel center of image coordinates obtained for the orbital sequence satellite pictures. The pointing estimates are based on an attitude control system and a scan platform calibration using a series of star pictures obtained during Rev. 72. Two exceptions are the first Rev. 161 picture, pointing for which was determined from observations of two stars, and the Rev. 676 picture, pointing for which was determined from observation of 10 stars. The table lists the revolution number during which the picture was taken, the target satellite, Greenwich Mean Time, camera identification, pointing angles and the line and pixel center of image coordinates.

All pointing angles are referenced to Canopus unless indicated otherwise. The symbols A and B in the camera column refer to the wide and narrow angle camera, respectively. A_f and B_f refer to false shutter images from the two cameras. False shutter images are residual images on the vidicon from the automatic shuttering of the cameras 84 seconds before programmed shutter time.

A complete catalog of all the Mariner 9 satellite pictures is to be published in the reference.* Included will be such information as range shutter time, phase angle and overlays for each satellite image.

*Veverka, J., et al, "Mariner 9 Satellite Picture Catalog"

Icarus 1974 (In press)

TABLE 1 SUMMARY OF ORBITAL SEQUENCE SATELLITE PICTURES

Rev. No.	Target	Day	GMT	Camera	Pointing-Deg.			Center of Image	
					Clock	Cone	Twist	Pixel	Line
25	Deimos	11/26/71	11 31 47.46	B _F	263.162	112.499	0.165	521	445
25	Deimos	11/26/71	11 33 11.46	B	263.101	112.426	0.141	240	127
27	Phobos	11/27/71	11 36 35.13	B _F	104.666	129.218	0.420	683	178
27	Phobos	11/27/71	11 37 17.13	A _F	103.954	129.080	30.332	462	378
27	Phobos	11/27/71	11 38 41.13	A	103.928	129.000	30.297	480	458
31	Phobos	11/29/71	13 10 10.54	B	110.933	103.626	0.177	660	175
33	Phobos	11/30/71	13 04 28.20	A _F	101.377	127.824	30.004	443	332
33	Phobos	11/30/71	13 05 52.25	A	101.370	127.814	29.949	498	300
34	Phobos	12/01/71	00 11 34.12	B	157.443	121.338	- 0.0240	805	63
34	Phobos	12/01/71	00 12 58.12	B	158.206	119.971	- 0.0737	733	450
35	Deimos	12/01/71	11 20 45.98	B _F	275.879	144.095	- 0.0608	648	283
41	Phobos	12/04/71	11 53 27.11	B	133.375	145.723	0.0484	355	652
41	Phobos	12/04/71	12 40 21.11	A	195.718	104.474	30.1762	368	287
41	Phobos	12/04/71	12 41 45.10	A	196.574	102.921	30.2113	378	282
41	Phobos	12/04/71	12 43 09.10	A	197.277	101.580	30.2335	379	282
43	Phobos	12/05/71	10 58 02.00	B	97.259	114.245	0.2419	521	540
43	Phobos	12/05/71	10 58 44.00	A	96.649	114.102	30.3205	460	423
43	Phobos	12/05/71	11 14 08.00	A	110.088	106.802	30.0342	443	460
47	Phobos	12/07/71	13 01 44.00	A	107.493	114.007	30.2123	479	273
48	Phobos	12/08/71	00 24 14.10	B	196.095	131.517	- 0.1960	247	347
48	Phobos	12/08/71	00 25 38.10	B	197.027	129.408	- 0.2597	536	616
53	Phobos	12/10/71	12 46 01.00	B	229.494	153.973	- .1739	364	246

L-2

182

TABLE 1 (continued)

Rev. No.	Target	Day	GMT	Camera	Pointing-Deg.			Center of Image	
					Clock	Cone	Twist	Pixel	Line
57	Phobos	12/12/71	11 31 36.00	B	148.870	128.126	- .1909	233	515
63	Deimos	12/15/71	10 19 11.00	B	256.899	106.617	- .0029	643	187
63	Deimos	12/15/71	10 19 53.00	A	256.248	106.437	30.2032	430	340
63	Deimos	12/15/71	10 21 17.00	A	256.125	106.335	30.2335	398	332
63	Deimos	12/15/71	10 22 41.00	A	255.971	106.379	30.3020	358	323
73	Deimos	12/20/71	9 38 46.53	B	299.413	158.426	- 0.0013	303	284
73	Phobos	12/20/71	10 40 22.52	B	121.174	122.601	0.249	306	391
77	Phobos	12/22/71	12 27 15.92	A	110.040	99.783	30.4422	361	539
77	Phobos	12/22/71	12 38 39.92	A	110.109	99.653	30.4307	397	472
77	Phobos	12/22/71	12 30 03.92	A	110.168	99.519	30.3740	431	403
77	Phobos	12/22/71	12 30 45.92	B	110.771	99.585	0.0679	546	356
77	Phobos	12/22/71	12 31 27.92	A	110.220	99.398	30.2742	461	328
80	Phobos	12/22/71	23 39 09.50	B	196.245	97.047	- 0.3101	366	219
87	Phobos	12/27/71	11 01 20.50	B	161.910	138.680	0.0461	493	329
87	Phobos	12/27/71	11 02 44.50	B	164.934	138.229	0.2142	337	235
89	Phobos	12/28/71	10 15 02.22	A	126.500	99.692	30.4149	452	333
89	Phobos	12/28/71	10 15 44.22	B	127.069	99.849	0.1743	508	603
111	Deimos	1/08/72	08 44 11.80	B	282.651	149.314	0.2010	544	466
117	Phobos	1/11/72	10 04 22.92	B	103.235	124.943	0.1086	268	349
121	Deimos	1/13/72	10 30 46.33	B	241.810	135.257	- 0.1059	610	236
129j	Phobos	1/17/72	11 22 09.17	B	171.474	161.372	- 0.2716	576	273

TABLE 1 (continued)

Rev. No.	Target	Day	GMT	Camera	Pointing-Deg.			Center of Image	
					Clock	Cone	Twist	Pixel	Line
129	Phobos	1/17/72	11 27 03.17	A	189.415	161.226	28.400	431	377
129	Phobos	1/17/72	11 28 27.17	A	197.984	160.193	28.345	438	300
129	Phobos	1/17/72	11 29 09.17	B	199.491	160.161	- 0.8730	691	334
129	Phobos	1/17/72	11 29 51.17	A	198.168	160.023	28.2088	467	408
131	Phobos	1/18/72	10 25 20.90	B	115.093	134.699	- 0.0813	558	348
133	Phobos	1/19/72	10 25 56.61	B	164.762	109.293	0.1736	628	214
145	Phobos	1/25/72	09 57 18.89	B	93.852	109.939	- 0.0374	379	278
149	Deimos	1/27/72	07 39 54.34	B	292.006	114.592	0.0142	571	505
150	Phobos	1/28/72	00 30 00.13	A	286.947	116.153	30.1702	461	343
150	Phobos	1/28/72	00 30 42.13	B	287.515	116.162	0.0945	455	342
159	Deimos	2/01/72	09 25 04.88	B	237.069	129.119	- 0.3428	601	446
161	Phobos	2/02/72	10 11 52.58	B	114.9596	126.6100	0.2155	238	228
161	Phobos	2/02/72	11 03 40.57	B _f	204.889	135.125	- 0.2897	642	211
171	Phobos	2/07/72	12 55 09.11	A	303.236	108.744	30.1777	493	348
171	Phobos	2/07/72	12 55 51.11	B	303.817	108.855	- 0.0129	715	410
197	Deimos	2/20/72	08 08 18.62	B _f	251.760	106.718	0.0999	660	655
197	Deimos	2/20/72	08 09 42.62	B	251.570	106.742	0.0542	512	405
207	Phobos	2/25/72	10 01 53.16	B	157.468	117.064	- 0.1189	465	462
221	Phobos	3/03/72	10 21 27.14	B	176.012	140.142	- 0.3932	390	250
676	Phobos	10/17/72	00 53 14.00	B	96.553*	106.872*	0.1401	446	278

*Clock and cone angles referred to VEGA

APPENDIX M
RESULTS OF ORBITAL PHASE NAVIGATION STUDY
USING SATELLITE DATA

APPENDIX M
RESULTS OF ORBITAL PHASE NAVIGATION STUDY
USING SATELLITE DATA

by
George H. Born

INTRODUCTION

The TV pictures of Phobos and Deimos taken by Mariner 9 have been used to improve the accuracy of the spacecraft trajectory estimate over the first 220 revolutions of the mission. The optical data used for this study is tabulated in Ref. 1 and consists of 62 A and B frames of Phobos and Deimos taken during revolution 25 through 220 of Mariner 9. The accuracy of the data and its temporal distribution is discussed more fully in Ref. 2.

It is well known that doppler solutions for the state of a spacecraft orbiting a distant body are an order of magnitude less accurate in the node of the orbit relative to the plane perpendicular to the Earth-Mars direction (referred to as Ω_{pos}) than any other component of the state. This is because determination of Ω_{pos} depends on relative Earth-Mars motion which is a slowly varying quantity. References 3 and 4 give more detail regarding the indeterminacy of Ω_{pos} . For Mariner 9 the standard deviation in the discontinuities for Ω_{pos} from solution to solution ranged from 0.02° to 0.04° throughout the mission depending on tracking coverage and data noise (Ref. 4). Figure 1, which is taken from Ref. 4, shows the deviation in the plane of the sky orientation angles relative to their values at the initial apoapsis value. As expected from pre-flight covariance analysis and illustrated by this figure, the inclination and argument of periapsis solutions are continuous while the nodal history has discontinuities from solution to solution.

The TV pictures of Phobos and Deimos can be used in conjunction with the radiometric data to yield continuous histories for Ω_{pos} throughout the period where optical data of the satellites is available. Although optical data can be very effective in determining Ω_{pos} when combined with short arcs of radiometric data (Ref. 5), the scarcity of optical data taken by Mariner 9 of the satellite

does not allow this fact to be demonstrated with real data. However, a long arc analysis of combined optical and radiometric data from Mariner 9 can be performed. This analysis is described here.

METHOD OF SOLUTION

The radio and optical data were processed in a two-stage filter. Apoapsis state vectors, as determined from one revolution fit of the doppler data, in the first stage of the filter, were used as the observables for the second stage of the filter. Here they are processed simultaneously with the line and pixel value for the center of mass (assumed to be at the center of figure) of the satellites to yield solutions for both the satellite's and the spacecraft's states, Mars gravity field, spin axis direction, mass, and TV camera parameters.

A first-order analytical theory which includes the effects of zonal and tesseral harmonics as well as solar gravity and radiation pressure is used to propagate the motion of Mariner 9, Phobos and Deimos. Since Mariner 9 is in shallow resonance with Mars' even-order tesseral harmonics, large down-track perturbations are induced in the orbital motion. As a result, a first-order analytical theory is inadequate to model the spacecraft's motion. Consequently, the theory was extended to include the dominant second-order effects of resonance (Ref. 2). Use of analytical theories allows rapid and inexpensive processing of the data. In addition, it allows long arc processing of the data. For example, in the results described here only two sets of initial conditions were estimated for the spacecraft: one at apoapsis number 5 and one after the second trim maneuver at apoapsis 95.

Optical Residuals Relative to the Plane of the Sky

In order to evaluate the potential of the optical data for determining Ω_{pos} it is convenient to rotate the residuals from the conventional camera coordinates to a coordinate system which has one component along and one component perpendicular to the Ω_{pos} direction. Figure 2 illustrates the geometry for this transformation. The angle θ varies from picture to picture as a function of viewing geometry. It is determined by

$$\theta = \tan^{-1} \left[\frac{\frac{\partial L}{\partial \Omega_{\text{pos}}}}{\frac{\partial P}{\partial \Omega_{\text{pos}}}} \right]$$

where L and P represent line and pixel. All plots in this appendix have their abscissa along and their ordinate perpendicular to the plane of the sky direction.

COMPARISON OF Ω_{pos} HISTORY FOR RADIOMETRIC AND SATELLITE DATA

The general perturbation theory described in Ref. 2 was used to determine a continuous spacecraft trajectory from a combination of radio and optical data. Since the radio solutions shown in Fig. 1 were discontinuous in Ω_{pos} from fit to fit, it is of interest to compare the continuous Ω_{pos} history from the combined data type with that of the radio-only solutions. These results are shown in Fig. 3. The solid line represents the continuous Ω_{pos} history as determined from the combined optical and radio data. The broken lines represent the Ω_{pos} history of the radio-only solutions. Prior to the trim maneuver at revolution No. 94, the combined solution differs from the mean of the radio solutions by $+0.0106^\circ$ and after the trim the combined solution differs from the mean of the radio solutions by -0.0107° . These variations from the radio mean are equivalent to approximately a 1 km shift in the spacecraft trajectory at periapsis.

Figure 4 presents the optical residuals in the pos coordinate system from both A and B frames when the spacecraft state is not included in the solution list. In other words, the spacecraft state has been fixed at values determined by doppler solutions. Included in the solution list were satellite states, the spin axis direction of Mars, and TV parameters. All A frame (wide angle) residuals have been multiplied by 10 to make them equivalent to B frame residuals. As seen from this figure the standard deviation in the Ω_{pos} direction is about 5 pixels greater than that normal to the Ω_{pos} direction. Figure 5 shows the residuals when the spacecraft state is included in the solution list. Note that the residual dispersion is practically circular now indicating that Ω_{pos} has been adjusted by the optical data. The a priori uncertainty on Ω_{pos}

for this solution was 0.05° . Values of other spacecraft state parameters were held at the radio values. The formal uncertainty on Ω_{pos} from the combined radio and optical data solution is $\sigma_{\Omega_{\text{pos}}} = 0.005^\circ$. If only the optical data is processed, $\sigma_{\Omega_{\text{pos}}} = 0.014^\circ$. This uncertainty should be realistic since it is compatible with the difference between the values of Ω_{pos} determined independently by the radio plus Phobos/Deimos data and the Mars landmark data, as discussed in the next section.

COMPARISON OF Ω_{pos} HISTORY FOR LANDMARK AND SATELLITE DATA

The combined radio and optical data solutions for Ω_{pos} are in very good agreement with independent results obtained from processing Mars landmark data. In fact, the radio plus Phobos/Deimos results agree to 0.007° with those obtained from the landmark data before trim II and within 0.005° after the trim. This is well within the formal uncertainties of the two solutions. More details on this comparison are given in Ref. 6.

CONCLUSIONS

Preflight covariance analysis has shown that natural satellite photographs containing stars, when combined with radiometric data, can improve short-arc estimates of Ω_{pos} over those made with radiometric data alone. This is accomplished in the same manner as in the long-arc analysis discussed here, i. e., allowing the optical data to determine Ω_{pos} and the radiometric data to determine the remaining state coordinates. Unfortunately, the scarcity of Phobos/Deimos pictures, combined with the lack of stars in the pictures, made it impossible to demonstrate the feasibility of short-arc orbit determination using combinations of optical and radiometric data in the orbital phase of Mariner 9. Based on the excellent agreement for Ω_{pos} as determined independently by the satellite and landmark data, however, it is concluded that either data type is an excellent complement to radiometric data in successfully determining the long-term state history of a planetary orbiter.

REFERENCES

1. Acton, C. H., Breckenridge, W. G., "MM'71 Orbital Sequence Satellite Picture Summary." (Appendix L of this report.)
2. Born, G. H., "Mars Physical Parameters as Determined from Mariner 9 Observations of the Natural Satellites," AAS/AIAA Astrodynamics Conference, July 16-18, 1973, Vail, Colorado, to be published in the Journal of Geophysical Research. (Appendix N of this report.)
3. Lorell, J., "Orbit Determination of a Lunar Satellite," The Journal of the Astronautical Sciences, Vol. XI, No. 1, pp. 1-7, Spring, 1964.
4. Born, G., Christensen, E., Ferrari, A., Jordan, J., and Reinhold, S., "The Determination of the Satellite Orbit of Mariner 9", Celestial Mechanics, Vol. 9, No. 2, 1974 (in press).
5. Duxbury, T., Born, G. H., "Tracking Phobos and Deimos Aboard an Orbiting Spacecraft," AAS Paper No. 71-372, AAS/AIAA Astrodynamics Conference, Ft. Lauderdale, Florida, August 1971. (Appendix D of this report.)
6. Mohan, S., "Results of Navigation Study Using Landmark Data," Appendix Q of this report.

150<

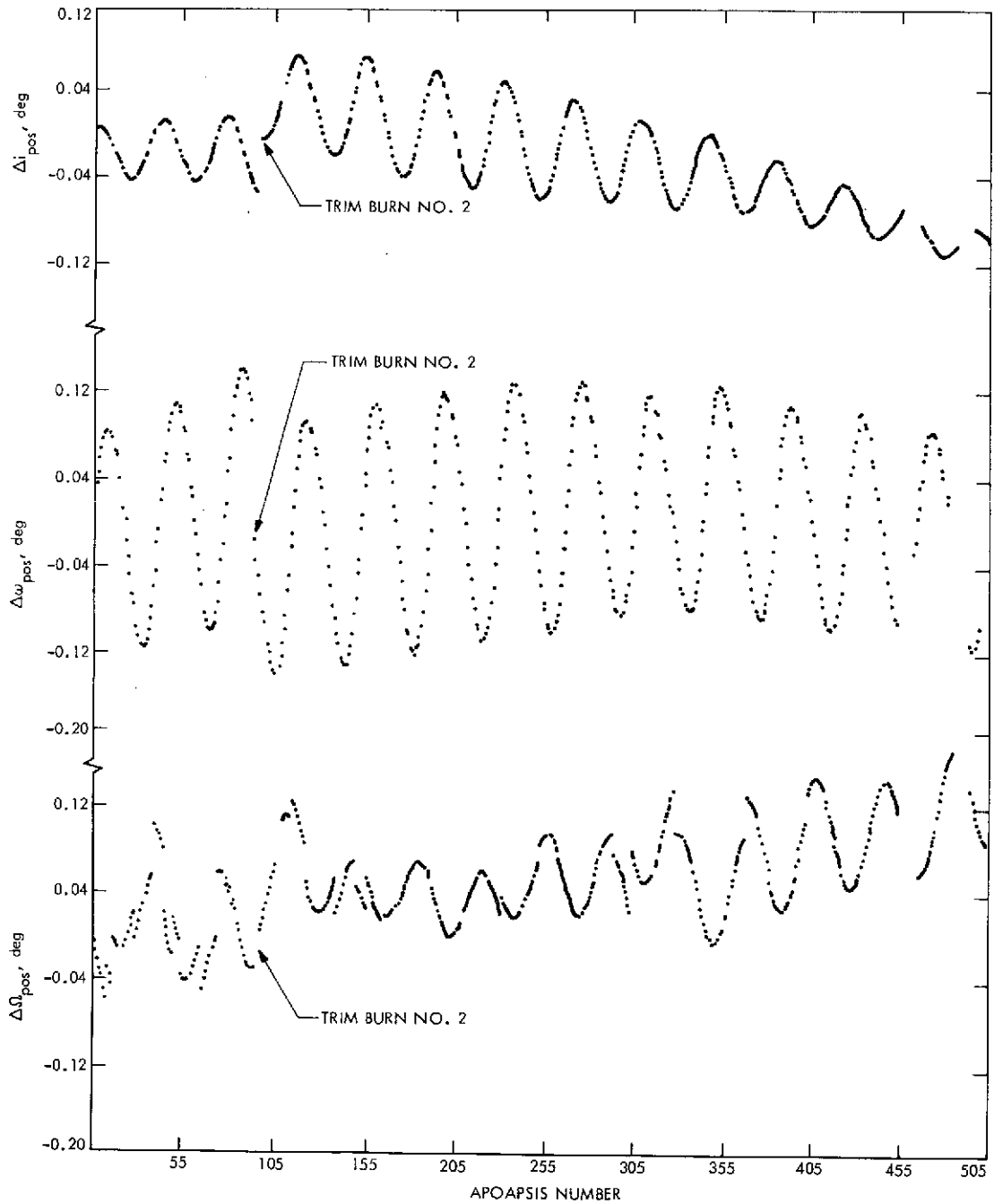


Fig. 1. Mariner 9 orientation angles relative to the plane of the sky

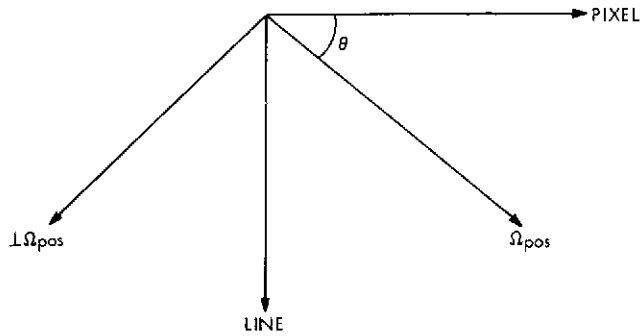


Fig. 2. Geometry of pos coordinates relative to conventional line and pixel coordinates

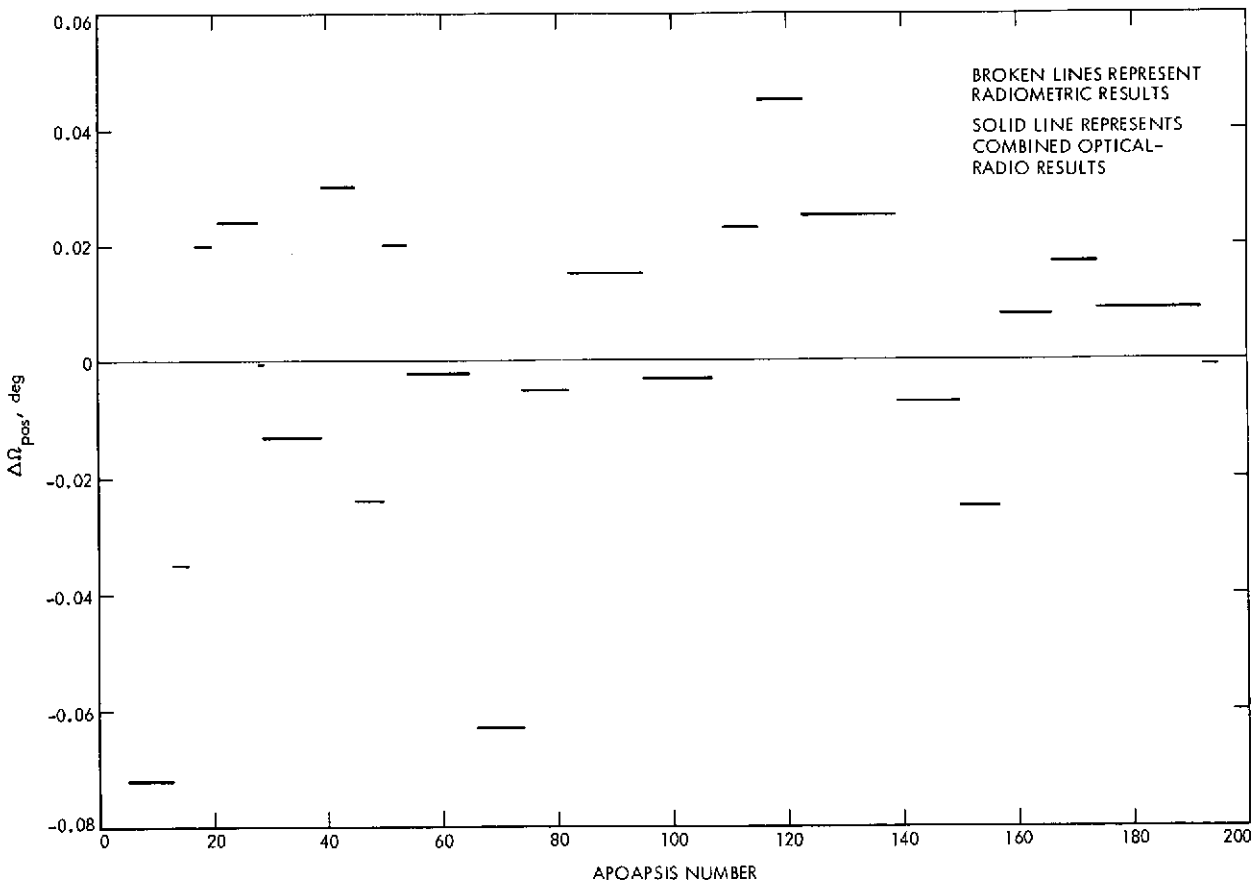


Fig. 3. Comparison of radiometric Ω_{pos} history with combined radiometric-optical results

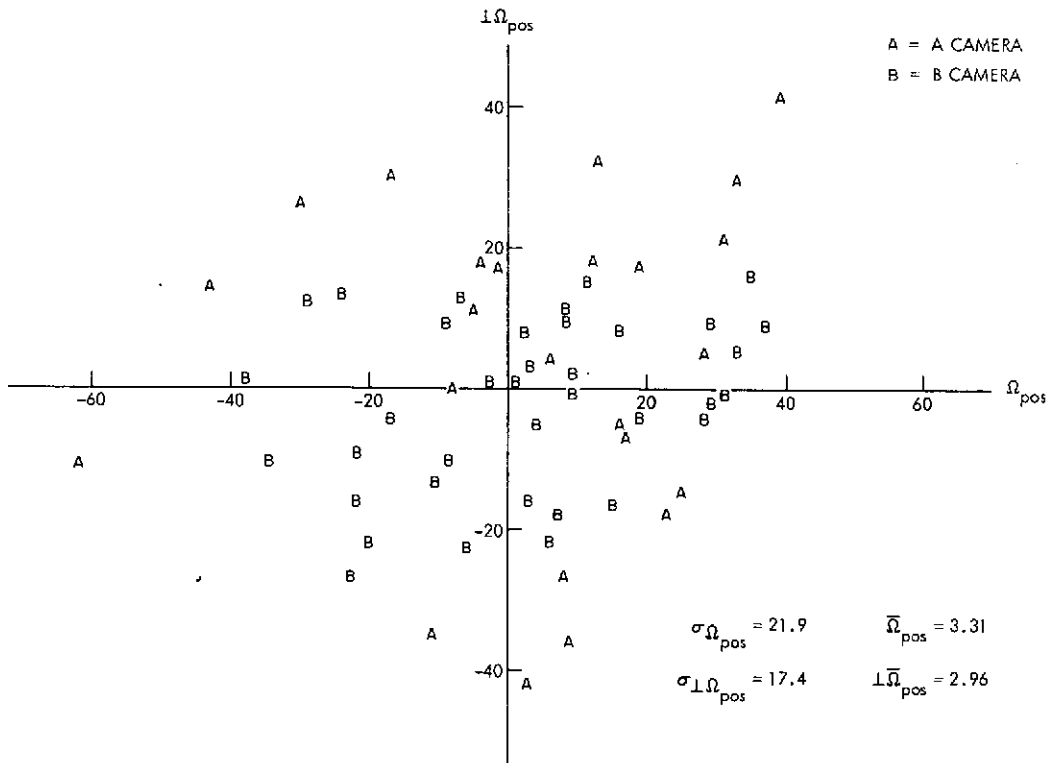


Fig. 4. Optical residuals before solving for Ω_{pos}

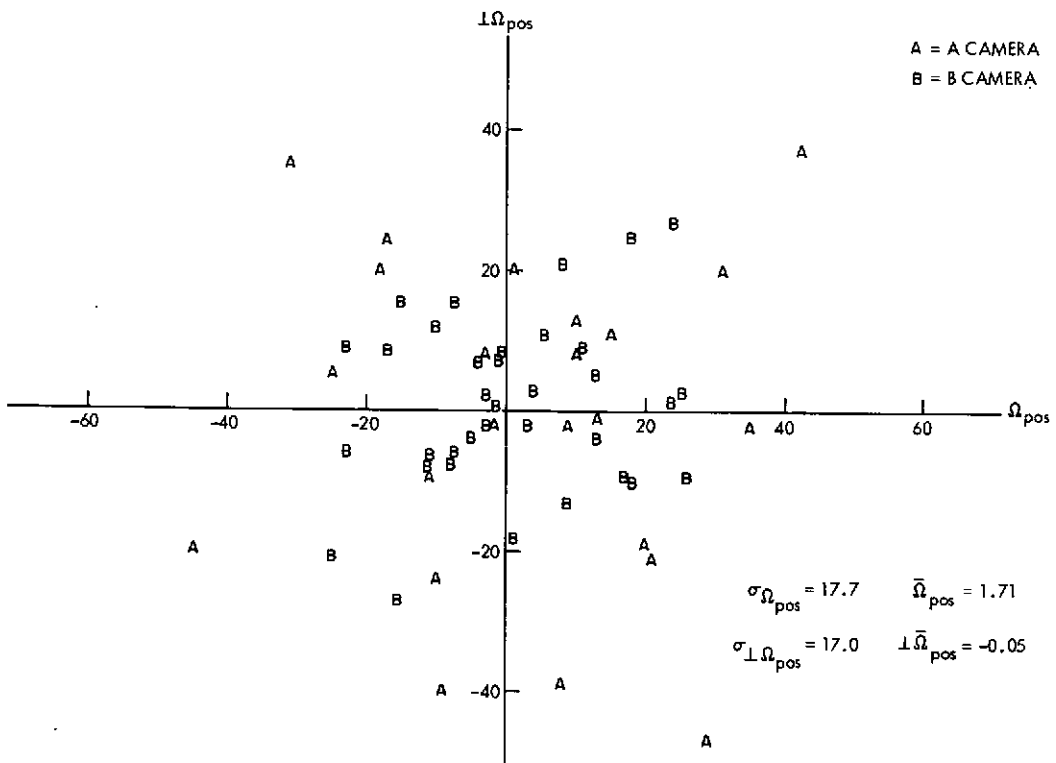


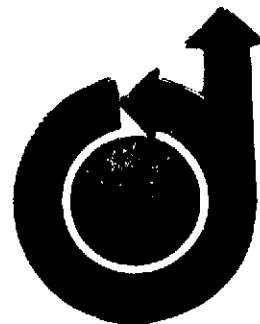
Fig. 5. Optical residuals after solving for Ω_{pos}

APPENDIX N

MARS PHYSICAL PARAMETERS AS DETERMINED FROM MARINER 9
OBSERVATIONS OF THE NATURAL SATELLITES

194<

628



MARS PHYSICAL PARAMETERS AS DETERMINED FROM MARINER 9 OBSERVATIONS
OF THE NATURAL SATELLITES

by

George H. Born
Jet Propulsion Laboratory
Pasadena, California

AAS/AIAA Astrodynamics Conference
July 16-18, 1973/Vail, Colorado

195<

Mars Physical Parameters as Determined from
Mariner 9 Observations of the Natural Satellites

ABSTRACT

This paper presents values for Mars gravity field, as well as mass and spin axis direction determined by processing combined radio and optical data taken with the Mariner 9 spacecraft. The optical data consists of 62 TV photographs of Phobos and Deimos taken during the Mars orbiting phase of Mariner 9. The radio data consists of apoapsis state vectors obtained from 195 one revolution fits of the doppler data. A first order analytical theory is used to model both the satellites and the spacecraft's motion. However, the shallow resonance condition of Mariner 9's orbit necessitated development of a partial second order theory to model the long period perturbations which derive from Mars even order tesseral harmonics. Use of an analytical theory allows rapid and inexpensive processing of both data types simultaneously. The results are in good agreement with those previously published from Mariner 9 doppler and landmark data.

196<

Introduction

This paper presents values for Mars gravity field, as well as mass and spin axis direction obtained from an analysis of combined radio data from the spacecraft and optical data of the natural satellites taken by the Mariner 9 spacecraft while orbiting Mars. Also, Mariner 9 photographed the satellites during its approach phase. These pictures formed the basis for a highly successful real time navigation demonstration to predict Mariner 9's encounter parameters using combined optical and radio data.⁽¹⁾

Details on the orbital element evolution and orbit determination strategy for Mariner 9 are given in Ref. (2). Briefly, Mariner 9 was inserted into orbit about Mars on November 13, 1971, and continued radio transmission until October 27, 1972. During this time it completed 676 orbits of Mars and returned several thousand TV pictures of the planet. In addition, over 100 pictures of Mars natural satellites, Phobos and Deimos, were taken and a subset of these constitute the optical data processed for this paper.

Table 1 presents the orbital elements for Mariner 9 subsequent to each of its two orbit trim maneuvers. Note that the inclination is near critical; consequently, the line of apsides rotated only 2.4° throughout the mission. Hence, the sub-periapsis latitude coverage of Mars is extremely small which imposes severe limitations on determination of global gravity information from Mariner 9 doppler data. In particular determination of the zonal harmonic coefficients beyond J_2 becomes difficult since only small long period variations are induced in the orbit elements. For example, the long term effects of solar radiation pressure are an order of magnitude greater than those induced by nominal size zonal harmonics. However, Mariner 9 orbital period is nearly in a 2:1 ratio with Mars rotational period, therefore, it is in a condition of shallow resonance, and the orbit perturbations

due to even order tesseral harmonics are amplified, thus simplifying their identification. The dominant effect of resonance is a 1000 km in-track perturbation whose period after the second trim maneuver is 18.3 days or 37 Mariner 9 orbits.

Phobos and Deimos, Mars two natural satellites, are in close proximity to Mars and move in nearly circular orbits with small inclinations to Mars equator. They have orbital period of 7.7 and 30.3 hours respectively. Their size is quite small being on the order of 10 km in diameter. Their orbits are strongly perturbed by Mars oblateness and in the case of Deimos solar perturbations are significant. For a discussion of their dynamical characteristics see Ref. 3.

The radio and optical data are processed in a two-stage filter. Apoapsis state vectors, as determined from one revolution fit of the doppler data,⁽⁴⁾ are used as the observables for the second stage of the filter. Here they are processed simultaneously with the line and pixel value for the center of mass (assumed to be at the center of figure) of the satellites to yield solutions for both the satellite's and the spacecraft's states, Mars gravity field, spin axis direction, mass and TV camera parameters.

A first order analytical theory which includes the effects of zonal and tesseral harmonics as well as solar gravity and radiation pressure is used to propagate the motion of Mariner 9, Phobos and Deimos.⁽⁵⁾ Since Mariner 9 is in shallow resonance with Mars even order tesseral harmonics, large down-track perturbations are induced in the orbital motion. As a result, a first order analytical theory is inadequate to model the spacecraft's motion. Consequently, the theory was extended to include the dominant second order

effects of resonance. Use of analytical theories allows rapid and inexpensive processing of the data as well as yielding valuable insight into the cause of various orbital perturbations.

There are several alternatives to the use of an analytical theory in the second stage of the filter. One approach is to fit the orbit element rates directly to determine system parameters.⁽⁴⁾ This method has the advantage of minimizing the effects of non-gravitational forces such as gas leaks on estimated parameters. However, the difficulty of properly generating element rates and attendant weighting matrices must be overcome. In the case of severe gas leaks or frequent venting this is probably the only feasible method of doing long arc filtering. However, in the case of Mariner 9 gas leaks do not appear to significantly corrupt gravity field information.⁽⁶⁾ Consequently, the use of an analytical theory is a viable alternative.

Another promising alternative suggested in Ref. (7) is to numerically integrate the equations of motion maintaining only long period, secular and resonance frequencies. The advantage here is that large integration steps can be taken. A disadvantage of this method, which is compounded for an analytical theory, is determining which terms to maintain in the differential equations. Direct terms pose no problem; however, short period terms which interact to yield first order long period terms in the solutions must be dealt with. For example, long period perturbations in the orbit elements proportional to J_2 result from the interaction of short period terms in the differential equations. In the case of resonance the problem of seemingly innocuous terms interacting to yield significant long period perturbations is more severe.

Furthermore, in the case of Mariner 9 where 24 and 36 hour frequency per-

turbations caused by non-resonance tesserals is significant one may wish to maintain these frequencies in the equations of motion so that for high eccentricity orbits computer time becomes a limiting factor. Actually it appears that a satisfactory compromise would be a hybrid method which numerically integrates long period and resonance effects and utilizes an analytical theory for higher frequency perturbations.

Discussions of the Data

The radio data processed for this paper consisted of an apoapsis state vector (normal points) for each of revolutions 5 through 195 obtained from one revolution fit of the doppler data.⁽⁴⁾ Beyond revolution 195 the doppler data becomes increasingly noisy because of only one station tracking and increasing Earth-Mars range.⁽²⁾

The optical data consisted of a selected set of 62 TV photographs of Phobos and Deimos taken between revolutions 25 and 221 of Mariner 9. Although many more pictures were taken, they were not used because of large uncertainties in camera pointing angle due to lack of spacecraft telemetry data or because images were partially outside the picture. The data from these pictures consists of camera pointing angles and the line and pixel locations of the center of figure of the Phobos or Deimos image.

The optical data are broken down as follows

- 21 Phobos A frames
- 27 Phobos B frames
- 3 Deimos A frames
- 11 Deimos B frames

The terms A and B refer to the wide and narrow angle camera respectively. For 51 of the pictures the mean longitude of Phobos and Deimos lies between 170° and 250° measured with respect to Mars mean equator and equinox of 1950.

Ten of the pictures lie between 20° and 70° while one B frame of Phobos lies at 135° . Consequently, there is approximately 130° of longitude between 250° and 20° which contains no pictures at all. This hampers somewhat the determination of short period motion of the moons from the optical data.

The shutter times, camera identification and pointing angles are taken from Ref. 8. Image center of figure locations were taken from hardcopy supplied by the JPL Image Processing Lab. For a discussion of optical measurement instruments and their associated calibration for the Mariner 9 system see Ref. 9 or 10.

1. Description of TV Cameras

The on-board imaging system of Mariner 9 consisted of a wide angle low-resolution camera (A camera) and a narrow angle high-resolution camera (B camera) mounted on a scan platform which could be positioned in two degrees of freedom relative to the spacecraft. The wide-angle camera had a focal length of 50 mm and a field of view of $11^{\circ} \times 14^{\circ}$, while the narrow angle camera had a focal length of 500 mm with a $1.1^{\circ} \times 1.4^{\circ}$ field of view. The majority of satellite images processed for this paper were taken with the narrow angle camera.

2. Optical Data Errors

Optical data errors are classified either as instrument or as model errors. Instrument errors include TV distortions, TV pointing errors, image center-finding errors and random measurement errors. TV distortion errors corrupt the relative geometry of images within a picture. They are caused by non-uniform deflection field that sweeps the electron readout beam across the vidicon target non-uniformly. TV distortion causes image loca-

tions errors in raw data of a few pixels near the center of the vidicon to tens of pixels near the edges of the vidicon. This distortion is modeled accurately as a 2nd order polynomial of the radial distance from the center of the vidicon.⁽¹⁰⁾ Distortion from the optics is negligible.

TV pointing errors cause a global shift of all images in a picture and also corrupt the relative image geometry within a picture due to the non-linearity of the TV distortion. TV pointing errors, which are caused by imperfect knowledge of TV pointing directions at shutter times, can be eliminated if stars with known directions are included in the picture. Unfortunately, only two orbital phase pictures of the satellites contain stars. Consequently, reduced telemetry data must be used to determine TV pointing. This pointing is good to approximately $.02^\circ$ which is 10 pixels for the narrow angle camera and 1 pixel for the wide angle camera.

Image center-finding errors result when dealing with finite size images such as those of Deimos and Phobos. Also, limit cycle motion during exposure, diffraction in the optics, and blooming of saturated images combine to distort finite size images and contribute to center-finding errors. These center-finding errors are of pixel and sub-pixel magnitude for Phobos and Deimos. Random measurement errors result from random center-finding errors and TV resolution.

Model errors include satellite and planetary ephemeris errors as well as planet gravity and spin axis errors. Additional model errors are induced by using an approximate analytical theory to model the motion of the satellites and spacecraft.

3. Radio Data Errors

The apoapsis state vectors determined from the one revolution fits suffer

from several errors. First, short arc doppler fits are extremely uncertain in the angle Ω_{pos} , node in the plane of the sky.⁽²⁾ Consequently, the value of this angle was constrained to that obtained from long arc fits performed by the Mariner 9 navigation team. However, its uncertainty is still on the order of $\pm .04^\circ$.

A second source of error in the radio data is the gravity model used in processing the data in the first stage of the filter. The model used here contained only the effects of J_2 , the sun and Jupiter. Although data within two hours of periapsis was not used in these fits, the effects of the even order tesserals are still felt to such an extent that a periodic (18.3 day) position error whose amplitude is about 0.1 km is induced into the apoapsis states.

Effects of Resonance

As previously stated, Mariner 9 is in shallow resonance with the even order tesseral harmonics of Mars gravity field. This induces large (1000 km) periodic in-track perturbations in the orbit. In addition, smaller (10 km) perturbations are induced in the cross track and radial directions. The period of these perturbations is 18.3 days after the first trim maneuver and 19.5 days after the second trim maneuver. These perturbations are first order in the resonance tesserals and derive almost completely from J_{22} . However, significant second order long period (periodic in the argument of periapsis) and secular perturbations also are caused by the resonance tesserals. These result from the interaction of the large in-track resonance perturbations with the smaller resonance perturbations. The theory describing these effects is derived in a later section of the paper. For a dis-

cussion of resonance of highly eccentric orbits see Ref. 11 and 12.

First Order General Perturbation Theory

The first order analytical theory used to model the spacecraft's and the satellite's motion utilizes Kaula's form of the disturbing function for both the primary and third body orbits.^(13, 14) Basically, the differential equations for a set of non-singular orbit elements are integrated assuming a secularly precessing ellipse as the reference solution.⁽⁵⁾ Perturbations of zonal and sectorial harmonics as well as solar gravity and radiation pressure are included. The theory is complete to J_2^2 in the secular terms and includes the first order long period terms in J_2 which result from a second order solution of the differential equations.

The non-singular orbit elements are

$$\begin{aligned} &a \\ &\sin I \sin \Omega \\ &\sin I \cos \Omega \\ &e \sin (\omega + \Omega) \\ &e \cos (\omega + \Omega) \\ &\Omega + \omega + M \end{aligned}$$

where

$$\begin{aligned} a &\sim \text{semimajor axis} \\ e &\sim \text{eccentricity} \\ I &\sim \text{inclination relative to Mars equator} \\ \Omega &\sim \text{longitude of ascending node} \\ \omega &\sim \text{argument of periapsis} \\ M &\sim \text{mean anomaly} \end{aligned}$$

Although a first order theory models the 18 day resonance effect in apoapsis state quite well (.2 km cross-track and 1 km downtrack) it does not contain resonance interaction effects which induce significant long period effects

into the orbit. These are discussed in the next section.

Resonance Interaction Effects

The major deficiency in the first order theory is that it does not account for interaction effects between the resonance induced perturbations in mean longitude and the resonance induced perturbations in the remaining orbital elements. In other words the assumption of a secularly precessing ellipse breaks down and the resonance induced periodic perturbations in the mean motion must be accounted for in the reference solution. This necessitates development of a partial second order solution. These interaction terms are developed as follows. The general expression for a perturbation solution of a system of differential equations through second order is

$$\frac{d\epsilon_1^{(1)}}{dt} = f_1(\epsilon_j, t) \quad i, j = 1 \text{----} 6 \quad (1)$$

$$\frac{d\epsilon_i^{(2)}}{dt} = \sum_{j=1}^6 \frac{\partial f_i}{\partial \epsilon_j} \epsilon_j^{(1)} \quad (2)$$

where f_i is evaluated on the secularly precessing ellipse. The problem now is to obtain the desired mean longitude interaction terms from the second order solution. The resonance induced mean longitude perturbation will be manifest almost entirely in mean anomaly. Hence the desired equation is

$$\frac{d\epsilon_i}{dt} = \frac{\partial f_i}{\partial M} \Delta M \quad (3)$$

to solve eq. (3) it is convenient to use Kaula' form of the disturbing
(13)
function which is given by

$$R_{\ell m} = \frac{\mu R^\ell}{a^{\ell+1}} \sum_{p=0}^{\ell} \sum_{q=-\infty}^{\infty} F_{\ell mp} (I) G_{\ell pq} (e) S_{\ell mpq} (\omega, M, \Omega, \theta) \quad (4)$$

where

$$S_{\ell mpq} (\omega, M, \Omega, \theta) = J_{\ell m} \begin{bmatrix} \cos \\ \sin \end{bmatrix}_{\ell-m}^{\ell-m \text{ even}} \Phi_{\ell mpq} \quad (5)$$

and

$$\Phi_{\ell mpq} = (\ell-2p)\omega + (\ell-2p+q)M + m(\Omega-\theta-\lambda_{\ell m}) \quad (6)$$

Resonance terms in the disturbing function are those for which $(\ell-2p+q) = m/2$.

When this substitution is made in eq. (6)

$$\Phi_{\ell mpq} = (\ell-2p)\omega + m\left(\frac{M}{2} + \Omega - \theta - \lambda_{\ell m}\right) \quad (7)$$

Let

$$\Psi_{\ell m} = m\left(\frac{M}{2} + \Omega - \theta - \lambda_{\ell m}\right) \quad (8)$$

then the average rate for $\Psi_{\ell m}$ is

$$\dot{\Psi}_{\ell m} = m\left(\dot{n}/2 + \dot{\Omega} - \dot{\theta}\right) \quad (9)$$

For Mariner 9, $\dot{\Psi} = .398 \times 10^{-5}$ rad/sec for $m = 2$, hence, the resonance terms in eq. (4) induce a perturbation of this period into the equations of motion.

Now eq. (3) may be written

$$\frac{d\mathbf{s}_i}{dt} = \sum_{\substack{\ell' m' s' j \\ \ell' m' s' j}} \int \left(\frac{\partial \dot{\mathbf{s}}_i}{\partial M} \right)_{\ell' m' s' j} \Delta M_{\ell' m' s' j} \quad (10)$$

where l, m, p, q represents the resonance term in the differential equation for any element and l', m', s, j , represents the resonance term in the mean anomaly.

Hence

$$\begin{aligned} l - 2p + q &= m/2 \\ l' - 2s + j &= m'/2 \end{aligned} \quad (11)$$

The resonance variation in M is dominated by the first order interaction term

$$\Delta M = \int \frac{\partial n}{\partial a} \Delta a \quad (12)$$

Equation (10) may now be integrated directly keeping in mind that all quantities on the right hand are evaluated on the secularly precessing ellipse. The summation in eq. (10) is carried out only for even order tesseral harmonics with the constraints of eq. (11) so that only resonance terms are considered.

The results are

$$\Delta a = \sum_{\substack{lm \\ l' m'}} \frac{3K}{a^2} \sum_{p,s} L \frac{mm'}{4} E_2$$

$$\Delta e = \sum_{\substack{lm \\ l' m'}} K \sum_{p,s} L \left[\frac{1-e^2}{e} \frac{m^2 m'}{8} - \frac{\sqrt{1-e^2}}{e} \frac{mm'}{4} (l-2p) \right] E_2$$

$$\Delta I = \sum_{\substack{lm \\ l' m'}} K \sum_{p,s} L \left[\frac{-\cot I}{\sqrt{1-e^2}} \frac{mm'}{4} (l-2p) - \frac{1}{\sin I \sqrt{1-e^2}} \frac{m^2 m'}{4} \right] E_2$$

207<

$$\Delta\Omega = \sum_{\substack{\ell, m \\ \ell', m'}} K \frac{1}{\sin I \sqrt{1-e^2}} \sum_{p,s} P \frac{mm'}{4} E_3 \quad (13)$$

$$\Delta\omega = \sum_{\substack{\ell, m \\ \ell', m'}} K \sum_{p,s} \left[\frac{-\cot I}{\sqrt{1-e^2}} P \frac{mm'}{4} + \frac{\sqrt{1-e^2}}{e} Q \frac{mm'}{4} \right] E_3$$

$$\Delta M = \sum_{\substack{\ell, m \\ \ell', m'}} -K \sum_{p,s} \left[5 L \frac{m'm}{8} E_1 + \left(-\frac{1-e^2}{e} Q \frac{mm'}{4} + (\ell+1) L \frac{mm'}{2} \right) E_2 \right]$$

where

$$K = -3 n^3 (R/a)^{\ell + \ell'}$$

$$L = F_{\ell mp}(I) G_{\ell pq}(e) F_{\ell' m' s}(I) G_{\ell' s j}(e) \quad (14)$$

$$P = \frac{\partial L}{\partial I}$$

$$Q = \frac{\partial L}{\partial R}$$

and only the functions $F_{\ell mp}(I)$ and $G_{\ell pq}(e)$ are differentiated in eq. (14).

Also, if $\ell-m$ and $\ell'-m'$ are even

$$E_1 = \frac{J_{\ell m} J_{\ell' m'}}{2} \left[\frac{\sin(\dot{\Phi} + \dot{\beta})}{\dot{\Phi} + \dot{\beta}} + \frac{\sin(\dot{\Phi} - \dot{\beta})}{\dot{\Phi} - \dot{\beta}} \right]$$

$$E_2 = -\frac{J_{\ell m} J_{\ell' m'}}{2} \left[\frac{\cos(\dot{\Phi} + \dot{\beta})}{\dot{\Phi} + \dot{\beta}} - \frac{\cos(\dot{\Phi} - \dot{\beta})}{\dot{\Phi} - \dot{\beta}} \right]$$

$$E_3 = \frac{J_{lm} J_{l'm'}}{2} \left[\frac{\sin(\dot{\Phi} - \dot{\beta})}{\dot{\Phi} - \dot{\beta}} - \frac{\sin(\dot{\Phi} + \dot{\beta})}{\dot{\Phi} + \dot{\beta}} \right] \quad (15)$$

for $l-m$ even and $l'-m'$ odd, then in eqs. (13) replace

$$\begin{aligned} E_1 &\text{ by } E_2 \\ E_2 &\text{ by } -E_1 \\ E_3 &\text{ by } -E_4 \end{aligned} \quad (16)$$

if $l-m$ odd and $l'-m'$ even, replace

$$\begin{aligned} E_1 &\text{ by } E_4 \\ E_2 &\text{ by } E_3 \\ E_3 &\text{ by } -E_2 \end{aligned} \quad (17)$$

if $l-m$ odd and $l'm'$ odd, replace

$$\begin{aligned} E_1 &\text{ by } E_3 \\ E_2 &\text{ by } -E_4 \\ E_3 &\text{ by } E_1 \end{aligned} \quad (18)$$

Furthermore, if $l-2p = l' - 2s$ and $m=m'$ and l and l' are even let

$$\begin{aligned} E_1 &= J_{lm} J_{l'm'} \left[t/2 + \frac{1}{4\dot{\beta}} \sin 2\beta \right]_{t_0}^t \\ E_2 &= J_{lm} J_{l'm'} \left[\frac{\sin^2 \beta}{2\dot{\beta}} \right]_{t_0}^t \end{aligned} \quad (19)$$

$$E_3 = J_{\ell m} J_{\ell' m'} \left[t/2 - \frac{1}{4\dot{\beta}} \sin 2\beta \right]_{t_0}^t$$

if $\ell-2p = \ell'-2s$ and $m = m'$ and ℓ and ℓ' are odd let

$$\begin{aligned} E_1 &= J_{\ell m} J_{\ell' m'} \left[t/2 - \frac{1}{4\dot{\beta}} \sin 2\beta \right]_{t_0}^t \\ E_2 &= J_{\ell m} J_{\ell' m'} \left[\frac{\sin^2 \beta}{2\dot{\beta}} \right]_{t_0}^t \\ E_3 &= J_{\ell m} J_{\ell' m'} - \left[t/2 + \frac{1}{4\dot{\beta}} \sin 2\beta \right]_{t_0}^t \end{aligned} \quad (20)$$

The arguments of the trigonometric functions are

$$\dot{\Phi} = (\ell-2p)\dot{\omega} + m (\dot{M}/2 + \dot{\Omega} - \dot{\theta} - \lambda_{\ell m}) \quad (21)$$

$$\dot{\beta} = (\ell'-2s)\dot{\omega} + m' (\dot{M}/2 + \dot{\Omega} - \dot{\theta} - \lambda_{\ell' m'}) \quad (22)$$

$$\dot{\Phi} = (\ell-2p)\dot{\omega} + m (\bar{n}/2 + \dot{\Omega} - \dot{\theta}) \quad (23)$$

$$\dot{\beta} = (\ell'-2s)\dot{\omega} + m' (\bar{n}/2 + \dot{\Omega} - \dot{\theta}) \quad (24)$$

It is of interest to note, if $\ell-2p \neq \ell'-2s$ and $m = m'$ that long period variations (periodic in the argument of periapsis) proportional to $J_{\ell m} J_{\ell' m'}$ are introduced into e , I , Ω , ω and M .

As an example of these interaction terms the error in the analytical theory with and without these corrections for I , ω and Ω are shown in figure (1) for one resonance cycle. The errors are obtained by comparing the

analytical theory with and without these interaction terms to numerical integrations. The model used contains J_2 , J_3 , J_4 , J_5 , J_6 , J_{22} and λ_{22} . As seen from the figure the error introduced by ignoring these resonance interaction terms is significant. In fact, the long period variation in these angles proportional to J_{22}^2 an order of magnitude greater than the long period variation due to the zonal harmonics. Consequently, any attempt to determine information on Mars zonal harmonics from Mariner 9 data utilizing an analytical theory must account for these terms.

Computational Procedure

The radio normal points and satellite images were processed as independent data types using a sequential filter. The solution was iterated to convergence. The filter had the capability to solve for the following parameters

- 1) Two spacecraft state vectors
- 2) Two satellite state vectors
- 3) Eighteen spherical harmonic coefficients
- 4) Six constant or time correlated camera biases angles
- 5) Three constant offsets of the wide angle camera with respect to the narrow angle camera
- 6) Right ascension and declination of Mars spin axis
- 7) Mass of Mars

Two spacecraft states are necessary since a trim maneuver was performed during revolution no. 94 altering Mariner 9's orbit (see Table 1). The a priori uncertainty used for the solution parameters was approximately 100 km for the spacecraft and satellites states, $.5^{\circ}$ in Mars spin axis, $4 \text{ km}^3/\text{sec}^2$ in the mass of Mars and $.05^{\circ}$ in the camera biases. The uncertainty in the

harmonic coefficients was obtained by extrapolating the values of the harmonic coefficients for a planet of Earth's mass and volume to that of Mars⁽¹⁵⁾. These uncertainties were then multiplied by 5 to make them compatible with the magnitude of the coefficients actually obtained.

The optical data were weighted at $.02^\circ$ which is equivalent to 10 B frame pixels and 1 A frame pixel. The radio normal points were weighted in a manner to be consistent with the accuracy of the analytical theory and the Ω_{pos} uncertainty of the short arc fits. These values were as follows

$$\begin{aligned}\sigma_a &= .5 \text{ km} \\ \sigma_e &= .2 \times 10^{-4} \\ \sigma_M &= .005^\circ \\ \sigma_{I_{\text{pos}}} &= .005^\circ \\ \sigma_{w_{\text{pos}}} &= .005^\circ \\ \sigma_{\Omega_{\text{pos}}} &= .05^\circ\end{aligned}$$

The angular uncertainty in the plane of the sky was then rotated to the Mars equatorial system for data processing.

The initial conditions for Phobos and Deimos relative to Mars equator and Equinox of date were taken from solutions based on pictures obtained during Mars approach⁽¹⁶⁾. Initial conditions for mass and spin axis directions were taken from Ref. 17.

Short period perturbations were retained in the analytical theory for J_2 and J_{22} . To avoid carrying the eccentricity expansions to extremely high powers (e^{20}) to obtain the mean value of semimajor axis for the spacecraft's orbit, Brouwer's theory⁽¹⁸⁾ was used to model the short period terms in J_2 .

Short period perturbations in J_{22} were carried through e^{10} . For the remaining harmonic coefficients only secular, long period, medium period, and resonance perturbations were retained. Briefly this means that all terms were retained for which the following conditions held

$$l = 2$$

$$l - 2p + q = 0$$

$$l - 2p + q = m/2$$

$$l - 2p + q = (m \pm 1)/2$$

Studies were made which show that the neglected terms have a negligible influence on the solutions.

Results

This section presents results on scientific as well as navigation aspects of the optical and radio data solutions. In particular, a gravity field of Mars is presented with the corresponding equipotential surface plot. Also, a set of mean orbital elements for Phobos and Deimos with their associated angular rates are presented and their accuracy discussed. In addition, values are given for the mass and spin axis direction for Mars. Finally, a discussion of the navigation accuracy of the combined data type is presented.

Mars Gravity Field

Table 2 presents a complete 4th degree and order field with 5th and 6th degree resonance tesserals. The lower degree tesserals and J_2 agree quite well with previously published results.^(13, 15) The values of the higher degree terms are quite uncertain and are presented only to show the complete solution list for this field. Furthermore, the values of the zonal coefficients beyond J_2 are highly suspect although the value of J_4 was quite

stable for all solutions attempted and agrees well with many of the long arc doppler solutions obtained by the Mariner 9 Celestial Mechanics team. The uncertainties quoted in Table 2 reflect formal statistics only but may be considered for terms through third degree and order.

This field is determined to a large extent from the motion of the spacecraft rather than the motion of Phobos or Deimos. In particular, the even order harmonics are derived exclusively by sensing the motion of the spacecraft relative to Phobos and Deimos from the optical data and relative to Mars from the radio normal points.

Figure 2 presents the equipotential surface corresponding to the gravity field of Table 2. The surface value is GM/R . Generally it is in good agreement with previously published results. For example, the large gravity high in the Tharsis region (105° W longitude) is discussed in Ref.s 13 and 15. There also is a high in the region above Hellas (280° W longitude) which is common to all gravity fields obtained to date.

Orbits of Phobos and Deimos

The orbit elements of Phobos and Deimos relative to Mars true Equator and vernal equinox of date are shown in Table 3. Also shown are the associated angular rates in node, periapsis and mean anomaly. Note that these elements are relative to Mars equator and not the Laplacian plane as published by Wilkins⁽¹⁹⁾ and Sinclair⁽²⁰⁾. The equatorial plane was used so that the satellite theory of Ref. (5) could be applied directly. The periodic perturbations due to the sun, discussed in Ref. (20), in the inclination and longitude of the node in the orbit of Deimos are modeled in the analytical theory used here and should present no problem. These perturbations have an amplitude of $.9^\circ$

for inclination and 26° for the longitude of the node and argument of periapsis and a period of 54 years which corresponds to the period of the ascending node of Deimos orbit relative to Mars equator. However, the large node and argument of periapsis variations cancel one another in the mean longitude ($\Omega+W+M$) so that the amplitude of the long period variation in longitude is only 0.3° . Since the majority of this perturbation comes from the mean anomaly it can not be removed by using an alternate reference plane such as the Laplacian plane. For Phobos the solar perturbation in the longitude of the node and argument of periapsis is $.7^\circ$ while the inclination perturbation is $.01^\circ$. The period of the nodal regression for Phobos is 2.4 years.

The daily mean motion in longitude for Phobos is in excellent agreement with Wilkins' and Sinclair's Value. However, the value for Deimos differs by $-.13 \times 10^{-3}$ deg/day from the previously accepted value. If the mean motion is corrected to the mean value of the inclination of Deimos orbit relative to Mars equator, a value of $285.16188^\circ/\text{day}$ is obtained. 1971 corresponds closely to a maximum of Deimos inclination, hence the mean motion will be a minimum.

The longitudes for Phobos and Deimos given in Table 1 are $.2^\circ$ less and $.3^\circ$ greater than the longitudes predicted for this epoch by Sinclair⁽²⁰⁾ from a solution which included secular acceleration terms for Phobos and Deimos. The longitude predicted for Phobos by Sinclair from a solution which does not contain a secular acceleration term is 2° less than that obtained from the Mariner 9 data*. This tends to confirm the existence of a secular acceleration for Phobos. However, the Mariner 9 results are in conflict with a secular deceleration for Deimos.

* A. T. Sinclair, personal communication, Nov. 1973.

The results presented here are still tentative in that 17 pictures of Phobos and Deimos taken during the approach phase of Mariner 9 as well as one Phobos picture transmitted during the last day of the spacecraft's operational life are not included in the solution. These pictures along with two Mariner 69 photographs of Phobos will yield a much longer baseline for estimating orbital elements as well as secular accelerations for the satellites. Consequently, a later publication will contain results of fitting all of this data and detailed comparisons to previously published results will be made.

Spin Axis Direction

The direction of Mars spin axis as determined from the orbital pictures of Phobos and Deimos are shown as entry 6 in Table 4. Also shown are several other recently determined values and the preflight value quoted in the American Ephemeris and Nautical Almanac. The spin axis direction is determined solely from the geometrical properties of the camera-satellite system. Camera pointing relative to the inertial reference frame for the scan platform is known to $\pm .02^{\circ}$; consequently given the orbital inclination of Phobos and Deimos it should be possible to determine the spin axis to this accuracy. Although errors in inclination of the satellites contribute to errors in the spin axis direction this error should be small since sufficient time is involved to allow determination of the orbital inclinations. In fact, several

solutions were generated with varying a priori uncertainties on the inclinations of Phobos and Deimos. The estimate of the spin axis and orbital inclination was unaffected.

A description of the various solutions follows

1. Mariner 9 (six revolutions), determined by the Mariner 9 Navigation Team from six revolutions of Doppler data.⁽¹⁵⁾
2. Mariner 9 (38 revolutions), determined by the Celestial Mechanics Team from 38 revolutions of doppler tracking.⁽¹³⁾
3. Landmark-Mariner 9, Approach Phase. Determination from television photos of the South Polar Cap region taken during spacecraft approach to Mars.⁽²¹⁾
4. Landmark-Mariner 9, Orbit Phase. Determination from television images of landmarks taken during the orbit phase, and using the radio tracking data for orbit reference.⁽²¹⁾
5. Star-Satellite-Approach. Determination from television images of Deimos against a fixed-star background taken during spacecraft approach to Mars.⁽²²⁾
7. Global Surfaces Images. Determined from landmark observations over 385 revolutions of Mariner 9.⁽²³⁾
8. Earth-Based Deimos-Phobos. Determination from Earth-based observations to 1969 of Deimos and Phobos.⁽²⁰⁾
9. American Ephemeris and Nautical Almanac. Determination from averaging the Earth-based pole values of Burton, obtained from observations of Phobos and Deimos to 1926, and of Camichel, obtained from observa-

tions of surface markings (both cited by de Vaucouleurs, Ref. 24).

All of the recently determined values of the Mars spin-axis direction, with the exception of the approach-landmark value, agree to within $0^{\circ} .05$ in right ascension and $0^{\circ} .15$ in declination. The new values differ by approximately $.5^{\circ}$ from de Vaucouleurs' value. The value of the spin axis direction determined here agrees most closely with that determined from the orbit phase landmark data.

Mass of Mars

The mass of Mars as determined from the combined radio and optical data is shown in Table 5. Also shown are the values determined from Mariner 4 and 6 flyby data, and Mariner 9 approach doppler and range data. (25, 26, 15, 27) Since a fixed value of Mars mass was used to determine the radio normal points, this data cannot be used for a mass determination. However, the optical data yields direct information on the semi-major axis ($\pm .01$ km) of Phobos and Deimos' orbit. Since the mean motions of the satellites also are well known ($.0001$ deg/day) the mass of Mars is determined to $\pm .5$ km³/sec² from the optical data.

Navigation Accuracy

As previously stated the doppler only solutions are deficient in the node in the plane of the sky. Although the optical data does not suffer from an indeterminacy in this angle the scarcity of data for this mission as well as the lack of stars in the field of view to eliminate pointing errors does not make it a particularly strong data type for navigation. For example the formal statistics for the solution discussed here was $\sigma_{\Omega_{pos}} = \pm .0042^{\circ}$ for

Ω_{pos} from the radio data only and $\sigma_{\Omega_{\text{pos}}} = \pm .0037^{\circ}$ for the combined data types. However, optical data can be a strong data type for navigation if the picture sequence is so designed.⁽²⁸⁾ The actual estimate for Ω_{pos} from the combined data solution is shown in Figure 3. The result is shown as a deviation from the value obtained by the Mariner 9 navigation team⁽²⁾. Note that the solution for the combined data types agrees well with the mean value obtained from the doppler fits during revolution 5 through 95 but is biased by about $.02^{\circ}$ from revolutions 95 through 195. This shift is due to the optical data.

Since an error in Ω_{pos} does not effect the Mars spacecraft range it is of interest to compare the magnitude of the range determined from the navigation team fits of the doppler data with the value determined from the combined data types using an analytical theory. This deviation in the Mars-spacecraft range in general is a few tenths of a km.

Residuals

The residuals for both the radio normal points and the optical data are shown as a function of apoapsis number in Figure 4 through 6. The radio normal point residuals are not random and reflect the inability of the analytical theory to completely model Mariner 9's motion. The magnitude and structure of these residuals is very similar to that obtained via numerical simulation; consequently, it is felt that the gravity field obtained from this fit is accurate at least in the lower order and degree terms.

The optical residuals for the wide and narrow angle camera are identified by an A or B respectively for Phobos and Deimos in Figure 6. The A camera residuals are multiplied by 10 to make them compatible with B

camera residuals. It is obvious from these plots that in general the A frames are not as accurate as the B camera pictures. This is attributed to the pointing for the A camera not being as accurately known since the orientation of the A camera with respect to the scan platform is not known as accurately for the A as the B camera. However, solutions were obtained in which all pictures having residuals greater than 30 pixels were not used. The results differ an insignificant amount from those reported here.

Conclusions

The following conclusions are drawn from this study

- 1) The feasibility of combining radio and optical data in long arc solutions to yield accurate determination of orbits and physical parameters has been demonstrated.
- 2) An analytical theory for the evolution of a highly eccentric orbit in shallow resonance has been developed which is accurate to ± 1 km in Mariner 9's apoapsis state vector over a period of 200 revolutions.
- 3) New solutions have been developed for Mars mass, spin axis direction and gravity field as well as the orbits of its two satellites Phobos and Deimos. These solutions are in good agreement with previously published results.
- 4) A determination of the history of the angle, node in the plane of the sky (a weakly determined parameter from doppler data) has been made for the first 200 orbits of Mariner 9 by using combined data types.

Acknowledgement

The author expresses his thanks to Dr. A. J. Ferrari and E. J. Christensen for providing the radio data for this paper. Thanks also is given to Mohan Ananda for programming support, Mark Coles for graphics and T. C. Duxbury for his suggestions on processing the optical data.

220<

References

1. Duxbury, T. C., Born, G. H. and Jerath, N., "Viewing Phobos and Deimos for Navigating Mariner 9" AIAA Paper No. 72-927 AIAA/AAS Astrodynamics Conference, Palo Alto, Calif., September, 1972.
2. Born, G. H., Christensen, E. J., Ferrari, A. J., Jordan, J. F., and Reinbold, S. J., "The Determination of the Satellite Orbit of Mariner 9" paper No. 72-928 AIAA/AAS Astrodynamics Conference, Palo Alto, Ca., Sept. 1972.
3. Burns, Joseph A., "Dynamical Characteristics of Phobos and Deimos", Review of Geophysics and Space Physics, Vol. 10, No. 2, May 1972.
4. Ferrari, A. J. and Christensen, E. J., "Mars Gravity derived from the Long Period Motion of Mariner 9" AIAA/AAS Astrodynamics Conference, Vail, Colorado, July, 1973.
5. Born, G. H. and Tapley, B. D. "An Approximate Solution for the Short Term Motion of a Lunar Satellite", Journal of Spacecraft and Rockets, May, 1969.
6. Christensen, E. J., "Toward State and Gravity Estimation in the Presence of Gas Leaks for the MM'71 Orbital Phase" JPL IOM 391.6-317, 17, April, 1973.
7. Breedlove, W. J., Jr., "Determination of the Atmospheric and Gravitational Parameters of Mars from a study of the Long-Period Motion of a Viking Orbiter", Technical Report, School of Engineering, Old Dominion University, Norfolk, Va., July, 1972.
8. Acton, C. H., Breckenridge, W. G., "MM'71 Orbital Sequence Satellite Summary", JPL IOM 343-4-73-098, February, 1973.
9. Acton, C. H., "Processing On-Board Optical Data for Planetary Approach Navigation", AIAA Paper No. 72-53, January, 1972.
10. Breckenridge, W. G. and C. H. Acton, "A Detailed Analysis of Mariner 9 TV Navigation Data", AIAA Paper No. 72-866, August, 1972.
11. Gedeon, G. S., "Tesseral Resonance Effects on Satellite Orbits", Celestial Mechanics 1, 167, 1969.
12. Allen, R. R., "Satellite Resonance", Space Science 15, 1829, 1967.
13. Kaula, W. M., "Theory of Satellite Geodesy", Blaisdell Publishing Co., Waltham, Mass., 1966.
14. Kaula, W. M., "Development of the Lunar and Solar Disturbing Functions for a Close Satellite", Astronomical Journal, V. 67, No. 5, June, 1962.
15. Lorell, J., et al. "Gravity Field of Mars from Mariner 9 Tracking Data", Icarus, V. 18, No. 2, February, 1973.

References (cont)

16. Born, G. H., T. C. Duxbury, "Determination of the Orbits of Phobos and Deimos from Mariner 9", Bull. Amer. Astron. Sci., V. 4, No. 3, 1972.
17. Lorell, J., et al. "Mariner 9 Celestial Mechanics Experiment: Gravity and Pole Direction of Mars", Science, Vol. 175, January 1972.
18. Brouwer, D., "The Problem of Artificial Satellite Theory Without Drag", Astronomical Journal, V. 64, No. 1274, No. v 1959.
19. Wilkins, G. A., "Orbits of the Satellites of Mars", H. M. Nautical Almanac Office, Tech Note No. 1, August 1965.
20. Sinclair, A. T., "The Motions of the Satellites of Mars", Mon. Not. R. Astr. Soc. 155, 249-274, 1972.
21. Mohan, S. N., "Pole Direction, Cartography and the Shape of Mars", presented at the 24th International Geological Congress, Montreal, Canada, August 1972.
22. Duxbury, T. C. et al. "Determination of Mars Spin Axis Direction from Mariner 9", Bull. Amer. Astron. Sci., Vol. 4, No. 3, 1972.
23. Davies, M., "Mariner 9 Control Net of Mars", Rand Corp. Report R-1301-JPL, June, 1973.
24. De Vaucouleurs, G., "The Physical Ephemeris of Mars", Icarus, 3, 326, 1964.
25. Null, G. W., "A Solution for the Sun-Mars Mass Ratio Using Mariner IV Doppler Tracking Data", Bull. Amer. Astron. Soc. V. 1, 356, 1969.
26. Anderson, J. D., et al. "Martian Mass and Earth-Moon Mass Ratio from Coherent S-Band Tracking of Mariner 6 and 7", Science, V. 167, 227, 1970.
27. Wong, S. K., "Mariner IX Postflight Interplanetary Orbit Determination Analysis", JPL TM 391-340, April 3, 1973.
28. Duxbury, T. C., and Born, G. H., "Tracking Phobos and Deimos Aboard an Orbiting Spacecraft", AAS No. 72-372, presented at AAS/AIAA Astrodynamics Specialists Conference, Ft. Lauderdale, Florida, August 1971.

222<

223

		Initial Parameters Nov 14 to Nov 16	Post Trim 1 Nov 16 to Dec 31	Post Trim 2 Dec 31
Semimajor Axis (km)	a	13055	12631	12647
Eccentricity	e	.63	.62	.60
Mean Orbital Period (hrs)	P	12.62	11.97	11.99
Longitude of Ascending Node* (degrees)	Ω	42.3	42.1	34.2
Argument of Periapsis (degrees)	w	-24.9	-24.3	-26.0
Inclination (degrees)	i	64.6	64.8	64.4
Height above surface at periapsis+ (km)	h_p	1396	1387	1641
Latitude of sub-periapsis passage (degrees)	φ_p	-22.3	-21.9	-23.3

* Keplerian elements referenced to Mars true equator of date.

+ Mean radius of Mars = 3394 km.

Table I. Areocentric Orbital Elements of Mariner 9

TABLE 2

Mars Gravity Coefficients

l	m	$C_{lm} \times 10^4$ *	$\sigma \times 10^4$	$S_{lm} \times 10^4$	$\sigma \times 10^4$
2	0	-19.6002	.183	--	--
2	2	-.5467	.004	.2996	.004
3	0	-.1075	.111	--	--
3	1	.0310	.155	.1584	.156
3	2	-.0773	.009	.0401	.010
3	3	.0447	.013	.0272	.013
4	0	.3217	.073	--	--
4	1	.0321	.146	-.0104	.146
4	2	.0205	.013	-.0187	.013
4	3	.0006	.009	-.0018	.009
4	4	.0019	.0008	-.0010	.0008
5	0	-.0766	.202	--	--
5	2	-.0114	.013	-.0181	.013
5	4	.0006	.0006	-.0015	.0006
6	0	-.1061	.2415	--	--
6	2	-.0058	.009	.0136	.009
6	4	-.005	.0003	-.0004	.0003
6	6	$.3 \times 10^{-9}$	$.1 \times 10^{-9}$	$.3 \times 10^{-9}$	$.1 \times 10^{-9}$

Mean radius = 3393.4 km.

* All exponents are 10^{-4} unless indicated otherwise

TABLE 3

Orbit Elements of Phobos and Deimos

	Phobos	Deimos
a	9378.529 ± .01 KM	23458.906 ± .03 KM
e	.0150 ± .0001	.00080 ± .0001
M _o	311.818° ± .36	232.565 ± 7°
I	1.04° ± .012	2.79° ± .02°
ω	269.873° ± .9°	235.625° ± 7°
Ω	100.509 ± .8°	10.913° ± .2°
λ _o = Ω+ω+M _o	322.20° ± .1°	118.9° ± .1°
\bar{n} (deg/day)	1128.4069	285.1438
$\dot{\omega}$ (deg/day)	.87481	.03610
$\dot{\Omega}$ (deg/day)	-.43744	-.0181
$\bar{n} + \dot{\omega} + \dot{\Omega}$ (deg/day)	1128.8443 ± .0001	285.16178 ± .0001

Angles Referred to Mars True Equator and vernal equinox of Date

Epoch JD 2441266.500, Nov 11, 1971

TABLE 4

Direction of the Spin Axis of Mars

Method	α^* (deg)	δ^* (deg)
1. Mariner 9 (six revolutions)	317.3 \pm 0.2	52.6 \pm 0.2
2. Mariner 9 (38 revolutions)	317.3 \pm 0.2	52.8 \pm 0.2
3. Landmark-Mariner 9, Approach Phase	317.5 \pm 0.9	52.9 \pm 0.9
4. Landmark-Mariner 9, Orbit Phase	317.3 \pm 0.2	52.7 \pm 0.1
5. Star-Satellite-Approach	317.4 \pm 0.2	52.8 \pm 0.2
6. Phobos-Deimos, Mariner 9, Orbit Phase	317.3 \pm .1	52.7 \pm .1
7. Global Surfaces Images (385 Revolutions)	317.4 \pm 0.2	52.7 \pm 0.1
8. Earth-Based Deimos-Phobos	317.31 \pm 0.05	52.65 \pm 0.03
9. American Ephemeris and Nautical Almanac	316.85	53.01

* Referred to the mean equinox and equator of 1950.0

TABLE 5

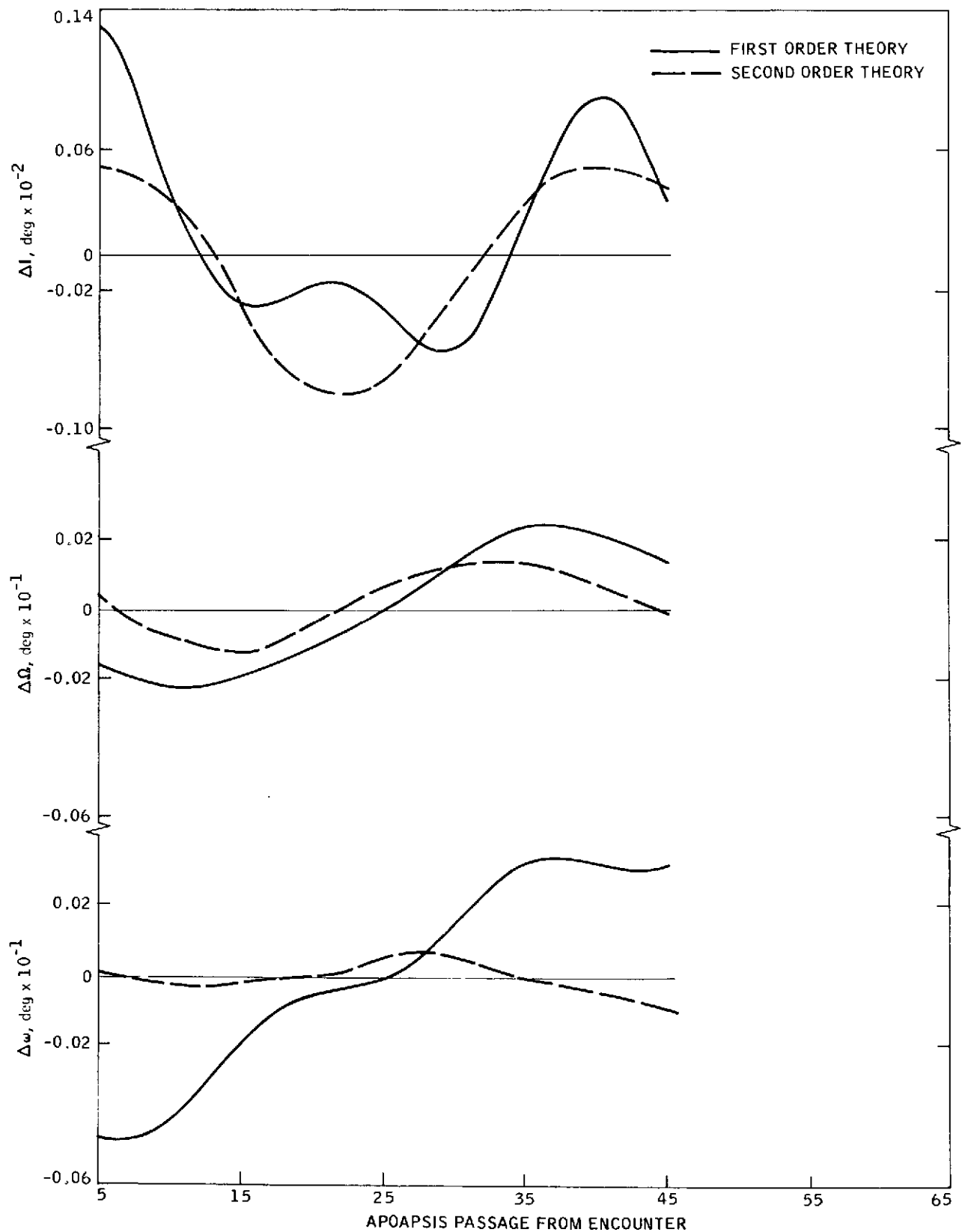
Mass of Mars Determined from Mariner Data

Method	GM ~ KM ³ /sec ²
Mariner 4 (Null) ⁽²⁵⁾	42828.3 ± .1
Mariner 6 (Anderson) ⁽²⁶⁾	42828.0 ± 2
Mariner 9 Approach ⁽¹⁵⁾ (Esposito and Wong)	42828.2 ± 1
Mariner 9 Approach ⁽²⁷⁾ (Wong)	42828.5 ± .4
Mariner 9 Observations of Phobos and Deimos (Born)	42828.1 ± .5

227<

Fig. 1.

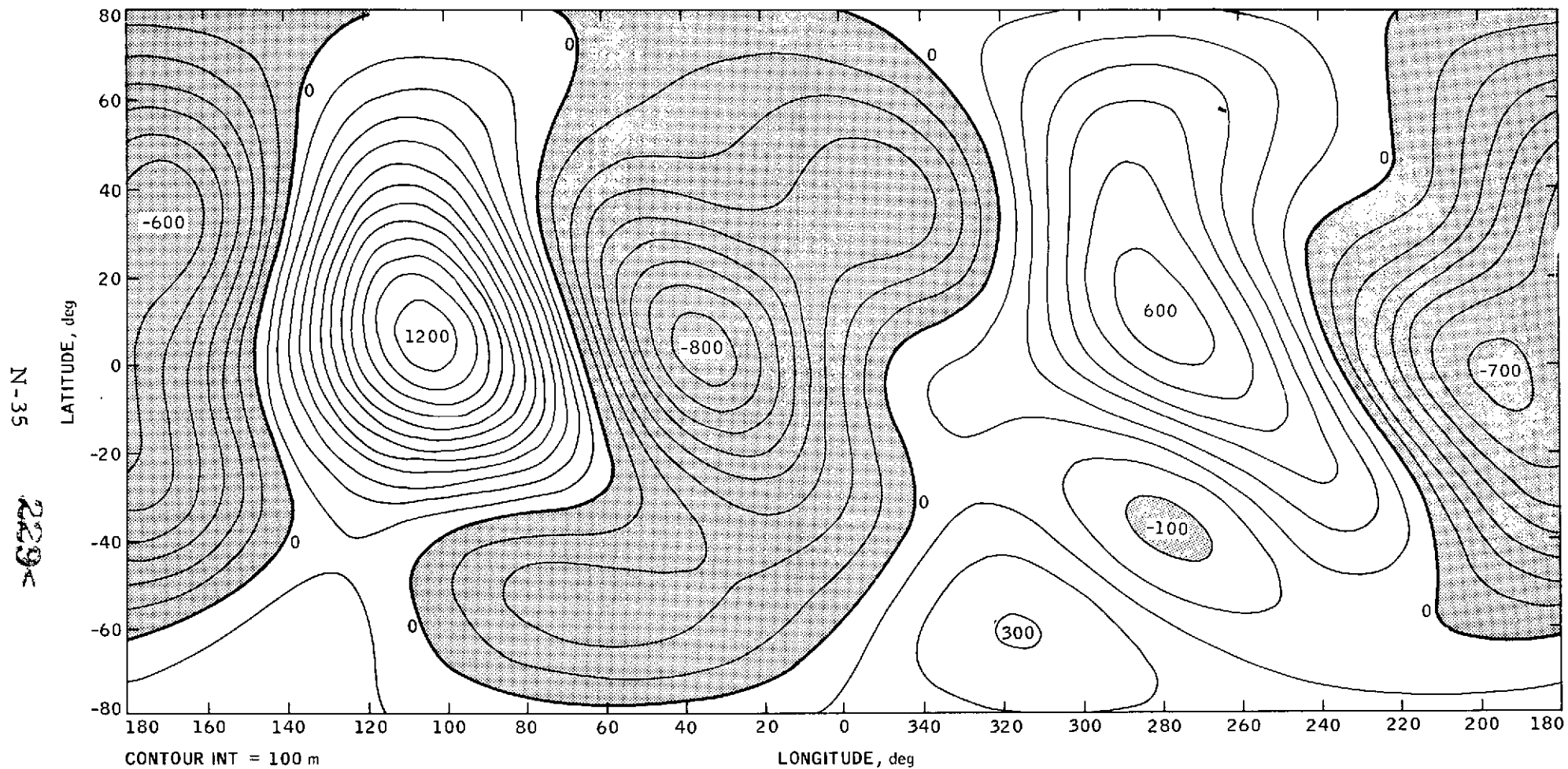
COMPARISON OF ERROR IN FIRST AND SECOND ORDER THEORY



228<

Fig. 2.

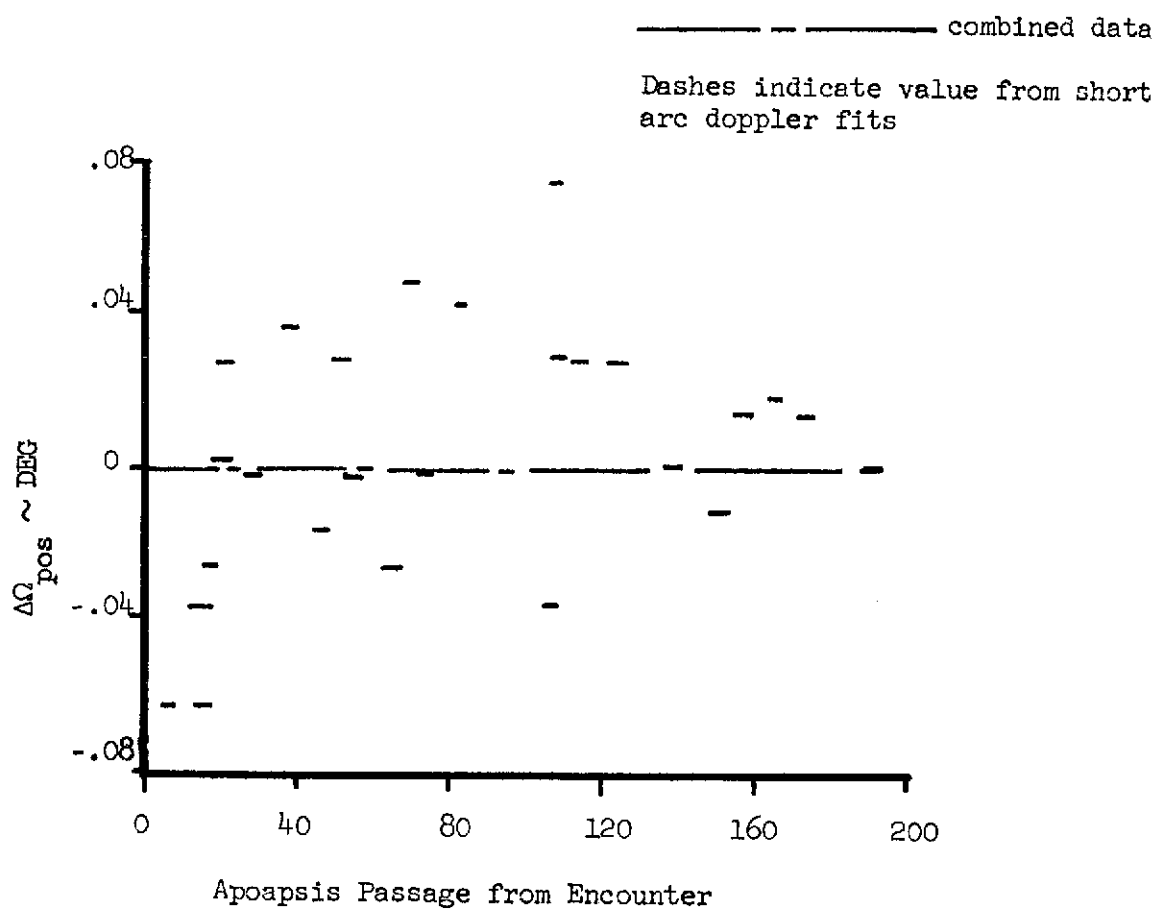
MARS GRAVITY FIELD EQUIPOTENTIAL SURFACE



622
N-35

Figure 3

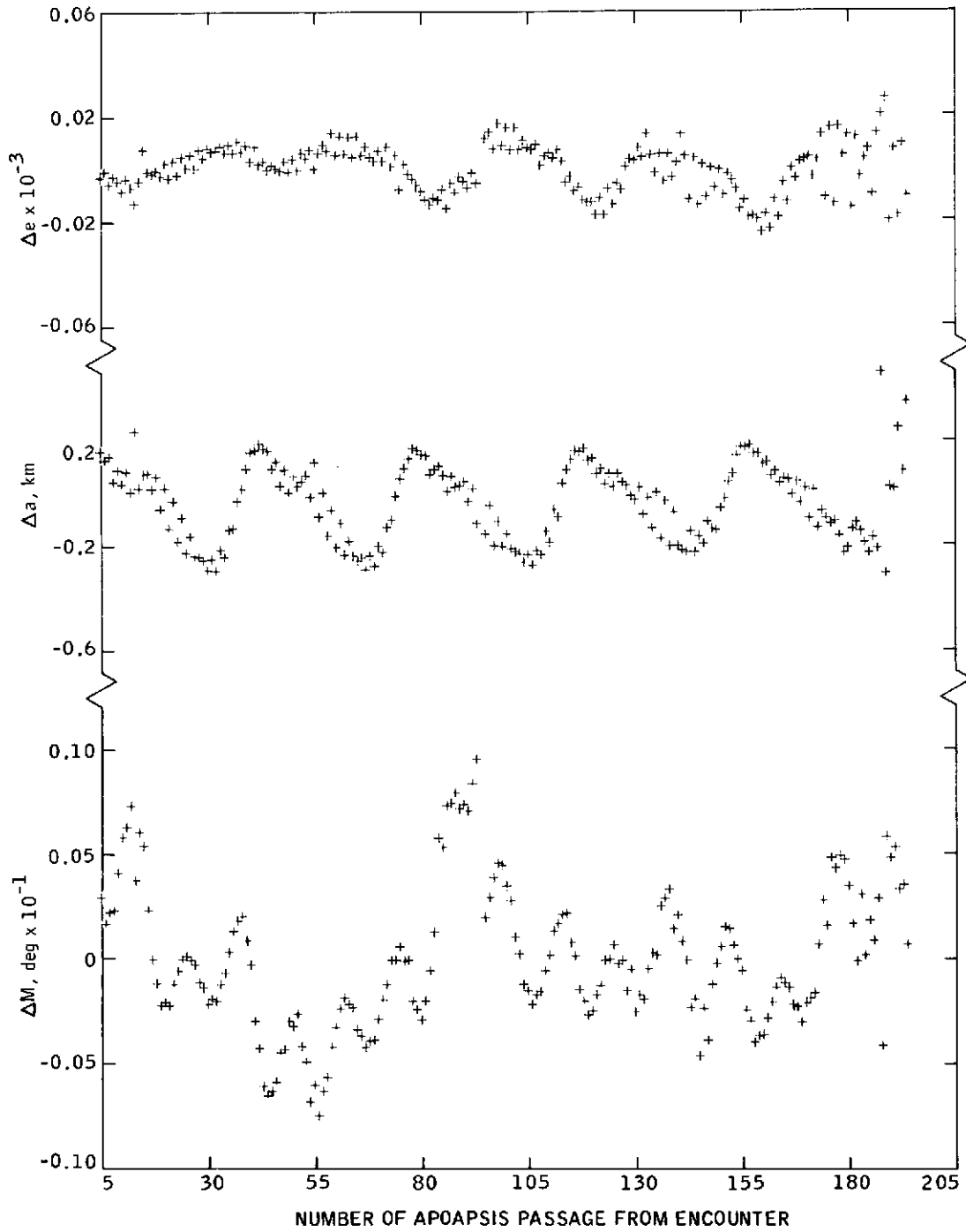
DEVIATION OF Ω_{pos} BETWEEN DOPPLER ONLY FITS AND COMBINED DATA FIT



230<

Fig. 4.

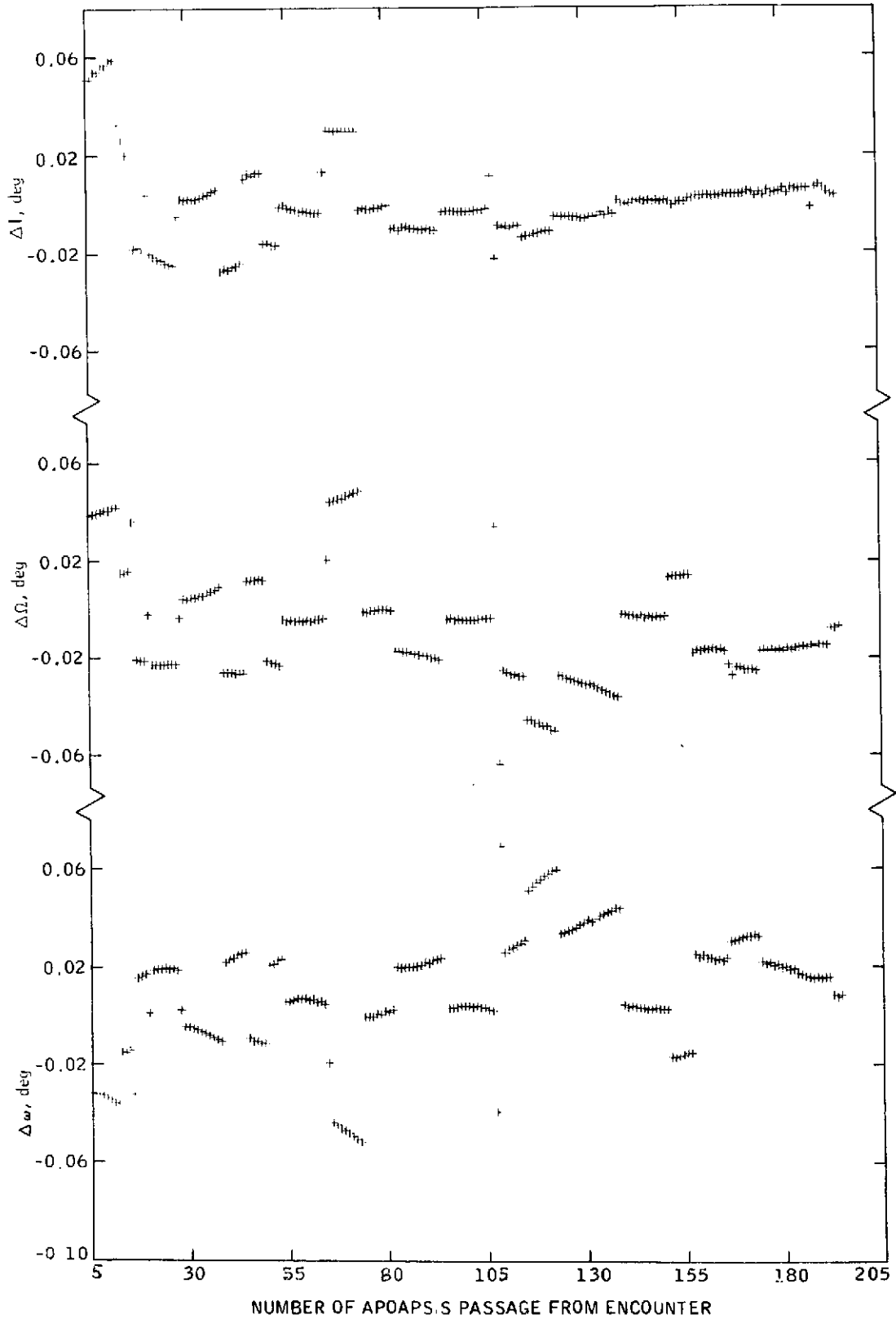
RESIDUALS IN IN-PLANE ORBIT ELEMENTS



231<

Fig. 5.

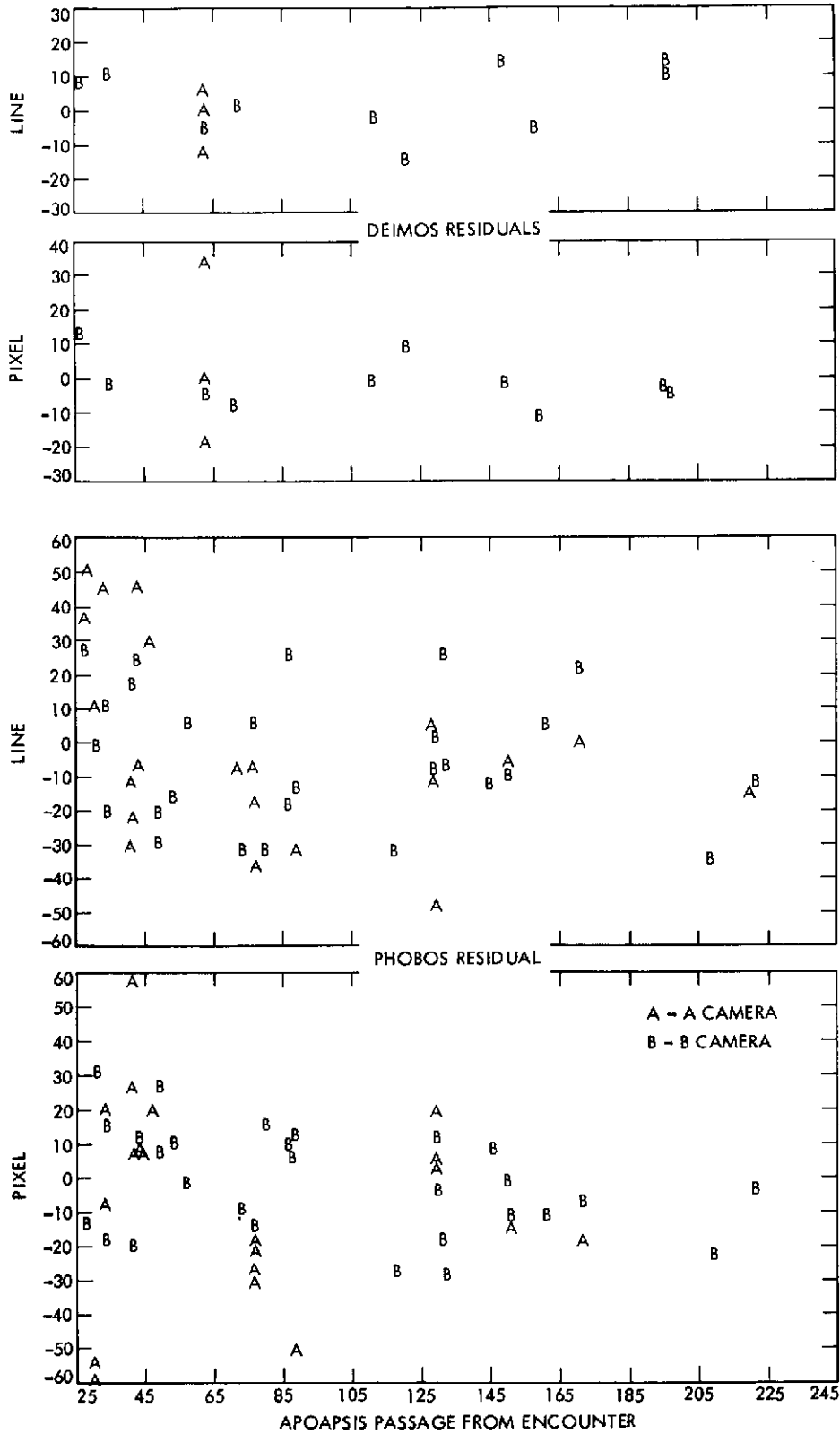
RESIDUALS IN ORIENTATION ANGLES RELATIVE TO MARS TRUE EQUATOR



232<

Fig. 6.

OPTICAL RESIDUALS



APPENDIX O
POLE DIRECTION, CARTOGRAPHY AND THE SHAPE OF MARS

POLE DIRECTION, CARTOGRAPHY, AND
THE SHAPE OF MARS*

Srinivas N. Mohan
Jet Propulsion Laboratory

ABSTRACT

The high resolution photography of Mars by Mariner 9 presents the first close-up view of the entire planet surface and an opportunity to evaluate new photographic data to improve the existing physical model of Mars. The results of data analysis presented here indicate a new location of the North pole of Mars, differing by $0^{\circ}45$ from what was believed to be its orientation in inertial space. Also estimated are the south polar radii and the heights of volcanic prominences in the Tharsis region; namely Nix Olympica, Pavonis Lacus, and Nodus Gordii. Favorable comparisons between existing and new data have been made using radii deduced from combined occultation, ultra-violet spectroscopy, infra-red radiometry, and planetary radar ranging data.

I. INTRODUCTION

With the accomplishment of an extensive mapping mission of Mars, the Mariner 9 spacecraft has returned over 7000 pictures, providing a considerable wealth of data. The purpose of this paper is to present the results of analyzing a select subset of this picture data in order to draw inferences on the celestial orientation of the pole of Mars, which was previously assumed known to an accuracy of 1° (1σ). Also demonstrated is the ability to extract topographical information, as evidenced by favorable comparisons with elevation results from other data types. These are discussed later at some length (cf. Reference 9 for previous work). It is appropriate at this point to introduce briefly the Mariner Mars 1971 mission, its objectives, experiments, and associated instrumentation relevant to this discussion.

Mariner 9 was launched on May 31, 1971, and encountered Mars on November 14, 1971, at 00 hrs 42 min UT. A 1600.5 m/sec retro maneuver slowed the spacecraft sufficiently to be placed in orbit about Mars with an initial orbital period of 12 hrs 37 min. The orbit was designed to satisfy the science requirements of the mission within fuel constraints and to maintain synchronism with the Earth's rotational period on alternate orbits for purposes of communication. The orbit was also selected to maximize longitudinal and latitudinal coverage of the planet for mapping purposes, to ensure early earth occultations so as to recover data on the planetary atmosphere in the early part of the mission, and to delay solar occultation as much as possible in order to keep the spacecraft solar arrays illuminated by the sun throughout the prime mission period. After two and one-half revolutions of the spacecraft about the planet, sufficient data was acquired to establish knowledge of the post insertion orbit and on the fourth periapsis passage the first orbital trim maneuver was performed by a 15.3 m/sec burn designed to decrease the orbital period to 11 hrs 58 min in order to synchronize the periapsis passage with the zenith of the Goldstone Station. A second trim maneuver was performed on the 94th periapsis passage to raise the periapsis altitude. The purpose was to allow more contiguous photographic coverage of the planet surface as well as to resynchronize the periapsis passage with the Goldstone zenith. The orbital elements after the three principal maneuvers are given in Table I.

The principal objective of the MM71 mission was to map the planet and its natural satellites Phobos and Deimos, and to study the atmosphere of Mars. The Mariner 9 spacecraft instrumentation included two television cameras, an ultra-violet spectroscope (UVS), and an infrared radiometer (IRR). Offshoots of the UVS and IRR experiments, relevant to the work reported here, are continuous profiles of local topographical variations over Pavonis Lacus and Nodus Gordii, respectively. This information is combined with the absolute radii derived from occultation data and planetary radar ranging data for purposes of comparison with the radii computed from optical data. The contribution to the shape of Mars stems from solutions to the south polar radii of Mars from the numerous TV pictures of the south polar region. In addition, radii have been calculated at the volcanoes in Tharsis, namely Nix Olympica, Pavonis Lacus, and

Table I. Aerocentric Orbital Elements of Mariner 9

		Initial Parameters Nov 14 to Nov 16	Post Trim 1 Nov 16 to Dec 31	Post Trim 2 Dec 31-
Semimajor Axis (km)	a	13055	12631	12647
Eccentricity	e	0.63	0.62	0.60
Mean Orbital Period (hrs)	P	12.62	11.97	11.99
Longitude of Ascending Node* (degrees)	Ω	42.3	42.1	34.2
Argument of Periapsis (degrees)	ω	-24.9	-24.3	-26.0
Inclination (degrees)	i	64.6	64.8	64.4
Height above surface at periapsis [†] (km)	h_p	1396	1387	1641
Latitude of sub-periapsis passage (degrees)	ϕ_p	-22.3	-21.9	-23.3
*Keplarian elements referenced to Mars true equator of date.				
†Mean radius of Mars = 3394 km.				

Nodus Gordii. The computed absolute radius at the summit of Nix Olympica is 3419.2 ± 2.6 km, which is equivalent to a relative height of 18.2 km to the summit caldera from its base.

The state of knowledge as regards the pole direction, surface feature location, and planetary radii before processing the picture data will be outlined briefly below.

Prior to the MM71 determination, the inertial direction of the spin-axis of Mars was obtained by averaging the celestial poles of the satellite orbits of Phobos and Deimos (Burton, 1929), together with a solution obtained from Earth-based observations of surface markings by Camichel (cf. G. Vaucouleurs). The Nautical Almanac adopted a somewhat different set of values for the pole direction (cf. Michaux) differing by about 1° from the above. Thus, the a priori knowledge uncertainty in pole direction

appears to be of the order of 1° . In this paper, a new solution is constructed that fits repeated visual observations of the same set of features over a time span of about 108 days. Further, corroboration with newly obtained Deimos-star data is shown by relating the Laplacian pole of Deimos to the spin-axis.

The a priori information available on surface feature location was limited by MM69 photography. The extent of such photography was small in comparison with the total unmapped planet surface, and, consequently, most of the surface features were viewed for the first time with no prior information as to their areographic locations, with the exception of Nix Olympica which is easily identified in Earth-based telescopic observations. The radii of Mars at these features were calculated (a priori) as a function of the latitude on an oblate spheroid of radius 3393.4 km and a polar flattening of 0.0107 (cf. Michaux). The a priori knowledge uncertainty associated with these radii were assumed to be 20 km (1σ), based on the consideration that the flattening values ranged over 0.005 to 0.0107 and global topographical variations of 12 km were discernible from planetary radar ranging data.

Earth-based telescopic observations, from which the physical model for Mars was constructed, was necessarily limited by the achievable resolution at the surface of Mars. The gains reported here are a reflection of the gains made in resolution by the proximity of Mariner 9 to Mars and in the accuracy of the measurement system comprised of the two TV instruments, whose position and celestial attitude were measured precisely.

II. DESCRIPTION OF ONBOARD INSTRUMENT AND OBSERVABLE

The imaging system on board the Mariner 9 spacecraft consisted of a wide-angle low-resolution camera and a narrow-angle high-resolution camera mounted on a scan platform which could be positioned relative to the spacecraft in two degrees of freedom. The wide-angle camera had an effective focal length of 50 mm and a field of view of $11^\circ \times 14^\circ$ with a surface resolution of 1 km at a slant range of 1750 km (approximately). The narrow-angle camera had a field of view of $1.1^\circ \times 1.4^\circ$ with a surface resolution ten times that of the wide-angle camera. The basic observable, called landmark tracking data, consisted of picture coordinates of images measured on photographic plates with a suitable reference system in the TV coordinates. A sample data product is shown in Figure 1.

The available collection of pictures transmitted by Mariner 9 was screened, and a select subset from the collection was filtered out for processing. The criterion for such selection was based on maximizing the repeated observability of the same set of surface features over as long a time span as was available. The dust storm obscuration of the planet, during the initial period following orbit insertion of Mariner 9, restricted visibility of the planet surface to its south polar region and to the volcanic prominences in the Tharsis region. As a result, much of the earlier data contained hazy images of Nix Olympica, Pavonis Lacus, and Nodus Gordii. There were many repeated observations of the south polar cap and surrounding terrain. As the dust storm cleared up in January 1972, the TV photography was aimed at systematic mapping of the planet. These pictures were taken in a manner to ensure minimum redundancy in imaging the surface of the planet. Thus, data became available only during special picture sequences, when the TV camera was trained on the south polar cap, and on the volcanic prominences in Tharsis, namely Nix Olympica, Pavonis Lacus, and Nodus Gordii. (The data containing Ascraeus Lacus was very scanty and of poor quality; hence, was not used.) The decreasing observational density after January 1972 is evident in the data (refer to Figure 10). Figure 2 shows the distribution of the total usable pictures relative to time of periapsis passage, in terms of target sighted, and type of camera used. A very large portion of the data is made up of wide-angle pictures of the south polar region, all taken 30 minutes before periapsis. This part of the data allows observation of the south polar cap from a nearly fixed position in space while the planet rotates underneath the spacecraft at the rate of 9.5° (approximately) per orbit of Mariner 9. These data are thought to be of value in the determination of the Martian pole and the south polar radius of Mars (referred to the planet-center-of-mass). A total of 13 landmarks was sighted. These are shown in Figure 3.

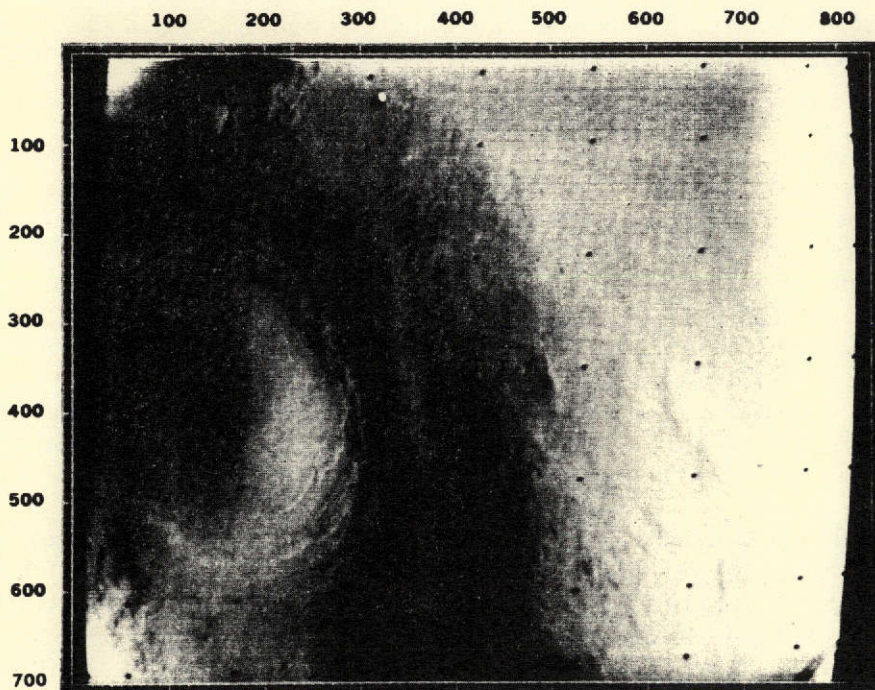


Figure 1. Sample raw data product—contrast enhanced

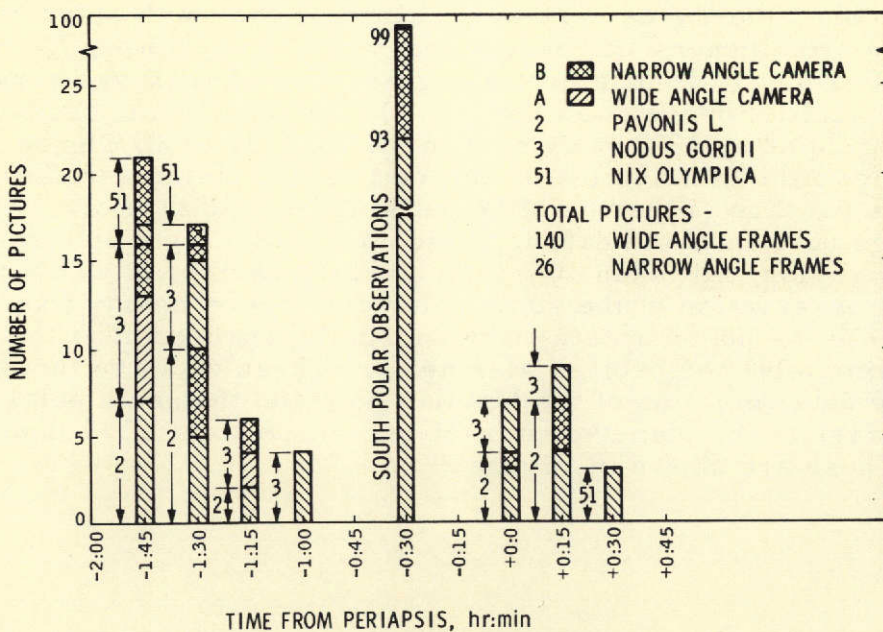


Figure 2. Distribution of observation times relative to time of periapsis passage of spacecraft

Reproduced from
best available copy.

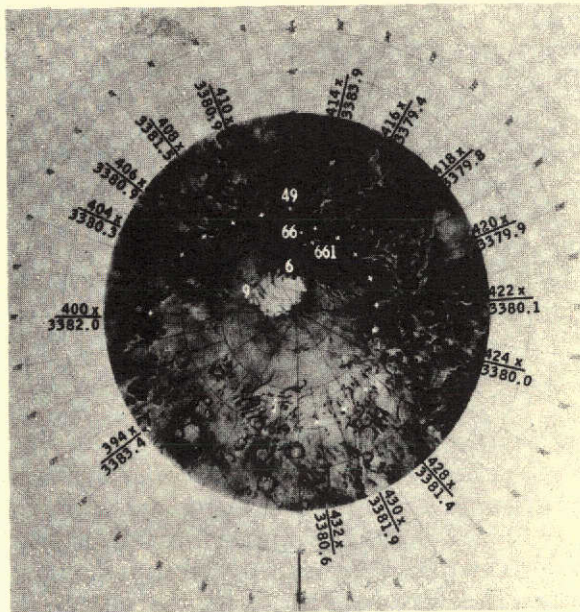


Figure 3a. Landmarks in the south polar region

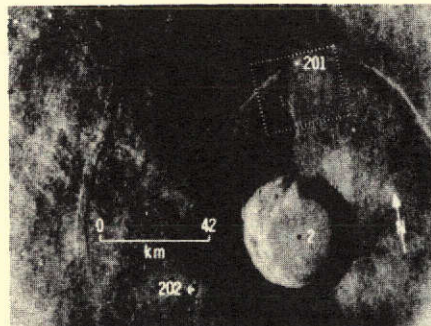


Figure 3b. Location of landmarks in Pavonis Lacus



Figure 3c. Landmark location in Nodus Gordii

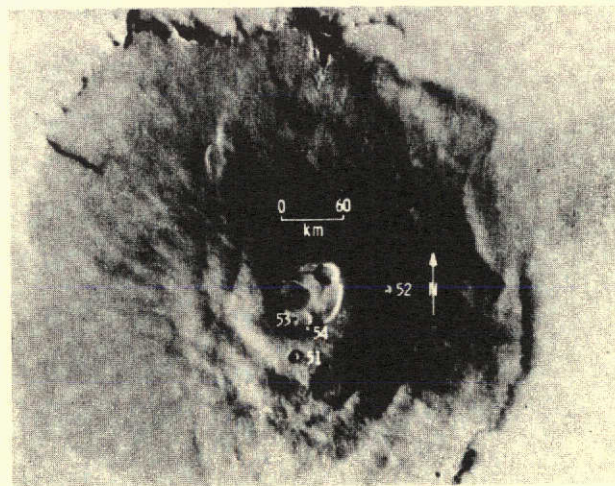


Figure 3d. Landmark locations in Nix Olympica

available to determine the switching condition of the spacecraft attitude control system, and thereafter fit an appropriate segment of the data, in the neighborhood of the shuttering instant. This procedure was adequate during the high data rate transmission, when the engineering data samples were obtained every 4.2 seconds. However, an appreciable portion of the pictures was taken when engineering data sampling rate was four times slower than the 4.2 seconds/sample rate. In these situations it was not always possible to deduce the trend of limit cycle excursions correctly within the allowed dead band. Such data were therefore hand-sifted to obtain the nearest two data samples containing the shuttering interval, and the readout was obtained by linear interpolation. In addition, problems were encountered, occasionally, in obtaining the cone and clock gimbal angle readouts. Because of the commensurability between the sampling interval for these readouts and the minimum interval between consecutive exposures, there were situations in which, when the telemetry channels were sampled, the scan platform was in the slewing mode. In such instances the gimbal angle readouts were not available; hence, they were furnished from the commanded DN values for those channels. The "open-loop" TV raster orientation, thus constructed, had appreciable errors associated with it. Hence, a "closed-loop" second stage determination of the TV camera pointing errors was essential in order to provide consistent solutions.

The second stage of processing consisted of solving for the most probable camera orientation at shuttering times, given the estimated direction of inertial pointing from the first stage of processing. It was noticed during early landmark data fits that there was a significant discontinuity in the data residuals whenever the cameras were switched, i. e., the narrow-angle camera residuals were observed to be offset from the wide-angle camera residuals. The obvious inference was that the model for pointing errors needed an additional three degrees-of-freedom in order to describe the wide-angle camera offsets in the platform coordinates relative to the narrow-angle camera optic axis. When these additional degrees-of-freedom were introduced, such discontinuity was noticeably reduced. In addition to these, a set of three fixed offsets of the narrow-angle TV target raster (relative to the scan platform pointing defined by the first stage estimates) was solved for. Superimposed on these was a random component which was modeled as being in the yaw, pitch, and roll directions of the spacecraft. Thus, a total of nine parameters was estimated in order to describe adequately the "true" TV orientation, with respect to the celestial reference made up by the spacecraft-sun, and spacecraft-Canopus directions.

In addition to the above mentioned discontinuity, there was another source of error stemming from the sun-sensor regulation problem. This is stated, briefly, below. It was noticed in fitting some close range landmark data that the data residuals were enormously large in comparison to the expected measurement error. It was also noticed that the peculiarity occurred only in the case of pictures shuttered within 20 minutes after periapsis passage of the spacecraft. An explanation for this behavior turned out to be associated with the design of sensor preamplifier circuitry. It was found, from some symptomatic behavior of the attitude control telemetry, that the Sun sensor went into an anomalous state whenever stray light

from Mars became sufficiently strong in intensity. The incident stray light from the planet rendered the voltage regulation mechanism of the acquisition Sun sensor ineffective. Due to an unfortunate design configuration, the primary Sun sensor was dependent on this very same mechanism to provide voltage regulation. The result was a floating voltage (and an unknown scale factor for the primary sun-sensor output) whenever the problem occurred. Since the engineering telemetry was rendered meaningless in these situations, it was necessary to discard all data taken in the vicinity of periapsis passage of spacecraft. This resulted in the elimination of the high-resolution data. The alternative of corrupting the covariance to solve for the camera pointing direction, in the absence of first stage processing, was not very successful.

B. Data Processing Software and Operational Procedure

The data processing software that is used for processing the engineering data consists of a data editing and polynomial fitting program, called the extractor (XTR); and a TV calibration program called the Optical Data Calibration and Rectification program (ODCR). The resulting camera pointing information, together with image locations and spacecraft trajectory, is input to the Optical Observables and Partial Generator Program (OOPG) to generate prefit data residuals, and data partials for differential correction. The final picture data fitting program is a landmark estimator (LMESTM) which is a sequential Kalman formulation with a capability to handle time correlations in the estimation parameters. All programs are operational on the UNIVAC 1108 computer. An operational flow chart is shown in Figure 5.

C. Filter Configuration

The filter configuration and associated software is more general in capability than that required for processing landmark data. The description given below is restricted to those portions required for the processing of data.

As mentioned in paragraph A above, the solution list consists of:

1. A constant correction to the node in the plane-of-sky associated with each probe ephemeris segment, obtained by processing Earth-based doppler data.
2. The RA, DEC of the true, of date Martian spin-axis referred to the Earth Mean Equator and Equinox of 1950 coordinates. (Secular variations are assumed known.)
3. Areographic latitude and longitude of each landmark and the radius of Mars referred to the planet center-of-mass at each of the landmark locations.

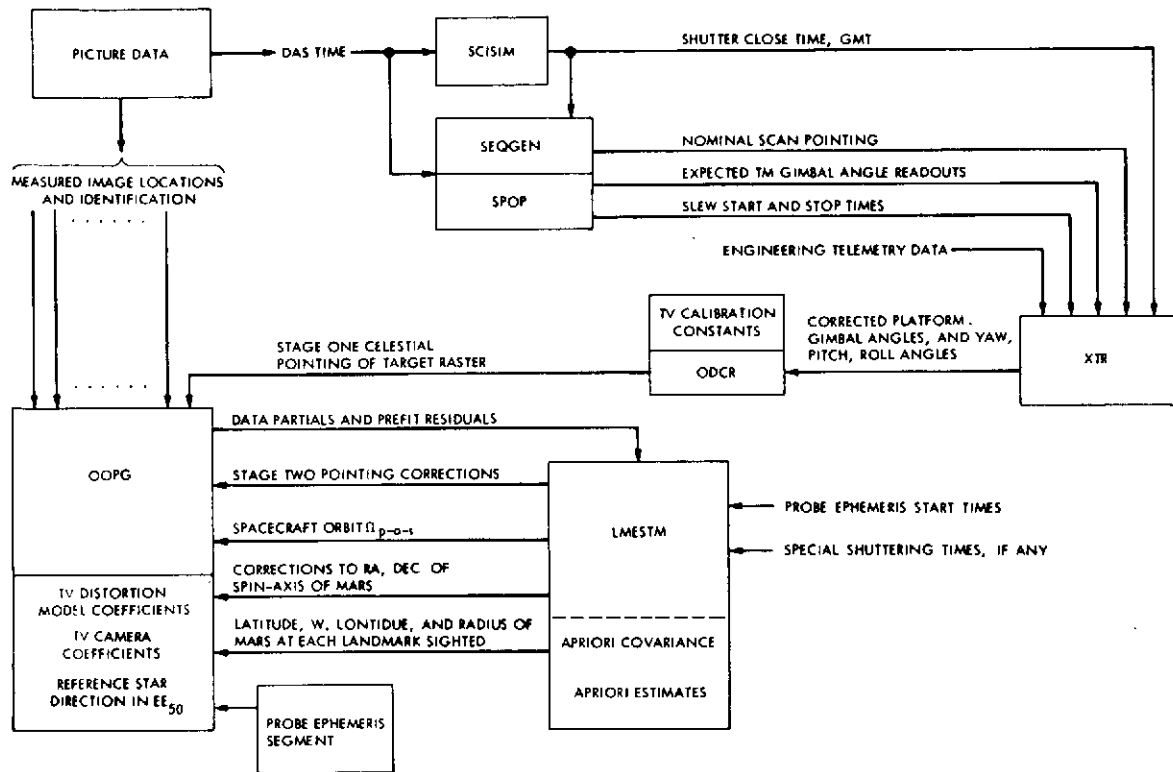


Figure 5. Landmark data processing flow chart

4. Second stage TV pointing errors made up of:
 - a. A set of three constant offsets of the narrow-angle target-raster in the platform coordinate system described by the increasing cross-cone, cone, and twist directions.
 - b. A set of three constant offsets of the wide-angle target-raster with respect to the narrow-angle target-raster, defined in the platform coordinate system.
 - c. A set of three random variations of the scan platform with respect to the celestial coordinate system described in the yaw, pitch, and roll directions.

Thus the implemented filter must have the ability to estimate a set of constant parameters over discrete time segments made up by the length of each of the available probe ephemerides; and additionally be able to model the discontinuity in the trajectory information by treating it as process noise between probe ephemeris segments.

The formulation is as follows. Let the measurement vector

$$z = Hx + v + Ac$$

where v is the measurement noise of "known" covariance R , and the vector c consists of correlated components of the solution vector. Vector c is modeled as follows:

$$c(t_1) = \rho(t_1 - t_0) \cdot c(t_0) + \sqrt{1 - \rho^2} q$$

and

$$\rho(t_1 - t_0) = e^{-(t_1 - t_0)/\tau}$$

Thus, by letting $\tau \rightarrow 0$, $\rho \rightarrow 0$; and hence, c can represent random coefficients in the solution list. Similarly, by letting $\tau \rightarrow \infty$, and $\rho \rightarrow 1$; $c(t_1) \rightarrow c(t_0)$ for all t_1 and t_0 .

If we define a new augmented state vector x which contains both the previously defined set of constants and the correlated coefficients c ; and, further define estimates and covariances in the usual notation, we have the filter as follows.

$$P^+ = P^- - P^- H^T (H P^- H^T + R)^{-1} H P^- \quad \text{(measurement update of covariance)}$$

$$\hat{x}^+ = \hat{x}^- + K(z - H\hat{x}^-) \quad \text{(update of estimate)}$$

$$K = P^- H^T (H P^- H^T + R)^{-1} \quad \text{(optimal filter gain)}$$

Whenever a new trajectory segment is encountered, we let

$$P^+ = P^- + DQD^T$$

and

$$\Omega_{p-o-s} = 0$$

In addition to the measurement update equations given above, the final solution consists of the final values of the constant parameters x and solutions c at each observation time (stored appropriately) as well as the node correction for each probe ephemeris segment. The post-fit data residuals are computed on a picture-to-picture basis with these final values.

D. A Priori Assumptions

We shall state here the a priori values assumed and the associated rationale for such choice in correspondence with the earlier mentioned solution parameters.

The spacecraft node in the plane-of-sky (designated Ω_{p-o-s}) for the various trajectory segments had discontinuities in it, which were on the order of $0^{\circ}05$; thus the a priori 1σ value was based on this state-of-the-art uncertainty.

The right ascension and declination of the spin-axis of Mars were determined from approach and orbiter data using both radio and optical observations (cf. Reference 1). The values thus obtained were used as the nominal spin-axis orientation. The associated uncertainty was set to a large a priori value of $10^{\circ}0$.

The areographic latitudes and longitudes were unknown, and hence, their a priori values were set at 10° (1σ), equivalent to a surface location uncertainty of 600 km, approximately. The polar longitude uncertainties were set at 60° to impart the same order of surface location uncertainty. The radii of Mars were assumed known to an accuracy of 20 km (1σ). The largest correction obtained was 26 km above the mean equatorial radius of 3393.4 km.

The TV pointing uncertainties were set at $0^{\circ}03$ (1σ), being comparable to a quantization step in the engineering telemetry data. Since limited star data were available to calibrate the wide-angle camera offsets, the a priori uncertainty was set at $0^{\circ}05$ (1σ).

The data were weighted independently for each of the various landmarks sighted. Measurement uncertainties are listed below (1σ values):

Landmark ID	Narrow-angle camera		Wide-angle camera	
	Pixel	Line	Pixel	Line
6	20	20	3	3
66	*	*	3	3
661	*	*	3	3
49	*	*	3	3
9	10	10	3	3
2	10	10	5	5
201	5	5	3	3
202	3	3	*	*
3	5	5	3	3
51	4	4	3	3
53	4	4	3	3
54	4	4	3	3

* Observations of the indicated type were not made.

IV. RESULTS AND ACCURACY

A. Landmark Locations in Areocentric Coordinates

The landmarks sighted are shown in Figure 3. For each of the landmarks sighted, estimates of latitude, W. longitude, and radii are listed in Table II. TV residuals corresponding to each of the landmarks in Pavonis Lacus, Nodus Gordii, Nix Olympica, and the South Polar cap are shown in Figures 6, 7, 8, and 9, respectively. Figure 10 shows the temporal distribution of all the data residuals. It may be observed that the 1σ value of these residuals is 3 pixels, and 3 lines in the wide-angle TV camera. The narrow-angle residuals, when reduced to an equivalent wide-angle residual, are well bounded by the above 1σ value. The only exceptions are observations affected by the sun-sensor regulation problem (discussed in paragraph III.A). These data points were deleted from the data fit. The corresponding residuals are shown encircled in Figures 6, 7, 8, and 9. The nominal locations of the landmarks were obtained from overlays, initially; and thereafter, from iterated solutions. The radius was set at 3393.4 km for the equatorial landmarks, and at 3380.0 km for the polar landmarks, initially. These values were iterated upon, subsequently. A priori uncertainties associated with landmark locations are given in Section III.

Table II. Elevation results from landmark data processing

Landmark	ID	Latitude, deg 1σ	W. Longitude, deg 1σ	Radius, km 1σ	Combined UVS and Occultation Radius, km	Combined Radar and Occultation Radius, km
South Polar Cap	6	-86.02 \pm 0.01	357.11 \pm 0.14	3384.67 \pm 2.0	Exit occulta- tion value at -78.8 latitude and 346.6 W. longitude is 3383.9 km	Outside limits of Earth based radar observability
	9	-84.12 \pm 0.01	57.69 \pm 0.11	3382.44 \pm 2.0		
	66	-80.22 \pm 0.03	354.11 \pm 0.10	3383.41 \pm 2.0		
	661	-81.00 \pm 0.02	341.42 \pm 0.11	3382.71 \pm 2.0		
	49	-76.97 \pm 0.03	1.33 \pm 0.11	3384.97 \pm 3.5		
Pavonis Lacus	2	0.50 \pm 0.04	113.17 \pm 0.03	3410.81 \pm 2.5	3411.5	3412.0
	201	1.58 \pm 0.03	113.00 \pm 0.03	3413.07 \pm 2.4	Nearest avail- able value is 3417.5	Nearest avail- able value is 3418.0
	202	0.28 \pm 0.03	113.96 \pm 0.03	3414.95 \pm 2.3		
Nodus Gordii	3	-10.25 \pm 0.03	120.82 \pm 0.03	3412.05 \pm 2.3	Base 3402.0	3403.5
Nix Olympica	51	17.21 \pm 0.03	133.73 \pm 0.03	3419.20 \pm 2.6	Base 3401.0	3402.5
	53	17.91 \pm 0.03	133.70 \pm 0.03	3416.22 \pm 2.7	No relative information available	
	54	17.77 \pm 0.03	133.45 \pm 0.03	3418.51 \pm 2.6		

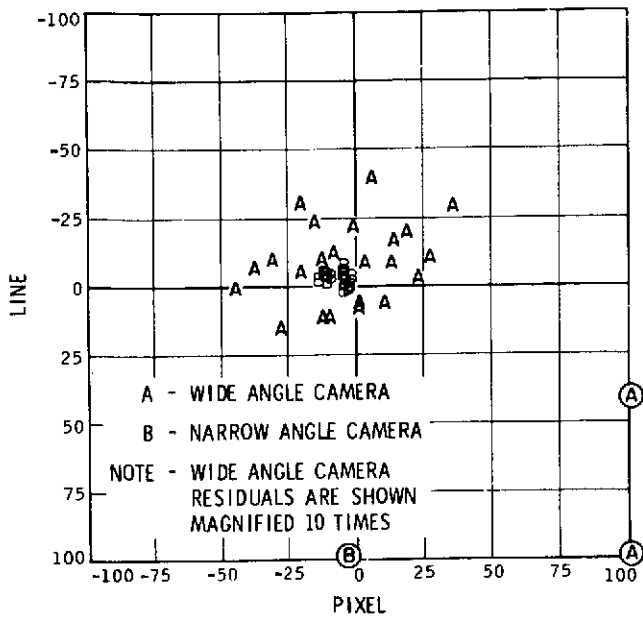


Figure 6. TV image residuals Pavonis Lacus

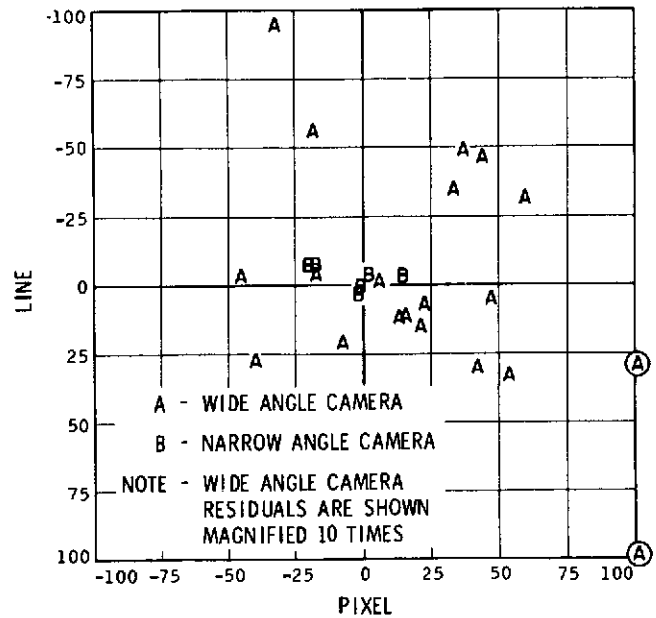


Figure 7. TV image residuals Nodus Gordii

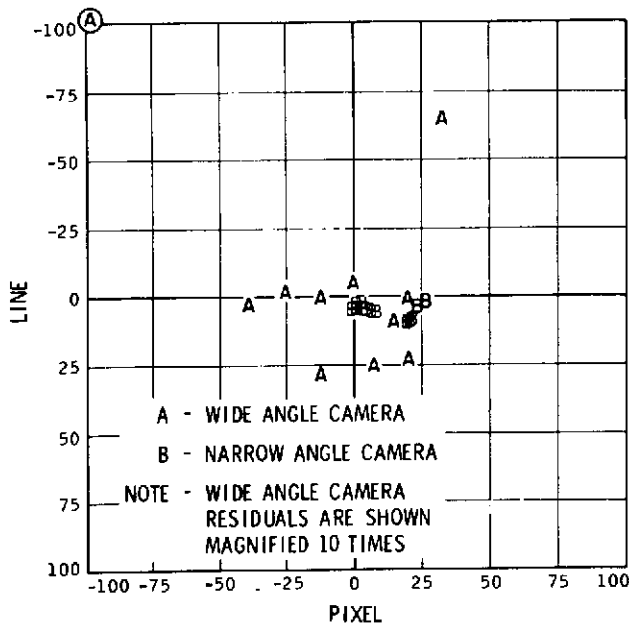


Figure 8. TV image residuals Nix Olympica

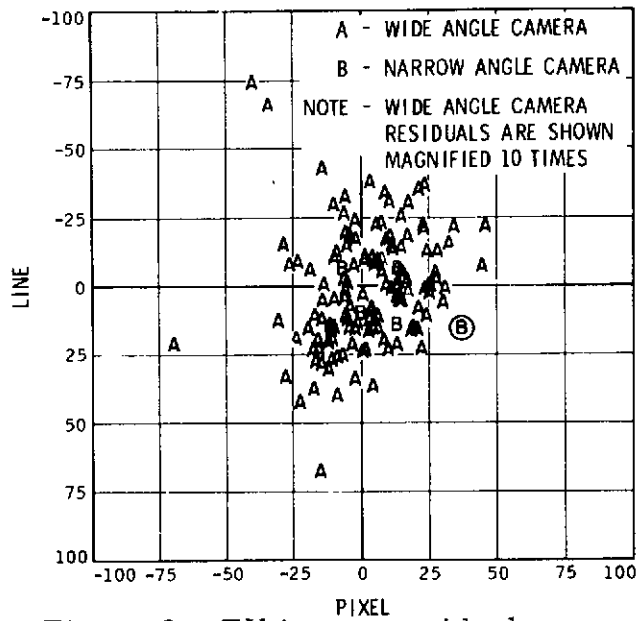


Figure 9. TV image residuals South Polar Region

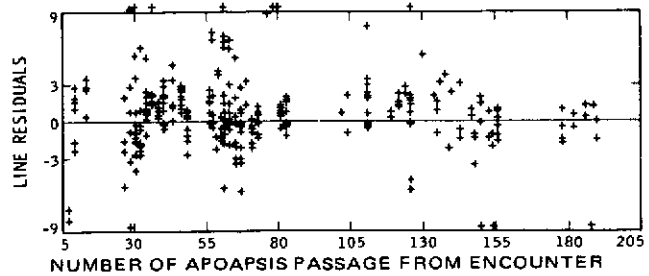
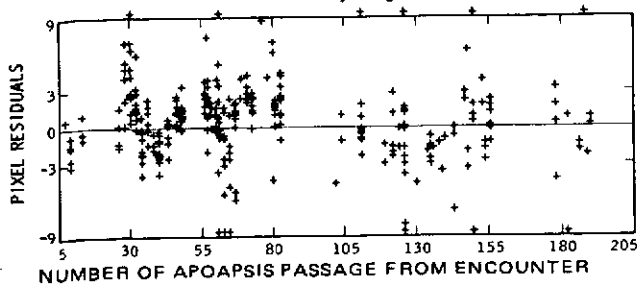


Figure 10. Landmark image residuals - An angular deviation of $0^{\circ}05$ is equivalent to 3 pixels (lines) in TVA and 30 pixels (lines) in TVB.

The results indicate that the landmark coordinates are obtained to an accuracy of $0^{\circ}03$, equivalent to 1.8 km (1σ) at the surface. These values compare favorably with the wide-angle camera resolution limit of 2 km at a slant range of 3500 km (approximately).

B. Comparison of Elevation Results

Table II shows the results of solving for the radius of Mars at the landmarks sighted. It must be pointed out that since the observations are referenced to the spacecraft position in orbit, the elevation values obtained here are referred to the center-of-mass of the planet.

In order to obtain correlation between solutions resulting from landmark data and those resulting from occultation, planetary radar ranging, UVS pressure, and infrared radiometry data, it is necessary to construct the absolute radii of Mars in the vicinity of the landmarks under consideration. This is done below.

It is known that both planetary radar ranging data and UVS pressure data yield information on relative heights of topographical features while occultation data yields the absolute radius both at signal extinction and reacquisition. Infrared radiometry provides indirect inferences on slopes of topographical features from measured temperature profiles which are integrable to yield relative height information. For details of these methods, we refer the reader to appropriate literature. (See References 10 and 11 for example.) We include here topographical maps generated from these data for reference. Figure 11 shows the radar map of Mars and Figure 12 shows the UVS pressure map calibrated to show relative heights. Both Figures 11 and 12 have occultation positions plotted in areographic coordinates. By matching occultation values of the radii of Mars at each of these positions with the nearest interpolated contour value, it is possible to calibrate the contour maps to show absolute information on heights instead of relative height information. This procedure yields 3393.4 km as the zero contour value in the UVS map and 3397.5 km in the radar map. Since both Figure 11 and Figure 12 are drawn on a macro scale in comparison to the landmarks used in this analysis, the contour values reflect base radii in the vicinity of Nix Olympica, Pavonis Lacus, and Nodus Gordii. These are 3401.0 km, 3403.0 km, and 3402.0 km, respectively, as read from the UVS map; and 3402.5 km, 3403.5 km, and 3403.5 km, respectively, as read from the radar map. The relative height from base to the summit is available from a detailed UVS profile of Pavonis Lacus and from an IRR profile of Nodus Gordii. These are shown in Figures 13 and 14, respectively. Direct comparison of values for the main caldera (identified as 2 in Figure 3) in Pavonis Lacus shows that the estimated radius is within 0.7 km of the combined UVS-occultation value and within 1.2 km of the combined radar-occultation value. Similar comparisons for Nodus Gordii show the estimated radius to be within 2.5 km of the combined UVS-occultation-IRR value, and within 3.5 km of the combined radar-occultation-IRR value. The formal 1σ uncertainties are tabularized in Table II. Figure 3 shows a map of the south polar region bounded by the 65° latitude band. It may be noticed from the map that the exit occultation position labeled 414x is the closest point to the

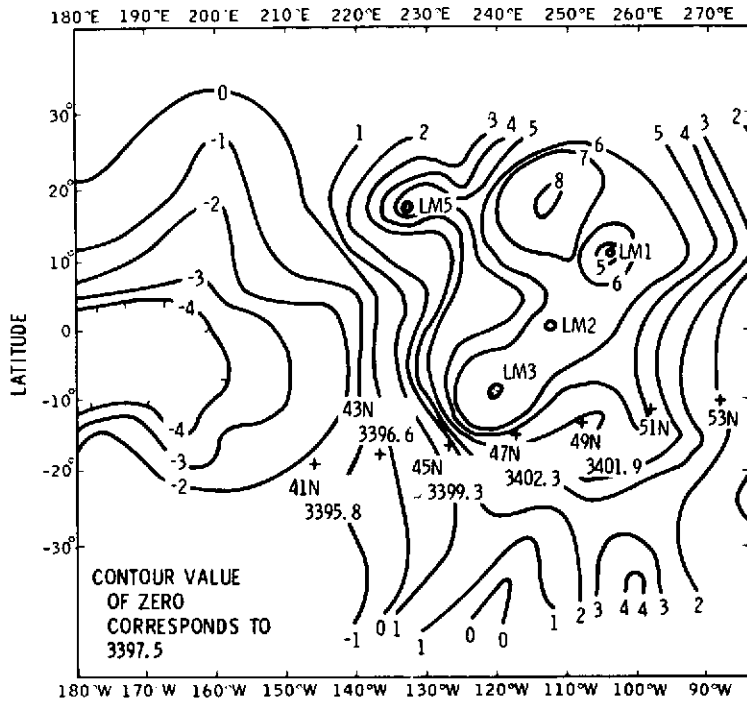


Figure 11. Topography of Mars (from radar ranging data)

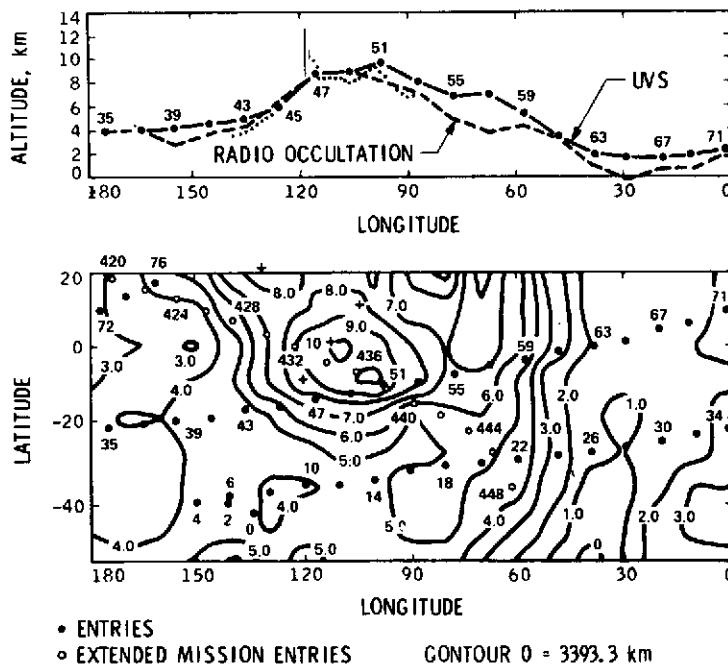


Figure 12. Topography of Mars (from UVS and occultation data)

251<

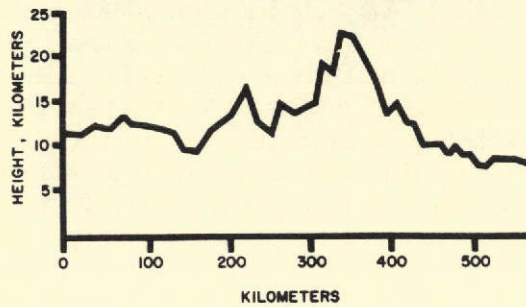
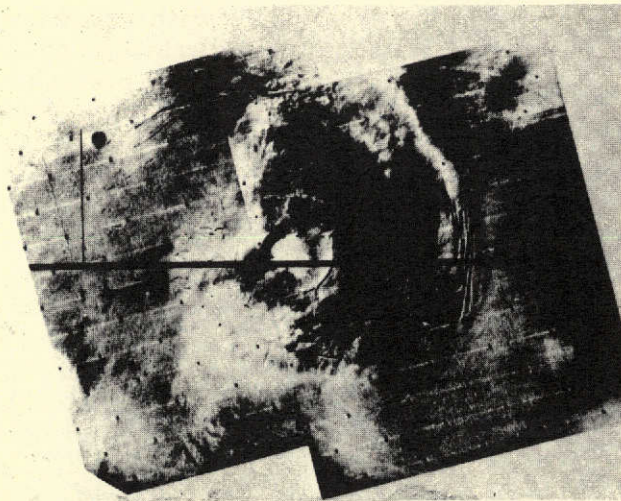


Figure 13. Mariner Mars 1971 UVS profile of Pavonis L.

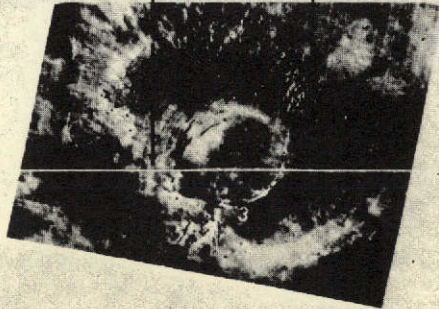
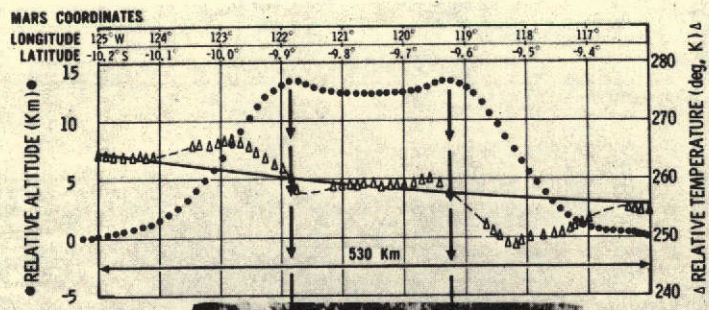


Figure 14. Mariner Mars 1971 IRR view of Nodus G.

252<

south polar landmarks. Comparisons to the radius value of 3383.9 km show that the estimate of radius value at LM66 is within 0.5 km and that of LM661 is within 1.2 km. The associated formal uncertainty of 2.0 km (1σ) appears quite representative. No comparisons are available for Nix Olympica.

C. Spin-Axis Solution

Prior to the Mariner Mars 1971 mission, it was believed that the inertial direction of the Martian north pole (described by the RA and DEC of the spin-axis in mean EE₅₀ coordinates at the 1950 epoch) was known to an accuracy of 1 degree. Figure 15 shows the pole solution obtained by various observers using surface markings and orbits of the natural satellites Phobos and Deimos since 1877. These were taken from Reference 2 and mapped into EE₅₀ coordinates and to the 1950 epoch. The solutions reflect a total spread of 4° in RA and 2° in DEC. The value adopted prior to the MM71 period was obtained by averaging the Laplacian pole of Phobos, the same of Deimos, and the spin-axis obtained by Camichel from surface markings. (cf. Reference 2 for details.) As will be shown later in this section, an offset was introduced by taking such unweighted average and by not accounting for the fact that the Laplacian pole of Deimos is separated from the Martian spin-axis by 0.89 as a result of significant solar perturbation of the orbit of Deimos. This offset was introduced a priori, in the direction connecting the Laplacian pole of Deimos and the true spin-axis of Mars, under the assumption that the Laplacian pole of Deimos' orbit is determined to an accuracy of

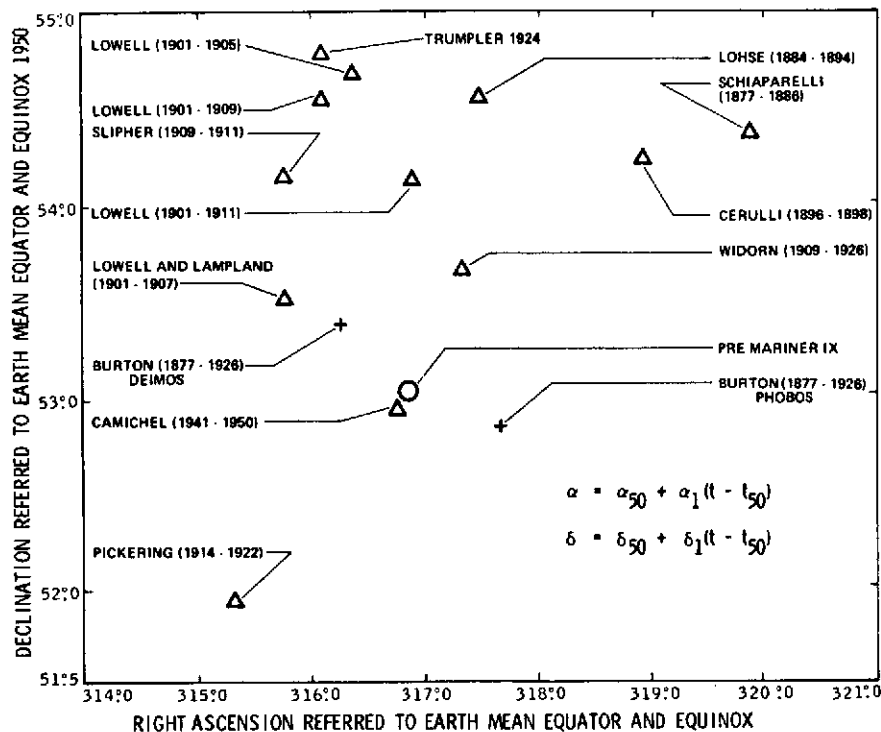


Figure 15. Celestial coordinates (1950) of the north pole of Mars

$\pm 0^{\circ}05$, as contained in Reference 3. The a posteriori estimates of the pole direction show that the resulting correction to the Camichel-Burton pole was along the preferred direction connecting the Laplacian pole of Deimos' orbit to the spin-axis. An explanation follows.

The spin-axis of Mars is shown plotted in the Laplacian plane of Deimos' orbit in Figure 16. Reference coordinates in this diagram are defined along the increasing RA and DEC directions as seen in mean EE₅₀ coordinates. The satellite orbit data is taken from Wilkins (cf. Reference 3) for purposes of comparisons and plotting. The larger of the two circles in the diagram represents the retrograde path of the instantaneous angular momentum vector of Deimos' orbit, with an inclination of 1:8 to its Laplacian pole, completing one period every 54.36 years, approximately. The smaller circle shows similar details of the orbit of Phobos, however, with a different inclination of 0:9 and a period of 2.26 years for the nodal regression. Reference is made to the Laplacian pole of Deimos, with the justification that the outer satellite inclination is measurable to greater precision in Earth-based telescopic observations than the inner satellite inclination with respect to inertial space and hence Wilkins' determination of the Laplacian pole is more accurate in the case of Deimos than in the case of Phobos. It is possible to construct a probable location of the spin-axis which agrees with solutions obtained from Mariner 9 data. Satellite data taken by Mariner 9 also confirms that the Wilkins orbit of Deimos predicts the satellite position at encounter very well, with the exception of a small shift in mean longitude,

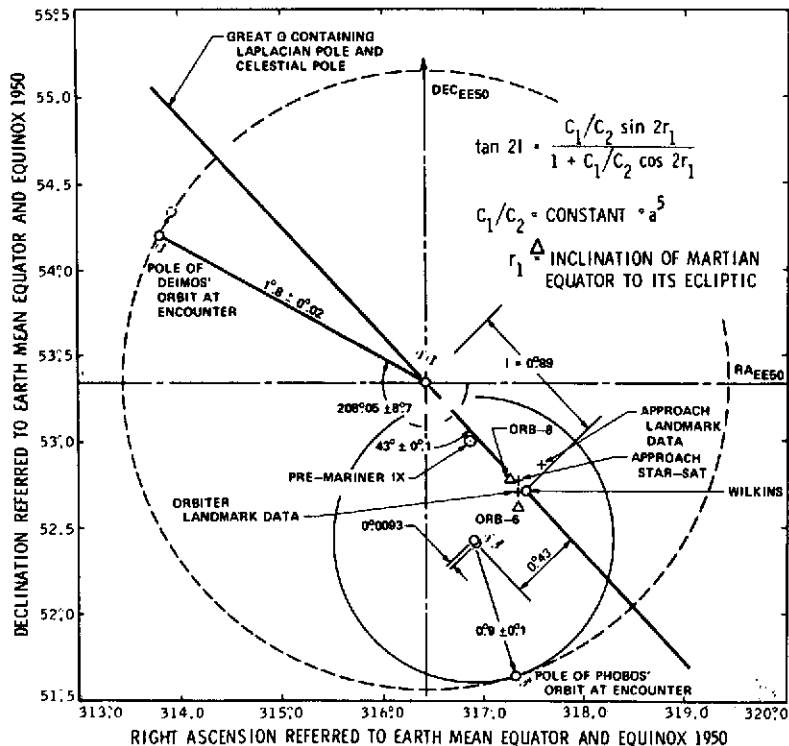


Figure 16. North pole of Mars in the Laplacian plane of Deimos

(cf. Reference 4). In the remainder of the discussion, we shall reference to the Laplacian pole of Deimos' orbit and we shall treat the Laplacian pole of Phobos' orbit as determined by Wilkins to be in substantially greater error than the same for Deimos' orbit. In the discussion to follow, we show the interrelation between the spin-axis and the satellite poles and show implications of the Mariner 9 data as regards accuracy of determination of each of these.

It is known that the dynamical oblateness effect of Mars on its satellite orbits is to cause a precession of the orbits about the maximum axis of inertia of the planet in the absence of all other forces. It can be shown that in the presence of significant solar perturbation of the orbit, in addition to the dynamical oblateness effect, the precessional axis (Laplacian pole) is moved towards the celestial pole (defined by the normal to the ecliptic) along the great circle connecting the "true" spin-axis to the celestial pole, (cf. Reference 5). Further, it can be shown that the magnitude of such separation, denoted I , is calculable from

$$\text{Tan } 2I = \frac{C_1/C_2 * \sin 2\gamma}{1 + C_1/C_2 * \cos 2\gamma}$$

where C_1 and C_2 are constants associated with the solar perturbation and the dynamical oblateness effect, respectively; and γ is the inclination of the equator of Mars to its ecliptic. It can be shown that the ratio C_1/C_2 is proportional to the fifth power of the semimajor axis of the satellite orbit. Thus the solar perturbation effect is more pronounced on the orbit of Deimos than on the orbit of Phobos. In fact, the calculated separation between the Laplacian pole of Deimos' orbit and the planet spin-axis is $0^{\circ}89$, and the same in the case of Phobos is $0^{\circ}0093$. Figure 16 shows the spin-axis of Mars (in the L_{eff} plane) referred to the respective Laplacian poles of Phobos and Deimos. It may be observed that the spin-axis corresponding to the Laplacian pole of Deimos correlates very well with the pole solutions obtained from Mariner 9 radio and optical data. One would expect to see the Laplacian pole of Phobos to coincide with the spin-axis solutions. Compared to this position, the Laplacian pole of Phobos, as determined by Wilkins, appears offset by $0^{\circ}43$, in a direction normal to the great circle containing the celestial pole and the spin-axis of the planet. If the reasoning thus far reflects the truth of the situation, one may expect to see a correction to the orbit of Phobos from Mariner 9 data. This confirmation is yet to be obtained from detailed analysis of all Phobos picture data transmitted by Mariner 9. With the available one-year spread of optical observations of Phobos, it will be possible to factor out a significant precession of Phobos' orbit about its Laplacian pole, due to the dominant J_2 effect; and to simultaneously determine the Laplacian pole itself.

The various radio and optical solutions of the spin-axis of Mars from Mariner 9 data are shown in Figures 16 and 17. As noted earlier in this section, it may be observed from these diagrams that the spin-axis is moved from its nominal position by $0^{\circ}45$ along the great circle containing the

celestial pole and the Laplacian pole of Deimos' orbit defined by Wilkins. The agreement in the various solutions can be seen from Figure 17 to be 0:1 in RA and 0:15 in DEC (with the exception of the approach landmark determination).

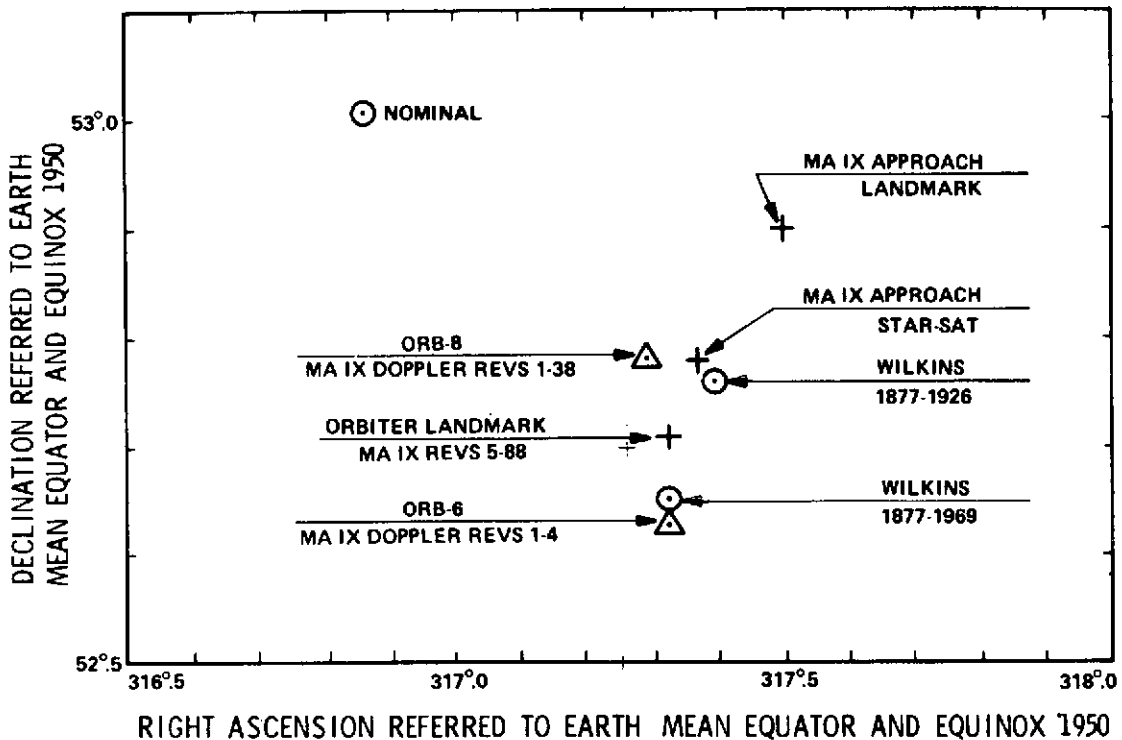


Figure 17. North pole of Mars from Mariner 9 data

256<

V. CONCLUSIONS

In summing up the discussion on the results of landmark data analysis, we have shown that

1. Landmark control coordinates for surface mapping can be determined to an accuracy of 2 km (corresponding to 0.03 in latitude and longitude). The accuracy of these coordinates, together with the new spin-axis solution would allow prediction of the landmark positions in inertial space to a comparable accuracy limit.
2. Landmark elevations have been obtained which correlate with similar values from other data sources to within 2 km. It must be pointed out that the accuracy limits of the various data types has not been taken into account in making such comparisons, and that the values were obtained by combining the occultation radii with relative height information from radar, UVS and IRR, where available. No comparative values are available for Nix Olympica. Landmark data on Nix-O indicates an absolute radius of 3419.2 ± 2.6 km at the summit caldera, which is equivalent to a relative height of 18.2 km to the summit from the base.
3. A new consistent pole solution has been obtained which is in agreement with radio solutions. Mariner 9 optical data (discussion in 4c) indicates that the Laplacian pole of the orbit of Phobos as calculated by Wilkins is in error by 0.43 . A confirmation is possible by the detailed analysis of Mariner 9 TV data on Phobos.
4. Various pointing offsets have been determined; however, no comparisons are available in the absence of simultaneous stellar imaging. The corrections are limited by the a priori uncertainty of 0.03 for the narrow angle offsets and 0.05 for the mutual offsets between the wide-angle camera and the narrow-angle camera. These corrections would be applicable after ground and in-flight calibration.

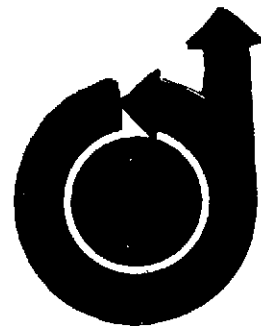
BIBLIOGRAPHY

1. Mohan, S. N., et al, "Determination of the Mars spin-axis direction from Mariner IX", paper presented at the Division of Planetary Sciences Meeting of the American Astronomical Society, held March 20-24, 1972, Kona, Hawaii. (Abstract in the Bulletin of the American Astronomical Society, V4, No. 3, Part II, 1972, p. 375.)
2. Vaucouleurs, G. De, "The Physical Ephemeris of Mars", ICARUS, V3, 1964, pp. 236-247.
3. Wilkins, G. A., "Orbits of the Satellites of Mars", H. M. Nautical Almanac Office, Technical Note 1, August 1965.
4. Born, G. H., et al, "Determination of the Orbits of Phobos and Deimos from Mariner IX", paper presented at the ASS/DPS meeting, March 20-24, 1972, Kona, Hawaii. (Abstract in the Bulletin of the American Astronomical Society, V4, No. 3, Part II, 1972, p. 368.)
5. Woolard, E. W., "The Secular Perturbations of the Satellites of Mars", The Astronomical Journal, V 51, No. 2, August 1944, pp. 33-36.
6. Born, G. H., et al, "The Determination of the Satellite Orbit of Mariner 9", paper presented at the AIAA/AAS Astrodynamics conference, Palo Alto, California, Sept. 11-12, 1972.
7. Jordan, J. F., et al, "Preliminary Results of the Satellite Orbit Determination of Mariner Mars 1971", paper presented at the Institute of Navigation National Space Meeting, held in Orlando, Florida, March 15-16, 1972.
8. Sinclair, A. T., "The Motions of the Satellites of Mars", Monthly Notices of the Royal Astronomical Society (1972), V 155, pp. 249-274.
9. Mohan, S. N., and Ransford, G. A., "Cartography and Orbit Determination using TV data from a Mars Orbiting Spacecraft", paper AAS-373 presented at the AAS/AIAA Astrodynamics Specialists Conference in Ft. Lauderdale, Florida, Aug. 17-19, 1971 (to appear in the Journal of the Astronautical Sciences).
10. Masursky, H., et al., "Mariner 9 Television Reconnaissance of Mars and its Satellites: Preliminary Results," Science, V 175, No. 4019, pp. 294-305. Kliore, A. J., et al., "Mariner 9 S-Band Martian Occultation Experiment: Initial Results on the Atmosphere and Topography of Mars," *ibid.*, pp. 313-317. Chase, Jr., S. C., et al., "Infrared Radiometry Experiment on Mariner 9," *ibid.*, pp. 308-309.
11. Pettengill, G. H., et al., "Martian Craters and a Scarp as Seen by Radar," Science, V 174, No. 4016, pp. 1321-1324; Downs, G. S., et al., "Mars Radar Observations, a Preliminary Report," *ibid.*, pp. 1324-1327.

APPENDIX P

TOPOGRAPHICAL COORDINATES FROM MARINER 9 OBSERVATIONS
OF THE MARTIAN SURFACE

259<



TOPOGRAPHICAL COORDINATES FROM MARINER 9
OBSERVATIONS OF THE MARTIAN SURFACE

by

Srinivas N. Mohan
Jet Propulsion Laboratory
Pasadena, California

AAS/AIAA Astrodynamics Conference
Vail, Colorado/July 16-18, 1973

260<

TOPOGRAPHICAL COORDINATES FROM MARINER 9
OBSERVATIONS OF THE MARTIAN SURFACE*

by

Srinivas N. Mohan

ABSTRACT

The object of the paper is to present results of Mariner 9 determinations of coordinates of select topographical features on Mars, and to project uncertainties in such determination, together with uncertainties in spin-rate and in the inertial orientation of the spin-axis of Mars, to some epoch in the distant future, and, to examine the impact of further imaging data from a Mars synchronous orbiter in reducing the knowledge uncertainty of location of any given surface feature on the planet relative to the orbiter. The effect of residual navigational uncertainties, and uncertainties in celestial orientation of the imaging system, on such determinations will be discussed. The orbiter relative determination of topographical coordinates of Mars, can find application in defining the target point precisely, in relation to a space probe designed to land on Mars.

*This paper presents the results of work carried out at the Jet Propulsion Laboratory, California Institute of Technology, under Contract NAS 7-100, sponsored by the National Aeronautics and Space Administration.

INTRODUCTION

Observations of Martian Surface features by Mariner 9 constitute a data type from which quantitative determinations of coordinates of topographical features are possible. The associated methodology is outlined in Ref. 1 and results of subsequent data analysis are presented in Ref. 2 and 3.

The precision of such determinations of topographical coordinates are of concern both from the standpoint of generating and calibrating cartographic products (cf. Ref. 4); and, from the standpoint of knowing specific target sites in application of landing a space probe on the planet, at some future date. The emphasis in this paper is on the latter aspect. In accordance with this general objective, the current effort is directed towards

- determining areocentric locations of select topographical features on Mars, photographed repeatedly by the Mariner 9 spacecraft;
- examining the consistency of such determinations from a data analysis standpoint, i. e., examining the sensitivity of the solution so obtained, to data content and assumptions in modeling error sources;
- projecting uncertainties in these determinations of coordinate locations, namely, areocentric latitude, longitude and radius of the planet at the target site (referred to the planet center-of-mass), together with knowledge uncertainties in inertial location of the spin-axis of the planet and any existing error in spin rate, to some epoch in the distant future;
- devising a hypothetical data gathering scheme to be utilized at the future epoch, the purpose of which would be to view the candidate target site from multiple positions, in orbit, of a Mars synchronous orbiter; and,
- examining the degree to which the above projected uncertainties can be reduced as a result of the data thus obtained; and, additionally
- taking advantage of the synchronous nature of the spacecraft orbit to update the target site coordinates (cartesian coordinates of the target site referred to an inertial reference system at some specified epoch) based on a single sighting of the target point from the orbiter.

The motivation here, stems from the need to assess the degree of precision with which available Mariner 9 data can be used to determine topographical

coordinates; and, from the need to examine ways in which further improvement could be effected as regards knowledge of the position of a candidate landing site at some future encounter of the planet Mars.

TOPOGRAPHICAL COORDINATES FROM MARINER 9 DATA

In view of the later significance of topographical coordinates as regards defining a target point on the planet in inertial space, it is appropriate to define topographical coordinates as the components of the instantaneous vector from the planet-center-of-mass to the chosen point on the planet surface expressed in a convenient inertial reference, such as the earth mean equator and equinox of 1950 system. In an alternate sense, this definition would therefore include, in addition to the areocentric latitude and longitude of the point on the surface whose position is to be defined; the radius, the inertial orientation of the spin axis, and the spin-rate of the planet.

The definition of the longitude, for current purposes, includes any changes in the Martian equinox with respect to its prime-meridian due to changes in the assumed inertial orientation of the spin-axis.

The starting point for the variational sequence to be followed, is the set of best estimates of topographical coordinates presented in Ref. 3. A brief description of the data used to derive these estimates will now be given.

Video data consisting of light intensity levels, (contrast enhanced and shading corrected, however, essentially unaltered as far as image locations were concerned) were available as part of the Image Processing activities during MM71, in the form of photographic plates from which image locations of surface features of interest were measured in two coordinates of line and picture element (pixel). Data residuals were computed by comparing expected line, pixel locations – which in turn, were computed based on a) (a priori) assumed values of the topographical coordinates, b) the inertial orientation of the spin-axis, c) the spacecraft position and d) measured celestial angles of the TV camera optic-axis – with the measured line, pixel locations. Additionally, calibrated corrections were added to the expected line, pixel values so computed, in order to compensate for electromagnetic and optical distortion of the image locations. An alternate data set consisting of geometrically corrected

photographic frames was also used. The data covered a total time span of approximately 95 days. The objects viewed were portions of the south polar cap, which exhibited little or no change over the above time span; and, impact craters in the vicinity of volcanic prominences in the Tharsis region in the 110° - 135° W longitude range on Mars. Distribution of data in relation to time of periapsis passage of the Mariner 9 spacecraft is shown in Figure 1. A total of 166 frames containing 12 surface features made up each data set, namely, the "raw" data set and the geometrically corrected data set.

INTERNAL CONSISTENCY OF THE SOLUTION VECTOR

The total raw data set previously described was segmented into two parts for the purpose of examining consistency of the estimates. Solutions were then obtained, using the two data segments independently of each other and also in combination. The results are presented in Figure 2. The maximum variation in defining the pole orientation thus obtained is $0^{\circ}045$ in RA and $0^{\circ}034$ in declination which compare favorably with the formal a posteriori 1 σ uncertainties obtainable after processing all the data. The latitudes and longitudes of the polar landmarks exhibit a smaller variation than those of the equatorial landmarks. The worst of these variations when expressed as linear distance over the surface, amounts to 7 km. The radii, which were also solved for, exhibit the greatest sensitivity to such data segmentation in the case of Nix Olympica and Nodus G. (labeled in Figure 2). This may be explained in view of the fact that data for these landmarks were very scanty in comparison to the rest; and consequently, segmentation may be expected to further impair the accuracy of these solutions.

The Mars-fixed coordinates so obtained were further expressed as traces in EE50 system over the period of one Martian day. The maximum discrepancy between these traces is comparable to that shown between the latitude, longitude and radii, however, is not necessarily equal to it, since, the worst knowledge of pole orientation may not coincide with the worst set of latitudes and longitudes obtained as solutions. It is also noticeable that there is a gradation of accuracy levels obtained among the various landmarks. This fact correlates on a 1 to 1 basis with the proportion of the total data made up by observations of each of the landmarks. For example, the polar landmarks are

more frequently observed than the equatorial landmarks, and consequently the consistency of solutions is better in the case of the polar landmarks than in the case of the equatorial ones. (See Figure 1). The increased degradation in determining coordinates of the equatorial landmarks is in part due to the sensitivity of the radius solution to the data content. Consequently, it would appear that emphasis needs to be placed on obtaining sufficient data before inferences regarding the radii can be drawn meaningfully.

SOLUTION SENSITIVITY TO VARIATION IN MODEL ASSUMPTIONS

An analysis of contributive factors which influence the calculation of expected image location in each of the frames, leads to three groups of error sources, namely, those associated with knowledge of the spacecraft position at times of observation, errors associated with the celestial orientation of the TV camera optic-axis, and those related to the physical properties of the planet.

The solution obviously depends, on how much confidence is expressed in knowledge of the spacecraft position, and knowledge of the celestial orientation of the TV camera. In processing observations, the calculated image locations are based on trajectory information derived from processing of Doppler data; and, the TV camera pointing is derived from telemetry data containing measured scan platform gimbal angles as well as primary sunsensor and Canopus tracker outputs.

Given all such information and given the fact that the TV camera orientation was calibrated against limited star imaging; one can obtain a solution assuming perfect knowledge both with regard to the spacecraft position and camera orientation; and, assume that an externally determined pole orientation is the "true" orientation[†], thus attributing the mismatch between observed and calculated image locations solely to the lack of precise knowledge of the topographical coordinates. Ignoring the poor quality of data fit obtained by such a procedure one can state that the data yields "averaged" coordinates in the light of the preceding assumptions. (The results of such an experiment are included in the total solution spread shown in Figure 3.)

[†]The pole orientation determined by Sinclair (Ref. 5) was used as the best estimate for this purpose.

The spread of residuals obtained with the above procedure may now be assumed to reflect random variations in pointing information. Thus, one can repeat the earlier solution, however, corrupt the covariance appropriately and construct a second solution. (Model* 4 included in the solution spread shown in Figure 3.)

One can on the other hand, take the view that the residuals obtained in the first instance (labeled model* 3) are a result of both a systematic error due to lack of precise knowledge of pole orientation; and, random variations in knowledge of instrument pointing. The result is yet a different solution listed as model* 2 in Figure 3. The spin-axis solution is observed to move to a value differing by $0^{\circ}014$ in right ascension and $0^{\circ}15$ in declination from that given in Ref. 5.

Model 2 can be further augmented to take into account any fixed, inertial offsets of the instrument and a markedly different solution results (Model* 1 in Figure 3).

Thus, we have demonstrated four different solutions based on four different models, each valid within its own framework of assumptions. These four models certainly do not exhaust all possible combinations of assumptions that could be used to construct the solution vector, but rather, reflect some obvious differences in error modeling. The resulting magnitude of variation in the surface feature locations are plotted in Figure 3, merely as a measure of the sensitivity to the previously stated assumptions regarding error sources, and not as a measure of consistency, for reasons to be discussed later.

SENSITIVITY OF SOLUTION TO DATA TYPE

In this paragraph, the results of processing geometrically corrected data; versus raw data processing, using a global, distortion calibration are stated. The model used for these solutions corresponds to model 1, previously described. The variations in the resulting solutions are shown plotted in Figure 4. In the light of all the previous assumptions, these variations together with the spread of solutions given in Figure 2, and plotted in Figure 5, reflect the more realistic level of accuracy, achievable by such TV imaging techniques in determining topographical coordinates of surface features on Mars.

*See list of terms and definitions at the end of the paper for an explanation of Models 1, 2, 3, and 4.

ERROR IN SPIN-RATE

The spin-rate of Mars as contained in Reference 6 was found to be sufficiently precise for the data span processed here. If any error was present, it was not detectable owing possibly to the degradation of the observations due to random errors in TV camera pointing. It is important, however, to take this error source into account, in addition to all those already mentioned; for purposes of mapping. This will be discussed in the next section.

MAPPING OF ERRORS

Having obtained a measure of the degree of precision in previous determinations of topographical coordinates and recognizing the possibility of an update to the currently determined spin-rate (given in Ref. 6), it is a simple matter to propagate the uncertainties in inertial location of topographical coordinates to a future date. An error of 1.5 msec/revolution of Mars is equivalent to a 2.1687 degree drift in longitude over a Julian century (i. e., equivalent to $0^{\circ}1084$ over 5 years). From Figure 5, achievable accuracy of determination of landmark coordinates on the basis of Mariner 9 data, appears to be approximately $0^{\circ}1$ in latitude and longitude in the worst sense. The accuracy of the spin-axis solution previously obtained may be stated as $0^{\circ}06$ in right ascension and $0^{\circ}04$ in declination. The longitude error needs to be augmented by an additional $0^{\circ}108$ attributable to probable spin-rate error, integrated for 5 years after Jan. 1971.

LANDMARK TRACKING FROM A MARS SYNCHRONOUS ORBITER

In an effort to reduce the mapped uncertainties, a hypothetical data set will now be described. Figure 6 shows ground track of a Mars orbiter which is inserted into a supra-synchronous orbit and is thereafter synchronized with the aid of an instantaneous motor burn at periapsis. The figure also shows a candidate landing site on Mars, which is chosen to allow near vertical viewing of the Martian surface as the spacecraft approaches periapsis position. In a somewhat arbitrary manner, positions of the spacecraft, from which the landing site can be viewed by an onboard imaging system, have been selected. The object here is to acquire data with as wide a variation in emission angle as possible, in order to obtain good triangulation to help locate the target point in

relation to the spacecraft orbit; and hence, the inertial space. The separation in ground track prior to synchronization is helpful in obtaining additional viewing positions of the spacecraft for this purpose. These are marked in Figure 6, labeled 1 through 7.

COVARIANCE ANALYSIS

Here we shall examine two possibilities, 1) where sufficient Mariner 9 data is available to obtain coordinates of the target site to an accuracy of 0.1° in latitude and 0.2° in longitude; 2) No previous data is available.

The results of covariance analysis are given in Tables I and II. The assumptions here are: a) There is a random error of 0.3° associated with each frame of observation, in ascertaining the celestial orientation of the viewing instrument (obtainable with gyroscopic attitude referencing), b) the prime parameters for differential correction, given the observations; are the latitude, longitude and radius of Mars at the target site. c) The effect of error sources such as the spin-axis, which one cannot hope to improve the knowledge of; fixed offsets in knowledge of celestial orientation of the instrument, and spacecraft related position error sources such as the node in the plane-of-sky and time of periapsis passage (cf. Ref. 7 for a discussion of the last two error sources and achievable accuracy limits) are "considered".

Comparing the two cases presented in Table I, the value of preprocessing with Mariner 9 data seems only slight as regards learning the coordinates of the target point. The ability to learn the radius is poor. The indicated sensitivity of the radius to the fixed "cone" bias (labeled BIASN) is only slight in a relative sense. The most significant sensitivity of the coordinates appears to be due to the node in the plane-of-sky error (Ω_{pos}) and the time of periapsis passage error. The next logical step therefore, is to include all the three parameters of indicated sensitivity in the total solution list. The results of such a computation are shown in Table II as Case 3. We notice that the change in the achievable accuracy of coordinate determination is insignificant. It is very apparent therefore, that the limiting error source was contained in the solution list to begin with, namely random variations from frame to frame of 1σ magnitude of 0.3° . This fact is further confirmed by the results presented in

Table II, case 4; where it is assumed that the random variation from frame to frame can be contained within $0^{\circ}03$ by having the spacecraft on celestial attitude referencing and by careful processing of telemetry data containing the attitude information. The results show a significant improvement in the ability to determine the radius. Also the uncertainty levels of the topographical coordinates are reduced to levels of uncertainty comparable to those of the spin-axis orientation.

Figure 7 depicts a summary of previous discussion relating to improvements in determination of location of the candidate landing site. Case 1 in Figure 7 corresponds to the total mapped 1σ error ellipse based on preprocessing with Mariner 9 data. Case 2 shows achievable accuracy limits without preprocessing and based on the additional data consisting of 12 TV frames previously described. Case 3 shows the extent of improvement attainable by including Mariner 9 data. Both cases 2 and 3 exhibit no significant ability to learn the topographical elevation, (equivalently, the radius). Cases 4 and 5 show significant improvement both in determining the East-West, North-South location and in determining the elevation at the landing site. The indicated improvement can be attributed to the assumed level of accuracy of attitude information with celestial referencing. A wide separation of spacecraft viewing positions has been introduced in obtaining the additional data; and, this may also be seen as a contributory influence. Both cases 4 and 5 show indifference to preprocessing with Mariner 9 data, owing clearly to the assumed accuracy of the additional data. Case 5 shows the improvement possible, if the error in knowledge of the spin-axis is ignored. The circumstances under which the spin-axis error is ignorable, will be discussed in the subsequent paragraphs.

The conclusion therefore is, that in order to be able to derive any benefit with regard to improving knowledge of topographical coordinates of the target point, by additional data gathering at future encounters; it is necessary to have knowledge of celestial orientation of the imaging instrument to a level considerably better than $0^{\circ}3$. In the optimistic sense of being able to constrain such accuracy levels to $0^{\circ}03$ by celestial attitude referencing, it would be possible to obtain the coordinates commensurable with uncertainty in the spin-axis orientation. More importantly, significant improvements in knowledge of the

radius at the target point would be possible. This may be of value in providing an independent determination of the radius for purposes of comparison with similar determinations from other data sources.

So far, we have treated the general problem of predicting accuracy levels given Mariner 9 data and additional data from a synchronous Mars orbiter. That is to say, we have not taken advantage of the synchronous nature of the orbit. It is possible, in this particular situation, to ignore the spin-axis as an error source, provided data is taken in the vicinity of periapsis passage, for the purpose of determination of the inertial position of the target point at subsequent periapsis passage points. It is obvious that the target point returns to the same position in inertial space, at all subsequent times synchronized with planetary rotation, irrespective of assumptions regarding the spin-axis location. The spin-axis error becomes significant only, when departure from the synchronous times is appreciable in relation to the rotational period of the planet. Thus, in this context, it is possible to achieve the limiting accuracy, dictated only by the accuracy of the available spacecraft attitude information.

It is possible, therefore, to simplify the previously described data gathering procedure to a single picture and compute the latitude and longitude from the observed image location, with some specified radius which cannot be solved for. The accuracy of such a determination would then depend merely on the slant range, accuracy of spacecraft celestial attitude information, and accuracy of knowledge of the spacecraft orbit. The accuracy limits then describe the error bounds within which the target point may be found in inertial space; only, at time intervals made up of integral multiples of the rotational period of Mars.

CONCLUSIONS

It has been shown as a result of sensitivity analysis included in the earlier part of the paper, that determination of topographical coordinates (reported in Ref. 3) exhibit a spread of 7 km in surface location. As shown in Figure 2, the polar features exhibit a considerably smaller spread amounting to no more than 2 km in their location with respect to a set of body fixed coordinates on Mars. In order to understand what similar accuracy levels in inertial location of these features might be, uncertainties in the inertial location of the spin-axis

and spin-rate of the planet need to be factored in. The indicated spread in the pole orientation is $0^{\circ}07$ in magnitude approximately, (see Figure 5).

As evidenced from Figures 2 and 4, solutions for the radii are most sensitive to variation in data content, data type or modeling. In fact, from Figure 3, it is apparent that radii are not included in the solution vector, since the sensitivity to modeling differences is significant enough to yield unrealistic solutions (with the exception of model* 1).

The spread in solutions resulting from variation in model assumptions dominate the spread obtained due to variation in data content or type. In the worst sense, the total spread of solutions is contained within 13 km on the surface, as shown in Figure 3. The pole direction exhibits its greatest sensitivity to the exclusion of fixed offsets in camera orientation from the solution vector. Such an exclusion of the fixed offsets from the solution vector corresponds to placing full confidence in the calibration of the imaging instrument, although conceding a small, zero mean, random variation about the indicated direction of camera orientation. It must be pointed out that calibration of the Mariner 9 imaging instrument, in orbit phase, was carried out with severely limited stellar imaging data all aggregated at a single time of observation. This does not eliminate the possibility of variation in the calibrated error sources at other times of observation, considering that the scan platform carrying the imaging instrument was continually in motion for routine observational purposes. Therefore, there is reason to believe that the averaged pointing direction, given all the data, may differ from the calibrated mean direction; and hence, model 1 may be a more realistic representation than model* 2 (which assumes that fixed offsets do not exist). Similar arguments can be presented to show that model 1 is a more realistic representation than models* 3 and 4. Thus, if one places greater faith in model 1 than the rest, the accuracy levels are much improved, although the estimates are more optimistic.

In the latter half of the paper, it has been shown that additional data gathering can be of benefit in improving Mariner 9 estimates of topographical features, provided the celestial orientation of the imaging instrument can be ascertained to a level of accuracy significantly better than $0^{\circ}3$ (1σ). It has also

*See list of terms and their definitions at the end of the paper for an explanation of Models 1, 2, 3 and 4.

been shown that in order to get estimates of the radius of Mars (referred to the planet's center-of-mass) at a candidate landing site, to a degree better than 2 km, it is necessary to reduce this uncertainty by a factor of 10. From an intuitive standpoint, it has been shown that errors in knowledge of the spin-axis are ignorable, provided, the determination of the target point location, and the rendezvous of a future planetary lander with the target point are synchronized with the rotational period of Mars. If the target point determination is not required to include inferences on absolute topographical elevations, the procedure of data gathering and processing can be simplified to a single observation of the target site at periapsis passage of the spacecraft. This will yield an estimate of the target point in inertial space, at the time of observation, which will be constrained within 8 km (1σ) corresponding to the 0.3 (1σ) accuracy level in attitude information, at all subsequent intervals of time which are integral multiples of the rotational period of Mars.

Table I. Knowledge Uncertainty of Topographical Coordinates of a Mars Landing Site (15°N, 100°W) with 12 Frames of Data.

Case 1: Previous data available, celestial pointing known to an accuracy of 0°3 (1σ)

Solution Parameter	A priori 1σ Uncertainty	Aposteriori 1σ Uncertainty	Contribution of Unsolved Parameters to Knowledge Uncertainty					
			Bias M	Bias N	RA	DEC	Ω _{pos}	t _p
Latitude	0°1	0°078	*	*	-0°015	*	-0°035	0°01
Longitude	0°2	0°108	*	*	0°035	*	-0°025	-0°04
Radius	10 km	5.4 km	*	1.17 km	*	*	*	*
Random Yaw	0°3	0°3	*	*	*	*	*	*
Random Pitch	0°3	0°11	*	*	*	*	*	*
Random Roll	0°3	0°12	*	*	*	*	*	*
			0°03	0°03	0°05	0°05	0°05	0.2 sec
			Assumed 1σ uncertainties of unsolved parameters listed in Tables I and II					
*Negligibly small								
NOTE: A linear distance of 60 km at the mean equatorial surface of Mars subtends an angle of 1 degree approximately, at the center of mass of the planet.								

P-14
273

Table I. Knowledge Uncertainty of Topographical Coordinates of a Mars Landing Site (15°N, 100°W) with 12 Frames of Data (Contd)

Case 2: No previous data available, celestial pointing known to an accuracy of 0°3 (1σ)

Solution Parameter	Apriori 1σ Uncertainty	Aposteriori 1σ Uncertainty	Contribution of Unsolved Parameters to Knowledge Uncertainty					
			Bias M	Bias N	RA	DEC	Ω_{pos}	t_p
Latitude	10°0	0°115	*	*	-0°025	*	-0°063	-0°024
Longitude	10°0	0°128	*	*	0°043	*	-0°038	0°048
Radius	10 km	5.4 km	*	1.17 km	*	*	*	*
Random Yaw	0°3	0°3	*	*	*	*	*	*
Random Pitch	0°3	0°12	*	*	*	*	*	*
Random Roll	0°3	0°12	*	*	*	*	*	*

*Negligibly small

P-15
279<

Table II. Knowledge Uncertainty after Solving for Fixed Cone Bias (Bias N)

Case 3: Previous data available, celestial pointing known to an accuracy of $0^{\circ}3$ (1σ)

Solution Parameter	Apriori 1σ Uncertainty	Aposteriori 1σ Uncertainty	Contribution of Unsolved		
			Bias M	RA	DEC
Latitude	$0^{\circ}1$	$0^{\circ}075$	*	*	*
Longitude	$0^{\circ}2$	$0^{\circ}106$	*	*	*
Radius	10.0 km	5.4 km	*	*	*
Random Yaw	$0^{\circ}3$	$0^{\circ}3$	*	*	*
Random Pitch	$0^{\circ}3$	$0^{\circ}11$	*	*	*
Random Roll	$0^{\circ}3$	$0^{\circ}11$	*	*	*
Fixed Cone Bias (Bias N)	$0^{\circ}03$	$0^{\circ}029$	*	*	*
Ω_{pos}	$0^{\circ}05$	$0^{\circ}043$	*	*	*
Time of Periapsis, t_p	0.20 sec	0.19 sec	*	*	*

*Negligibly small.

P-16
275

Table II. Knowledge Uncertainty after Solving for Fixed Cone Bias (Bias N) (Contd)

Case 4: Previous data available, celestial pointing known to an accuracy of $0^{\circ}03$ (1σ)

Solution Parameter	A priori 1σ Uncertainty	Aposteriori 1σ Uncertainty	Contribution of Unsolved Parameters		
			Bias M	RA	DEC
Latitude	$0^{\circ}1$	$0^{\circ}044$	$0^{\circ}020$	$0^{\circ}025$	$0^{\circ}022$
Longitude	$0^{\circ}2$	$0^{\circ}052$	*	$0^{\circ}043$	*
Radius	10.0 km	1.53 km	0.75 km	0.13 km	0.5 km
Random Yaw	$0^{\circ}03$	$0^{\circ}03$			
Random Pitch	$0^{\circ}03$	$0^{\circ}02$			
Random Roll	$0^{\circ}03$	$0^{\circ}02$			
Fixed Cone Bias	$0^{\circ}03$	$0^{\circ}02$	*	*	*
Ω_{pos}	$0^{\circ}05$	$0^{\circ}04$			
Time of Periapsis, t_p	0.20 sec	0.14 sec			

*Negligibly small.

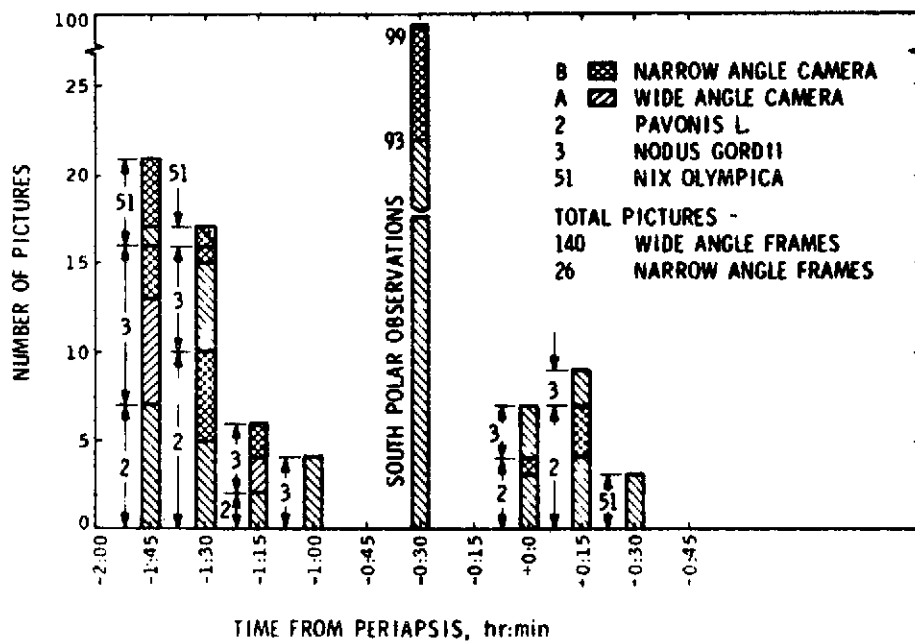


Figure 1. Distribution of Observation Times Relative to Time of Periapsis Passage of Spacecraft

277<

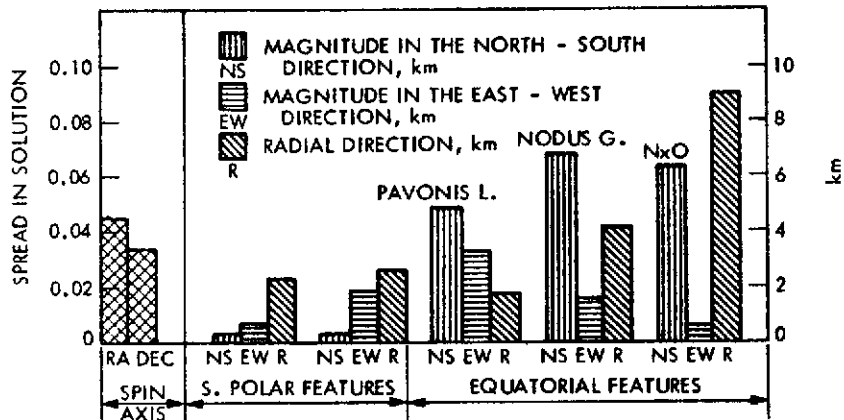


Figure 2. Solution Spread as a Result of Data Segmentation

- MODEL 1: SOLVE FOR POLE ORIENTATION, RANDOM AND FIXED OFFSETS IN CAMERA ORIENTATION
- MODEL 2: SOLVE FOR POLE ORIENTATION AND RANDOM OFFSETS IN CAMERA ORIENTATION
- MODEL 3: SOLVE FOR COORDINATES ONLY. SET POLE VALUES AS GIVEN IN REF. 5
- MODEL 4: AUGMENT MODEL 3 BY ADDING RANDOM OFFSETS

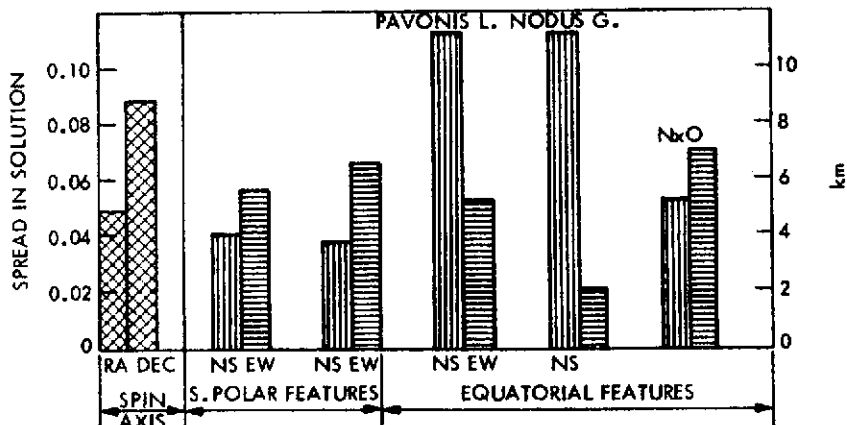


Figure 3. Solution Sensitivity to Model Assumptions

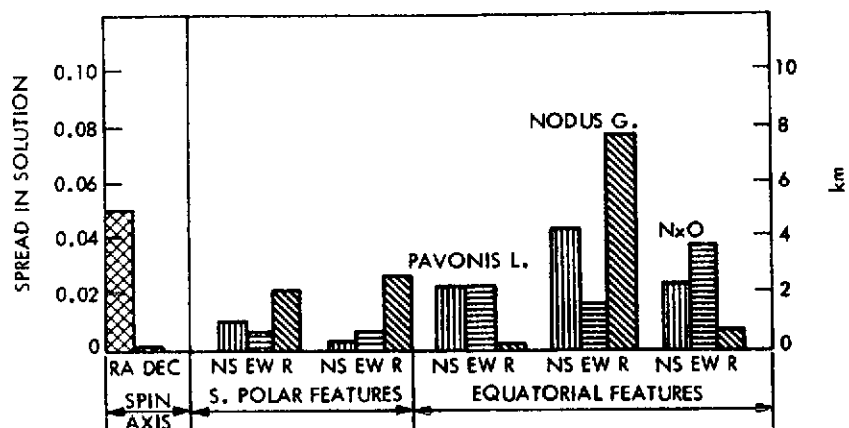


Figure 4. Solution Spread as a Result of Processing Distortion Corrected Data

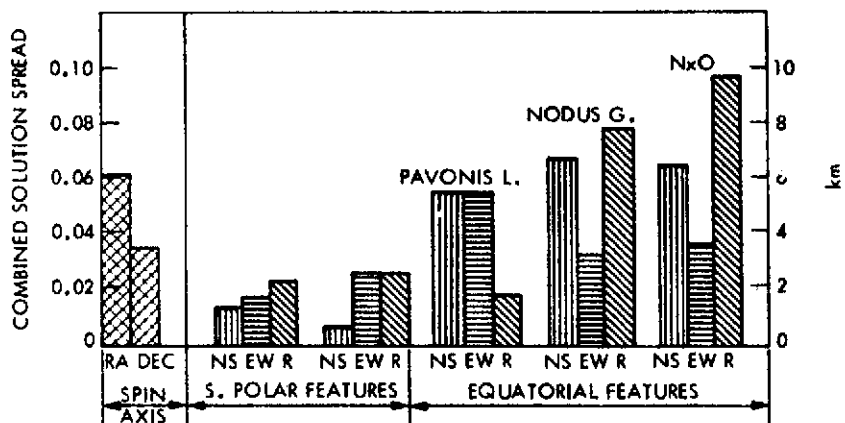


Figure 5. Combined Solution Spread Shown in Figures 2 and 4

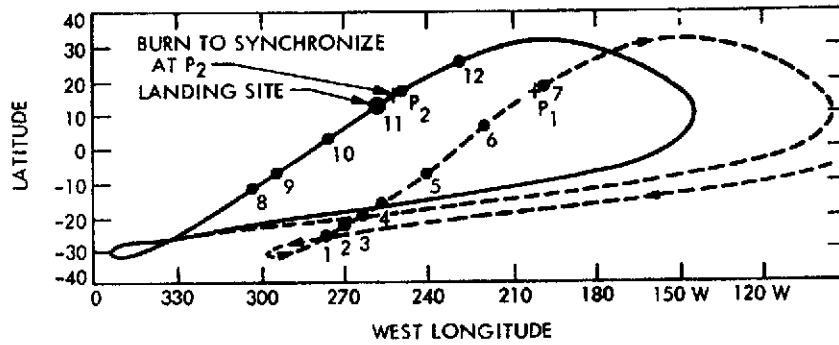
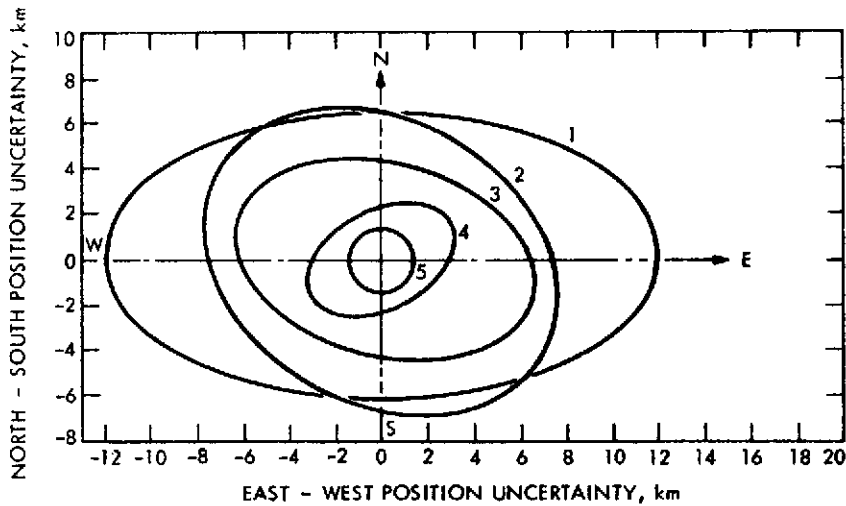


Figure 6. Ground Track of Synchronous Mars Orbiter - ● Denote Sub-Spacecraft Points at Times of Observation, P₁ and P₂ Show Periapsis Positions



RADIUS, km	CASE	PRE-PROCESS	ADD	GYRO	STELLAR	CONSIDER
		MM71 DATA	12 DATA FRAMES	REFERENCE	REFERENCE	POLE ERROR
12	1	■	□	□	□	■
10	2	□	■	■	□	■
8	3	■	■	■	□	■
6	4	■	■	□	■	■
4	5	■	■	□	■	□

Figure 7. Error Ellipses at Landing Site

LIST OF TERMS AND THEIR DEFINITIONS

pixel, line	These are the basic measurement units which define each discrete element of any television picture. Pixel is an abbreviation of picture element
EE50	Represents the Earth Mean Equator and Equinox system of coordinate reference at the epoch of 1950.0
RA, DEC	Represent the right ascension and declination, respectively. In the text, these define the orientation of the spin-axis of Mars referred to the EE50 coordinate system.
Ω_{pos}	Represents the node of the spacecraft orbit as seen in the Earth's plane-of-sky. For significance of this parameter as regards precision of knowledge of the spacecraft orbit Ref. 7 may be consulted.
t_p	Time of periapsis passage of spacecraft (Cf. Ref 7).
yaw, pitch, roll	Angular displacements about orthogonal directions in space, which describe the celestial attitude of the spacecraft.
Bias M, N	Represent offsets in orientation of the optic-axis of the imaging instrument.
landmark	Used interchangeably with surface feature.
Emission Angle	Angle subtended by the spacecraft, as seen by an observer on the surface, with the local vertical.
Model 1	Refers to the assumption that parameters for differential correction are: latitude, longitude and radius of surface features; inertial orientation of the spin-axis of Mars; fixed and random offsets in the inertial orientation of the imaging system described by BIAS M, N and yaw, pitch roll angles, respectively.
Model 2	Same as Model 1 with the exception that the fixed offsets BIAS M, N are assumed to be zero at all times, and the radius of the planet at the surface feature being viewed is assumed known perfectly.

- Model 3 Same as Model 2 with the exception that the spin-axis orientation is assumed known perfectly and is set at the values of RA and DEC given by Sinclair in Ref. 5. Also, inertial attitude of the imaging system is assumed known perfectly.
- Model 4 Same as Model 3 with the exception that random variations in the imaging system attitude information are acknowledged, by solving for yaw, pitch and roll angles.

REFERENCES

1. Mohan, S. N., and Ransford, G. A., "Cartography and Orbit Determination from a Mars Orbiting Spacecraft", paper No. 71-373 presented at the AAS/AIAA Astrodynamics Specialists Conference, Ft. Lauderdale, August 17-19, 1971.
2. Mohan, S. N., et al, "Determination of the Mars Spin-Axis Direction from Mariner IX", paper presented at the Division of Planetary Sciences Meeting of the American Astronomical Society, held March 20-24, 1972, Kona, Hawaii (Abstract in the Bulletin of the American Astronomical Society, V4, No. 3, Part II, 1972, p. 375).
3. Mohan, S. N., "Pole Direction, Cartography and the Shape of Mars" paper presented at the 24th International Geological Congress, IAP Symposium, held in Montreal, Canada, August 1972.
4. Davies, M. E., "Mariner 9 Control Net of Mars: August 1972", Rand Report R-1122-JPL, October 1972, Davies, M. E. "Mariner 9 Control Net of Mars: April 1973", Rand Report R-1266-JPL, April 1973; Davies, M. E. and Arthur, D. W. G., "Martian Surface Coordinates", Rand Report R-1252-JPL, April 1973.
5. Sinclair, At. T., "The Motions of the Satellites of Mars", Monthly Notices of the Royal Astronomical Society (1972), V155, pp. 249-274.
6. Melbourne, W. G., et al, "Constants and Related Information for Astrodynamics Calculations, 1968", NASA Technical Report 32-1306, July 15, 1968, pp. 28-29.
7. Born, G. H., et al, "The Determination of the Satellite Orbit of Mariner 9", AIAA Paper No. 72-928, presented at the AIAA/AAS Astrodynamics Conference, Palo Alto, California, Sept. 11-12, 1972, pp 2-6.

APPENDIX Q

RESULTS OF ORBIT PHASE NAVIGATION STUDY USING LANDMARK DATA

APPENDIX Q
RESULTS OF ORBIT PHASE NAVIGATION STUDY
USING LANDMARK DATA

by

S. N. Mohan

TV images of the surface of Mars returned by Mariner 9 are treated as a navigational data type. The purpose of this appendix is (1) to provide a description of the data selected for this purpose, (2) to outline the computational procedures used in data reduction, (3) to document the achieved enhancement of navigational accuracy resulting from addition of optical data to radiometrically derived orbit information and (4) to indicate science-related results obtained from optical data processing.

I. GENERAL DISCUSSION OF ORBITAL PHASE DATA AVAILABLE FOR NAVIGATION APPLICATION

The observed surface features are shown in Fig. 1. These features can be grouped into equatorial (Tharsis) and south polar regions. Estimated areo-centric locations of these features appear in Table 1. A landmark data summary has been included in Table 2. It is apparent from Table 2 that the data arc is spread over 114 days, from Rev. 5 to Rev. 232 of the Mariner 9 orbits. The table also shows distribution of the data in relation to the 21 reference trajectory segments used for generating computed observables and data partials. Distribution of data in relation to observed surface features appears in Fig. 2. Surface resolution of the optical observations is variable, depending on the type of camera used and the range of the spacecraft from the planet. Figure 2 also shows the approximate position in orbit from which the various observations were made.

II. COMPUTATIONAL PROCEDURE FOR COMBINING RADIO AND OPTICAL DATA

An outline of computational procedures is given below. (Details concerning filter formulation and mechanization can be found in Ref. 1.) Briefly, the method consists of

284<

- (1) Generation of prefit data residuals using the estimated spacecraft state, given all Earth-based doppler observations and celestial attitude of the imaging instrument estimated from engineering telemetry data.
- (2) Generation of a time history of orbital elements of the doppler-determined orbits in the Earth's plane-of-sky coordinates (instantaneous), after deleting known effects of geometry (from the moving plane-of-sky) and secular dynamic effects contributed by the second-degree gravity harmonic.
- (3) The time history of the node of the orbit in the moving plane-of-sky reveals obvious discontinuities (see Figs. 4 and 5). The actual node can be compared with an a priori continuous node, thus ascribing an a priori δ node (designated $\delta \Omega_{pos}$) corresponding to each orbit.
- (4) Using the prefit data residuals generated in step 1, seek a constant correction to the a priori continuous node. The resulting solution can then be compared with the a priori radio mean, as well as the best estimate resulting from observations of the natural satellites of Mars. (These results appear in Appendix M.)

The process of physically reducing photographic information to a computationally useful form, and the steps involved in the total processing, are described in Ref. 2. A brief functional description of the associated software is also included. The software was tested by (1) use of simulated data and (2) comparisons for numerical accuracy against other certified programs such as the DPODP.

A. FILTER DESCRIPTION

The filter algorithm used for effecting OD solutions was a sequential processor. The sequential formulation was particularly suited to modeling random errors associated with the TV pointing of each picture. A detailed description of the filter is to be found in Ref. 1.

B. A PRIORI ASSUMPTIONS

A priori information on scan platforms pointing (from ground calibration) was updated using star data on approach, and some limited star data obtained during Rev. 72 in the orbital phase. Similarly, distortion effects (optical and electromagnetic) were calibrated out using star fields, both in the narrow-angle and wide-angle field of view. Residual distortion after calibration was within 1 picture element, making this error source insignificant in relation to random uncertainty in TV pointing and measurement noise. A comparison between results obtained from (1) calibrated data and (2) IPL distortion-corrected data is given in Ref. 3. The above considerations led to the following a priori assumptions: (1) constant biases in reduced engineering telemetry information after calibration were assumed to be contained within 0.03 deg (1σ), (2) as outlined before, residual errors following calibration of distortion effects were ignorably small in comparison with TV pointing errors and measurement errors. Magnitudes of errors in measurement of image locations were assigned on the basis of size of crater images measured. A rule of thumb of 1/3 the extent of the image was used in assigning measurement uncertainties. (Actual values used appear in Table 3.)

A detailed description of the method used to reduce engineering telemetry data is given in Ref. 2. The magnitude of the residual error after data reduction was assumed to be within a single quantization step of the various telemetry readouts. The resulting equivalent random uncertainty in TV pointing was assumed to be 0.03 deg (1σ). In addition, the relatively weakly determined constant offset between the wide-angle and narrow-angle TV cameras was assigned an a priori uncertainty of 0.05 deg (1σ).

The node of the spacecraft orbit in the Earth's plane-of-sky was modeled in two ways: (1) it was assumed that the doppler-determined orbits had an associated node which was within 0.05 deg of the "true node" ("Radio and Optical" solution), and (2) no a priori value was assumed (resulting in the "optical only" solution).

Areocentric coordinates of the various surface features observed were assumed unknown, as was the spin-axis of Mars.

III. RESULTS OF NAVIGATION STUDY

The results of effecting OD solutions (given at the end of this section) show that imaging data can be effective in improving radiometric accuracies, particularly the node of the orbit in the plane-of-sky. The estimated uncertainty in time of periapsis passage was too small to be sensed by this method. Similarly, contributions from the residual uncertainty in the rest of the orbital elements after doppler tracking were too small to be sensed -- hence, only Ω_{pos} was solved for. Preflight covariance analysis showed the possibility of effecting small improvements over radiometric accuracies. Preflight studies were carried out with modified picture sequences and under different a priori assumptions and consequently do not relate to the postflight results in a one-to-one sense.

To give a graphic demonstration of the effectiveness of the imaging data in improving Ω_{pos} , raw data residuals have been plotted in Fig. 3. Figure 3a shows the residuals when Ω_{pos} is aligned with the a priori values, discontinuous nodes associated with the doppler-determined orbits. Figure 3b shows the residuals after removing these known discontinuities. For ease of interpretation, the x-axis of Figs. 3a and 3b correspond to the instantaneous increasing Ω_{pos} direction. From Fig. 3b, it appears that the pointing uncertainty is approximately 0.08 deg (1σ). In Fig. 3a, we note an identical dispersion along the y-axis (by definition, changes in Ω_{pos} are reflected along the x-axis); however, the contribution of a priori node discontinuities is "visible" along the x-axis. The inherent accuracy of the data (dictated by the available precision of pointing information), appears to be marginally adequate to sense node errors.

It has been established in Ref. 4 that the dominant residual navigation uncertainty in the doppler-determined orbits of Mariner 9 is seen in the discontinuous history of the node of the orbit referenced to the Earth's plane-of-sky (referred to as Ω_{pos}). The actual node history, when compared to a mean continuous node determined from combined doppler and Phobos/Deimos observations, appears in Fig. 5. The total span of imaging data used (see landmark data summary, Table 2) in the present study corresponds to 21 segments of doppler-determined orbits referred to as PET segments. Figure 5 shows a comparison of this actual Ω_{pos} with the previously mentioned

287<

continuous Ω_{pos} . It can be seen that the a priori uncertainty in $\delta \Omega_{\text{pos}}$ is less than 0.05 deg (1σ). The radio mean (i.e. the average of $\delta \Omega_{\text{pos}}$) is seen to be -0.021 deg prior to the second trim maneuver and +0.016 deg after the trim maneuver. The result of adding imaging data to this a priori knowledge will be detailed next.

Based on the knowledge of discontinuities in the actual Ω_{pos} history, it is possible to align the node value for each probe ephemeris segment, with the reference node (defined by $\delta \Omega_{\text{pos}} = 0.0$ deg). It is now possible to seek a mean node differing by an unknown constant value from the reference node, given additional observations in the form of the planetary imaging data. There are two possible variations in assumptions regarding the a priori knowledge of Ω_{pos} :

- (1) The radio mean Ω_{pos} differs from the "true" mean Ω_{pos} , (to be determined) by a constant value contained in the 1σ dispersion of the node values. In other words, it is assumed that the absolute Ω_{pos} as determined from doppler observations has a mean value whose uncertainty is limited to 0.05 deg (1σ). Under this assumption, the result obtained after addition of imaging data will be referred to as the "radio and optical" solution.
- (2) In this case, it is assumed that although the dispersion in $\delta \Omega_{\text{pos}}$ is contained in a band of ± 0.05 deg, the "true" mean is unknown. The solution resulting from addition of imaging data is therefore labeled as the "optical only" solution.

The purpose of including the variations is to study the consistency of results under both hypotheses outlined above.

Results are summarized in tabular form below:

	Pre-Trim II mean $\delta \Omega_{\text{pos}}$ deg	Post-Trim II mean $\delta \Omega_{\text{pos}}$ deg
1. A priori radio mean	-0.021	+0.016
2. Optical only	+0.005	+0.013

	Pre-Trim II mean $\delta \Omega_{\text{pos}}$ deg	Post-Trim II mean $\delta \Omega_{\text{pos}}$ deg
3. Radio + optical	+0.012	+0.014
4. Radio + Phobos/Deimos	+0.005	+0.009
2 - 4	+0.000	+0.004
3 - 4	+0.007	+0.005

The results show close agreement between the optical only, radio + optical, and radio + Phobos/Deimos solutions. The mean Ω_{pos} values from 2, 3, and 4 listed in the table have a mutual disagreement contained within ± 0.00 deg. The a priori radio mean is somewhat removed (by 0.03 deg) from the value obtained after the addition of imaging data.

In summary, it has been shown that observations of natural satellites and of the planetary surface independently yield consistent solutions of the mean Ω_{pos} . The magnitude of inconsistency is contained within ± 0.00 deg, demonstrating the effectiveness of imaging data in improving radiometric accuracies.

IV. MARS SPIN-AXIS DIRECTION

The results of Mariner 9 picture processing also led to new spin-axis solutions, resulting in a correction of the pre-Mariner 9 spin-axis value by 0.5 deg (approx). A detailed discussion of Mars spin-axis determinations from various independent data sources such as (gravity sensing) doppler, satellite, and landmark imaging data, is given in Ref. 2. The consistency of solutions is discussed in Ref. 3. In addition, comparison of the newly determined spin-axis with Laplacian poles of Phobos/Deimos (as determined by Wilkins and Burton) is shown to exhibit remarkable consistency. The mutual separation between the newly determined solutions is 0.15 deg, giving a realistic measure of the probable uncertainty associated with the average of these solutions. The error in spin-rate, if any, could not be detected over the data span of 114 days. Consistency of associated landmark coordinate solutions was examined in detail in Ref. 3 and showed that the solutions differed in the

worst case by 7 km at the surface. Additionally, some comparisons were made between the estimated Mars radii at the observed surface features and Mars topography from occultation, UVS, IRIS and radar ranging data. The differences were in the range of ± 3 km. A detailed discussion of the results of topographical solutions is contained in Refs. 2 and 3.

V. GENERAL RECOMMENDATIONS FOR ACQUISITION AND USE OF OPTICAL DATA FOR FUTURE MISSIONS

With the results contained in this report, the value of imaging data for orbit determination has been demonstrated. Its operational feasibility in the context of a mission remains deferred to future interplanetary encounters. There are many variables that contribute to the effectiveness of imaging data as an OD effective data type. Many of these variables were not truly variable in the context of the Mariner 9 photographs -- to mention a few: geometry of acquired pictures, density of acquired data, precision of attitude information, the resolution of the camera system, etc. As to the impact of any one variation on the achieved OD accuracy, it would be necessary to perform covariance analyses to yield a quantitative measure. However, in view of the Mariner 9 experience, it is possible to draw some conclusions with regard to the more obvious variants. For example, the limiting error source was quite obviously the random error in instrument pointing knowledge. Any improvement in pointing knowledge can be expected to reflect in an improvement in all the rest of the solution parameters, namely the spacecraft orbit, the spin-axis, position coordinates of surface features, and topography.

The need for redundancy of observations is very great. The effects of geometry are significant and the possibility exists that more favorable picture sequencing and geometry could have been selected than was available with actual Mariner 9 photography. For example, a greater spread in spacecraft emission angle (i. e., oblique viewing) would have improved the strength of the topographical solutions. Such a geometry could also benefit the OD effort since the observations would be more evenly spread out along the orbit. Similarly, a more even distribution of data with respect to slant range of observation might lead to better observability of node errors since a constant node error would reflect a variable error in spacecraft position at varying spacecraft ranges, all of which would map into the data.

From the foregoing, an "optimal" sequence would be one that has the maximum variation in spacecraft emission angle as well as in azimuth angle. The Mariner 9 data consisted of limited variation in emission angle (typically ± 20 deg off vertical viewing). The Mariner 9 data density was variable over the total data arc. As yet another example of geometrical effects, it may prove to be more beneficial to choose spacecraft observation positions as far removed from the instantaneous Earth-Mars axis as possible, in order to improve observability of the node. This may show a preferred location of the surface feature for maximum observability of the node.

The process of orbit determination using landmark data as described in this report could be adapted to near-real-time operations on future missions.

REFERENCES

1. Jordan, J. F., et al., "Satellite Orbit Determination Section," in Mariner 9 Navigation, Technical Report 32-1586, Jet Propulsion Laboratory, Pasadena, California (to be published).
2. Mohan, S. N., "Pole Direction, Cartography and the Shape of Mars," presented at the IAP Symposium of the 24th International Geological Congress, Montreal, Canada, August 1972.
3. Mohan, S. N., "Topographical Coordinates from Mariner 9 Observations of the Martian Surface," paper presented at the AAS/AIAA Astrodynamics Conference, Vail, Colorado, July, 1973.
4. Born, G. H., et al., "The Determination of the Satellite Orbit of Mariner 9," paper presented at the AAS/AIAA Astrodynamics Conference, Palo Alto, California, Sept. 11-12, 1972.

C-4

Table 1. Elevation results from landmark data processing

Landmark	ID	Latitude, deg 1σ	W. Longitude, deg 1σ	Radius, km 1σ	Combined UVS and Occultation Radius, km	Combined Radar and Occultation Radius, km
South Polar Cap	6	-86.02 ±0.01	357.11 ±0.14	3384.67 ±2.0	Exit occulta- tion value at -78°8 latitude and 346°6 W. longitude is 3383.9 km	Outside limits of Earth based radar observability
	9	-84.12 ±0.01	57.69 ±0.11	3382.44 ±2.0		
	66	-80.22 ±0.03	354.11 ±0.10	3383.41 ±2.0		
	661	-81.00 ±0.02	341.42 ±0.11	3382.71 ±2.0		
	49	-76.97 ±0.03	1.33 ±0.11	3384.97 ±3.5		
Pavonis Lacus	2	0.50 ±0.04	113.17 ±0.03	3410.81 ±2.5	3411.5	3412.0
	201	1.58 ±0.03	113.00 ±0.03	3413.07 ±2.4	} Nearest avail- able value is 3417.5	} Nearest avail- able value is 3418.0
	202	0.28 ±0.03	113.96 ±0.03	3414.95 ±2.3		
Nodus Gordii	3	-10.25 ±0.03	120.82 ±0.03	3412.05 ±2.3	Base 3402.0	3403.5
Nix Olympica	51	17.21 ±0.03	133.73 ±0.03	3419.20 ±2.6	Base 3401.0	3402.5
	53	17.91 ±0.03	133.70 ±0.03	3416.22 ±2.7	No relative information available	
	54	17.77 ±0.03	133.45 ±0.03	3418.51 ±2.6		

Table 2. Landmark data summary

PROBE EPHEMERIS SEGMENT 1

SHUTTER CLOSE GMT	LANDMARKS OBSERVED	TV	CLOCK DEG	CONE DEG	TWIST
71 11 16 14 33 27	6, 0, 0, 0, 0	A	240.952	140.152	-1.03
71 11 16 14 34 51	6, 0, 0, 0, 0	A	241.049	140.113	-1.01
71 11 17 14 20 2	6, 0, 0, 0, 0	A	167.363	155.136	-1.26
71 11 17 14 21 26	6, 0, 0, 0, 0	A	175.753	155.148	-1.72
71 11 17 14 24 14	6, 0, 0, 0, 0	A	195.436	153.698	-1.91
71 11 17 14 25 38	6, 0, 0, 0, 0	A	205.287	151.840	-1.34
71 11 17 14 27 2	6, 0, 0, 0, 0	A	214.314	149.675	-1.31
71 11 17 14 28 26	6, 0, 0, 0, 0	A	222.837	146.703	-1.14
71 11 19 14 12 49	6, 0, 0, 0, 0	A	171.470	159.721	-1.70
71 11 19 14 14 13	6, 0, 0, 0, 0	A	171.133	159.628	-2.06
71 11 19 14 15 37	6, 0, 0, 0, 0	A	170.817	159.606	-2.36
71 11 19 14 17 1	6, 0, 0, 0, 0	A	170.678	159.770	-2.48

PROBE EPHEMERIS SEGMENT 2

SHUTTER CLOSE GMT	LANDMARKS OBSERVED	TV	CLOCK DEG	CONE DEG	TWIST
71 11 26 0 53 24	2, 3, 0, 0, 0	A	121.826	110.673	.13
71 11 26 1 48 0	6, 9, 0, 0, 0	A	149.092	158.611	-1.99
71 11 27 0 35 46	3, 2, 0, 0, 0	A	115.231	106.650	.13
71 11 27 0 46 58	2, 3, 0, 0, 0	A	121.301	110.524	-.19
71 11 27 1 41 34	6, 9, 0, 0, 0	A	149.067	159.625	-2.15

PROBE EPHEMERIS SEGMENT 3

SHUTTER CLOSE GMT	LANDMARKS OBSERVED	TV	CLOCK DEG	CONE DEG	TWIST
71 11 28 0 20 17	51, 54, 0, 0, 0	B	119.484	118.930	.04
71 11 28 0 21 41	51, 52, 53, 54, 0	B	120.045	118.281	-.11
71 11 28 0 26 35	2, 3, 0, 0, 0	A	120.768	115.871	-.29
71 11 28 0 37 47	2, 3, 0, 0, 0	A	128.038	118.577	-.12
71 11 28 0 51 5	3, 0, 0, 0, 0	B	131.970	120.558	.27
71 11 28 1 37 59	6, 9, 0, 0, 0	A	149.452	159.269	-1.72
71 11 28 1 38 41	6, 0, 0, 0, 0	B	157.093	158.481	-.01
71 11 28 1 39 23	6, 9, 0, 0, 0	A	155.549	158.407	-1.50
71 11 28 1 40 47	6, 0, 0, 0, 0	A	161.837	159.560	-1.23
71 11 29 0 22 59	2, 0, 0, 0, 0	A	120.605	115.695	-.32
71 11 29 0 24 23	3, 0, 0, 0, 0	A	110.979	119.719	-.28
71 11 29 0 34 11	2, 0, 0, 0, 0	A	127.843	119.662	-.10
71 11 29 0 35 35	3, 0, 0, 0, 0	A	117.514	123.824	-.30
71 11 29 1 34 23	6, 9, 0, 0, 0	A	150.329	155.933	-1.22
71 11 29 1 35 47	6, 9, 0, 0, 0	A	156.347	156.094	-1.38
71 11 29 1 37 11	6, 9, 0, 0, 0	A	161.878	156.296	-1.87

PROBE EPHEMERIS SEGMENT 4

SHUTTER CLOSE GMT	LANDMARKS OBSERVED	TV	CLOCK DEG	CONE DEG	TWIST
71 11 30 0 14 29	3, 0, 0, 0, 0	B	110.809	118.194	.28
71 11 30 0 15 53	3, 0, 0, 0, 0	B	110.526	118.497	.28
71 11 30 0 19 23	2, 0, 0, 0, 0	A	117.960	113.364	-.42
71 11 30 0 30 35	2, 3, 0, 0, 0	A	122.162	116.709	.01
71 11 30 1 30 46	6, 9, 0, 0, 0	A	149.944	156.165	-1.43
71 11 30 1 32 10	6, 9, 0, 0, 0	A	156.161	155.926	-1.36
71 11 30 1 33 34	6, 9, 0, 0, 0	A	162.318	156.126	-1.13
71 12 1 1 26 27	6, 0, 0, 0, 0	B	145.123	154.239	.01
71 12 1 1 27 9	6, 9, 0, 0, 0	A	143.993	154.269	-1.12
71 12 1 1 28 33	6, 9, 0, 0, 0	A	150.155	153.915	-.94
71 12 1 1 29 57	6, 0, 0, 0, 0	A	155.531	153.742	-1.26
71 12 2 1 24 58	6, 9, 0, 0, 0	A	147.817	154.432	-1.18
71 12 2 1 26 22	6, 9, 0, 0, 0	A	154.078	154.035	-.99
71 12 2 1 27 46	6, 0, 0, 0, 0	A	159.791	154.134	-1.39

Table 2. Landmark data summary (contd)

PROBE EPHEMERIS SEGMENT 5

SHUTTER CLOSE GMT	LANDMARKS OBSERVED	TV	CLOCK DEG	CONE DEG	TWIST
71 12 3 1 21 22	6, 9, 0, 0, 0	A	149.297	154.568	-.93
71 12 3 1 22 46	6, 66, 661, 9, 0	A	154.130	154.178	-1.18
71 12 3 1 24 10	49, 6, 66, 661, 9	A	159.630	154.066	-1.65
71 12 4 13 18 51	6, 9, 0, 0, 0	A	142.672	159.664	-2.20
71 12 4 13 20 15	6, 9, 0, 0, 0	A	148.540	159.763	-1.94
71 12 4 13 21 39	6, 9, 0, 0, 0	A	154.915	159.876	-1.63

PROBE EPHEMERIS SEGMENT 6

SHUTTER CLOSE GMT	LANDMARKS OBSERVED	TV	CLOCK DEG	CONE DEG	TWIST
71 12 6 1 14 51	6, 66, 661, 49, 0	A	145.990	147.243	-1.30
71 12 6 1 16 15	66, 661, 49, 0, 0	A	152.141	147.079	-1.23
71 12 6 1 17 39	66, 661, 49, 0, 0	A	157.362	147.247	-1.13
71 12 7 1 12 39	6, 66, 9, 0, 0	A	151.870	154.941	-1.75
71 12 7 1 14 3	6, 66, 9, 0, 0	A	157.924	154.739	-1.22
71 12 7 1 15 27	6, 66, 661, 0, 0	A	164.103	154.747	-1.21

PROBE EPHEMERIS SEGMENT 7

SHUTTER CLOSE GMT	LANDMARKS OBSERVED	TV	CLOCK DEG	CONE DEG	TWIST
71 12 11 0 56 49	66, 661, 49, 0, 0	A	159.342	148.749	-.76
71 12 11 0 59 13	66, 661, 0, 0, 0	A	164.918	148.598	-1.11
71 12 11 0 59 37	661, 0, 0, 0, 0	A	170.592	148.698	-1.49
71 12 11 11 39 43	51, 54, 0, 0, 0	B	118.603	96.446	.16
71 12 11 12 53 37	6, 9, 0, 0, 0	A	131.336	153.161	-.94
71 12 11 12 55 1	6, 9, 0, 0, 0	A	137.439	153.044	-.89
71 12 11 12 56 25	6, 9, 0, 0, 0	A	143.505	153.098	-1.03
71 12 12 0 51 49	6, 0, 0, 0, 0	A	136.416	152.343	-.61
71 12 12 0 53 13	6, 0, 0, 0, 0	A	141.914	152.220	-1.19
71 12 12 11 50 31	51, 54, 0, 0, 0	B	127.373	101.076	-.02
71 12 13 0 46 49	6, 9, 0, 0, 0	A	138.509	153.931	-1.50
71 12 13 0 48 13	6, 9, 0, 0, 0	A	145.260	154.048	-1.20
71 12 13 0 49 37	6, 0, 0, 0, 0	A	151.751	154.039	-.90
71 12 13 11 25 55	51, 53, 54, 0, 0	B	118.039	99.171	.16
71 12 13 11 37 49	2, 3, 0, 0, 0	A	113.312	95.870	.21
71 12 13 11 42 43	3, 0, 0, 0, 0	B	118.316	96.534	-.02
71 12 13 11 44 7	3, 0, 0, 0, 0	B	118.238	96.472	.00
71 12 13 12 43 37	6, 9, 0, 0, 0	A	127.362	149.552	-.63
71 12 13 12 44 19	6, 0, 0, 0, 0	B	134.336	149.695	.35
71 12 13 12 45 1	6, 9, 0, 0, 0	A	133.079	149.589	-.78
71 12 13 12 46 25	6, 9, 0, 0, 0	A	138.877	149.703	-.94
71 12 14 11 15 18	51, 53, 54, 0, 0	B	115.450	99.848	.07
71 12 14 11 29 36	51, 0, 0, 0, 0	A	118.275	102.931	.04
71 12 14 11 39 6	2, 201, 202, 0, 0	B	121.830	97.453	.03
71 12 14 11 40 30	2, 201, 202, 0, 0	B	122.719	97.015	.07
71 12 15 11 23 36	2, 3, 0, 0, 0	A	118.408	99.627	-.06
71 12 15 11 29 12	2, 3, 0, 0, 0	A	112.906	95.910	.16
71 12 15 11 34 6	2, 201, 202, 0, 0	B	122.165	99.753	-.04
71 12 15 11 35 30	2, 201, 0, 0, 0	B	122.877	99.153	.07
71 12 16 11 31 54	2, 201, 202, 0, 0	B	123.933	102.976	-.12
71 12 16 11 46 36	2, 3, 0, 0, 0	A	131.000	109.769	-.18
71 12 16 11 59 30	3, 0, 0, 0, 0	B	142.348	114.163	.17
71 12 16 12 30 0	6, 9, 0, 0, 0	A	132.114	147.856	-.43
71 12 16 12 31 24	6, 9, 0, 0, 0	A	131.876	147.885	-.53
71 12 16 12 32 48	6, 9, 0, 0, 0	A	131.561	147.948	-.66
71 12 17 11 43 0	2, 3, 0, 0, 0	A	130.737	109.621	-.23
71 12 18 12 22 47	6, 9, 0, 0, 0	A	129.320	146.004	-.43

Table 2. Landmark data summary (contd)

71 12 18 12 24 11	6,661, 9, 0, 0, A	129.211	145.978	-.59
71 12 18 12 25 35	6,661, 0, 0, 0, A	129.370	146.071	-.80
71 12 19 12 20 35	6, 9, 0, 0, 0, A	138.544	149.762	-1.29
71 12 19 12 21 59	6, 9, 0, 0, 0, A	138.493	149.812	-1.27
71 12 19 12 23 23	6,661, 9, 0, 0, A	138.393	149.878	-1.26
71 12 21 0 55 47	3, 0, 0, 0, 0, A	274.764	115.685	-.26
71 12 22 0 52 10	3, 0, 0, 0, 0, A	257.407	102.019	-.03
71 12 23 0 49 58	2,202, 0, 0, 0, A	235.432	103.548	-.23
71 12 23 0 50 40	201, 0, 0, 0, 0, B	236.088	103.688	-.03
71 12 23 12 10 22	6, 9, 0, 0, 0, A	126.039	144.742	-.63
71 12 23 12 11 46	6, 9, 0, 0, 0, A	131.920	144.634	-.76
71 12 23 12 13 10	6,661, 66, 0, 0, A	137.790	144.722	-.97
71 12 24 12 9 18	6, 9, 0, 0, 0, A	142.210	145.902	-1.08
71 12 24 12 9 34	49, 6,661, 66, 9, A	142.075	145.957	-1.09
71 12 24 12 10 58	6, 66,661, 0, 0, A	141.899	146.034	-1.10

PROBE EPHEMERIS SEGMENT 9

SHUTTER CLOSE GMT	LANDMARKS OBSERVED	TV	CLOCK DEG	CONE DEG	TWIST
72 1 2 23 17 2	3, 0, 0, 0, 0, A	A	148.977	107.927	-.23
72 1 3 23 10 37	3, 0, 0, 0, 0, A	A	144.571	109.529	.01
72 1 3 23 16 13	3, 0, 0, 0, 0, A	A	148.727	112.365	-.19

PROBE EPHEMERIS SEGMENT 9

SHUTTER CLOSE GMT	LANDMARKS OBSERVED	TV	CLOCK DEG	CONE DEG	TWIST
72 1 7 11 28 6	9, 0, 0, 0, 0, B	B	116.314	130.308	-.01
72 1 7 11 33 0	9, 6, 0, 0, 0, A	A	122.334	139.087	-.39
72 1 7 11 34 24	9, 6, 0, 0, 0, A	A	124.164	142.371	-.81
72 1 7 11 35 48	9, 6, 0, 0, 0, A	A	124.756	143.694	-1.07
72 1 7 12 15 0	3, 0, 0, 0, 0, A	A	282.050	135.785	-.67
72 1 7 12 24 48	51, 52, 53, 54, 0, A	A	270.399	99.126	.03

PROBE EPHEMERIS SEGMENT 10

SHUTTER CLOSE GMT	LANDMARKS OBSERVED	TV	CLOCK DEG	CONE DEG	TWIST
72 1 11 12 15 59	2,202, 0, 0, 0, A	A	252.853	102.044	.03
72 1 12 23 7 35	9, 66, 49,661, 6, A	A	110.425	100.043	-.16
72 1 13 23 6 46	49, 6, 0, 0, 0, A	A	110.499	99.719	.04

PROBE EPHEMERIS SEGMENT 11

SHUTTER CLOSE GMT	LANDMARKS OBSERVED	TV	CLOCK DEG	CONE DEG	TWIST
72 1 14 23 32 34	6, 66,661, 0, 0, A	A	129.281	136.843	-.63
72 1 14 23 33 16	6, 0, 0, 0, 0, B	B	129.185	136.917	-.03
72 1 14 23 33 58	9, 66,661, 6, 0, A	A	128.502	136.736	-.59
72 1 14 23 34 40	6, 0, 0, 0, 0, B	B	132.522	140.183	-.08
72 1 14 23 35 22	9,661, 6, 0, 0, A	A	131.652	140.398	-.89
72 1 16 23 2 58	6, 0, 0, 0, 0, A	A	110.151	97.990	-.03

PROBE EPHEMERIS SEGMENT 12

SHUTTER CLOSE GMT	LANDMARKS OBSERVED	TV	CLOCK DEG	CONE DEG	TWIST
72 1 18 22 59 33	6, 0, 0, 0, 0, A	A	109.437	95.960	-.07
72 1 19 11 24 45	9, 6, 0, 0, 0, A	A	125.879	134.593	-.64
72 1 19 11 26 9	9, 6, 0, 0, 0, A	A	125.835	134.717	-.64
72 1 19 22 56 21	6, 0, 0, 0, 0, A	A	109.342	96.202	.25
72 1 20 22 54 8	6, 0, 0, 0, 0, A	A	109.278	96.041	.00
72 1 21 10 57 56	3, 0, 0, 0, 0, A	A	143.532	95.889	-.07
72 1 21 22 51 56	6, 0, 0, 0, 0, A	A	109.394	96.015	.08

Table 2. Landmark data summary (contd)

PROBE EPHEMERIS SEGMENT 13

SHUTTER CLOSE GMT	LANDMARKS OBSERVED	TV	CLOCK DEG	CONE DEG	TWIST
72 1 23 11 15 56	9, C, 0, 0, 0,	A	127.317	125.948	-.15
72 1 23 11 17 20	9, 6, 0, 0, 0,	A	126.720	136.149	-.77
72 1 25 11 12 55	9, 6, 0, 0, 0,	A	120.964	128.234	-.32
72 1 26 0 15 31	51, 52, 53, 54, 0,	A	303.378	95.346	-.02
72 1 27 0 10 31	51, 52, 53, 54, 0,	A	299.263	96.140	-.04
72 1 27 0 11 55	51, 52, 53, 54, 0,	A	293.233	96.314	-.15

PROBE EPHEMERIS SEGMENT 14

SHUTTER CLOSE GMT	LANDMARKS OBSERVED	TV	CLOCK DEG	CONE DEG	TWIST
72 1 28 11 11 54	9, 6, 0, 0, 0,	A	121.928	127.687	-.55
72 1 29 0 9 54	2,201,202, 0, 0,	A	303.447	95.859	-.13
72 1 29 23 59 42	2,201,202, 0, 0,	A	280.498	113.131	-.26
72 1 30 0 1 6	2,201,202, 0, 0,	A	280.251	113.449	-.26

PROBE EPHEMERIS SEGMENT 15

SHUTTER CLOSE GMT	LANDMARKS OBSERVED	TV	CLOCK DEG	CONE DEG	TWIST
72 2 9 22 57 39	9, 66,661, 6, 0,	A	113.147	116.407	-.40
72 2 11 22 57 26	9, 6, 0, 0, 0,	A	122.719	125.199	-.38

PROBE EPHEMERIS SEGMENT 16

SHUTTER CLOSE GMT	LANDMARKS OBSERVED	TV	CLOCK DEG	CONE DEG	TWIST
72 2 13 22 54 33	9, 6, 0, 0, 0,	A	120.806	123.028	-.57
72 2 15 10 53 20	6, 0, 0, 0, 0,	A	116.438	118.642	-.29
72 2 15 22 54 20	9, 6, 0, 0, 0,	A	116.688	124.113	-.24
72 2 17 11 35 8	3, 0, 0, 0, 0,	A	281.169	135.722	-.65

PROBE EPHEMERIS SEGMENT 17

SHUTTER CLOSE GMT	LANDMARKS OBSERVED	TV	CLOCK DEG	CONE DEG	TWIST
72 2 18 11 27 19	3, C, 0, 0, 0,	A	209.316	141.774	-1.04
72 2 19 11 34 55	2,201,202, 0, 0,	A	251.229	127.397	-.57
72 2 19 22 53 55	9, 6, 0, 0, 0,	A	119.570	123.742	-.02

PROBE EPHEMERIS SEGMENT 18

SHUTTER CLOSE GMT	LANDMARKS OBSERVED	TV	CLOCK DEG	CONE DEG	TWIST
72 2 25 10 48 5	9, 6, 0, 0, 0,	A	115.317	114.568	.02

PROBE EPHEMERIS SEGMENT 19

SHUTTER CLOSE GMT	LANDMARKS OBSERVED	TV	CLOCK DEG	CONE DEG	TWIST
72 2 27 10 43 41	9, 6, 0, 0, 0,	A	115.979	112.944	-.25
72 2 29 10 39 16	9, 6, 0, 0, 0,	A	117.041	112.425	-.30

PROBE EPHEMERIS SEGMENT 20

SHUTTER CLOSE GMT	LANDMARKS OBSERVED	TV	CLOCK DEG	CONE DEG	TWIST
72 3 8 10 30 44	6, C, 0, 0, 0,	B	112.697	101.281	.17

PROBE EPHEMERIS SEGMENT 21

SHUTTER CLOSE GMT	LANDMARKS OBSERVED	TV	CLOCK DEG	CONE DEG	TWIST
72 3 8 23 9 50	2,202, 0, 0, 0,	A	177.886	146.187	-1.17
72 3 9 23 22 8	201, C, 0, 0, 0,	B	295.265	124.177	-.21
72 3 8 23 23 32	201, 0, 0, 0, 0,	B	298.103	120.545	-.23
72 3 8 23 24 56	201, C, 0, 0, 0,	B	300.003	117.173	.03

296<

Table 3. Measurement uncertainties of observed surface features

Landmark ID	Narrow-angle camera		Wide-angle camera	
	Pixel	Line	Pixel	Line
6	20	20	3	3
66	*	*	3	3
661	*	*	3	3
49	*	*	3	3
9	10	10	3	3
2	10	10	5	5
201	5	5	3	3
202	3	3	*	*
3	5	5	3	3
51	4	4	3	3
53	4	4	3	3
54	4	4	3	3

*Observations of the indicated type were not made.

297<

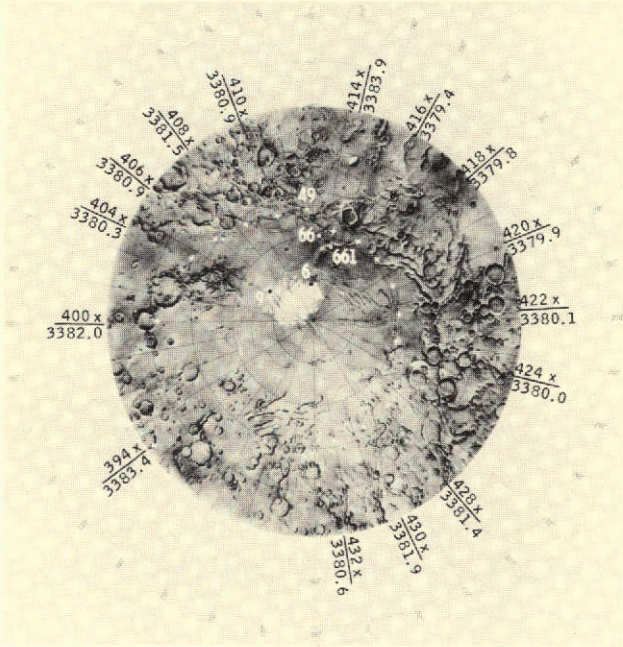


Figure 1a. Landmarks in the south polar region

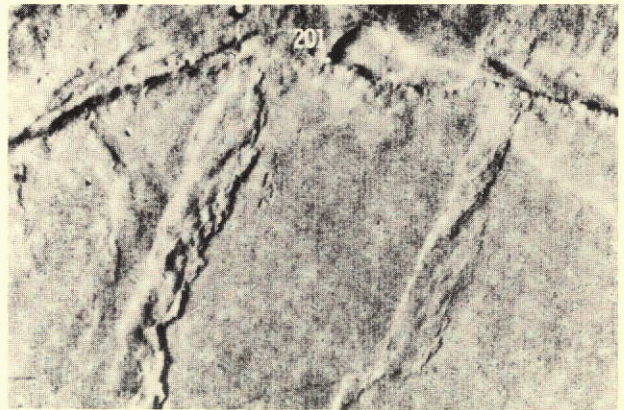
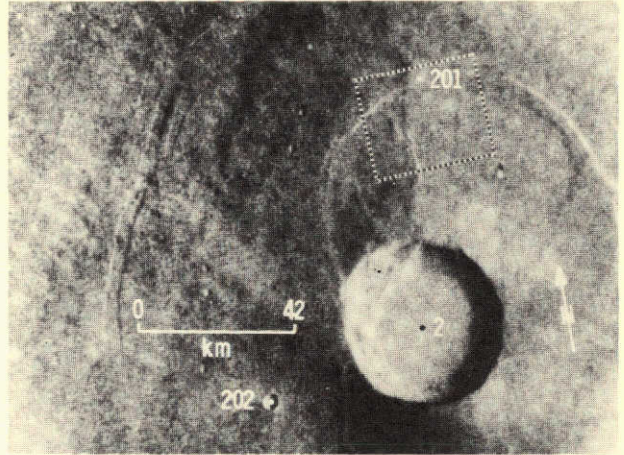


Figure 1b. Location of landmarks in Pavonis Lacus

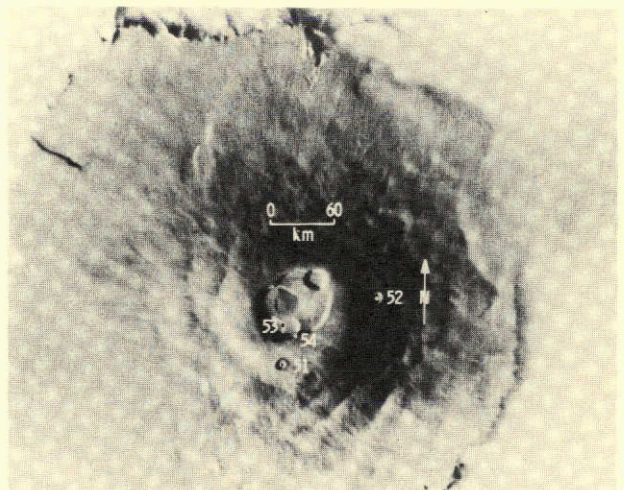


Figure 1c. Landmark location in Nodus Gordii

Figure 1d. Landmark locations in Nix Olympica

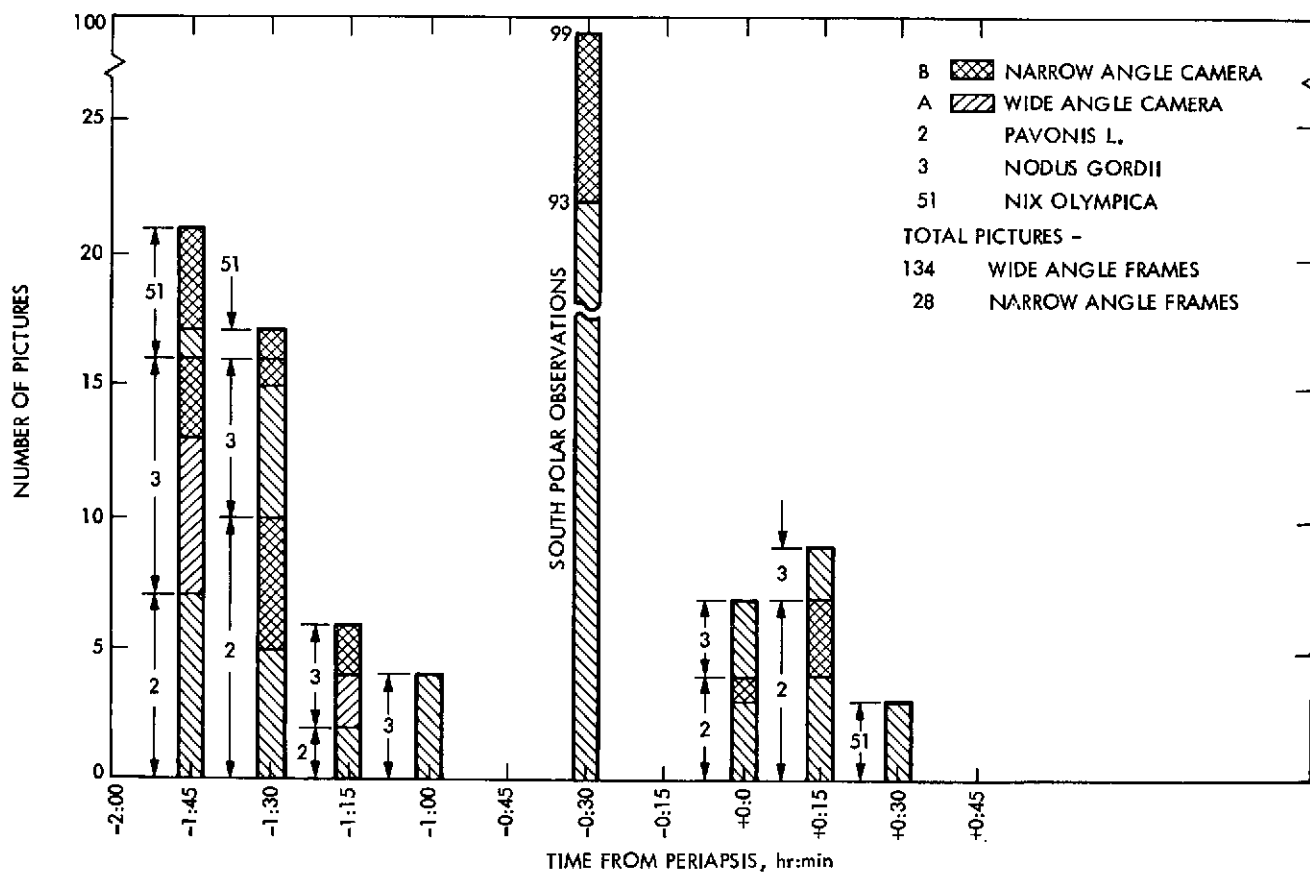
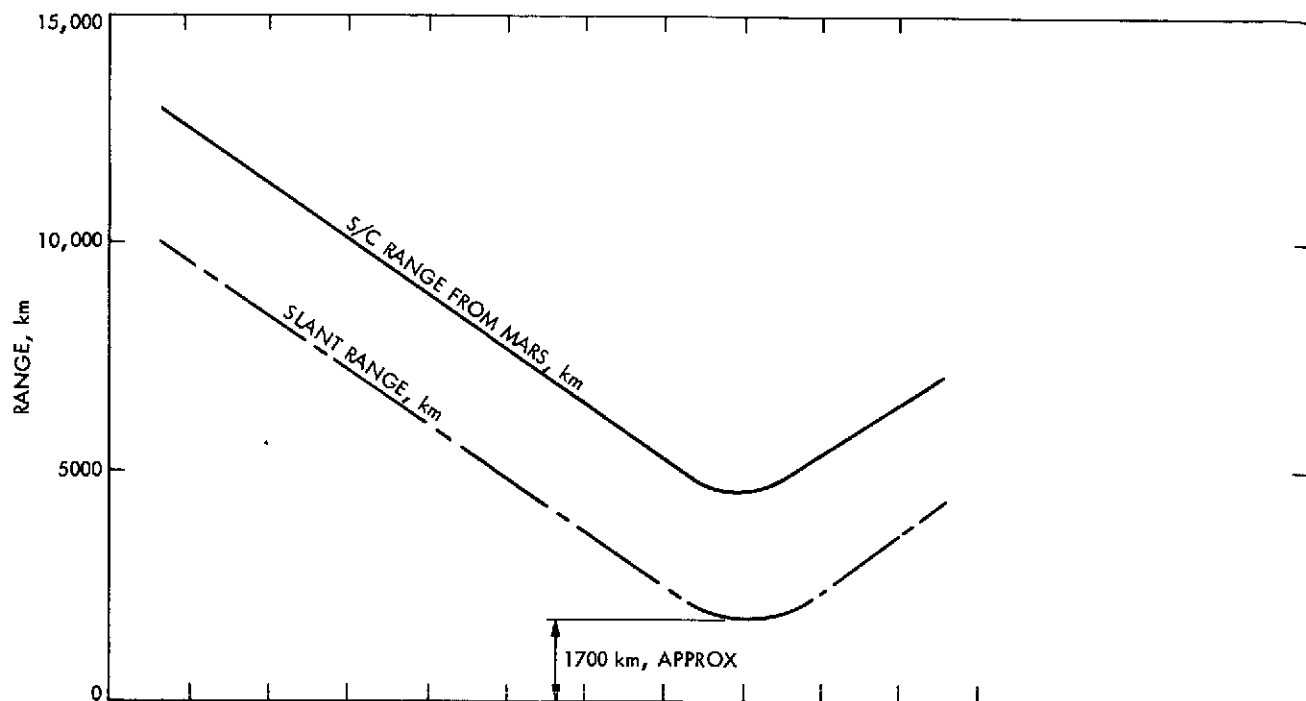


Figure 2. Distribution of observation times relative to time of periapsis passage of spacecraft

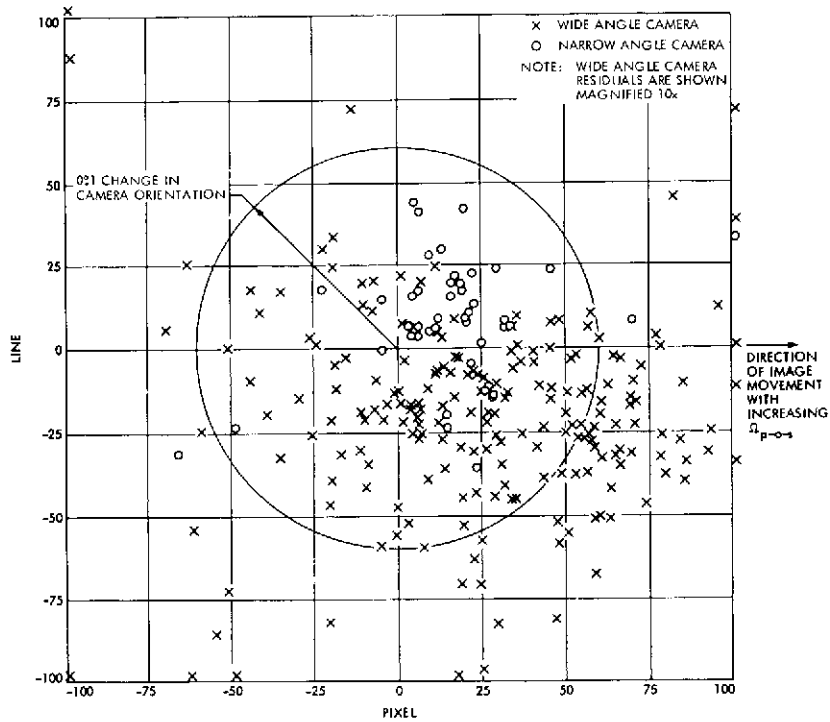


Figure 3a. Raw data residuals - Ω_{p-o-s} = discontinuous node
(Doppler data)

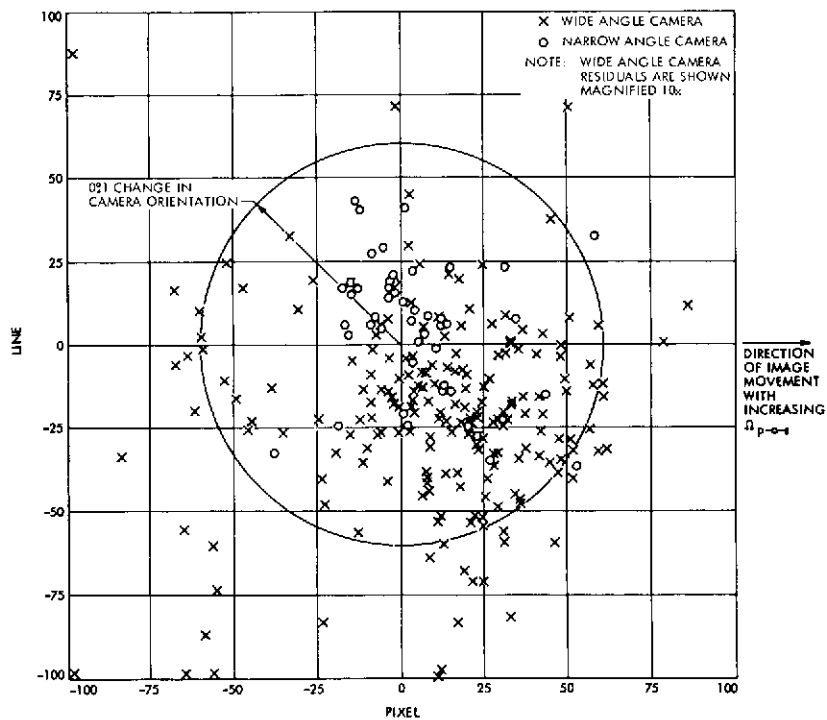


Figure 3b. Raw data residuals - Ω_{p-o-s} = continuous node
(Doppler + Phobos/Deimos data)

300<

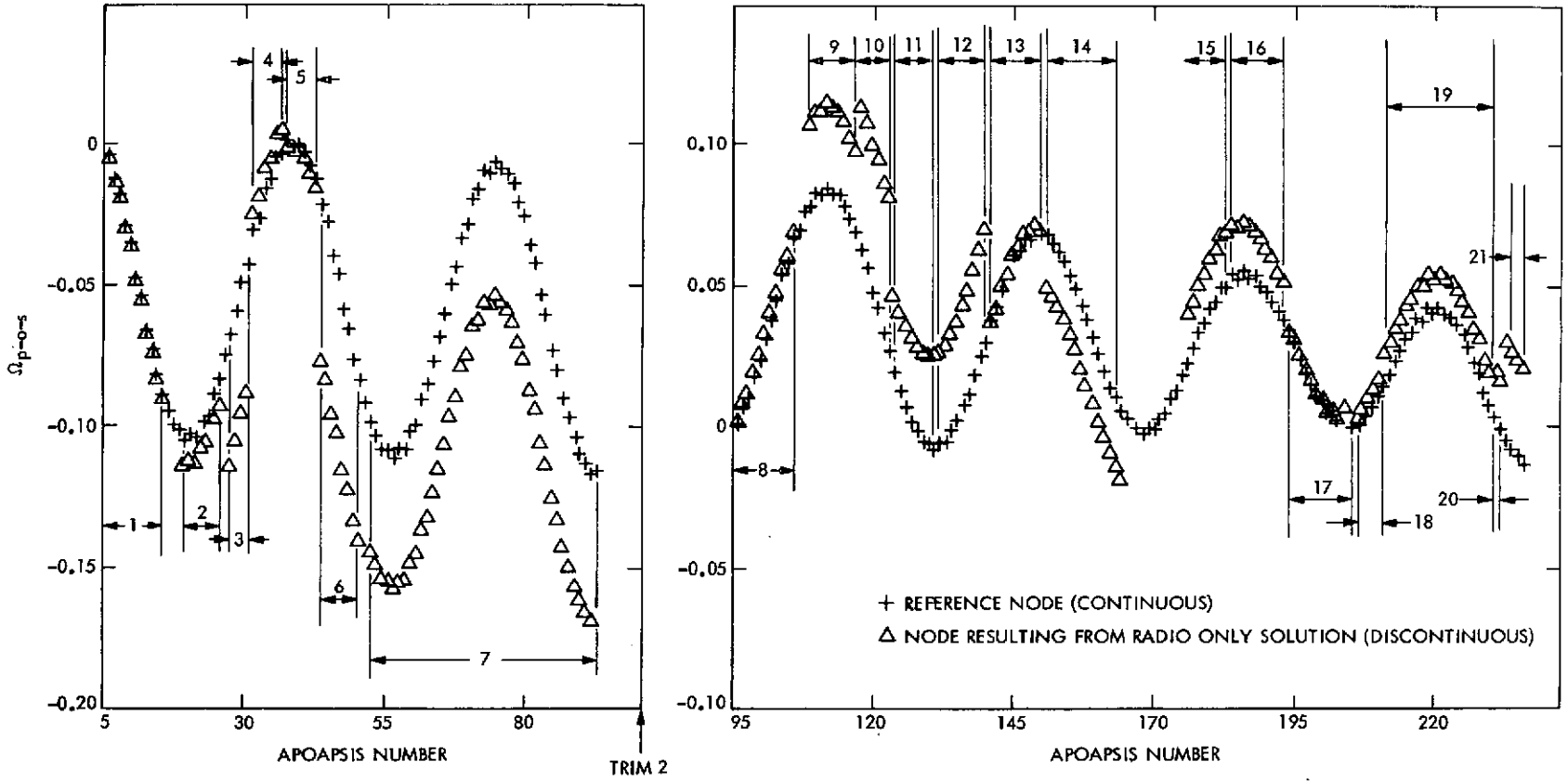


Figure 4. History of Node in the plane of sky (Ω_{p-o-s})

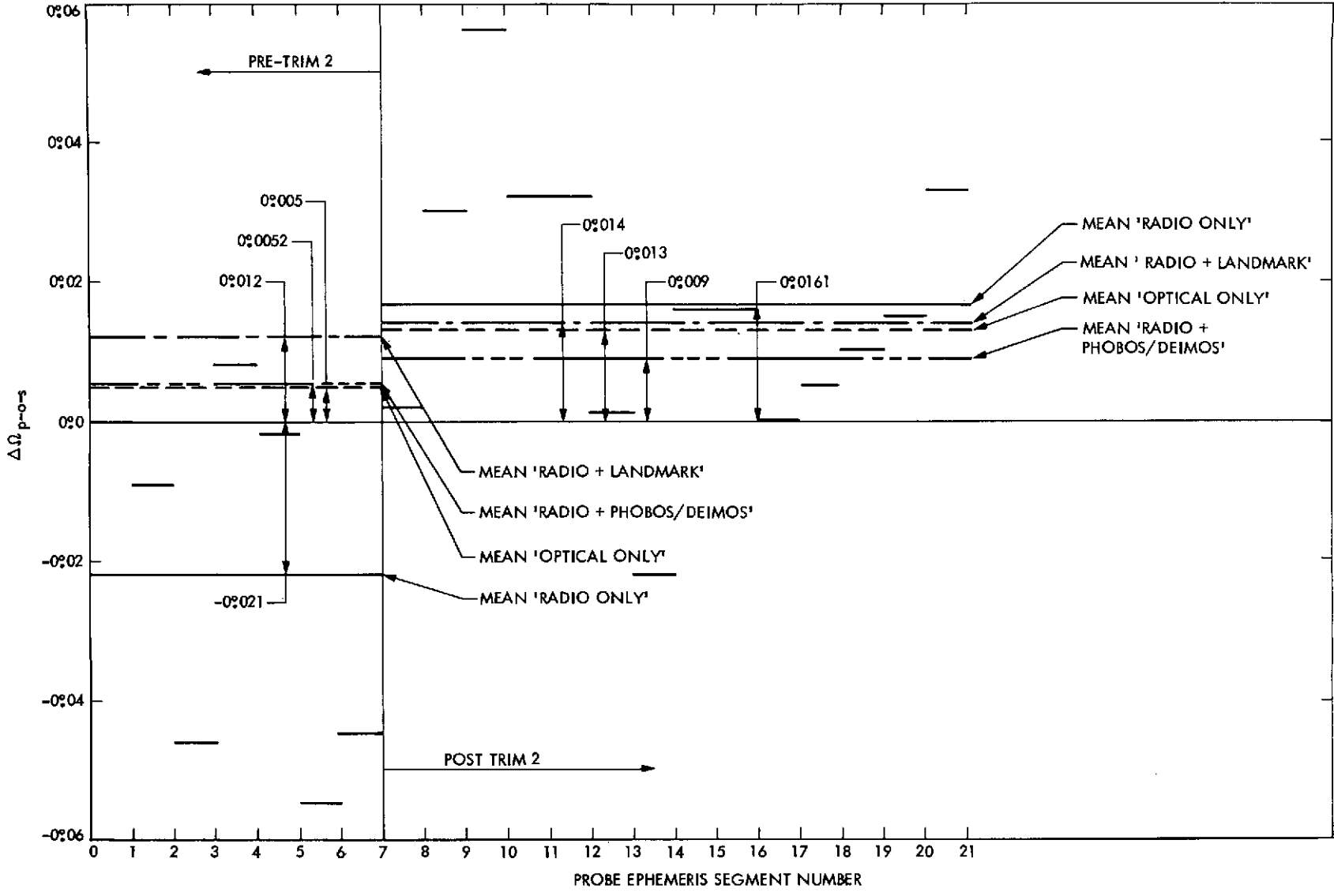
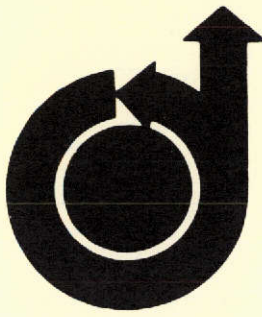


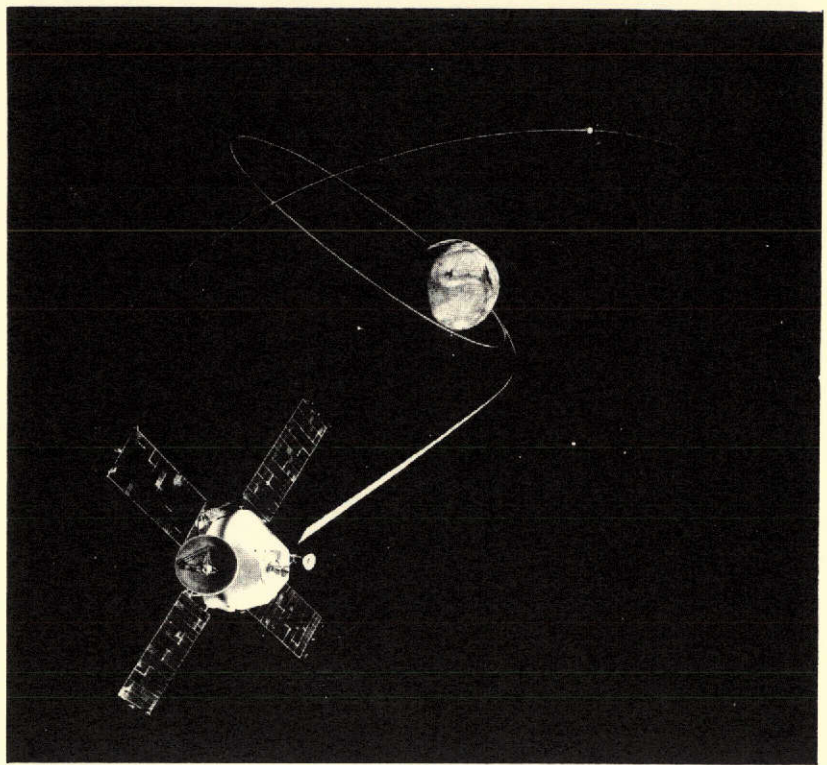
Figure 5. Ω_{p-o-s} solutions

APPENDIX R

MARINER MARS '71 OPTICAL LIT LIMB DATA MEASURING TECHNIQUES
AND NAVIGATION RESULTS



**AIAA Paper
No. 73-251**



MARINER MARS '71 OPTICAL LIT LIMB DATA
MEASURING TECHNIQUES AND NAVIGATION RESULTS

by
H. OHTAKAY and N. JERATH
Jet Propulsion Laboratory
Pasadena, California

AIAA 11th Aerospace Sciences Meeting

WASHINGTON, D.C. / JANUARY 10-12, 1973

First publication rights reserved by American Institute of Aeronautics and Astronautics.
1290 Avenue of the Americas, New York, N. Y. 10019. Abstracts may be published without
permission if credit is given to author and to AIAA. (Price: AIAA Member \$1.50. Nonmember \$2.00).

Note: This paper available at AIAA New York office for six months;
thereafter, photoprint copies are available at photocopy prices from
AIAA Library, 750 3rd Avenue, New York, New York 10017

MARINER MARS '71 OPTICAL LIT LIMB DATA MEASURING TECHNIQUES AND NAVIGATION RESULTS*

Hiroshi Ohtakay** and Navin Jerath†
Jet Propulsion Laboratory
Pasadena, California

Abstract

Optical spacecraft navigation data, i. e., the lit limb TV image of Mars, has been successfully demonstrated to augment the radio spacecraft tracking data during the approach phase of the Mariner IX spacecraft to Mars. Accurate in-flight calibration of the TV instrument and the scan platform was performed by referencing stars and planets. Simulated real-time processing and the detailed post-flight analyses of the onboard optical data have shown that planet limb data is an important data source which could be especially significant in a far-encounter period for which other types of onboard optical measurements, e. g., natural satellite(s) of the target planet with star background, are not available.

Introduction

Optical Navigation has been demonstrated to be an effective method for interplanetary navigation (Ref. 1, 2). Various optical data types (3) which can be obtained from science and engineering instruments normally aboard such spacecraft can be used. Television (TV) cameras are used to view planets or satellites and stars for celestial references. This paper presents the results of post-flight optical navigation investigations using data on the lit-limb of Mars obtained from the Mariner Mars '71 (MM'71) mission.

The sources of data were the digitally transmitted TV picture along with supporting engineering data. Processing of the raw data included the elimination of systematic errors occurring in the on-board measurement system and the reduction of the TV lit limb image data to image center location data. These measurements were used to determine the relative location of the spacecraft with respect to the target planet.

The navigation analysis deals with two aspects of the Mars limb data. The first is an evaluation of the performance that could have resulted had the processing been performed in real time for computing the Mars Orbit Insertion (MOI) maneuver, and the second is its sensitivity to Mars ephemeris errors and the amount of radio tracking data. The investigation indicates that though the estimate obtained from the real-time simulation would have been within MM'71 mission accuracy requirements, the uncertainty of the estimate is large. Performance has been found to be somewhat sensitive to the amount of radio tracking data but not to Mars ephemeris error.

Onboard Measurement Systems

Instruments onboard the Mariner spacecraft which were utilized to obtain the data included the

narrow and wide angle science TV cameras and the attitude control sensors. TV cameras were mounted on a scan platform provided with two degrees of freedom. The 1.1-deg x 1.4-deg and 11-deg x 14-deg field-of-view vidicons with 9.6 mm x 12.5 mm selenium targets were electronically scanned in 700 lines with 832 picture elements (pixels) per line. Continuous video intensity level was sampled and digitized to 9 bits (512 levels) prior to transmission to Earth. The attitude control subsystem provided spacecraft stabilization and orientation. Its celestial sensors, i. e., Sun-sensors and star (Canopus) sensor, produced pitch, yaw and roll position signals. The attitude control signals, together with the scan platform gimbal position data, were transmitted to the ground station through the engineering telemetry channels.

TV picture-taking sequences were commanded and supervised by the onboard computer. Video data of about 30 TV frames for one picture-taking sequence were temporarily stored on magnetic tape. The magnetic tape playback for data transmission to the Earth was commanded when the Goldstone antenna station was in a favorable position for direct communication with the Mariner IX spacecraft (Fig. 1).

Inflight Calibration of Onboard Measurement Instruments

Calibrations of the onboard measurement instruments were subject to change due to factors such as mechanical shock experienced during spacecraft launch and midcourse maneuvers as well as gravity and electromagnetic environmental changes. This necessitated inflight instrumental calibration to be performed prior to spacecraft guidance/navigation data acquisition.

Calibration of the TV camera geometric distortion was necessary to establish undistorted image direction relative to the TV coordinate system. This was performed by utilizing both reseau marks etched on the vidicon target and celestial references (stars) with known locations. The former allows calibration of electromagnetic geometric distortion arising inside the vidicon, while the latter is used to calibrate optical distortion in the camera optics combined with electromagnetic distortion. Since ground calibration of the TV cameras has revealed practically no optical geometric distortion for the narrow angle TV camera and small optical distortion (<2.5 pixels), for the wide angle TV camera, no attempt was made during flight to estimate optical distortion parameters.

Electromagnetic geometric distortion was calibrated by fitting 63 and 111 reseau images observed in the narrow and wide angle TV calibration pictures, respectively, to the analytical geometric

*This paper presents the results of one phase of research carried out at the Jet Propulsion Laboratory, California Institute of Technology, under Contract No. NAS 7-100, sponsored by the National Aeronautics and Space Administration.

**Senior Engineer, Systems and Research Section, Jet Propulsion Laboratory.

†Research Engineer, Tracking and Orbit Determination Section, Jet Propulsion Laboratory.

distortion model.⁽⁴⁾ Electromagnetic geometric distortion, for the narrow angle TV calibrated to the accuracy of 0.5 (1 σ) pixels and 0.7 (1 σ) pixels in the line and pixel directions, respectively, is depicted in Fig. 2(a) and (b), showing small or linear distortion in the center portion, and larger and highly nonlinear distortion in the edges of the TV frame. The wide angle TV showed similar distortion characteristics. More interestingly, changes of observed reseau locations in narrow and wide angle TV pictures between preflight and inflight calibrations are illustrated in Fig. 3(a) and (b), indicating a linear rotational and translational shift in narrow angle TV pictures and a translational shift in wide angle TV pictures. These shifts of observed reseau image locations were caused by the absence of Earth's magnetic field, and possibly a slight displacement of TV beam deflection coils, especially in the narrow angle TV instrument.

Calibration of the scan platform subsystem was necessary to establish the true scan platform orientation (hence TV image direction) relative to the spacecraft. The scan platform errors were characterized by systematic errors such as gimbal mounting errors, gimbal axis misalignments and TV instrument mounting offsets placed on the scan platform. Attitude control sensor signal values were needed to define the spacecraft attitude relative to the celestial references. Systematic errors of the telemetered attitude control sensor signals are characterized by sensor null offsets and scale factor errors. Inflight calibration of the scan platform subsystem and attitude control sensors was performed by referencing to the orientation of the narrow angle TV imaged stars and planets whose locations were known a priori. Mechanical misalignments of the wide angle TV were calibrated with respect to the narrow angle TV. Two sequences of 31 pictures aimed at star clusters (Fig. 5), single stars, Mars and Saturn, provided a good set of data for calibration of the scan platform subsystem and attitude control sensors. The star-referenced inflight calibration⁽⁵⁾ determined the scan platform subsystem and attitude control errors to a total accuracy of 0.005° (1 σ) about the TV line of sight (LOS) for the narrow angle TV camera (Fig. 4), and 0.015° (1 σ) and 0.17° (1 σ), respectively, for the wide angle TV camera.

Limb Data Algorithm and Processing

During the two Mars calibration sequences which took place 5 and 4 days before Mars encounter (abbreviated as E-5d and E-4d, respectively), 22 narrow angle TV pictures which contained Mars lit limb images (Fig. 6) were taken. Wide angle TV pictures of Mars during the Mars calibration sequences were not processed because of poor angular resolution. During POS (preorbit Science) I, II, and III sequences which started from E-3.1d, E-1.9d and E-0.7d, respectively, 36 narrow angle TV pictures and 4 wide angle TV pictures were selected for lit limb data processing where POS-I and II pictures were available in real-time before MOI (Fig. 7). Towards the end of POS-II and throughout POS-III sequences, the Mars images taken by the narrow angle TV were so large that only a small portion of the lit limb was visible; hence such frames were not processed.

Raw TV data of Mars' image⁽¹⁾ was first processed to determine the lit limb in the TV

coordinate system. The limb finding algorithm searched the digital video data TV scan line by scan line. That is, the limb search started from a point off the planet image and continued onto the limb. The first of three adjacent pixels, all having video intensity levels exceeding a predetermined threshold level, was selected as the location of lit limb on that line. The requirement for three adjacent pixels eliminated the detection of false limb point caused by one or two pixel-bit error noise (Fig. 8(b)). Typical lit limb structure imaged by the narrow angle camera is shown in Fig. 8(a) and (b), indicating a relatively sharp decline in brightness near the equator and a gradual decline at the pole regions. The transition region between the dark background and the apparent limb ranged from 15 km to 25 km wide near the equator, and 25 km to 30 km wide at the pole regions.

To interpret the imaged Mars lit limb, Mars was assumed to be an ellipsoid with small eccentricity (= 0.145). Since the Mariner spacecraft approached Mars only about 20-degrees off the equatorial plane of Mars, TV image of Mars can be reasonably well modeled by an ellipse, with the center of the ellipse being coincident with the center of the ellipsoidal planet body.

The apparent lit limb data was processed for TV distortion rectification based upon the inflight calibration of the TV instruments. Then, a minimum-variance estimation algorithm was used to identify the true image shape, size and orientation as well as the image center location, which rendered significant uncertainty. The observable equation used in the estimation process to fit the distortion corrected lit limb data was the following function:⁽⁹⁾

$$\phi = \left(1 - \frac{c^2}{a^2}\right)x^2 + y^2 - a^2 + c^2 + \xi \quad (1)$$

$$\begin{bmatrix} x \\ y \end{bmatrix} = \begin{bmatrix} \cos \theta & -\sin \theta \\ -\sin \theta & -\cos \theta \end{bmatrix} \begin{bmatrix} p - p_0 \\ \ell - \ell_0 \end{bmatrix}$$

where

a, c = semi-major axis and focus of ellipse

θ = inclination of Mars spin axis relative to the TV coordinate system

ℓ_0, p_0 = image center location in line and pixel

ℓ, p = limb data point

ξ = observation noise

In this equation, the observable, ϕ , takes a zero value if ξ , the observation noise, is zero.

The identified size of the planet, illustrated in Fig. 9, has a slightly larger value than the known mean equatorial radius (3393.4 km) determined by the S-band occultation experiment.⁽⁶⁾ Similarly, the identified shape parameter of the planet, illustrated in Fig. 10, is smaller than the known value (e = 0.145) by about 3 percent. That is, the Mars

images were somewhat larger and more circular than expected. These results also indicate that the lit limb of the imaged planet does not represent the Martian surface but a light scattering surface from the Martian atmosphere. They may also have been caused by the limb darkening effect at the polar regions and lightening near the south polar cap, maked albedo change near the lit limb, atmospheric activities, i.e., the dust storm which prevailed in the Martian atmosphere throughout the approach phase, and the spectral response characteristics of the TV camera subsystem, including the particular filter (minus blue) used for the narrow angle TV throughout the mission.

The limb fit residuals, which are a measure of the observation data noise after a successful limb parameter estimation process, were evaluated for each scan line containing a limb measurement (Fig. 11) with the units of (pixel)². The observation data noise had been caused by quantization in picking discrete limb points, uncalibrated geometric distortion of the TV, residual limb image from the previous picture (triggering a false limb data), and limb model approximation error. To interpret the limb residual statistics with nearly zero-mean and a standard deviation of several tens of (pixel)², the residual random process is mapped onto an equivalent random process along the limb image in the TV coordinate system. From Eq. (1), we obtain

$$\text{Var}(d\phi) = c_p^2 \text{Var}(dp) + c_l^2 \text{Var}(dl) \quad (2)$$

where

$$c_p^2 = 4 \left[- \left(1 - \frac{c^2}{a^2} \right) x \cos \theta + y \sin \theta \right]^2$$

$$c_l^2 = 4 \left[\left(1 - \frac{c^2}{a^2} \right) x \sin \theta + y \cos \theta \right]^2$$

Var() = variance of argument

If it is assumed that the observation noise affects equally in line and pixel directions, Eq. (2) can be rewritten as

$$\text{Var}(dp) = \text{Var}(dl) = \frac{\text{Var}(d\phi)}{c_l^2 + c_p^2} \quad (3)$$

or for typical values for the known parameters relations, e.g.,

$$\frac{c}{a} = 0.145, \quad \text{and} \quad x^2 + y^2 \approx a^2$$

Eq. (3) is approximated by

$$\text{Var}^{1/2}(dp) = \text{Var}^{1/2}(dl) \approx \frac{\text{Var}^{1/2}(d\phi)}{2a} \quad (4)$$

Eq. (4) typically took a value of 0.3 pixels, reasonably well coinciding with the limb quantization error statistics (a uniform distribution over a pixel). Eq. (4) was also evaluated for each TV frame and was mapped along the planet limb by using the equation of colinearity (Fig. 12). Similar results from the Mariner Mars 1969 missions are shown in the same figure for comparison. The improvements by a factor of at least two are owing to the accurate inflight calibration of the TV instruments and the scan platform.

Optical Data Errors

Optical navigation observables were defined as the image locations (pixel and line numbers) of the center of Mars. Optical data errors are classified as model and instrument errors.

Model errors include Mars ephemeris, shape and gravity field errors. Instrument errors include TV distortions, TV pointing errors, image center-finding errors and random measurement errors.

TV distortion errors corrupt the relative geometry of images within a picture. TV pointing errors cause a global shift of all images in a picture and also corrupt the relative image geometry within a picture due to the nonlinearity of the TV distortion. TV pointing errors are caused by imperfect knowledge of scan platform pointing directions at shutter times. Knowledge of TV pointing can be obtained from reduced spacecraft telemetry data. This yields TV pointing errors of tens of pixels.

The center-finding errors, as discussed above, result from TV image distortion and errors in the mathematical models of the planet figure and the lit limb. These errors are modelled as a combination of a constant error proportional to the image size, along with random errors. These random errors are a few pixels in magnitude.

Approach Trajectory Analysis

The target parameters used for accuracy analysis are the B plane parameters defined in Figure 13. The uncertainty in these parameters is mapped into the 1σ aim plane dispersion ellipse.

The following definitions for the B-plane refer to Figure 13.

<u>Parameter</u>	<u>Definition</u>
<u>B</u>	The vector from the center of the target body directed perpendicular to the incoming asymptote of the target centered approach hyperbola.
<u>T</u>	Unit vector from the center of target body, defined by the intersection of the plane normal to the incoming asymptote with a reference plane (usually at the true ecliptic of data) centered at the target body.
<u>R</u>	Unit vector perpendicular to <u>T</u> in the <u>B</u> , <u>T</u> plane positive toward the -z direction of the reference plane.

<u>Parameter</u>	<u>Definition</u>
$\underline{B} \cdot \underline{R}$	The component of \underline{B} along \underline{R} .
$\underline{B} \cdot \underline{T}$	The component of \underline{B} along \underline{T} .
SMAA	The semi-major axis of the one-sigma uncertainty ellipse in the \underline{R} , \underline{T} plane.
SMIA	The semi-minor axis of the one-sigma uncertainty ellipse.
θ	The orientation angle of SMAA measured positive clockwise from \underline{T} to \underline{R} .
T_f	The uncertainty of time of closest approach to the target.

Optical observations involve the measurement of angles between the target planet and a fixed reference direction. Such angular measurements suffer from the inability to determine the velocity (V_∞) of the spacecraft as well as accurate time of flight. To illustrate this, consider a spacecraft moving on trajectory No. 1 (Fig. 14). Let θ_1 and θ_2 represent two angular measurements of the direction between the reference direction (which we have for simplicity assumed to be along V_∞) and the target planet. Then the observable equation is

$$\tan \theta_i = \frac{B}{V_\infty T_i}$$

where

$$T_i = T - t_i$$

B = the magnitude of the B vector

V_∞ = the velocity on the approach asymptote

t_i = the time of the i^{th} observation.

Two perfect observations θ_1 and θ_2 enable one to determine the time of flight. However, since the observation history for any trajectory parallel to trajectory No. 1 will have the same time of flight as the true trajectory, all trajectories parallel to the true trajectory are indistinguishable using these angular measurements. The determination of V_∞ then requires further information on the flight history. For small angles θ , the limiting accuracy for B with perfect observation is then given by

$$\frac{\delta B}{B} = \frac{\delta V_\infty}{V_\infty} \quad (6)$$

Information on V_∞ is obtained from planetary bending of the approach trajectory. For computing the MOI maneuver; doppler data would have to be used, since planetary bending of the spacecraft trajectory sets in only when the planet is in very close proximity.

So far, it has been assumed that the angular measurements θ_i are perfect. However, various sources of errors arise in these measurements--some of the most common of which are the camera pointing errors and the center-finding errors.

These errors lead to inaccuracies in the calculated time of flight.

For small observation angles θ_1 and θ_2

$$T = \frac{t_2 \theta_2 - t_1 \theta_1}{\theta_2 - \theta_1} \quad (7)$$

and

$$\delta T = \frac{(t_2 - t_1)(\theta_2 \delta \theta_2 - \theta_1 \delta \theta_1)}{(\theta_2 - \theta_1)^2} \quad (8)$$

Assuming independent observations, the standard deviation, σ_T , of T becomes

$$\sigma_T = \left[\frac{V_\infty T_1 T_2 (T_1^2 + T_2^2)^{1/2}}{B(T_1 - T_2)} \right] \sigma_\theta \quad (9)$$

Equation 9 indicates that the uncertainty in the time of flight is very sensitive to the uncertainty in the pointing angle when the spacecraft is far from the planet. It is seen that the error is minimized for smaller V_∞ which decreases the range at which the observations are taken, and by larger B values, which increase parallax.

Simulated Real-Time Results

The TV data available in real-time for computing the MOI maneuver, namely the data through POS II, was processed using as a a-priori the best trajectory available at that time. This trajectory was based on radio tracking data processed through E-13 hours. The picture data from Mars calibration sequences I and II and POS sequences I and II were used for the analysis. Of these pictures the Mars calibration II pictures (at E-4 days) were dropped due to very large data residuals caused by large pointing errors.

Figure 15 shows the B-plane solution history of the trajectory estimate obtained by processing the optical data. The parameters estimated were the spacecraft cartesian state at epoch, TV pointing biases and errors, and image center finding errors. The origin in the figure is at the current best estimate⁽⁷⁾ (CBE). The a-priori shown for the optical data arc was the a-posteriori estimate from a short radio data arc (5 days) through E-13 hours. The estimate stabilized only towards the last few pictures. Two iterations were performed, indicated by the dashed and full lines, respectively, with the last two points on the full line representing the estimates obtained from POS III data. This latter data was played back after orbit insertion (Fig. -7) so was not available in real-time. The final estimate at the end of POS II data had an SMAA of 70 km. This was within 25 km of the CBE, well within MM'71 mission navigation requirements (50 km) for MOI.

Figure 16 shows the raw and fitted data residuals, in the pixel and line directions, for the POS data. Figure 16(b) shows the residuals after the solved for pointing biases and trajectory error have been removed. The magnitude of the pointing biases estimated agreed with scan calibration results.⁽⁵⁾ The center-finding errors, modeled here as being proportional to the image size, appeared to be very small. The pointing errors in the raw data are not random.

The raw data residuals for the Mars calibration sequence I pictures are shown in Figure 17. The expanded time scale facilitates the identification of attitude control limit cycle motion of the spacecraft with a period of about 1.2 hours. This residual limit cycle motion may be due to scale factor errors in the attitude control model. These were, however, not separately included in the estimation but were absorbed in the pointing errors.

The orbit determination (OD) accuracies (Fig. 18) indicate a slow reduction of the SMAA and SMIA with time up to about E-50 hours. Rapid reduction in uncertainty occurs thereafter. At the end of POS II the SMAA is about 70 km while at the end of POS III it is about 30 km. The time of flight uncertainty shows little improvement, as would be anticipated from our discussion of the approach trajectory.

The Mariner IX optical navigation performance was considerably better than that of MM'69⁽¹⁾. The B-plane accuracy was better by a factor of two, while the estimate of the simulated real-time trajectory solution was an order of magnitude better. TV pointing was the major source of error.

Sensitivity to Mars Ephemeris

Planetary ephemeris constitutes a major source of error in navigation estimates obtained using radio-tracking by stations on the Earth⁽⁸⁾. However, from onboard optical data the spacecraft state is directly related to the target planet. To study the effect of Mars ephemeris on the spacecraft trajectory estimate using limb data in conjunction with radio data, a heliocentric error of about 500 km in the orbit of Mars was introduced. The B-plane solution history (Fig. 19) shows that the first pass through the data moves the estimate by 300 km from the a-priori, which is more than 500 km from the CBE(origin). The final iteration moves the estimate to within 40 km of the CBE. The relative insensitivity of optical data to Mars ephemeris errors makes combined radio and optical solutions an attractive mode of navigation.

Sensitivity to Radio-Tracking

As indicated before, optical data suffer a serious limitation in that an accurate determination of the time of flight and V_{∞} is not obtained. However, these are precisely the parameters that can be accurately determined from radio data. A combination, then, of optical and radio data, to give better estimates of encounter conditions much earlier than either data separately could, would be ideal. To study the reliance of optical limb data solutions on a-priori obtained from radio data arcs, two different analyses were carried out. In the first, a few hours of radio tracking was assumed beyond the first midcourse maneuver at launch (L) + 5 days, and no more radio data thereafter. The spacecraft state estimate and covariance at that time were input as a priori to the optical data arc. The mapped B-plane uncertainties were very large at this point owing to large maneuver execution uncertainties being mapped several months forward. The analysis was conducted using only the TV pictures through POS II---that is, the pictures that could have been used for a real-time "optical only" solution before computing the Mars orbit insertion maneuver.

The B-plane solution is shown in Figure 20. The a-priori was more than 2500 km from the CBE in the B-plane. The first pass moved the estimate at the end of POS II to within 450 km of the CBE. The next pass did not appreciably move the POS II solution, but the POS III data moved the estimate to within 30 km. This accuracy is within mission requirements for inserting the Mariner IX into orbit.

The second analysis was performed with no radio data at all. The injection conditions, for purposes of planetary quarantine (PQ), had a 25,000 km aim-point bias and 22 hours lag in time of flight at Mars. The analysis made here for this optical-only solution was not cognizant of the mid-course maneuver performed at L + 5 days which removed the PQ bias. The B-plane trajectory solution (Fig. 21) stabilized at about 7000 km from the CBE, with negligible improvement in time of flight.

The large final error involved here indicates that for optimum results both radio and optical limb data types are necessary. Even small radio data arcs when used to give a priori estimates and covariances, improve the effectiveness of optical limb-data enormously (Fig. 20).

Conclusions

It has been successfully demonstrated that the TV pictures of Mars taken during the approach to Mars on the MM'71 mission were a good source of navigational data.

The inflight calibration of the scan platform, performed by referencing star images in TV pictures, significantly improved the onboard optical data accuracy. Inflight TV cameras resulted in the accuracy of 0.7 (1σ) and 0.5 (1σ) in pixel and line directions, respectively. Observed Mars image through TV cameras was found to represent light scattering surface in the Martian atmosphere rather than the Mars surface. A simple limb fit algorithm yielded sufficient accuracy (~ 30 km 1σ) to estimate the center location of Mars.

The Mars limb data combined with radio data gave a B-plane estimate within 25 km of the current best estimate, with an uncertainty of 70 km. The addition of Mars limb data to radio data reduces sensitivity to planetary ephemeris errors, nongravitational spacecraft acceleration errors and Earth-based tracking station location errors. The limb data was found to be somewhat sensitive to the amount of radio data used but not to Mars ephemeris errors. A combination of optical and radio data yields best results, and much earlier than either data can separately.

Results from Mariner IX were an order of magnitude better than those from the MM'69 mission. This can be attributed primarily to better TV pointing estimation owing to the inflight calibration performed. Despite this the major source of error was still found to be the TV pointing. For future missions significant improvement in navigation using limb data would result from two TV cameras wherein one of them would be used for imaging stars to reduce TV camera pointing errors.

ACKNOWLEDGEMENT

The authors wish to acknowledge the efforts of C.H. Acton, Jr., M. Ananda, M.H. Bantell, Jr., G.H. Born, W.G. Breckenridge, T.C. Duxbury, S.N. Mohan in support of this analysis, and JPL's Image Processing Laboratory for providing photographs and reseau locations.

REFERENCES

1. Duxbury, T. C., and Breckenridge, W. G., "Mariner Mars 1969 Optical Approach Navigation," paper presented at the AIAA 8th Aerospace Sciences Meeting, New York, N. Y., January 19-21, 1970.
2. Duxbury, T. C., Born, G. H., and Jerath, N., "Viewing Phobos and Deimos for Navigating Mariner 9," paper presented at the AIAA/AAS Astrodynamics Conference, Palo Alto, California, September 11-12, 1972.
3. Jerath, N., "Evaluation of Optical Data for Mars Approach Navigation," paper presented at the Institute of Navigation Annual Meeting, West Point, N. Y., June 27-29, 1972.
4. Duxbury, T. C., and Ohtakay, H., "In-flight Calibration of an Inter Planetary Navigation Instrument," Journal of Spacecraft and Rockets, Vol. 8, No. 10, October 1971.
5. Breckenridge, W. G., and Acton, Jr., C. H., "A Detailed Analysis of Mariner Nine TV Navigation Data," paper presented at the AIAA Guidance and Control Conference, Stanford University, Palo Alto, California, August 14-16, 1972.
6. Steinbacker, R. H., et al., "Mariner to Mars," Science, January 21, 1972.
7. Personal Communication with S. K. Wong of the Jet Propulsion Laboratory.
8. Jordan, J. F., et al., "The Effects of Major Error Sources on Planetary Spacecraft Accuracies," AIAA paper No. 70-1077; August 1970.
9. Duxbury, T. C., "Navigation Data from Mariner Mars 1969 TV Pictures," Navigation, Vol. 17, No. 3, Fall 1970.

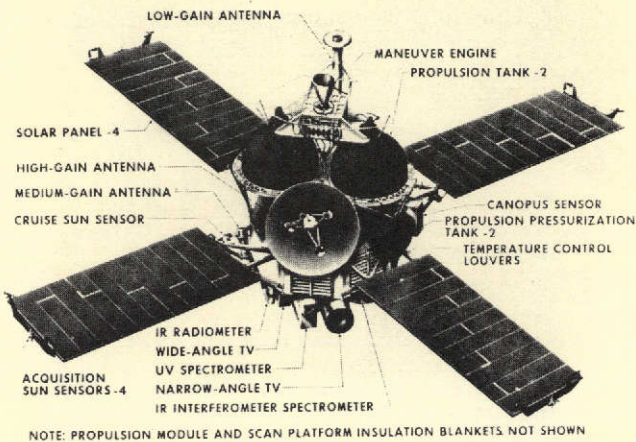


Fig. 1 Mariner Mars 1971 spacecraft, showing scan platform, science instruments, and sensors.

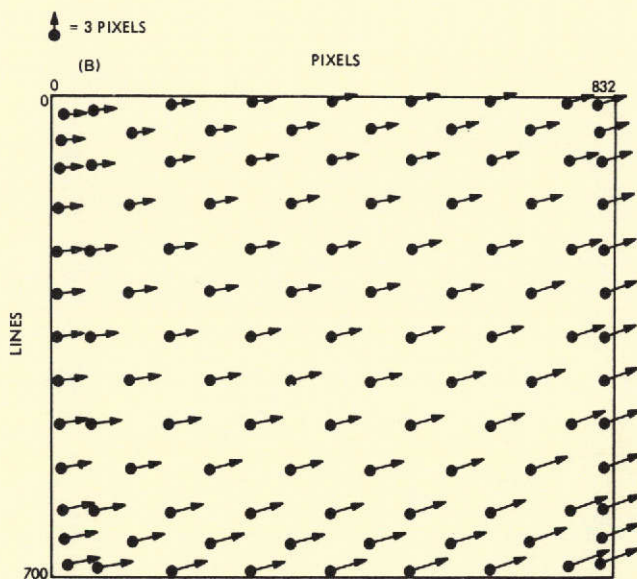
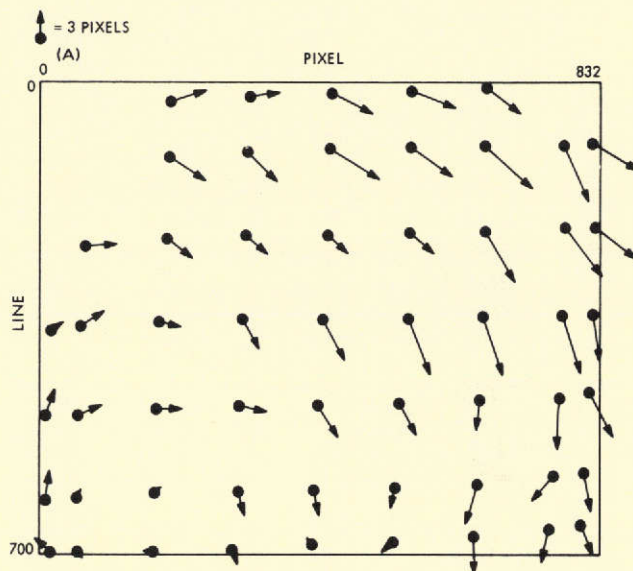


Fig. 3 Change in observed reseau locations of (a) narrow-angle TV, and (b) wide-angle TV.

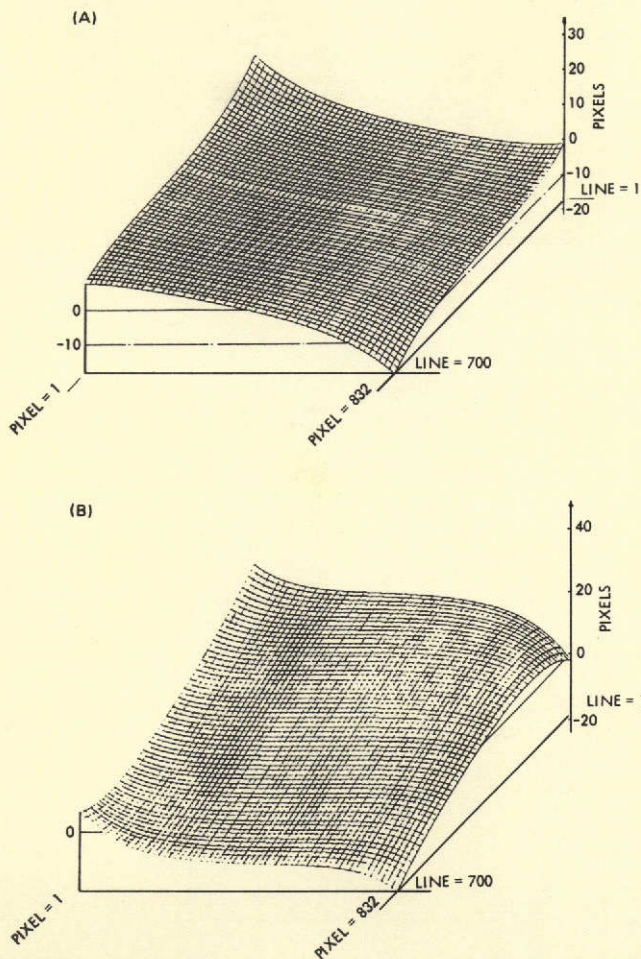


Fig. 2 Narrow angle TV geometric distortion (a) in line direction, and (b) in pixel direction.

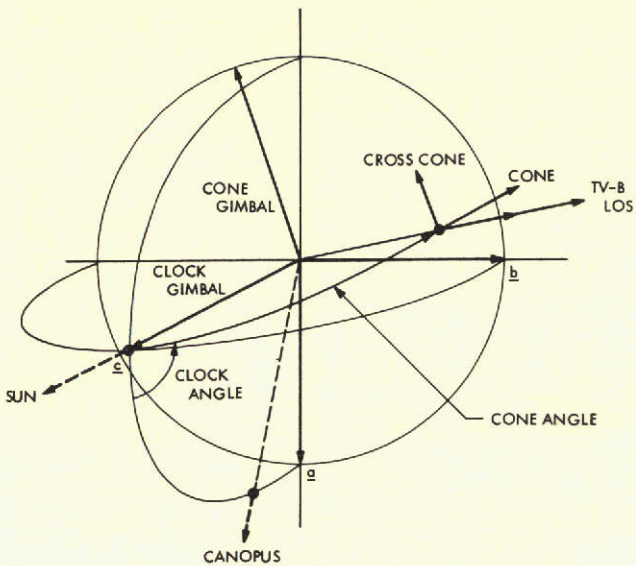


Fig. 4 Clock-Cone, scan platform gimbal, and TV coordinate systems.

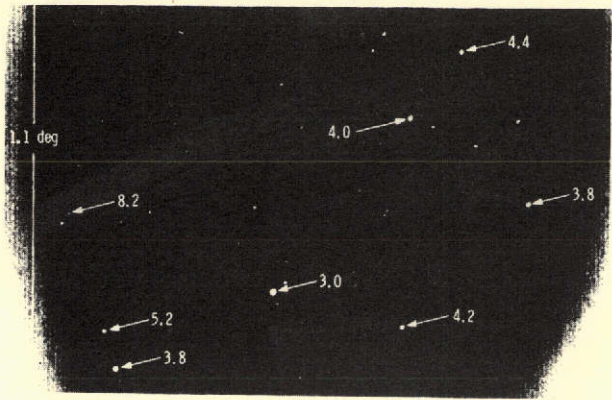


Fig. 5 Typical TV picture of the Pleiades.

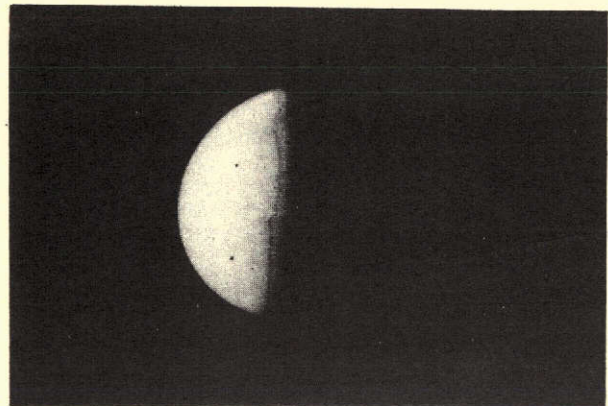


Fig. 6 Typical Mars lit limb TV picture.

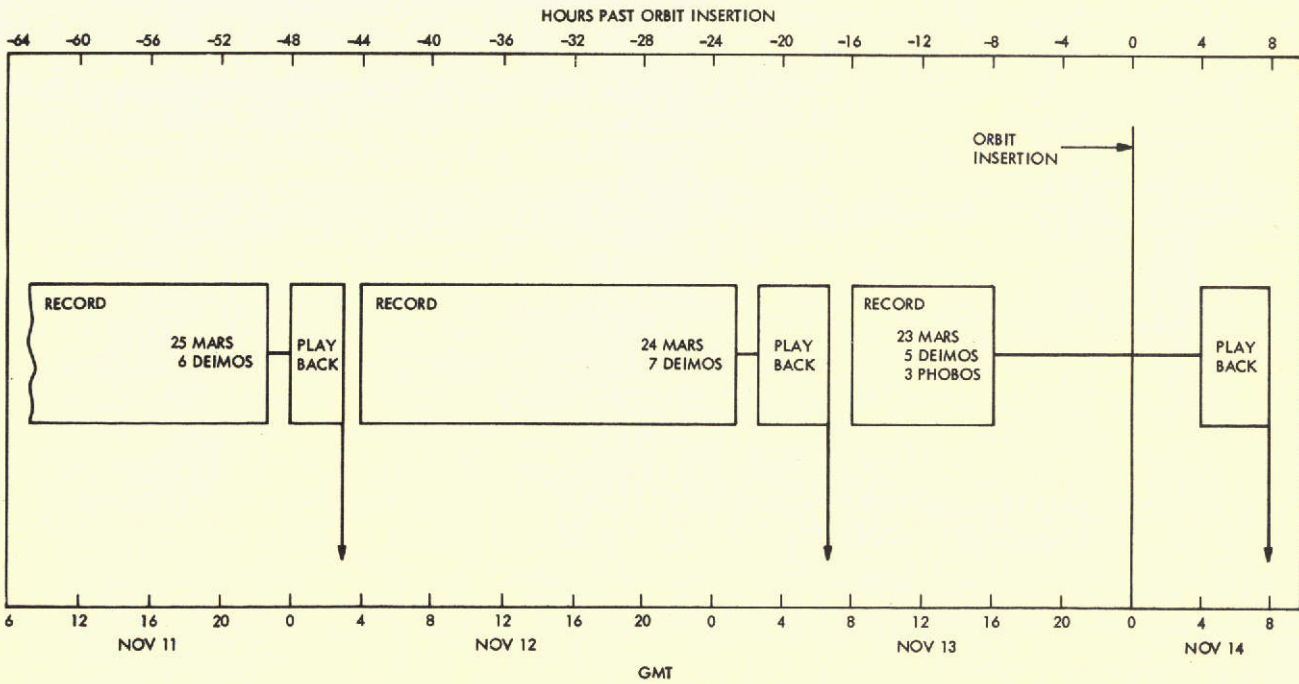


Fig. 7 Approach picture sequence.

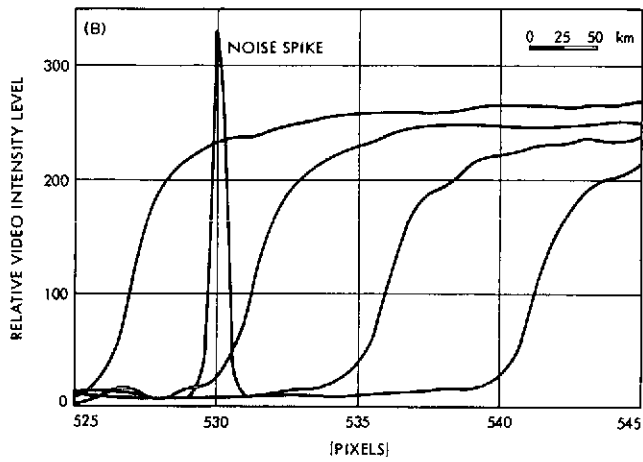
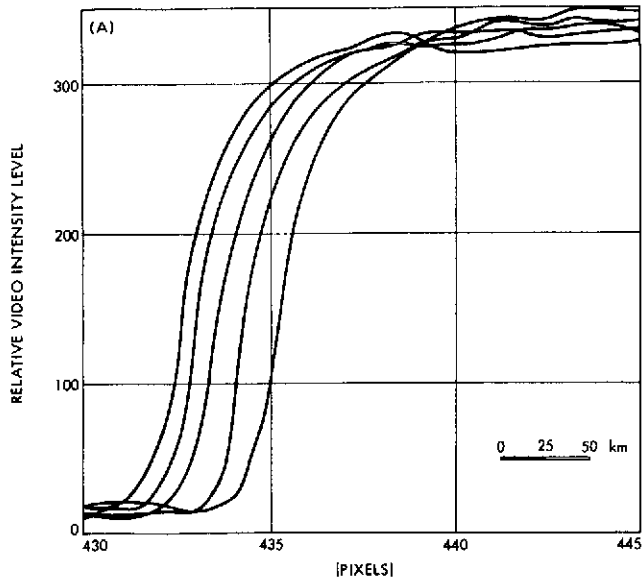


Fig. 8 Mars limb image structures (a) near the equator, and (b) in the polar regions.

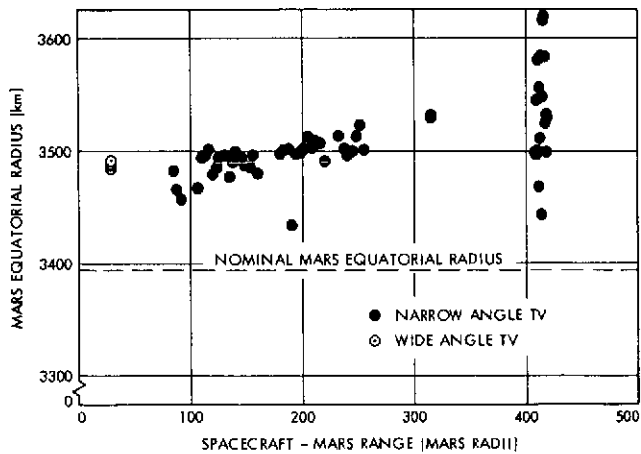


Fig. 9 Observed Mars mean equatorial radius.

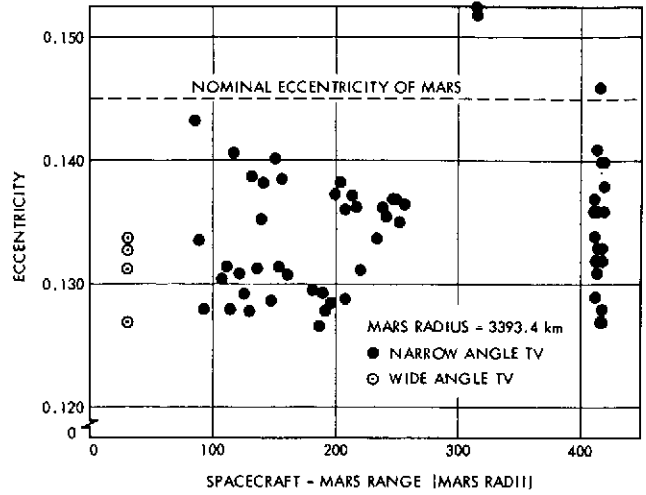


Fig. 10 Observed Mars shape parameter.

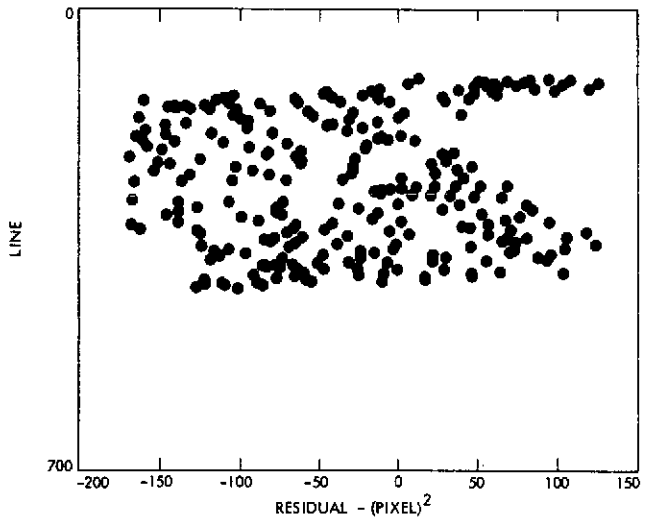


Fig. 11 Mars lit limb fit residuals.

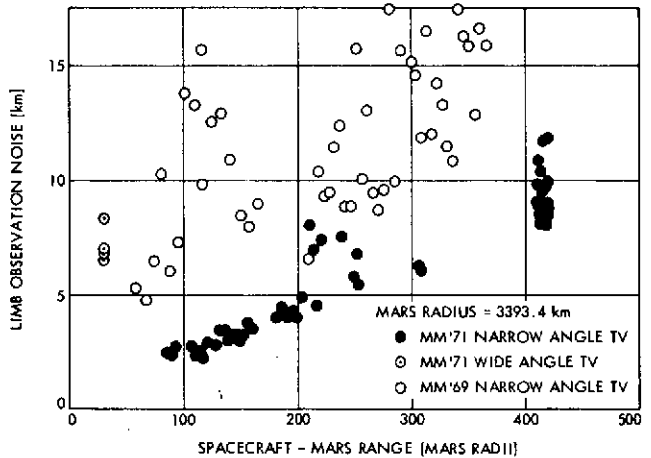


Fig. 12 Mars lit limb observation noise statistics.

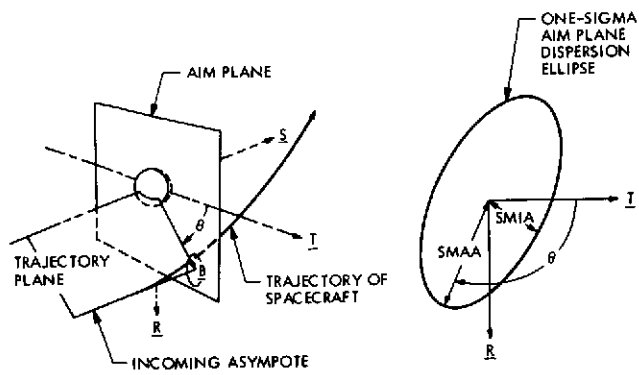


Fig. 13 B-plane definitions.

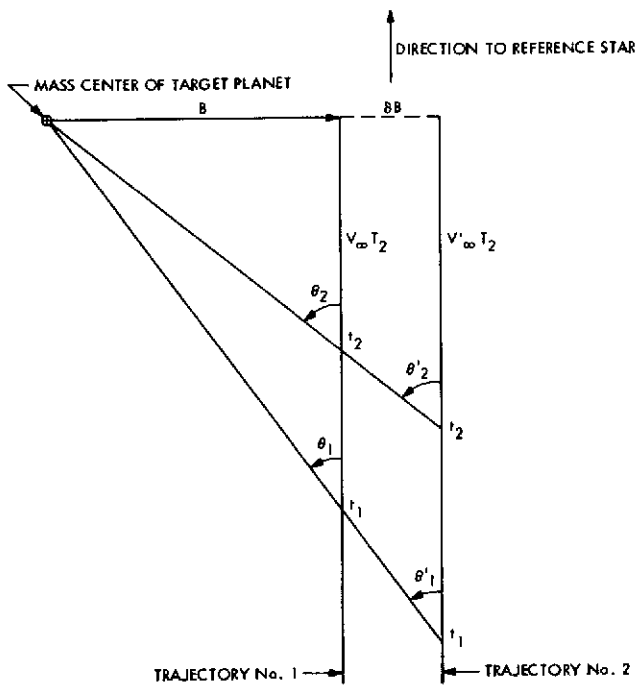


Fig. 14 Approach trajectory geometry.

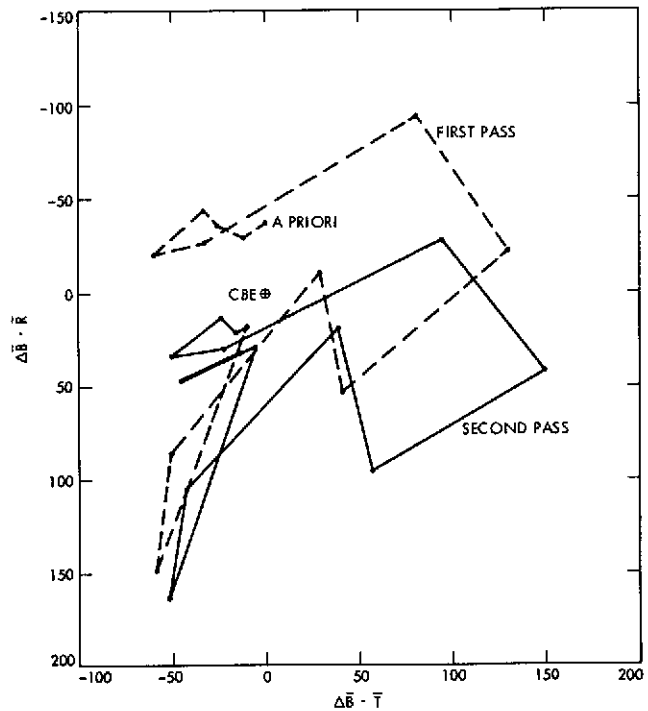


Fig. 15 Simulated real-time results.

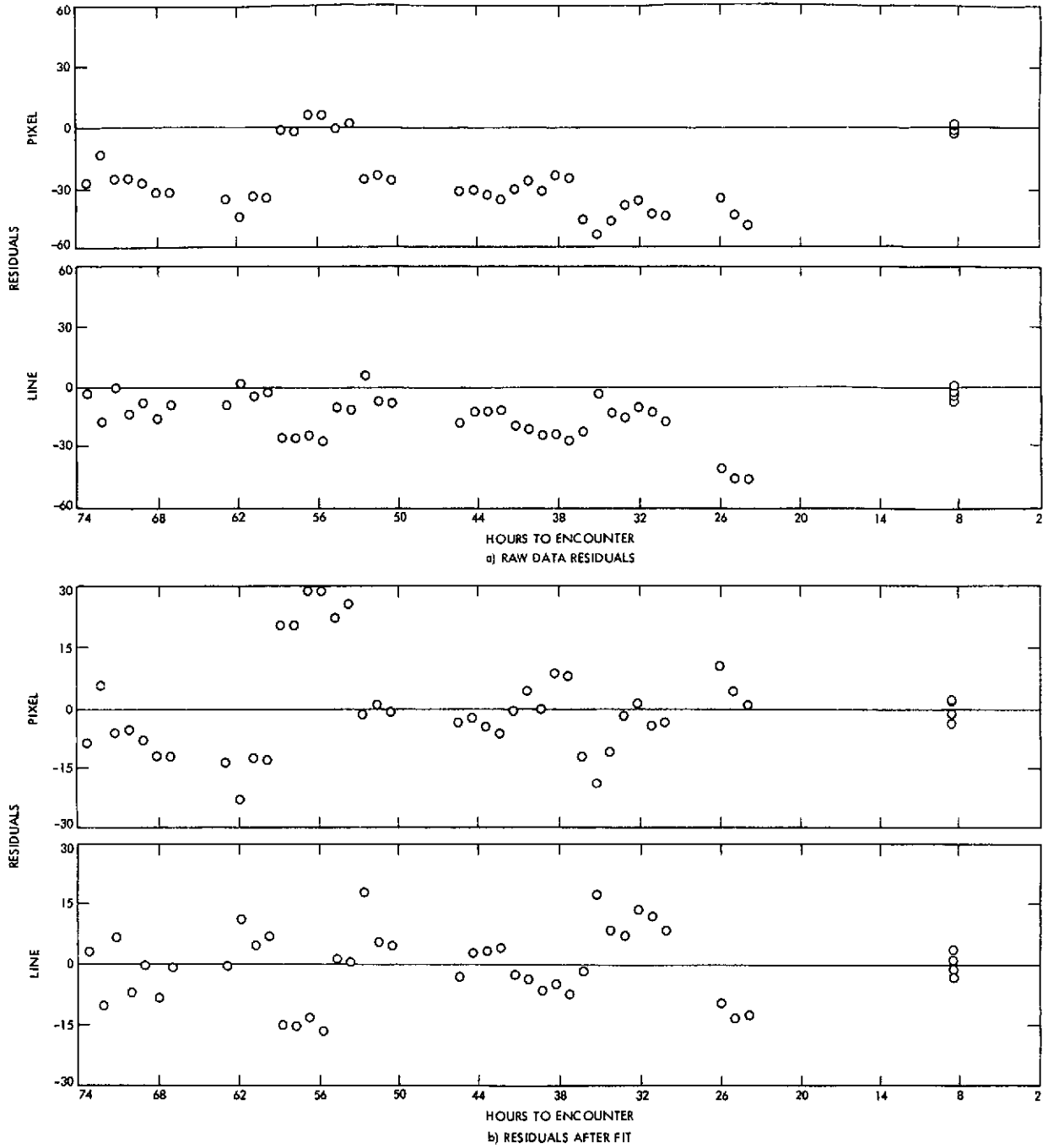


Fig. 16 POS data residuals.

315<

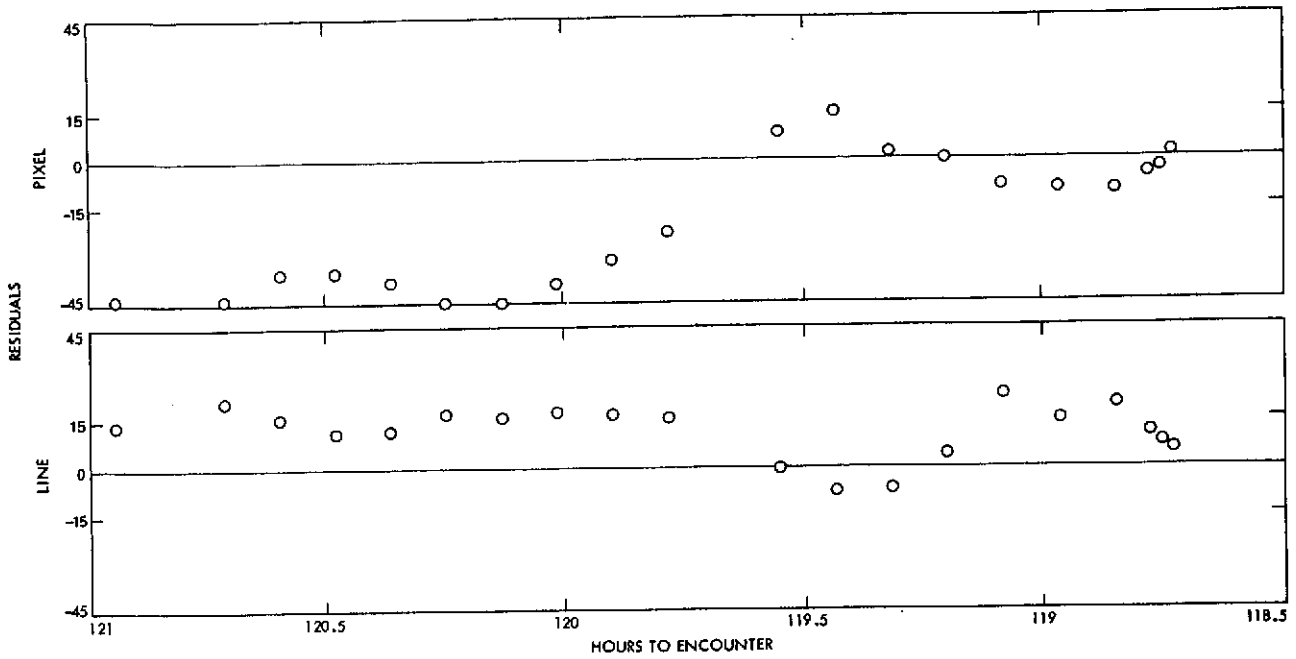


Fig. 17 Mars-Calibration sequence raw data residuals.

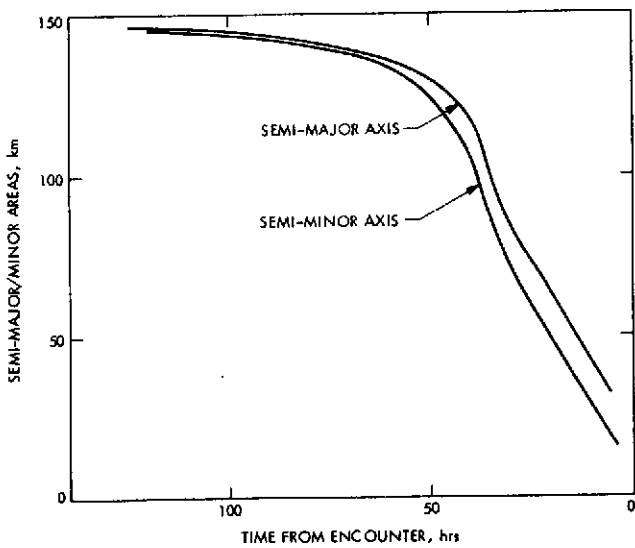


Fig. 18 Expected trajectory estimation accuracy.

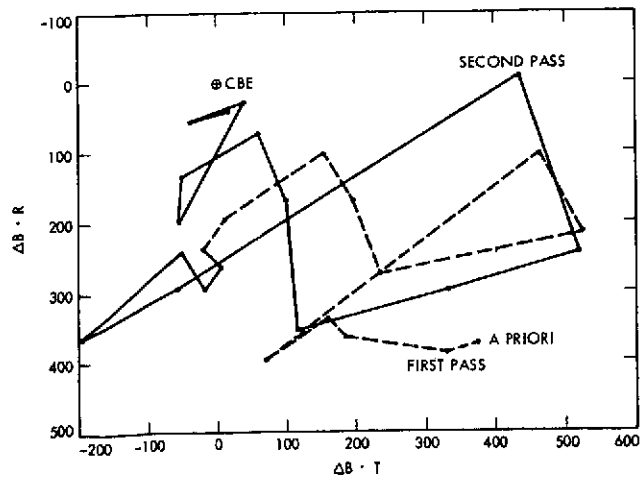


Fig. 19 Sensitivity to Mars ephemeris error.

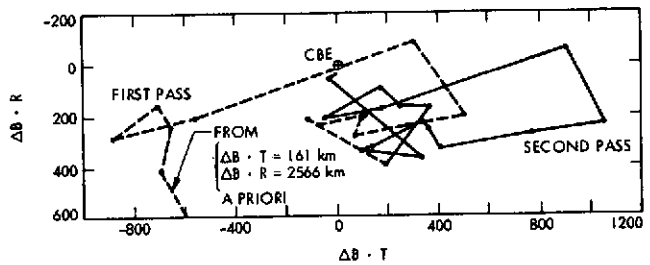


Fig. 20 Optical data solution from mid-course maneuver.

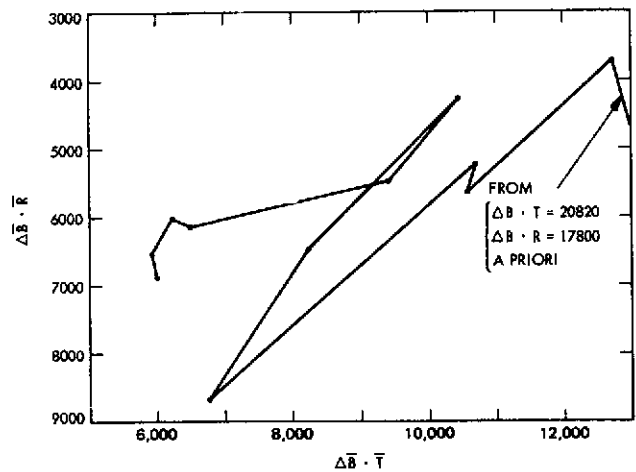


Fig. 21 Optical data solution from injection.

APPENDIX S
PHOBOS: CONTROL NETWORK ANALYSIS

317<

PHOBOS: CONTROL NETWORK ANALYSIS

Thomas C. Duxbury

Jet Propulsion Laboratory

California Institute of Technology

Pasadena, California

ABSTRACT

Initial analysis of the Mariner 9 high resolution pictures of Phobos surface features has been completed. A control network of fifty landmarks has been established and used to determine the physical size, shape, orientation, libration, and topography properties of Phobos. The results verified the synchronous rotation of Phobos and revealed a libration of approximately 5 deg in the orbit plane of Phobos. A preliminary map of Phobos, based on the control network analysis, is given.

318<

SYMBOLS

a		length of ellipsoid longest axis
b		length of ellipsoid intermediate axis
c		length of ellipsoid shortest axis
h		height of surface feature relative to local mean surface
\bar{p}		inertially referenced, Mars-centered Phobos position vector
R		(3 x 3) small angle rotation matrix for libration
\bar{u}		surface feature position vector in Phobos body-fixed coordinates
\bar{v}		inertially referenced, Mars-centered Phobos velocity vector
u_x	}	direction cosines of \bar{u} in body-fixed coordinate system
u_y		
u_z		
\bar{x}	}	Phobos centered, body-fixed reference system axes
\bar{y}		
\bar{z}		
ϕ		body-fixed latitude of surface feature
λ		body-fixed longitude of surface feature
θ_x	}	small angle rotation (libration) angles about \bar{x} , \bar{y} and \bar{z}
θ_y		
θ_z		

319<

I. INTRODUCTION

The Mariner Mars 1971 mission (Steinbacher and Haynes, 1973), directed by the Jet Propulsion Laboratory of the California Institute of Technology, obtained over one hundred TV pictures of the two moons of Mars-Phobos and Deimos. The TV team was headed by Harold Masursky of the U. S. Geological Survey and James Pollack of NASA/Ames Research Center led the Satellite Astronomy Discipline Group within the TV team. The satellite pictures allowed about seventy percent of Phobos and about forty percent of Deimos to be viewed for the first time at kilometer level resolution.

This article presents the initial analysis of surface feature locations observed in the Mariner TV data to determine physical properties of Phobos. Additional results on satellite ephemerides, photometry, existence of a regolith, search for additional satellites, internal structure, rotational evolution, age and crater density are discussed by Pollack et al., 1972 and Pollack et al., 1973. Also, a catalog of the Mariner 9 satellite pictures is given by Veverka et al., 1974 in this issue of ICARUS.

Initially, a body-fixed coordinate system and reference surface was chosen to define the locations of surface features comprising a control network. TV image coordinates of the control points were processed to determine the body-fixed coordinates of the control points, the topography of Phobos, and to search for the existence of libration. Also improved knowledge of the size and shape of Phobos would be obtained over previous published values (Pollack et al., 1973) determined from computer generated picture overlays.

Processing a control network of 50 surface features revealed the existence of an in-plane libration of about 5 deg, surface height variation of over 10 percent of the local radius and a mean surface slightly smaller than previously published.

An initial map of Phobos is presented based on the processed control points together with a listing of the control point locations.

II. BODY-FIXED COORDINATES

In defining the locations of surface features, a body-fixed reference system and reference surface were established. For planetary mapping, it is common practice to use a sphere or spheroid as the reference surface (Davies and Arthur, 1973). Planet shapes, constrained by internal gravitational forces, are of general spherical form. However, for a small body such as Phobos, the gravitational forces are too small to constrain its shape and marked variations from a sphere are noted. Surface models considered for Phobos were an oblate spheroid, an ellipsoid and a general harmonic expansion with zonal and tesseral terms. An ellipsoid was chosen for the Phobos reference surface to give additional model flexibility over the sphere and spheroid while still maintaining simple physical interpretation which can be lost with a harmonic expansion.

A body-fixed orthogonal reference system \overline{xyz} was defined with \overline{x} along the longest axis of the ellipsoid, \overline{y} along the intermediate axis and \overline{z} along the shortest ellipsoid axis (Fig. 1). A point on the surface of the ellipsoid expressed in the \overline{xyz} reference system is defined by:

$$\overline{u} = u \begin{bmatrix} \cos \phi \cos \lambda \\ - \cos \phi \sin \lambda \\ \sin \phi \end{bmatrix} = u \begin{bmatrix} u_x \\ u_y \\ u_z \end{bmatrix} \quad (1)$$

where λ is the longitude of the point (measured positive west), ϕ is the latitude of the point, u is the distance from the center of figure to the point on the surface, and u_x, u_y, u_z are the direction cosines of \overline{u} in \overline{xyz} . For an ellipsoid whose

longest, intermediate, and shortest axes are of lengths a, b, and c respectively, the radius u is given by:

$$u = (abc) / (b^2 c^2 u_x^2 + a^2 c^2 u_y^2 + a^2 b^2 u_z^2)^{1/2} + h \quad (2)$$

where h is the height relative to the local mean surface.

The orientation of the body-fixed \overline{xyz} system in a Mars-centered, inertial reference system was defined as if Phobos was in a dynamically stable, synchronous rotation about Mars (as indicated by initial observations). Under these conditions, the longest axis (\overline{x}) would be along the Phobos-Mars direction, the intermediate axis (\overline{y}) would be in the orbit plane and the smallest axis (\overline{z}) would be normal to the orbit plane of Phobos (Fig. 2). Given the position vector \overline{p} and the velocity vector \overline{v} of Phobos in a Mars-centered, inertial reference system (e.g., 1950.0 Earth Equator), the body-fixed coordinate axes in the inertial reference system are computed by

$$\begin{aligned} \overline{x} &= -\overline{p}/|\overline{p}| \\ \overline{z} &= \overline{p} \times \overline{v} / |\overline{p} \times \overline{v}| \\ \overline{y} &= \overline{z} \times \overline{x} \end{aligned} \quad (3)$$

A rotation matrix R (eqn 4) comprised of three small angle rotations θ_x , θ_y , and θ_z about the $\overline{x\overline{y}\overline{z}}$ axes was introduced to account for orientation differences (libration) between the assumed \overline{xyz} orientation and the true body-fixed \overline{xyz} system.

$$R = \begin{bmatrix} 1 & -\theta_z & \theta_y \\ \theta_z & 1 & -\theta_x \\ -\theta_y & \theta_x & 1 \end{bmatrix} \quad (4)$$

It is noted that this formulation ties the body-fixed reference system to a mean surface that will be determined from data processing and not to an adopted pole or surface feature as is done with planetary bodies.

III. CONTROL NETWORK

Using the above equations, computer generated overlays were drawn for each of the high resolution satellite pictures with θ_x , θ_y , and θ_z (Eq. 4) set to zero. The ellipsoid axes a, b, and c (Eq. 2) were varied until a reasonable match was obtained between the drawn ellipsoids and the lit limb of Phobos (Fig. 1). Because of the highly irregular surface which was only partially illuminated in the pictures, the drawn ellipsoids for Phobos represent more of an upper bound of the surface as indicated by the surface generally being inside the overlays. These overlays with a latitude and longitude grid network were sufficient to initially verify that Phobos was in a synchronous rotation about Mars with a libration amplitude of less than ten degrees. Overlays were then used in identifying surface features from picture to picture to establish a control network of 50 landmarks. A priori body-fixed coordinates (ϕ , λ) were obtained by interpolating the positions of the surface features relative to the latitude/longitude grids and assuming the landmarks were on the mean surface (e.g., $h = 0$).

The selection of surface features was significantly limited by the total surface coverage obtained, the amount of overlap in the pictures and the lighting geometry. Figure 3 indicates the total surface coverage obtained. Sub Mariner 9 points, at the times when high resolution pictures were obtained, are plotted in Phobos fixed coordinates as a function of the range to Phobos. Good southern hemisphere coverage was obtained with overlapping pictures taken at ranges of 5 to 10 thousand km. Northern hemisphere coverage was very limited and at ranges of 10 to 20 thousand km. Also, the sub Mars point on Phobos had very poor coverage with essentially no coverage of the eastern equatorial region of Phobos. Figure 4 gives an example of the viewing coverage obtained. In all, only about

70 percent of Phobos was viewed at a surface resolution greater than 1 km. Twelve of the Phobos pictures, processed for this analysis, are indicated in Figure 3 by the symbols which are darkened in.

IV. DATA REDUCTION

For the data reduction, special hardcopy products of the TV imaging data were used. High pass filtering, stretching and magnification of the Phobos imaging data were performed by the JPL Image Processing Laboratory (Levinthal, et al., 1973) to accentuate the surface features from the limb to the terminator. Image locations in picture coordinates were measured manually from hardcopy and used as observables in the data reduction. Computed observables were based on a priori control point locations determined from overlays, spacecraft trajectory data determined from earth-based radio metric data, celestial TV camera pointing data determined from telemetered spacecraft data and Phobos ephemerides obtained by using Mariner 9 imaging data to update parameter values in Wilkins' Theory (Wilkins, 1967).

The data reduction employed a sequential formulation of the minimum variance filter which estimated the following 213 parameters: 1) coordinates (ϕ , λ , h) of each control point; 2) the 3 ellipsoid axes a , b , c which define the mean surface; 3) 3 TV pointing errors for each picture; and 4) three libration angles θ_x , θ_y , θ_z for each picture. It was assumed that the spacecraft trajectory and orbit of Phobos were perfectly known. The relative spacecraft-Phobos position uncertainty of 30 km would be interpreted by the estimation process as a rotation (libration) of Phobos with a maximum amplitude of 0.3 deg. TV camera pointing errors and libration angles were assumed to be independent from picture to picture reducing the number of parameters to be estimated at any single time to 159. The data was iterated five times to obtain convergence. Data residuals of 0.3 of a picture element (1σ) were obtained after convergence.

V. RESULTS

Results of the data processing verified that Phobos is in a synchronous rotation about Mars and that it is in a dynamically stable orientation with its longest axis toward Mars, its intermediate axis in the orbit plane of Phobos, and its smallest axis normal to the orbit plane. The axes of the ellipsoid which define the mean surface were determined to be slightly smaller than those determined using overlays as expected.

A libration amplitude of about 5 deg was suggested by the data processing as shown in Figure 5. Image location residuals represented by arrows give the difference between the computed locations (tip of arrows) and the observed locations (base of arrows) of the control points. The computed locations in Figure 5a were based on control point coordinates determined from nine other pictures and with the libration angles (Eq. 4) constrained to be zero for this picture. The systematic residuals reflect a rotation about the south pole which is removed in Figure 5b, giving much smaller and more random residuals. A 5 deg rotation in θ_z was determined which corresponds to a 5 deg libration angle in the Phobos orbit plane. This is consistent with previous predictions (Burns, 1971). Libration periods were not determined because of the time separation between pictures (days to weeks) and because the pictures were taken in a limited region of the Phobos orbit. Therefore, this angle represents the largest angle observed and may not be the libration amplitude.

VI. RECOMMENDATIONS

As was evidenced by Figure 3 and the map of Phobos, a significant portion of Phobos still remains unobserved. Only about one half of Deimos was viewed. Future missions such as Viking should attempt to complete the coverage of Phobos and Deimos with pictures giving high resolution and stereo coverage. The

sub-Mars point and other potential landing sites for future planetary exploration should be given priority. Also, the coverage should be obtained throughout the orbits of the satellites and with a sufficient frequency to allow the determination of both the amplitudes and periods of libration. Pictures obtained outside of 10,000 km by Mariner 9 were of little use to the satellite cartography effort. Spacecraft orbits with low inclinations to Mars equator are ideal for satellite photography giving many opportunities for close encounters. These close encounters could possibly be used to determine the satellite masses from radio metric tracking of spacecraft accelerations.

The major errors limiting the reduction of the Mariner 9 imaging data of the satellites for cartography were TV pointing errors and relative spacecraft-satellite position errors. Also, the limited coverage and overlap of the Mariner 9 pictures restricted a complete separation of mean surface, feature heights and libration parameters. Viking instrumentation, however, can allow a significant reduction in these limiting errors. The Viking orbiter has two high resolution (narrow angle) cameras whose optical axes are not boresighted. Satellites could be imaged with one camera at normal exposures while stars could be imaged using long exposures with the second camera. The star images would yield an accurate determination of camera pointing allowing the spacecraft and satellite orbit parameters to be included in the cartography process to minimize relative position errors.

VII. ACKNOWLEDGMENTS

The author wishes to thank Mike Wolf of the JPL Image Processing Laboratory for the picture processing support. This paper presents one phase of research carried out at the Jet Propulsion Laboratory, California Institute of Technology, Pasadena, California under NASA Contract No. NAS7-100.

VIII. REFERENCES

- Burns, J. A. (1971). The Dynamical Characteristics of Phobos and Deimos, Rev. Geophysics, Space Phys. 10, 463.
- Davies, M. E., and Arthur, D. W. G., (1973). Martian Surface Coordinates. JGR 78.
- Levinthal, E. C., Green, W. G., Cutts, J. A., Jahelka, E. D., Johansen, R. A., Sander, M. J., Seidmann, J. B., Young, A. T., and Soderblom, L. A., (1973). Mariner 9 - Image Processing and Products. ICARUS 18, 1
- Pollack, J. B., Veverka, J., Noland, M., Sagan, C., Hartmann, W. K., Duxbury, T. C., Born, G. H., Milton, D. J., and Smith, B. A. (1972), Mariner 9 Television Observations of Phobos and Deimos. ICARUS 17, 2.
- Pollack, J. B., Veverka, J., Noland, M., Sagan, C., Duxbury, T. C., Acton, C. H., Born, G. H., Hartmann, W. K., Smith, B. A., (1973). Mariner 9 Television Observations of Phobos and Deimos II., JGR 78.
- Steinbacher, R. H. and Haynes, N. R., (1973). Mariner 9 Mission Profile and Project History. ICARUS 18, 1.
- Veverka, J., Noland, M., Logan, C., Quam, L., Tucker, W., Eross, B., Duxbury, T., and Green, W. (1974). High Resolution Photography of Phobos and Deimos. ICARUS in press.
- Wilkins, G. A., (1967). In Mantles of the Earth and Terrestrial Planets, edited by Runcorn, John Wiley, London.

327<

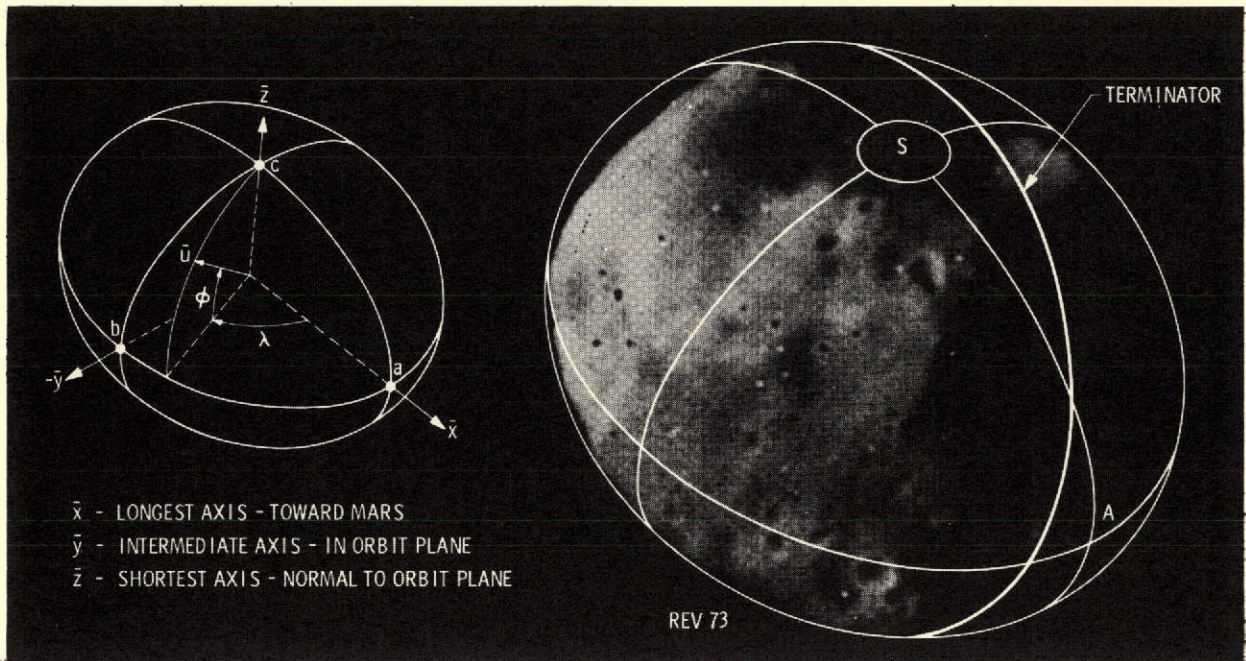


Fig. 1. Computer-drawn overlays were initially used to determine the mean surface of Phobos. The axes a, b, c of the ellipsoid were varied to match the pictures as is shown for a picture obtained on the 73rd revolution (Rev 73) of Mariner 9 about Mars. The letter A indicates the anti-Mars point and S indicates the south pole.

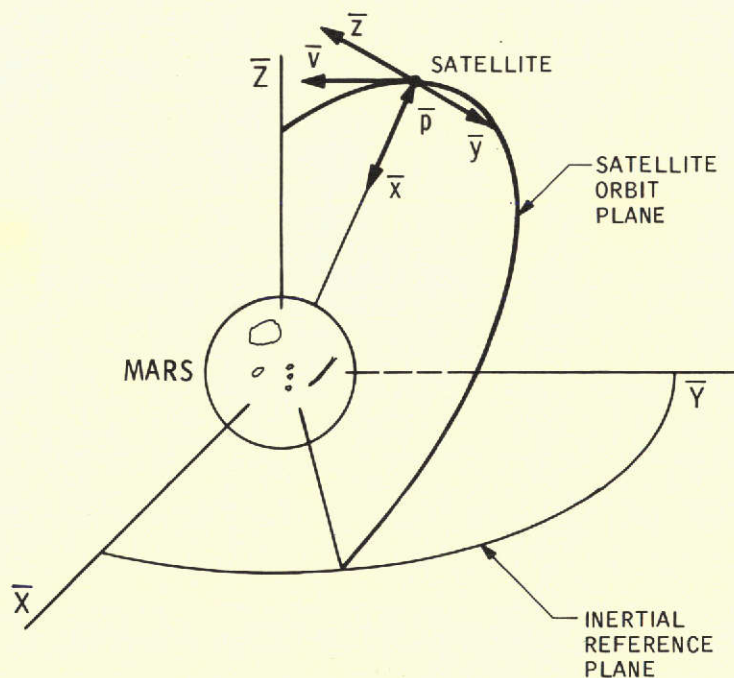


Fig. 2. The satellite position vector \bar{p} and velocity vector \bar{v} are used to define a body-fixed reference system $\bar{x} \bar{y} \bar{z}$ for a satellite in synchronous rotation.

328<

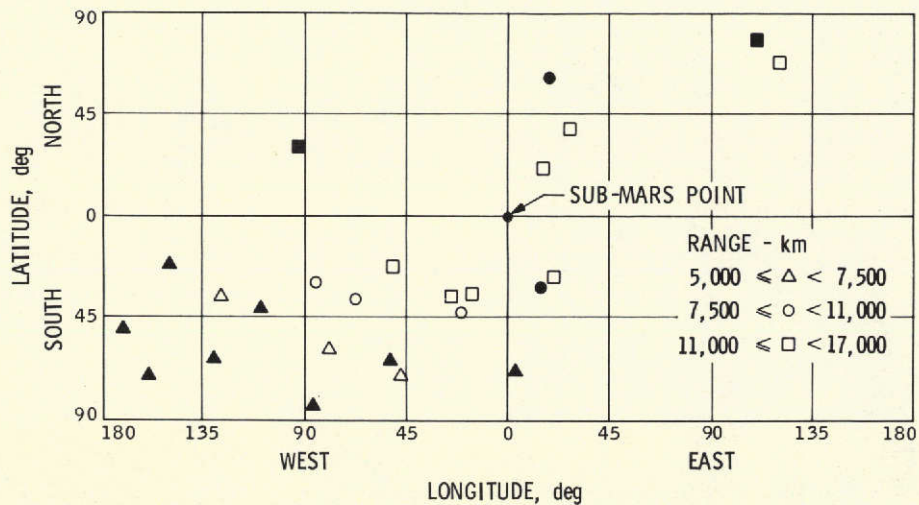


Fig. 3. The sub-Mariner 9 points are indicated as a function of range at which the high-resolution Phobos pictures were obtained. The symbols which are filled in indicate the picture used in the data analysis.

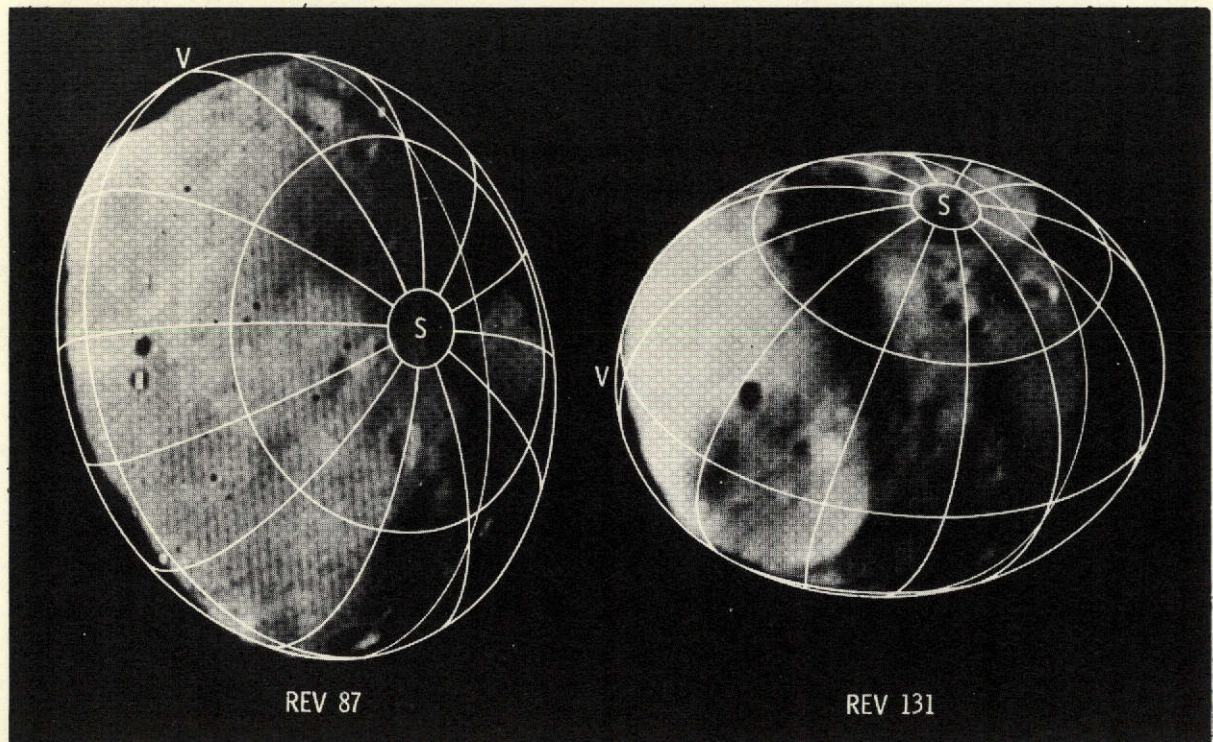


Fig. 4. Overlays with latitude-longitude grids were used to initially verify a synchronous rotation and to establish a control network of surface features. These pictures obtained on revolutions 87 and 131 give an indication of the surface coverage obtained. The pictures have not been scaled to account for the difference in ranges to Phobos. The letter V indicates the sub-Mars point.

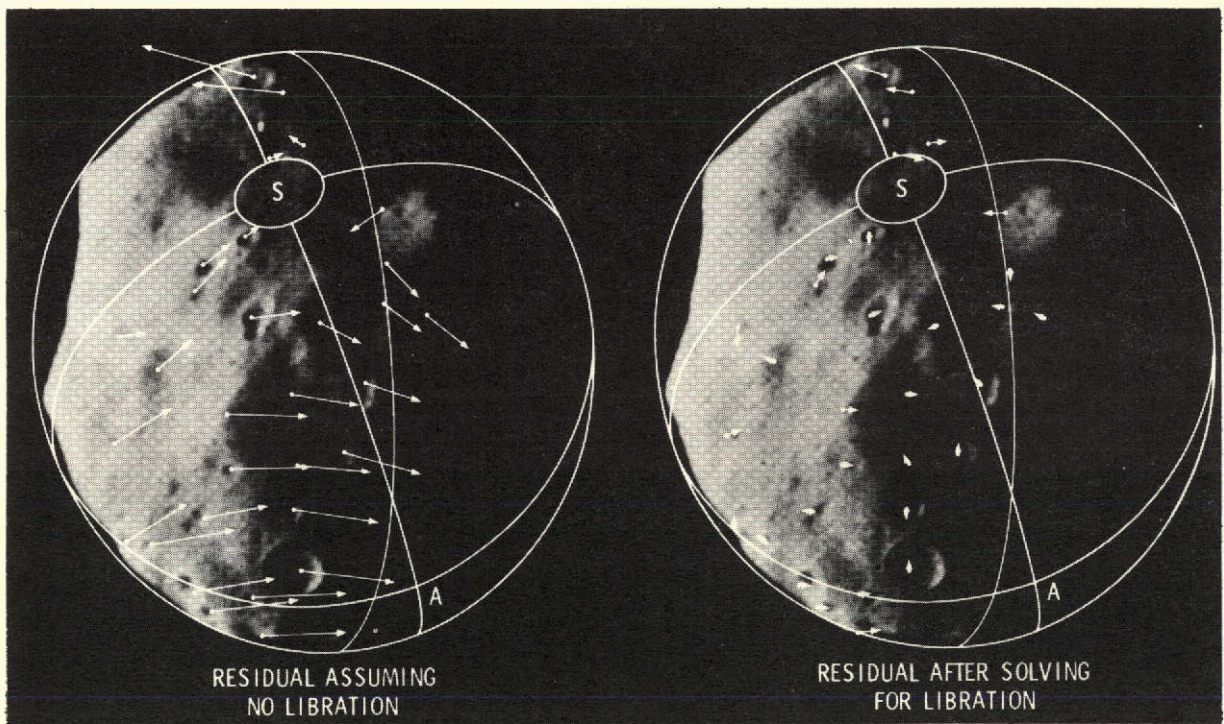


Fig. 5. Data processing residuals are displayed which indicate the existence of a 5-deg in-plane libration. The residuals were magnified by a factor of 10.